

Review

A multi-decadal view of seismic methods for detecting precursors of magma movement and eruption

Bernard A. Chouet ^{a,*}, Robin S. Matoza ^b

^a U.S. Geological Survey, Menlo Park, CA, USA

^b Institute of Geophysics and Planetary Physics, Scripps Institution of Oceanography, La Jolla, CA, USA

ARTICLE INFO

Article history:

Received 16 May 2012

Accepted 29 November 2012

Available online 7 December 2012

Keywords:

Volcano seismology

Volcanic earthquakes

Volcanic unrest

Seismic source mechanisms

Seismic imaging

Radiographic imaging

ABSTRACT

With the emergence of portable broadband seismic instrumentation, availability of digital networks with wide dynamic range, and development of new powerful analysis techniques made possible by greatly increased computer capacity, volcano seismology has now reached a mature stage where insights are rapidly being gained on the role played by magmatic and hydrothermal fluids in the generation of seismic waves. Volcanoes produce a wide variety of signals originating in the transport of magma and related hydrothermal fluids and their interaction with solid rock. Typical signals include (1) brittle failure earthquakes that reflect the response of the rock to stress changes induced by magma movement; (2) pressure oscillations accompanying the dynamics of liquids and gases in conduits and cracks; and (3) magma fracturing and fragmentation. Oscillatory behaviors within magmatic and hydrothermal systems are the norm and are the expressions of the complex rheologies of these fluids and nonlinear characteristics of associated processes underlying the release of thermo-chemical and gravitational energy from volcanic fluids along their ascent path. The interpretation of these signals and quantification of their source mechanisms form the core of modern volcano seismology. The accuracy to which the forces operating at the source can be resolved depends on the degree of resolution achieved for the volcanic structure. High-resolution tomography based on iterative inversions of seismic travel-time data can image three-dimensional structures at a scale of a few hundred meters provided adequate local short-period earthquake data are available. Hence, forces in a volcano are potentially resolvable for periods longer than ~1 s. In concert with techniques aimed at the interpretation of processes occurring in the fluid, novel seismic methods have emerged that are allowing the detection of stress changes in volcanic structures induced by magma movement. These methods include (1) ambient noise interferometry, in which the ambient seismic noise is used to probe temporal changes in volcanic structures; (2) the measurement of seismic anisotropy, where changes in the alignment of fluid-filled microcracks and pore space are monitored to assess the response of the crust to pressurization of a magmatic system; and (3) the detection of systematic changes in fault plane solutions of volcano-tectonic earthquakes caused by local stress perturbations during conduit pressurization. As new seismic methods refine our understanding of seismic sources and behavior of volcanic structures, we face new challenges in elucidating the physico-chemical processes that cause volcanic unrest and its seismic and gas-discharge manifestations. Future important goals toward meeting those challenges must include a better understanding of the key types of magma movement, degassing and boiling events that produce characteristic seismic phenomena, along with a quantitative understanding of multiphase fluid behavior under dynamic volcanic conditions. Realizing these goals will be essential for the development of an integrated model of volcanic behavior and will require multidisciplinary research involving detailed field measurements, laboratory experiments, and numerical modeling.

Published by Elsevier B.V.

Contents

1. Introduction	109
2. Seismic sources in volcanoes	110
2.1. Waveform inversion	112
3. VLP seismicity	115

* Corresponding author.

E-mail addresses: chouet@usgs.gov (B.A. Chouet), rmatzo@ucsd.edu (R.S. Matoza).

3.1.	Source mechanisms representative of silicic systems	116
3.2.	Source mechanisms representative of basaltic systems	118
3.3.	Source mechanisms representative of magma-hydrothermal interactions	125
4.	LP Seismicity	127
4.1.	Fluid resonance and crack waves	127
4.2.	Excitation mechanism of LP seismicity	128
4.3.	Hybrid events	130
4.4.	Self-sustained oscillations	130
4.5.	Magmatic-hydrothermal interactions	131
4.6.	Magmatic degassing	135
4.7.	Brittle failure of melt	140
4.8.	Solid extrusion dynamics and near-vent plug stick-slip	143
4.9.	Deep Long-Period (DLP) seismicity	147
5.	VT Seismicity	147
5.1.	Intrusive geometry and related seismicity	148
5.2.	Large-scale dike intrusions	148
5.3.	Lower-crustal dike injections	150
5.4.	Gas-driven intrusions	151
5.5.	Local-regional stress interactions	152
5.6.	Changes in seismic anisotropy related to volcanic activity	153
6.	Classic and new methodologies	154
6.1.	Seismic interferometry	155
6.2.	Tomography	157
6.3.	Muon radiography	159
6.4.	Frequency-slowness method	159
6.5.	Spatial auto-correlation method	160
6.6.	Automatic detection and classification of volcanic signals	163
7.	Future trends	164
8.	Conclusions	165
Acknowledgments		166
References		166

1. Introduction

Magma transport is fundamentally episodic in character as a result of the inherent instability of magmatic systems at all time scales. This episodicity is reflected in seismic activity, which originates in dynamic interactions between gas, liquid and solid along geometrically complex magma transport paths. The geometrical complexity plays a central role in controlling flow disturbances and also providing specific sites where pressure and momentum changes in the fluid are effectively coupled to the Earth. In concert with this activity originating in the fluid are processes occurring in the solid rock, which manifest themselves mainly in the form of earthquakes associated with shear failures in the volcanic edifice. Whereas events originating in the fluid represent volumetric modes of deformation involving a localized conduit response to flow processes, the shear failures act as gauges that map stress concentrations distributed over a large volume surrounding magma conduits and reservoirs. These are called Volcano-Tectonic (VT) earthquakes to differentiate them from pure tectonic earthquakes, although they are indistinguishable from the latter in their broadband spectral characteristics and failure mechanisms.

Seismic signals originating in the dynamics of magmatic and hydrothermal fluids typically include Long-Period (LP) events and tremor (Chouet, 1996a). This terminology stems from the appearance of these signals on the short-period seismometers that have traditionally been used in volcano monitoring. LP events resemble small tectonic earthquakes in duration but differ in their characteristic frequency range and harmonic signature (see Section 4). Tremor is characterized by a signal of sustained amplitude lasting from minutes to days, and sometimes for months or even longer. In many instances, LP events and tremor are found to have essentially the same temporal and spectral components (Latter, 1979; Fehler, 1983), suggesting that a common source process, differing only in duration, underlies the two types of events. Accordingly, LP events and tremor are often

grouped under the common appellation LP seismicity. The periods at which LP seismicity is observed typically range from 0.2 to 2 s (Chouet, 1996a), and the characteristic oscillations of LP signals are commonly viewed as a result of acoustic resonance in a fluid-filled cavity or crack (see Section 4).

It is fairly straightforward to understand why resonance is such a pervasive phenomenon in volcanoes. Degassing is the main driving force behind most volcanic phenomena. The separation of vapor and melt phases leads to the formation of bubbles, whose presence decreases magma density, enhances magma buoyancy and propels magma ascent (Wilson and Head, 1981). The presence of bubbles in magma and hydrothermal fluids lowers the sound speed of these fluids, inducing a sharp contrast in velocity between the fluid and encasing solid, which favors the entrapment of acoustic energy in the fluid volume source region. For short-lived excitation, energy losses due to elastic radiation and dissipation processes at the source are the main factors affecting the duration of resonance, hence longer-duration signals are naturally enhanced in low-viscosity bubbly liquids. Other types of gaseous fluid mixtures may be even more efficient at sustaining source resonance. For example, gases laden with solid particles, or gases mixed with liquid droplets, may produce velocity contrasts that are similar to, or stronger than, those associated with bubbly liquids. In particular, dusty gases made of micron-sized particles, or misty gases made of micron-sized droplets, can sustain resonance at the source over durations that far exceed those achieved with bubbly fluids (Kumagai and Chouet, 2000).

In hydrothermal systems, a common LP excitation mechanism involves surges in the heat transfer from an underlying magma body (Kumagai et al., 2002a; Nakano et al., 2003; Kumagai et al., 2005; Waite et al., 2008; Matoza et al., 2009a). Heating by magmatic activity increases pressure in a steam-filled fracture to a critical threshold, at which point an abrupt opening of a pathway allows gas to escape suddenly, initiating a rapid pressure loss, collapse of the fracture, and

attendant resonance of the fluid remaining in the fracture. Once pressure is lost, lithostatic pressure seals the escape pathway shut, allowing the next cycle of pressure recharge to begin.

In low-viscosity basaltic systems, LP signals have been observed to be closely related to a broadband source process associated with the unsteady transport of magma and gases through conduits (Ohminato et al., 1998; Chouet et al., 2010). Conduit discontinuities apparently play a key role by providing sites where pressure and momentum changes resulting from flow processes associated with the ascent of large pockets of gas are coupled to the Earth, or where the elastic response of the conduit can couple back to pressure and momentum changes in the fluid (Chouet et al., 2008). The resulting processes are oscillatory in nature and feature complex dynamics that reflect the diverse behavior of multiphase fluids in basaltic systems. LP seismicity is also characteristically linked with Vulcanian activity (Gil Cruz and Chouet, 1997; Arciniega-Ceballos et al., 2003; Neuberg et al., 2006; Arciniega-Ceballos et al., 2008). At Galeras in particular, LP events accompanying bursts of ash-laden gases were noted to involve a pumping mechanism in shallow fractures similar to that inferred for hydrothermal LP events (Gil Cruz and Chouet, 1997). At Soufrière Hills Volcano at Montserrat, LP events have been conceptually linked to a process involving the brittle failure of flowing magma undergoing glass transition near the conduit wall, and escape of gases through fractures permeating the brecciated zone at this boundary (Neuberg et al., 2006). The complex magma rheology, marked by a strong nonlinear dependence of viscosity on water content and temperature (Hess and Dingwell, 1996; Zhang et al., 2003), finite yield strength, strain rate dependent viscosity, and transition to brittle solid behavior at high strain rates (Tuffen et al., 2003; Ichihara and Rubin, 2010) contributes to the wide variety of signals observed in Vulcanian systems.

With the increased use of portable broadband seismometers in the 1990s, slower processes associated with unsteady mass transport began to be observed at many volcanoes. These types of signals, with periods extending over the range from 2 to 100 s, fall under the appellation of Very-Long-Period (VLP) seismicity. They are typically attributed to fluid–rock interactions, as with LP events, and may involve oscillations at much longer periods than commonly observed in LP events (Kumagai, 2006; Chouet and Dawson, 2011), or may result from longer-term inertial volume changes in fluid-filled conduits (Chouet et al., 2005, 2010).

Forces associated with very large eruptions may also produce signals with periods extending beyond 100 s. For example, mantle Rayleigh waves with periods near 230 s observed during the Mount Pinatubo eruption of 15 June 1991 were linked by Kanamori and Mori (1992) to an oscillatory vertical single force applied at the surface of Mount Pinatubo, which was attributed to the acoustic coupling of atmospheric oscillations induced by the sustained energy flux from the volcano. A secondary peak at 270 s was also observed in the Rayleigh wave spectrum from the Pinatubo eruption. Watada and Kanamori (2010) demonstrated with normal mode modeling that the mode with period of 230 s is the first overtone of atmospheric waves trapped in the low sound-velocity channels in the lower atmosphere, while the mode at 270 s is the fundamental mode. Simulating the coupling between the solid Earth and atmosphere, they showed that Rayleigh waves and the fundamental and first overtone of a stratified atmosphere share the same horizontal wavelength and frequency at periods of 230 and 270 s, a necessary condition for efficient wave coupling at the Earth's surface. Kawakatsu et al. (2000) observed signals with periods >100 s associated with minor phreatic activity at Aso, which they attributed to a slow increase in fluid pressure in a source located 1–1.5 km below the west side of Naka-dake first crater on the central cone of Aso. Signals falling in this category were classified as Ultra-Long-Period (ULP) signals in the terminology of Chouet (1996b). Beyond the ultra-long periods are processes associated with mass transport over time scales of minutes, hours, and days that are more effectively observed with geodetic techniques.

An example is the 30-min scale of the injection process recorded by Linde et al. (1993) during the 1991 Hekla eruption.

It is clear that oscillatory processes are ubiquitous to magma flow, and feature a large variety of signals over a wide range of periods, which require very-wide-band measurements for their study. The present paper offers a review of the state of the art in volcano seismology and addresses basic issues in the quantitative interpretation of processes operative in active volcanic systems. As the title indicates, this review adopts a multi-decadal view of progress, outstanding issues, and research directions in the field of volcano seismology. Several review papers and books already exist in the literature covering various aspects of volcano seismology (e.g., Chouet, 1996a,b, 2003; McNutt, 2005; Kawakatsu and Yamamoto, 2007; Lees, 2007; Chouet, 2009; Kumagai, 2009; Lane and James, 2009; Neuberg, 2011; Nishimura and Iguchi, 2011; Zobin, 2012). Apart from providing a more current snapshot of the state of the field of volcano seismology, the present work attempts a degree of completeness and comprehensiveness in reviewing volcano-seismic phenomena and their inferred source processes.

Section 2 offers a brief introduction of the seismic methodology used to quantify the sources of volcano seismicity, with an emphasis on sources originating in the movement of magma and/or hydrothermal fluids. This is followed in Sections 3 and 4 by a discussion of representative source mechanisms of VLP and LP signals and their implications for volcanic processes. Investigations of VT seismicity associated with magma movement are addressed in Section 5, and Section 6 summarizes classic and new methodologies used in the elucidation of volcanic structures and processes. These methodologies include the tomographic method used in the elaboration of the three-dimensional velocity structures of volcanoes, the ambient noise seismic interferometry method used for probing temporal changes in these structures, array-processing methods used in tracking tremor sources, and waveform correlation and Hidden Markov Model (HMM) pattern recognition techniques used for the automatic identification and classification of event families commonly observed to accompany volcanic activity. Although not a seismic method, Muon radiography is also featured in this section because of the potential it holds to resolve shallow density structures at a scale difficult to achieve with other geo-physical techniques. We conclude with a discussion of other non-seismological methods, whose use in tandem with seismic methods is considered to be critical to a refined understanding of volcanic processes.

Our emphasis in Sections 2–5 is on the physical processes leading to volcano seismic phenomena. In volcano seismology, terminology has sometimes proven problematic. Observed signals and processes do not always fit neatly into separate categories, but rather form a spectrum of physical processes and a resultant diverse range of signal types. Throughout this review paper we use current widely adopted volcano-seismic terminology, but we make important clarifications (e.g., Section 4.3) where necessary to avoid (and hopefully clear up) confusion.

2. Seismic sources in volcanoes

A general kinematic description of seismic sources in volcanoes can be based on a moment tensor and single force representation of the source (Aki and Richards, 1980). The seismic moment tensor consists of nine force couples, with each corresponding to one set of opposing forces (dipoles or shear couples) (Fig. 1). This symmetric second-order tensor allows a description of any generally oriented discontinuity in the Earth (such as slip across a fracture plane, or the opening of a crack) in terms of equivalent body forces. For example, slip on a fault can be represented by an equivalent force system involving the superposition of two force couples of equal magnitudes—a double couple (Fig. 2a). Similarly, a tensile crack has an equivalent force system made of three vector dipoles, with dipole

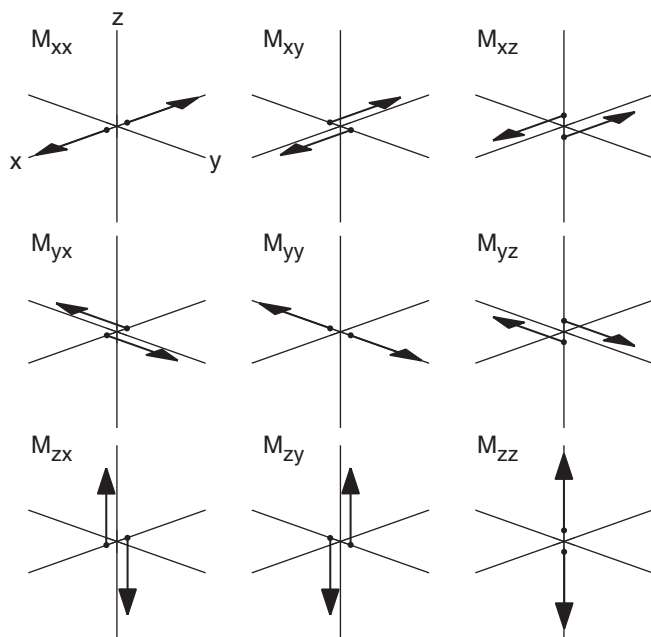


Fig. 1. The nine possible couples corresponding to the moment tensor components describing the equivalent force system for a seismic source in the Earth.

magnitudes with ratios $1:1:(\lambda+2\mu)/\lambda$, in which λ and μ are the Lamé coefficients of the rock matrix (Chouet, 1996b), and where the dominant dipole is oriented normal to the crack plane (Fig. 2b). Injection of fluid into the crack will cause it to expand and act as a seismic source. In general, magma movement between adjacent segments of conduit can be represented through a combination of volumetric sources of this type.

Because mass advection processes can also generate forces on the Earth, a complete description of volcanic sources commonly requires the consideration of single forces in addition to the volumetric source components expressed in the moment tensor. An example is the recoil force in the equivalent force system representing a volcanic eruption in the model of Kanamori et al. (1984) (Fig. 3). In general

terms, a single force can be generated through an exchange of linear momentum between the source and the rest of the Earth (Takei and Kumazawa, 1994). Thus, whenever some mass gains momentum, the counter force due to this accelerating mass is felt by the Earth. When the mass eventually decelerates and comes to rest, it induces another force on the Earth in the deceleration direction. Momentum conservation requires that the net change of linear momentum in the overall source system must cancel out over the total duration of an event (Takei and Kumazawa, 1994), so that the two pulse-like single forces associated with the acceleration and deceleration phases must counterbalance each other.

Landslides are examples of external single-force sources (Kanamori and Given, 1982). On a time scale of minutes a landslide may be viewed as a box sliding down a slope. As the sliding mass gains momentum, a counter force is felt by the Earth in the up-dip direction. When the sliding mass eventually loses momentum, a frictional force is applied to the underlying ground in the down-dip direction. Kawakatsu (1989) developed a centroid single force (CSF) inversion method and applied it to analyses of landslide and slump events recorded by the global seismic network. The CSF inversion method was applied by Ekström et al. (2003) to quantify the stick-slip, downhill sliding of a glacial ice mass. The massive landslide observed at the start of the 1980 eruption of Mount St. Helens, Washington, is a classic example of single-force mechanism (Kanamori and Given, 1982; Kawakatsu, 1989). A single-force source model was also proposed by Uhira et al. (1994) to explain the mechanism of dome collapses at Unzen Volcano, Japan.

In a fluid-filled conduit, an exchange of linear momentum may occur when the center of mass of the fluid accelerates upward or downward as a result of a change in mass distribution in the source volume. Momentum exchange takes place through a normal force applied at the top and bottom boundaries of the source volume, or through a shear force exerted on the boundaries oriented parallel to flow. Conduit discontinuities play a central role in controlling flow disturbances and also providing specific sites where pressure and momentum changes in the fluid are effectively coupled to the Earth (Chouet et al., 2003, 2005, 2008, 2010; Waite et al., 2008; Chouet and Dawson, 2011; Lyons and Waite, 2011). An example is the transient movement of liquid accompanying the disruption of a large slug of gas ascending through a region of changing cross section. As demonstrated in analog experiments with a vertical, liquid-filled tube featuring a flare (James et al., 2006), gas slugs undergo an abrupt flow pattern change upon rising through the flare (Fig. 4a). Rapid expansion of the slug into the wider cross section of the tube is accompanied by the downward and inward motion of a liquid piston formed by the thickening film of liquid falling past the slug. As it impinges the narrower inlet to the lower segment of tube the liquid piston rapidly decelerates, generating a pressure pulse in the liquid and a downward force on the apparatus holding the tube (Fig. 4b).

Another example of a fluid-induced single force is that caused by the movement of liquid accompanying the rapid near-surface expansion and burst of a gas slug in a conduit (James et al., 2008). This is illustrated in Fig. 5 for a scenario representative of a volcanic system (Chouet et al., 2010). The simulations in Fig. 5 represent a 250 m tall, vertical, rigid cylinder (no elastic deformation) of radius 5 m, closed at the base and filled to a depth of 150 m with an incompressible Newtonian fluid. As the slug ascends and expands, viscous shear along the conduit wall provides support for an increasing mass of liquid. Consequently, the static pressure below the slug decreases, reducing the downward force exerted by pressure on the base of the tube (a similar effect would be produced with any upward-facing section of conduit such as a flare or an elbow), and effectively imparting an upward force on the conduit. During most of the slug ascent, this increasing upward force on the conduit due to the decreasing basal pressure is compensated by the increasing downward shear force exerted on the conduit wall by the descending film of liquid surrounding the slug body. Downward shear gradually

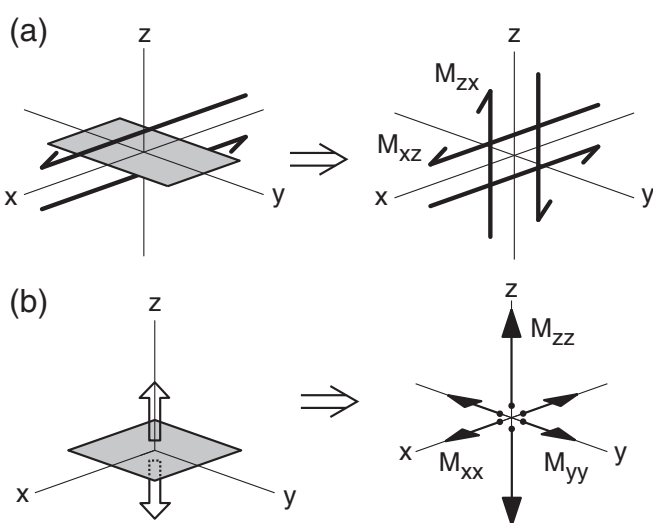


Fig. 2. (a) Slip on a fault can be described by a superposition of two force couples, in which each force couple is represented by a pair of forces offset in the direction normal to the force. Sources involving slip on a fault thus have an equivalent force system in the form of a double couple composed of four forces. (b) A tensile crack has a representation in the form of three vector dipoles, in which each dipole consists of a pair of forces offset in the direction of the force.

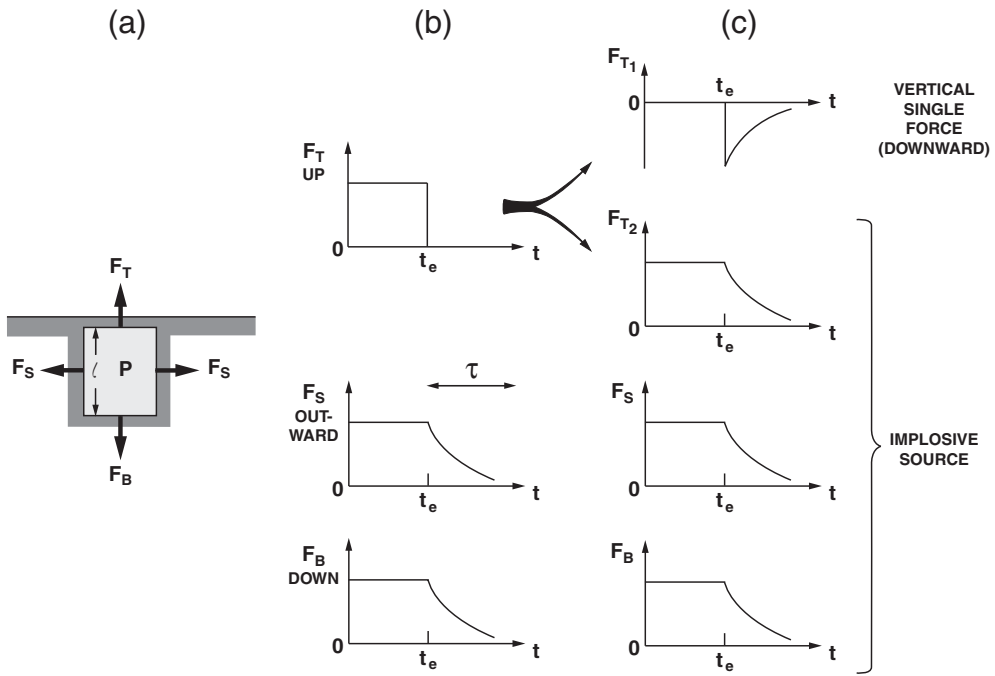


Fig. 3. Force system equivalent to a volcanic eruption. (a) Pressurized cavity model for a volcanic eruption. A shallow vertically oriented cylindrical cavity initially sealed at the top by a lid contains a pressurized inviscid fluid which exerts an upward vertical force F_T on the lid, a horizontal outward force F_S on the sidewall, and a vertical downward force F_B on the bottom of the cylinder. (b) Time histories of forces acting on the top, side, and bottom walls of the cavity. The eruption is simulated by the sudden removal of the lid at time $t = t_e$, at which point the force F_T vanishes instantaneously and the fluid pressure in the cylinder starts to decrease with a characteristic time constant τ fixed by the mass flux of the eruption, i.e., $\tau \sim l/v$, where l is the length of the cylinder and v is the mean fluid velocity inside the cylinder. Since the forces F_S and F_B are proportional to pressure, they decrease with the same time constant τ . (c) Decomposition of the force system to a downward single force and implosive source. The force F_T in (b) is decomposed into a vertical downward component F_{T_1} and vertical upward component F_{T_2} in such a way that F_{T_2} has the same time history as F_S and F_B . As a result, the three forces F_{T_2} , F_S , and F_B form an implosive source so that the eruption mechanism is represented by the superposition of a downward vertical force (the reaction force of the volcanic jet) with this volumetric implosion. After Kanamori et al. (1984).

increases as the slug expands and lengthens, until runaway expansion of the slug just prior to reaching the surface induces a component of upward-directed shear in the region around and above the slug nose (James et al., 2008), which opposes most of the downward shear due to the descending liquid film around the slug body. Upon slug burst, expansion no longer drives upward shear. Upward shear is then provided solely by liquid inertia and declines rapidly, leaving only the downward shear force, which decays slowly back to zero as the draining liquid thins out. The slumping of the liquid film surrounding the slug back to the top of the liquid column after the slug has burst induces a simultaneous rise in static pressure and increase in basal pressure. The slug expansion and burst thus result in a net upward force transient with both shear and pressure components being exerted on the conduit.

2.1. Waveform inversion

Waveform inversions solving for the amplitudes and time histories of the moment tensor and single force components of the source have become the primary tool to identify and understand the mechanisms of generation of LP and VLP signals recorded by broadband seismometers. Unlike more conventional seismic analysis techniques based on fitting the arrival times of seismic phases, waveform inversion seeks to fit the entire seismogram. The main advantage of this method is that it is readily applicable to any type of seismic signal, including those that are produced by the interactions between gas, liquid, and solid.

When the wavelengths of observed seismic waves are much longer than the spatial extent of the source, the source may be approximated by a point source, and the force system represented by the moment tensor and single force components is localized at this

point. The waveform inversion procedure requires a calculation of the impulse responses (Green's functions) of the medium to this force system for each receiver component. The displacement field generated by a seismic source is described by the representation theorem which, for a point source, is expressed as (Chouet, 1996b)

$$u_n(\mathbf{x}, t) = M_{pq}(t) * G_{np,q}(\mathbf{x}, \xi, t) + F_p(t) * G_{np}(\mathbf{x}, \xi, t), \quad (1)$$

where $u_n(\mathbf{x}, t)$ is the n -component of seismic displacement observed at a point \mathbf{x} at time t , $M_{pq}(t)$ is the time history of the pq -component of the moment tensor at position ξ of the source, $F_p(t)$ is the time history of the force applied in the p -direction at ξ , and $G_{np}(\mathbf{x}, \xi, t)$ is the Green tensor which relates the x_n -component of displacement at \mathbf{x} with the x_p -component of impulsive force applied at ξ . The notation $,q$ indicates spatial differentiation with respect to the ξ_q -coordinate at the source and the symbol $*$ denotes convolution. The summation convention is assumed throughout for repeated subscripts.

A common approach to the quantification of the seismic source mechanism relies on a discretized representation of the volcanic edifice based on a digital elevation model. Using this discretized model, Green's functions may then be calculated by the finite difference method (Ohminato and Chouet, 1997; Ripperger et al., 2003) or lattice method (O'Brien and Bean, 2004; O'Brien, 2008). Once the Green's functions are known, the nine independent mechanisms in Eq. (1) (three force components and six independent components of the moment tensor) are retrieved through least-squares inversion expressing the standard linear problem $\mathbf{d} = \mathbf{Gm}$ in this equation (Ohminato et al., 1998; Chouet et al., 2003, 2005). The procedure involves calculation of Green's functions for individual moment and single force components applied at a preset position representing the anticipated location of the point source in the edifice. As the actual position of the source is unknown a priori, calculations are usually

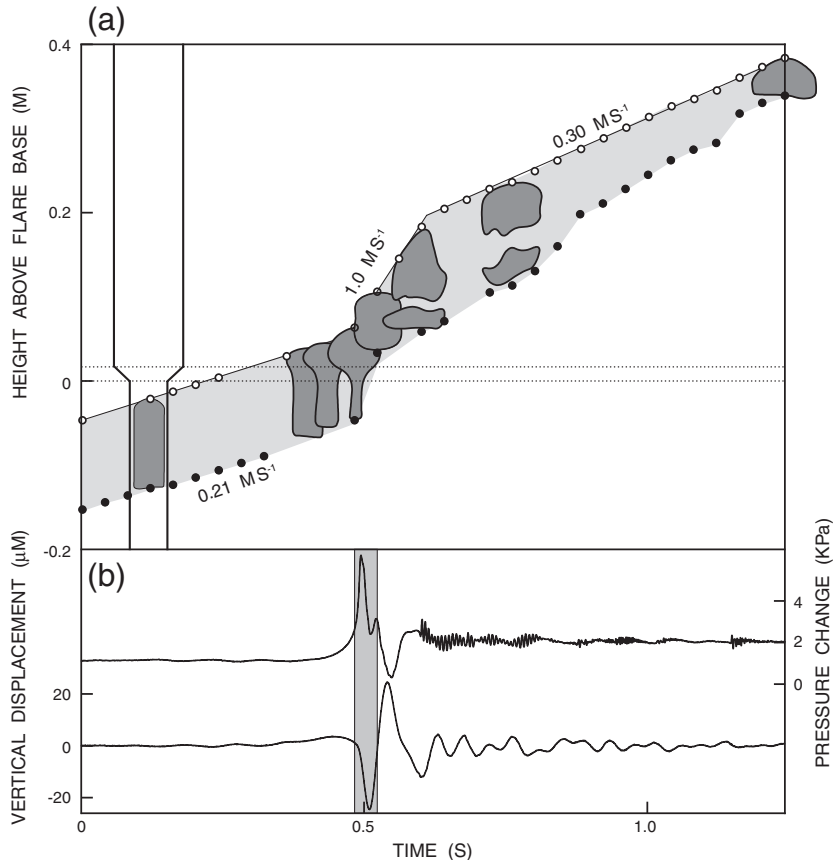


Fig. 4. Slug ascent from small to large diameter tube in the laboratory experiments of James et al. (2006). (a) Sketches of bubble at different positions in the tube shown at the left (diameter drawn to scale, but only short vertical segment of tube illustrated). The bubble is shown by the outline filled with dark gray. Circles and solid dots, respectively, mark the positions of the nose and tail of the bubble obtained from video data. Dotted lines mark the inlet and outlet of the flare. The slug is disrupted by turbulence shortly after entering the larger tube, with resulting daughter bubbles rapidly coalescing. (b) Pressure change (upper trace) measured at the base of the apparatus, and vertical displacement (lower trace) of the apparatus. The gray stripe represents the interval between video frames during which the slug tail passed through the flare. Note the increase of pressure synchronous with the downward displacement (downward acceleration) of the tube. The higher frequency signal starting near 0.6 s in the pressure trace probably results from the turbulence responsible for the disruption and breakup of the bubble. The fluid used is a 0.1 Pa s sugar solution. Slug outlines and positions modified from James et al. (2006, Fig. 5b); pressure and displacement data supplied by Mike James (see James et al., 2006 for details).

repeated for point sources distributed over a uniform mesh encompassing the anticipated source region and the number of point sources considered may be quite large. To reduce the number of calculations required to derive the Green's functions, use is made of the reciprocal relation between source and receiver (Aki and Richards, 1980). Further speedup in computations is achieved by performing the waveform inversion in the frequency domain (Auger et al., 2006; Chouet et al., 2008, 2010; Waite et al., 2008).

The selection of an optimum solution is based on the residual error, the relevance of the free parameters used in the model, and the physical significance of the resulting source mechanism. As the actual number of parameters in the source mechanism is unknown, a typical approach generally considers waveform inversions carried out for (1) a point source including six moment and three force components to fully account for the possible expansion or contraction of a conduit/reservoir and single force due to mass advection; (2) a point source including six moment tensor components but no single force components; and (3) a point source consisting of three single force components. Multiple point sources may be considered as well if warranted by adequate data (Chouet et al., 2008). The significance of the number of free parameters is evaluated by calculating Akaike's Information Criterion (AIC) (Akaike, 1974), which is defined as

$$\text{AIC} = N_{\text{obs}} \ln E + 2N_{\text{par}}, \quad (2)$$

where N_{obs} is the number of independent observations, E is the residual error between the synthetics and the data (Ohminato et al., 1998), and N_{par} is the number of free parameters used to fit the model. Additional free parameters in the source mechanism are considered to be physically relevant when both the residual error and AIC are minimized.

A final consideration is the physical relevance of the solution. As formulated in Eq. (1), the source inversion does not use the constraint of a shared time history for the moment tensor. Rather, the time histories of individual moment-tensor components are obtained independently of each other. For a realistic interpretation of the source mechanism consistent waveform shapes among individual moment tensor components are required. Differences among the time histories of individual moment tensor components may arise due to the presence of noise in the data, inadequate receiver coverage, or an inadequate starting assumption concerning the source mechanism. In the latter case, the introduction of single force components may help minimize distortion of the source-time functions of moment components (e.g., Chouet et al., 2003). For a robust estimation of the source mechanism, appropriate network coverage of the entire volcanic edifice is necessary. Dawson et al. (2011) determined that for VLP sources at Augustine, ideally ten or more three-component receivers ringing the edifice within a range of 5 km from the source should be considered. At the very least, five three-component receivers surrounding the source at close range are required to gain

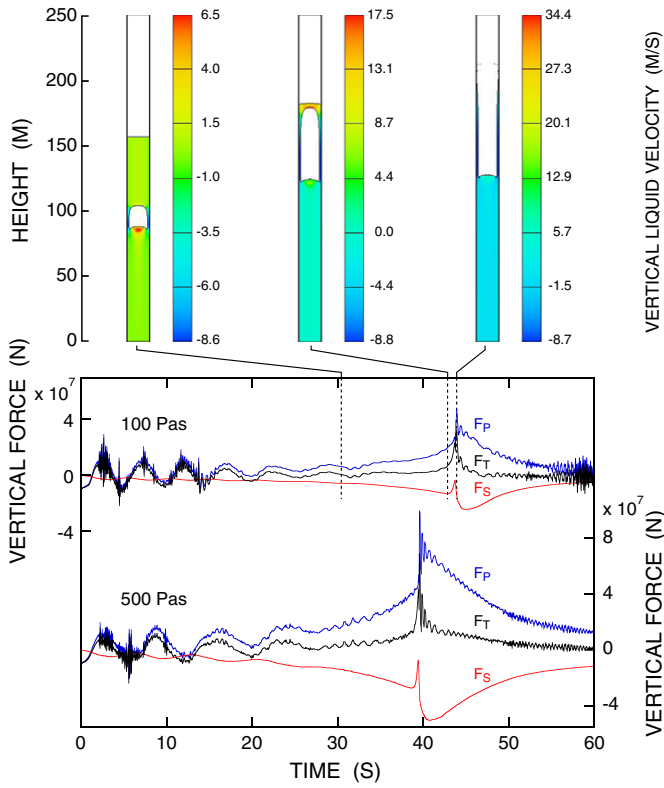


Fig. 5. Liquid motions and forces during the final ascent stage of a simulated gas slug in a liquid-filled vertical cylindrical conduit, closed at the base. The z-axis is positive upward. In the graph, traces from two simulations are given for liquids with viscosities of 100 and 500 Pa s. For both simulations, the vertical force, F_s , exerted on the conduit by liquid shear (red trace) and vertical force, F_p , due to pressure variation at the base of the conduit (blue trace) are plotted along with the net force $F_t = F_s + F_p$ (black trace). In the simulations, the slug is initially stationary close to the base of the conduit and subsequently displays decaying longitudinal oscillations with periods of ~5–7 s resulting from pressure equilibration and the establishment of flow. The snapshot images show vertical cross sections of the conduit in the 100 Pa s simulation at the times indicated by the dashed lines. Note the amplified horizontal scale; the conduit is 10 m in diameter. The colors indicate the z-component of the liquid velocity, which represents the dominant component of liquid motion. (Simulations carried out with the general purpose 3-D fluid dynamics simulation package FLOW-3D; see James et al. (2008) and Chouet et al. (2010) for details).

Reproduced from Chouet et al., 2010, Fig. 12).

a rough idea of the source mechanism, provided noise in the data is not an issue (Dawson et al., 2011). Such network constraints are generally adequate for VLP sources, but more stringent conditions may apply for shallow LP sources (depth < 500 m), for which experience dictates that at least 7–8 receivers are required within 2–3 km of the source to obtain a realistic estimate of the source mechanism (Kumagai et al., 2002a, 2005; Waite et al., 2008). The moment tensor estimated from waveform inversion can be interpreted through a comparison with the theoretical moment tensors describing cracks or pipes, or geometries made of composites of such sources (see Section 3 below).

For the wavelengths of tens to hundreds of kilometers typically associated with VLP signals, the assumption of a homogeneous velocity structure is sufficient to guarantee a reliable source mechanism from inversion. Simulations carried out by Chouet et al. (2003) for VLP data at Stromboli Volcano, Italy, confirm that the source mechanism is relatively insensitive to the choice of velocities used to invert the data. The use of faster velocities to calculate the Green's functions may lead to an overestimation of the amplitude of the moment tensor components and also introduce a small spurious downward single force component in the solution, while the use of slower velocities has the opposite effect (Chouet et al., 2003). This can be readily

understood from a theoretical consideration of the radiation from a moment tensor \mathbf{M} (e.g., Eq. (4.29) of Aki and Richards, 1980), which shows that faster seismic velocities produce smaller displacement amplitudes, while the converse is true for slower velocities. Although the absolute amplitude of the moment tensor determined from VLP data is affected by the error in velocity structure, the source centroid location, shape of the source time functions, and source mechanisms are not sensitive to it. This derives from the fact that, in near field observations of VLP events, the travel time is negligibly small compared to the event duration, while the effect of velocity structure on the signal amplitude remains a significant factor.

For the shorter wavelengths of LP signals, the situation is more delicate as stated above. Near-surface, low-impedance layers and three-dimensional structural heterogeneity may lead to a strong distortion and damping of the wave fields radiated by shallow LP sources, making it difficult to quantify their source mechanisms (e.g., Chouet, 1996a, Fig. 4). Path effects must be properly accounted for as these may leak into the solution and result in a spurious source mechanism. The problem is exacerbated by inadequate receiver coverage, in which case the use of a priori source information from structural geology to reduce the number of free parameters in the inversion may be of critical importance for a proper interpretation. A case study by Bean et al. (2008) well illustrates the issue of network coverage in relation to the source. Bean et al. (2008) performed detailed 3-D wave field simulations for 8 receivers mimicking the Mount Etna network, where most stations are quite far from the summit crater. Simulating a point source buried under the summit with a crack-like mechanism and source time function in the form of a Ricker wavelet with dominant frequency of 0.7 Hz, they computed synthetic seismograms in media with and without near-surface low-velocity layers, taking into account the Etna topography. Unsurprisingly, resonance in a soft superficial layer produces long-lasting ringing synthetics at distant stations that tend to mask the source signature (Chouet, 1996a; Bean et al., 2008). This ringing becomes particularly pronounced for a shallow source embedded in the layer due to the efficient entrapment of radiated energy in this low-impedance channel (Chouet, 1996a). Bean et al. (2008) caution that when the effect of near-surface structure is unaccounted for, the result may be excessively long source time functions, spurious single forces, mis-orientated conduit geometry, and poor estimates of moment magnitudes. As made clear from such simulations, a lack of detailed knowledge of the small-scale three-dimensional velocity structure is the main limitation in our ability to resolve source mechanisms for frequencies above 1–2 Hz.

Another challenge may arise when dealing with VLP signals from a shallow source, where dynamic tilts induced by the source may affect long-period horizontal seismometers through their sensitivity to gravitational acceleration, producing apparent horizontal displacements that are proportional to the second integral of the tilt-angle time history (Rodgers, 1968; Aki and Richards, 1980). In contrast, for a precisely vertical sensor the effect of tilt is essentially negligible so that this sensor will show a pure displacement waveform (Graizer, 2006).

Maeda et al. (2011) proposed an efficient method to deal with horizontal seismograms contaminated by tilt motions. In their approach the effect of tilt motions is included into the Green's functions used in the waveform inversion. Expressed in the frequency domain the observed ground displacement, $U_n^{obs}(\omega)$, is obtained as (Maeda et al., 2011)

$$U_n^{obs}(\omega) = U_n^{trans}(\omega)I_n^{trans}(\omega) + \theta_n(\omega)I_n^{tilt}(\omega), \quad (3)$$

where ω denotes the angular frequency and the subscript n stands for both receiver location and component of seismogram. In this expression, $U_n^{trans}(\omega)$ represents the contribution from ground translation, $\theta_n(\omega)$ represents the contribution from ground tilt, and $I_n^{trans}(\omega)$ and $I_n^{tilt}(\omega)$

represent the seismometer translational and tilt responses, respectively. The Fourier transform of ground tilt motion is given by

$$U_n(\omega) = M_{pq}(\omega)G_{np,q}^{\text{tilt}}(\omega) + F_p(\omega)G_{np}^{\text{tilt}}(\omega), \quad (4)$$

and the Fourier transform of translation displacement is obtained from Eq. (1) as

$$U_n^{\text{trans}}(\omega) = M_{pq}(\omega)G_{np,q}^{\text{trans}}(\omega) + F_p(\omega)G_{np}^{\text{trans}}(\omega), \quad (5)$$

where $M_{pq}(\omega)$ is the Fourier transform of the pq -component of the moment tensor, and $F_p(\omega)$ is the Fourier transform of the p -component of single force at the source, $G_{np}^{\text{tilt}}(\omega)$ is the Green tensor for tilt motion, $G_{np}^{\text{trans}}(\omega)$ is the Green tensor for translation motion, and the notation $,q$ indicates a spatial differentiation with respect to the ξ_q -coordinate at the source (see Eq. (1)). Substitution of Eqs. (4) and (5) into Eq. (3) yields the expression

$$\begin{aligned} U_n^{\text{obs}}(\omega) &= M_{pq}(\omega) \left[G_{np,q}^{\text{trans}}(\omega)I_n^{\text{trans}}(\omega) + G_{np,q}^{\text{tilt}}(\omega)I_n^{\text{tilt}}(\omega) \right] \\ &\quad + F_p(\omega) \left[G_{np}^{\text{trans}}(\omega)I_n^{\text{trans}}(\omega) + G_{np}^{\text{tilt}}(\omega)I_n^{\text{tilt}}(\omega) \right]. \end{aligned} \quad (6)$$

The horizontal seismometer response to tilt, $I_n^{\text{tilt}}(\omega)$ is obtained simply as (Maeda et al., 2011)

$$I_n^{\text{tilt}}(\omega) = \frac{g}{(i\omega)^2} I_n^{\text{trans}}(\omega), \quad (7)$$

where g is the gravitational acceleration and i is the imaginary unit. For vertical components, $I_n^{\text{tilt}}(\omega) \sim 0$. Maeda and Takeo (2011) applied this procedure to VLP pulses recorded at Asama Volcano, Japan. They used data from 14 broadband seismometers deployed in the summit area of Asama and performed waveform inversions including Green's functions for both translational and tilt motions in which they assumed a source mechanism represented by a moment tensor only (no single force). They obtained a best-fitting point source location at depth of 100–150 m below the crater floor. Their moment tensor solutions point to a rapid inflation (time scale~10 s), followed by more gradual deflation (time scale~100 s) of a volumetric source. Maeda and Takeo (2011) attributed this behavior to a pressurization and depressurization of the source cavity due to the inflow and outflow of gases generated either by the boiling of ground water or by the exsolution of volatiles from a deeper magma reservoir (see Section 3.3 for details).

3. VLP seismicity

Very-Long-Period (VLP) signals, within the frequency band 0.01 to 0.5 Hz, are commonly associated with volcanic activity. Due to their very long wavelengths in the range of tens to hundreds of kilometers, seismic waves in the VLP band suffer little path distortion, which greatly facilitates their analysis. Unlike LP signals, which are mainly interpreted as manifestations of acoustic resonance (see Section 4), VLP signals are typically attributed to inertial forces associated with perturbations in the flow of magma and gases through conduits, and as such these signals provide a window into important source processes related to magma transport. The ability to record VLP signals in the near field of volcanic sources is a recent development in volcano seismology, but in the two decades since its discovery this type of seismicity has been observed worldwide. Distinct VLP events, with durations less than 300 s, have been observed at many volcanoes, including Sakurajima (Kawakatsu et al., 1992, 1994; Uhira and Takeo, 1994), Unzen (Uhira et al., 1994), Aso (Kaneshima et al., 1996; Yamamoto et al., 1999; Kawakatsu et al., 2000; Legrand et al., 2000), Satsuma-Iwojima (Ohminato and Ereditato, 1997; Ohminato, 2006), Iwate (Nishimura et al., 2000), Miyakejima (Kumagai et al.,

2001; Fujita et al., 2004), Usu (Yamamoto et al., 2002), Bandai (Nishimura et al., 2003), Hachijo (Kumagai et al., 2003; Kumagai, 2006), Ontake (Nakamichi et al., 2009), and Asama (Ohminato et al., 2006; Kazahaya et al., 2011; Maeda and Takeo, 2011; Maeda et al., 2011) in Japan; Stromboli (Neuberg et al., 1994; Neuberg and Luckett, 1996; Chouet et al., 1999, 2003; Auger et al., 2006; Chouet et al., 2008) in Italy; Merapi (Hidayat et al., 2000, 2002, 2003) in Indonesia; Kilauea (Dawson et al., 1998; Ohminato et al., 1998; Almendros et al., 2002; Dawson et al., 2004, 2010; Chouet et al., 2010; Chouet and Dawson, 2011) in Hawaii; Mammoth Mountain (Hill et al., 2002; Hill and Prejean, 2005) in California; Mount St. Helens (Waite et al., 2008) in Washington; Augustine (Dawson et al., 2011), Okmok (Haney, 2010), and Redoubt (Haney et al., 2012a) in Alaska; Erebus (Rowe et al., 1998; Aster et al., 2003, 2008) in Antarctica; Popocatépetl (Arciniega-Ceballos et al., 1999, 2003, 2008; Chouet et al., 2005) in Mexico; Fuego (Lyons and Waite, 2011) in Guatemala; and Cotopaxi and Tungurahua (Kumagai et al., 2007, 2010, 2011; Molina et al., 2008) in Ecuador.

Inversions of VLP waveforms have imaged crack geometries in the form of dikes or sills (Ohminato et al., 1998; Yamamoto et al., 1999; Chouet et al., 2003; Kumagai et al., 2003), as well as more complicated geometrical configurations involving sill-dike composites (Chouet et al., 2005; Dawson et al., 2011; Haney et al., 2012a), composites of intersecting dikes (Chouet et al., 2008; Chouet and Dawson, 2011), or two chambers connected to each other by a narrow channel (Nishimura et al., 2000). Based on the characteristic period of VLP signals observed at Hachijo Island, Japan, Kumagai (2006) estimated a source with dimensions of a few km. The decaying harmonic oscillations with periods near 10 s and duration up to 300 s of the VLP signals at Hachijo are similar to the features of LP events with periods near 1 s (see Fig. 17) and appear consistent with the resonance of a dike containing a bubbly basalt (Kumagai, 2006). In that sense, the Hachijo signals probably represent a unique end member of the family of sources associated with resonant conduit excitation. They are unusual because such periods are more commonly associated with mass advection, as stated above. Interestingly, the dominant period and related decay characteristics of the signals at Hachijo were both found to vary with time, and these temporal variations were attributed by Kumagai (2006) to a change in source dimensions, assuming fixed acoustic properties of the fluid at the source. A spread of about 4 km was also estimated by Nishimura et al. (2000) for two chambers at Iwate Volcano, Japan. Detailed inversions of VLP waveforms at Stromboli by Chouet et al. (2008) have imaged sets of intersecting dikes whose relative positions and orientations represent individual conduit segments with dimensions of a few hundred meters. Systematic modeling of VLP signals accompanying degassing bursts at Kilauea Volcano, Hawaii, has evidenced a complex magma pathway made of a plexus of intersecting dikes extending over the depth range of 0.2–3.1 km below the summit caldera (Chouet and Dawson, 2011). A crack-like conduit extending over the depth range of 0.3–2.5 km has also been inferred under Aso Volcano, Japan (Yamamoto et al., 1999).

Contrasting these findings are results obtained by Ohminato et al. (2006) from waveform inversions of VLP signals associated with Vulcanian explosions at Asama Volcano, Japan. At Asama, the contribution from a vertical single force with magnitude of 10^{10} – 10^{11} N was found to dominate the observed waveforms, and no obvious volumetric component was identified at the source. The depth of the VLP source is ~200 m beneath the crater floor, and the source-time histories feature two downward force components separated by an upward force component. The initial downward component was attributed by Ohminato et al. (2006) to the sudden removal of the lid capping the pressurized conduit (this force is analogous to the force F_{T_1} in Fig. 3), and the subsequent upward force was interpreted by these authors as a drag force induced by viscous magma moving up the conduit. Ohminato et al. (2006) also attributed the final

downward force component to an explosive fragmentation of the magma, which effectively cancels viscous drag and results in the downward force due to jet recoil again dominating the VLP signal.

Below, we review representative seismic source mechanisms of VLP signals associated with degassing bursts in silicic (Section 3.1) and basaltic (Section 3.2) systems, and follow with a description of mechanisms related to magma–hydrothermal interactions (Section 3.3).

3.1. Source mechanisms representative of silicic systems

Inversions of VLP waveforms recorded during two mild eruptions of Popocatépetl Volcano, Mexico, provide an integrated view of the fundamental mechanisms underlying Vulcanian degassing bursts observed in April–May 2000 (Chouet et al., 2005). Using data in the 15–70 s band recorded by a network of nine broadband seismometers ringing the edifice within 2.4 km of the active crater, Chouet et al. (2005) imaged a simple point source located 1.5 km below the summit crater. The inferred source mechanism includes both moment tensor and single force components. From detailed modeling of the moment tensor solutions, Chouet et al. (2005) derived a well-constrained mechanism composed of a sub-horizontal sill intersecting a steeply dipping northeast striking dike. The surface extension of the dike bisects the vent and this dike was interpreted to represent the main conduit in the top 1.5 km below the crater (Chouet et al., 2005). The largest moment release occurs in the sill in both eruptions, indicating a maximum volume change of 500–1000 m³, pressure drop of 3–5 MPa, and amplitude of recovered pressure equal to 1.2 times the amplitude of the pressure drop. In comparison, the maximum volume change in the dike is 200–300 m³, with a corresponding pressure drop of 1–2 MPa and pressure recovery equal to the pressure drop. Accompanying these volumetric sources is a single force with magnitude of 10⁸ N, whose in-plane components in the sill and dike are consistent with melt advection in response to pressure transients. The source time histories of the volumetric components of the source indicate that significant mass movement originates in the sill and triggers a mass movement response in the dike within a few seconds. This picture is consistent with the opening of a pathway for escaping gases accumulated in the sill in response to slow pressurization of the sill driven by magma crystallization. The opening of this pathway and rapid evacuation of pent-up gases induce the pressure drop.

The amplitude of pressure recovery in the sill is much larger than the anticipated pressure variation associated with the movement of the magma column perched above the sill in response to the passage of the gas pocket. Rather, Chouet et al. (2005) inferred that the pressure recovery in the magma filling the sill is likely to have been driven by diffusion of gases from the resulting supersaturated melt into bubbles. Accordingly, these authors proposed a model in which static magma in the sill becomes supersaturated due to groundmass crystallization. In this conceptual view, volatile exsolution and diffusion of gas from the melt into bubbles increase the internal pressure of the bubbles, because bubble expansion is impeded by the viscous resistance of the surrounding liquid and by the confining effects due to the finite yield strength of the overlying column of magma and surrounding solid rock. Elastic inflation of the sill occurs as a result of bubble pressurization, and this inflation proceeds until the critical yield strength of the magma column is exceeded and magma starts to flow out of the sill. Magma fragmentation induced by viscous shear near the conduit wall then causes the coalescence and collapse of bubbles intersected by fractures, allowing gas escape through a transient network of fractures. This, in turn, induces a pressure drop in the sill, which results in the collapse and welding of the fracture network that shuts down the gas-escape pathway. Repeated cycles of shear-induced fracture and welding of magma provide a ratchet mechanism by which the separated gas phase in the magma can be

recharged and evacuated (see Section 4.7 for further discussion of the solid-like brittle behavior of silicic melts).

The expansion dynamics of bubbles in supersaturated magma have been addressed in many previous studies under conditions of constant melt pressure (Scriven, 1959; Sparks, 1978; Proussevitch et al., 1993; Lyakhovsky et al., 1996; Proussevitch and Sahagian, 1998; Lensky et al., 2002, 2004) or constant decompression rate (Toramaru, 1989, 1995; Proussevitch and Sahagian, 1996). A canonical model of bubble growth in magma that includes the effect of finite spacing of bubbles in the melt was first developed by Proussevitch et al. (1993). This model considers a suspension of gas bubbles in an incompressible volatile-bearing liquid. The suspension is modeled as a three-dimensional lattice of closely-packed spherical shells, where each identical elementary cell is composed of a gas bubble surrounded by a shell of liquid. A step drop in pressure in the melt induces volatile exsolution and bubble expansion is driven by the diffusion of gas into the bubble. In this model, only the volatiles contained in the shell of liquid surrounding the bubble contribute to bubble expansion so that bubble growth is limited by how closely packed the bubbles are in the liquid. Using the model of Proussevitch et al. (1993), Chouet et al. (2006) and Shimomura et al. (2006) obtained a dynamic solution that includes the effect of melt compressibility. In their models, pressure recovery is driven by bubble growth in a supersaturated magma that is stressed by the surrounding crust as the magma volume increases with bubble expansion. Both models consider the pressure recovery following an instantaneous pressure drop in the melt. The magma is embedded in an infinite, homogeneous, elastic solid and consists of melt containing numerous small spherical gas bubbles of identical size. No new bubbles are created and no bubbles are lost during pressure recovery, and the gas in the bubbles is assumed to be a perfect gas. Gravity and other body forces are not considered.

The conduit geometry considered by Chouet et al. (2006) applies specifically to the source inferred for Popocatépetl (Chouet et al., 2005) and consists of a penny-shaped crack containing a melt with an isotropic distribution of bubbles (Fig. 6a). The initial oversaturation of the melt resulting from a pressure drop ΔP_0 is distributed uniformly in the melt, and each bubble grows by diffusion of volatiles from a surrounding shell of melt with finite radius (Fig. 6b). As diffusion is a slow process, with time scale much longer than that of heat transfer into the bubble (Ichihara and Kameda, 2004), bubble growth is assumed to be isothermal. The mathematical model describing an elementary cell therefore consists of three equations: (1) a diffusion equation governing the transfer of volatiles in the melt shell; (2) an equation expressing the radial motion of the bubble; and (3) a relation representing the ideal gas approximation. These equations are then subjected to three boundary conditions expressing the phase equilibrium at the bubble wall, mass flux at the bubble wall, and zero mass transfer through the outer shell wall. As the bubble grows by mass transfer from the melt, the melt is compressed and the surrounding rock matrix is deformed as a result. The pressure in the melt is balanced by the stress applied by the surrounding elastic medium, and in both Chouet et al. (2006) and Shimomura et al. (2006), this is formalized by assuming a quasi-static deformation of the magma conduit. Melt shrinkage from dehydration (Ochs and Lange, 1999) is assumed to be negligible compared to melt compression due to bubble growth and is not considered.

Fig. 7 shows the pressure recovery calculated by Chouet et al. (2006) for input pressure drops ΔP_0 of 0.01, 0.1, and 1 MPa applied to a bubbly rhyolitic melt encased in a penny-shaped crack with radius of 100 m and thickness of 5 m under ambient pressure of 40 MPa appropriate for the depth of the source imaged for Popocatépetl (Chouet et al., 2005). The bubbles have a fixed initial radius of 10⁻⁶ m, and the bubble number density is 10¹² m⁻³. Melt density, viscosity, and diffusivity are 2300 kg m⁻³, 10⁶ Pa s, and 10⁻¹¹ m² s⁻¹, respectively; surface tension is 0.2 N m⁻¹, and the bulk modulus of melt and elastic rigidity of the rock are both 10¹⁰ Pa. The amplitude ratio of pressure recovery to

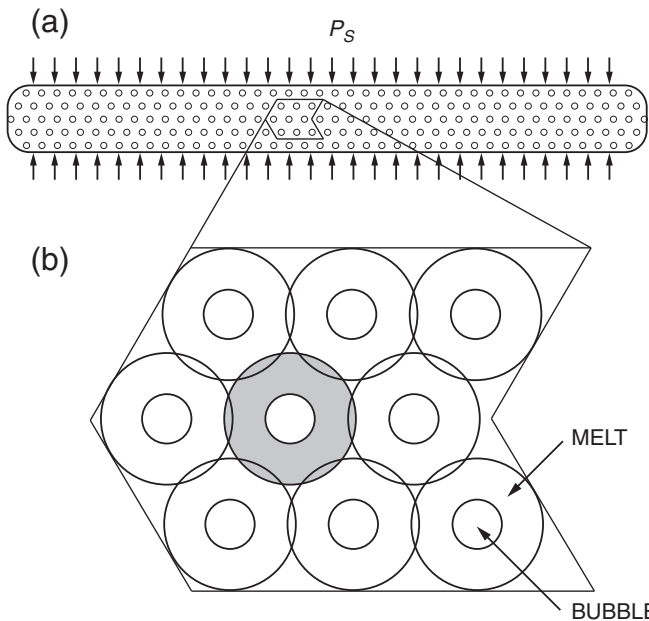


Fig. 6. Model used by Chouet et al. (2006) to interpret the source mechanism of Vulcanian degassing bursts at Popocatépetl Volcano. (a) Schematic illustration (cross section) of penny-shaped crack embedded in an elastic solid. The crack is under confining pressure P_s , and contains a melt with an isotropic distribution of gas bubbles of identical sizes. (b) Detailed view of the distribution of elementary cells composing the bubbly liquid (after Prousevitch et al., 1993). Each cell (as in gray-shaded example) consists of a gas bubble surrounded by a finite volume of melt. The elementary cells are organized in a three-dimensional lattice with slight overlap of the cells, where the volumes of intersecting melt and gaps are equal, so that the gas-volume fraction is $(R/S)^3$, where R is the bubble radius and S is the outer shell radius.

initial pressure drop displays a strong nonlinear sensitivity to the magnitude of the input pressure drop, resulting in magnifications ranging from about 1 to nearly 30 over the range of input transients considered (Fig. 7). This overpressurization upon recovery was previously noted in a static solution obtained by Nishimura (2004) and becomes largest for tiny bubbles and a stiff elastic medium (Chouet et al., 2006; Shimomura et al., 2006). Fig. 7 also shows that the speed of recovery is a function of the input transient, with the crack response becoming markedly more sluggish for small pressure transients compared to larger ones.

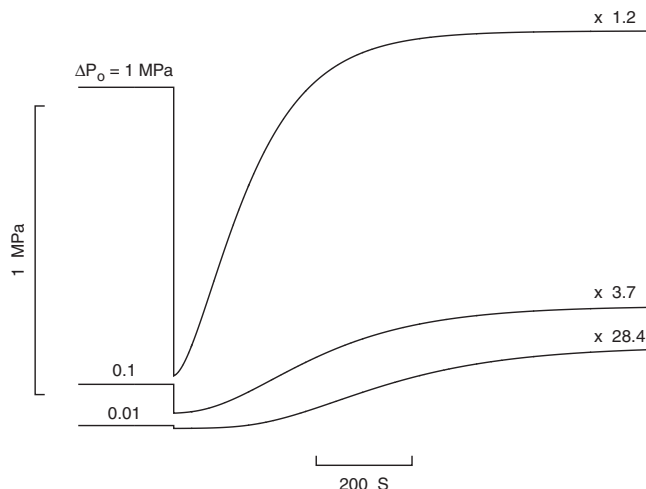


Fig. 7. Dependence of pressure recovery on the size of the input transient, ΔP_0 , in the model of Chouet et al. (2006). The magnification factor associated with each response is indicated at the upper right of each pressure trace.

The variation in time and amplitude scales seen in Fig. 7 suggests that a wide range of responses may be possible for cracks containing melts with a wider population of bubble sizes than the single-size bubble populations considered by Chouet et al. (2006). The net drop in volatile concentration associated with diffusion-driven bubble growth is quite small. Indeed, the results obtained by Chouet et al. (2006) suggest concentration drops $\sim 0.003\text{--}0.035$ wt.% for initial bubble radii of $10^{-5}\text{--}10^{-7}$ m in penny-shaped cracks with aperture to radius ratios of 0.01–0.25. The net concentration drop is small because pressure recovery in the melt acts to raise the saturation level of volatiles in the melt. This has important implications for the overall history of degassing in a Vulcanian system as it suggests that this process may be repeated many times without significantly depleting the gases in the melt body.

The source process imaged under Popocatépetl begins with inflation (pressurization) and executes 2–3 cycles of deflation–reinflation (depressurization–repressurization) within a time interval of 3–5 min (Chouet et al., 2005). The volumetric component of the source process in the sill associated with an eruption on 23 May 2000 is shown in Fig. 8. Other eruptions at Popocatépetl were found to produce similar waveform characteristics, hence the source time function in Fig. 8 may be viewed as an adequate representation of overall source dynamics associated with these Vulcanian eruptions. For comparison, Fig. 8 also shows the volume change of a magma-filled sill calculated with the model of Chouet et al. (2006). The sill response in this model has been band-pass filtered in the same band (15–70 s) as the observed signal, and is illustrated for three distinct pressure drops. The model parameters in Fig. 8 are identical to those used in Fig. 7. A realistic fit of the peak-to-trough amplitude of volume change inferred at Popocatépetl is obtained for an input pressure drop ΔP_0 of 3.25 MPa.

Unfortunately, the longer-period components and other specific features of the sill response in the model are lost in the band-limited version of the signal compatible with observations made at Popocatépetl, so that the responses obtained in this band for different model parameters are all very similar (Chouet et al., 2006). Although it is not possible to infer specific values of melt viscosity, volatile diffusivity, initial bubble radius, bubble number density, or sill aperture to radius ratio based on available seismic data, these results strongly support the idea that diffusion pumping of bubbles in the magma under Popocatépetl provides a viable mechanism for pressure recovery following a pressure drop induced by a degassing event.

Dawson et al. (2011) carried out an investigation of the seismic source mechanism of an explosive eruption that occurred on 11 January 2006 at Augustine Volcano, Alaska, using inversions of very-long-period waveforms recorded by a limited network of five broadband seismometers.

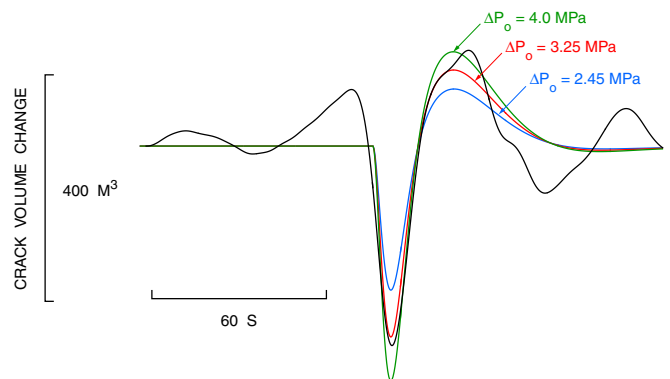


Fig. 8. Source-time function of volume change obtained by Chouet et al. (2005) for a sill under Popocatépetl Volcano during a degassing burst on 23 May 2000 (black line), and corresponding volume changes in a sill filled with a bubbly melt in response to a step drop ΔP_0 in pressure (colored lines). The data from Popocatépetl and solutions from the crack model have both been band-pass filtered in the 15–70 s band.

The moment tensor they obtained points to a volumetric source located near sea level, approximately 1 km below the summit of Augustine. Through detailed reconstruction of the source mechanism, Dawson et al. (2011) inferred that the source consists of a sill-like structure combined with either a sub-vertical east–west trending dike or a sub-vertical pipe and a weak single vertical force. The dike strike in their best constrained dual-crack model is sub-parallel to the east–west trending Augustine–Seldovia arch, suggesting a structural relationship to this arch (Dawson et al., 2011). The moment tensor at Augustine exhibits a characteristic source process consisting of inflation–deflation–reinflation of the sill with the second inflation featuring an amplitude larger than the initial inflation. This pattern is consistent with a pressurization, depressurization, and repressurization of the sill over a period of about 1 min. The duration of this process is mainly constrained by the band-limited (10–30 s) response of the broadband sensors used at Augustine. This pattern is similar to that inferred for the source of degassing bursts at Popocatépetl, although the very-long-period source centroid is deeper (1.5 km below the summit) at Popocatépetl. Dawson et al. (2011) estimated volume changes of 13,000 m³ for the sill and 3000 m³ for the dike under Augustine, significantly larger than those inferred for Popocatépetl and representative of a more energetic explosion at Augustine. The results obtained by Dawson et al. (2011) suggest that the same model of dynamic diffusive bubble growth and pressure recovery following a sudden pressure drop, as invoked by Chouet et al. (2006) at Popocatépetl, may provide a realistic explanation for the Vulcanian explosion at Augustine.

VLP signals were observed to accompany explosions during the 2009 eruption of Redoubt Volcano, Alaska. Haney et al. (2012a) used five three-component broadband seismometers deployed on the flanks of the edifice to invert data in the 10–30 s band recorded during an explosion on 28 March 2009. Unfortunately, two of the horizontal components in their network were inoperative at the time, limiting the number of available data channels to thirteen and posing a challenge for a detailed interpretation of the source mechanism based on moment and force components. Consequently, Haney et al. (2012a) constrained their waveform inversions to moment only. They found the mechanism of the VLP signals to be well-described by a volumetric source located 1.4 km below the summit crater. The time history of the moment tensor displays a pattern of pressurization and depressurization that resembles the seismic source mechanisms associated with explosions at Popocatépetl and Augustine Volcanoes. Similar to the sources inferred at these two volcanoes, the volumetric source imaged by Haney et al. (2012a) features a sill intersecting a dike. Haney et al. (2012a) estimated a volume change of 19,000 m³ and a pressure change of 7 MPa in the dominant sill and an out-of-phase volume change of 5000 m³ and pressure change of 1.8 MPa in the subdominant dike.

Interestingly, the VLP source imaged by Haney et al. (2012a) is essentially co-located with the source of the 23-hour-long precursory swarm of LP events observed during the 1989–90 eruption of Redoubt. Based on careful analysis of the repetitive LP events, Lahr et al. (1994) argued that the entire swarm likely originated from a single point at this location. The repeated activity at this location after a 20-year interval of repose suggests that the sill imaged by Haney et al. (2012a) may represent a shallow magma storage reservoir that may already have been active during the previous eruption in 1989–90. The long-lasting presence of such a reservoir suggests the existence of some mechanical discontinuity at the contact between the edifice of Redoubt and underlying batholith. The abrupt change in mechanical stiffness between soft pyroclastic deposits above and stiff rock matrix below could have produced a barrier that arrested upward dike propagation, leading to the formation of a sub-horizontal sill-like structure (Gudmundsson, 2002). Repeated injection of magma may have contributed to a gradual homogenization of the local stress field, which then allowed a dike to break through this zone and propagate toward the surface (Gudmundsson, 2002).

3.2. Source mechanisms representative of basaltic systems

In low-viscosity basaltic systems, VLP seismicity is often part of a broadband source process associated with the unsteady transport of magma and gases through conduits. Classic examples of such systems are Stromboli Volcano, Italy, and Kilauea Volcano, Hawaii.

Eruptive behavior at Stromboli is characterized by mild, intermittent explosive activity, during which well-collimated jets of gases laden with molten lava fragments burst in short eruptions typically lasting 5–15 s. Detailed measurements were carried out at this volcano in September 1997 by Chouet et al. (2003) using a network of 21 three-component broadband (0.02–60 s) seismometers. The receiver layout was selected to provide homogeneous coverage in both azimuth and distances for sources located at shallow depths beneath the summit crater, and featured three rings of sensors surrounding the edifice at crater level, mid-flank elevations, and near sea level, with stations ranging in distance between 0.3 and 2.2 km from the active crater. Explosive activity at the time was limited to two vents located at the northern and southern perimeters of the crater, and two characteristic types of waveforms representative of eruptions from these vents were observed. Using these data, Chouet et al. (2003) and Chouet et al. (2008) carried out systematic inversions of eruption signals and imaged two distinct conduit structures underlying the two vents.

Figs. 9 and 10a show two representations of the conduit geometry underlying the northern vent area. Fig. 9 illustrates the seismic source mechanisms obtained from inversion of VLP waveforms for a characteristic eruption at this vent. Two point sources are illustrated in Fig. 9, each composed of a set of intersecting cracks (colored red and gray). We note that the mathematical representation of a point source does not differentiate two intersecting cracks from a crack elbow. This is a more reasonable geological interpretation and both solutions in Fig. 9 were viewed as such by Chouet et al. (2008). Each point source represents a flow disruption site along the upper conduit. The upper source (Fig. 9a), located ~300 m below the crater floor, represents a bifurcation in the conduit; this is the main flow disruption site for gas slug ascending toward the northern vent. The lower source (Fig. 9b), located ~500 m below the upper source, involves a sharp corner in the conduit and represents a secondary flow disruption site.

Fig. 10a shows a picture of the upper conduit geometry consistent with the seismic source mechanisms imaged in Fig. 9a and b. The conduit structure is obtained simply by extending the two crack planes imaged at the upper point source up to the surface, extending the plane of the dominant crack imaged at the lower point source up to its intersection with the dominant crack at the upper point source, and viewing the subsidiary crack at the lower point source as the downward extension of the conduit. The closely matching dips of the two dominant cracks in Fig. 9 point to a conduit that extends essentially straight from 80 m below sea level to the crater floor, 760 m above sea level. At a depth of 80 m below sea level the conduit features a sharp corner leading into a dike segment dipping 40° to the southeast. The upper dominant dike segment, and deep segment below the abrupt corner both strike northeast–southwest along a direction parallel to the elongation of the volcanic edifice and a prominent zone of structural weakness, as expressed by lineaments, dikes, and brittle structures. The surface trace of the main dike segment trends through the northern vent area, while that of the upper subsidiary segment extends northwest–southeast in rough alignment with several vents active in the northwest quadrant of Stromboli in 2002–2003 (Acocella et al., 2006); the subsidiary dike trace intersects the main dike trace ~170 m north of the northern vent area.

Fig. 10b shows results of a similar analysis carried out for a characteristic eruption at the southern vent (Chouet et al., 2008). The uppermost conduit geometry below the southern vent is composed of a northeast striking dike dipping 51° northwest, intersecting a west striking dike dipping 58° north. At 520 m elevation, the two dikes

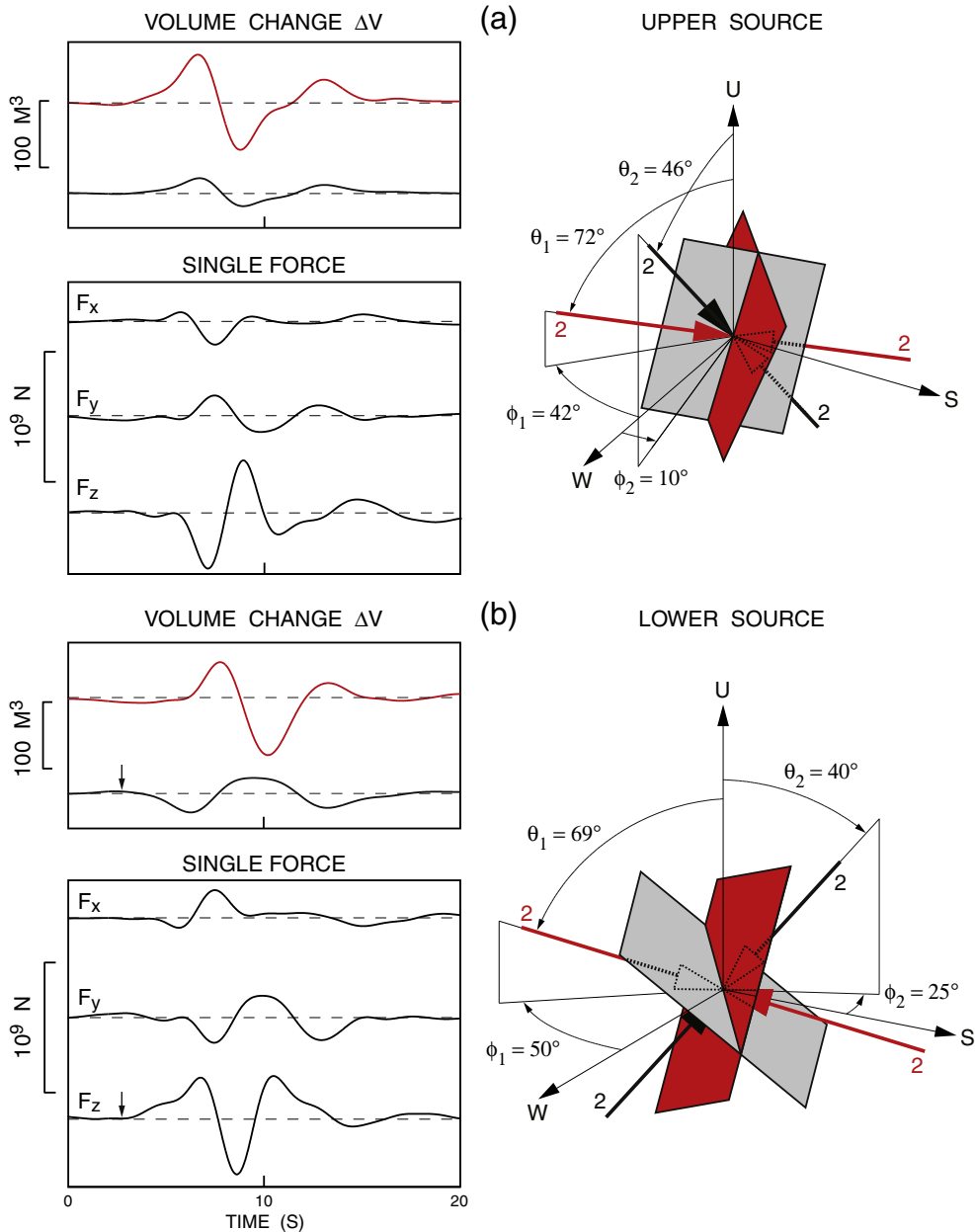


Fig. 9. Seismic source mechanisms imaged for the two flow disruption sites in the shallow conduit structure underlying the northern vent area at Stromboli. The two point source mechanisms were obtained by Chouet et al. (2008) from inversions of VLP waveforms recorded during explosions at Stromboli, and are positioned at different depths in the volcanic edifice (see text for details). Each source consists of two intersecting cracks and a single force with components F_x (east), F_y (north), and F_z (up). Volume changes are color-coded with the color of the cracks they represent in each source. Crack orientations are provided by the azimuth ϕ and polar angle θ of the dominant dipole normal to the crack plane, with arrow directions marking crack deflation (see Fig. 2b). The reference coordinates are W (west), S (south), and U (up). (a) Upper source. (b) Lower source. Arrows in left panels mark the onset of deflation of the lower dike (gray dike in right panel) and synchronous start of the upward force.

Reproduced from Chouet et al. (2008).

merge into a sub-vertical dike striking northeast, and at depth of 280 m below sea level the conduit features a second, more abrupt corner leading into a fracture dipping 50° south. The upper seismic source in this case represents a bifurcation of the main conduit coupled with a marked change in conduit dip. This geometry suggests that a fluid disruption mechanism similar to that inferred under the northern vent may be operative at this location. Fig. 10c illustrates the two conduit structures imaged below the northwest flank of Stromboli. These two structures are distinct within the uppermost 1 km of the edifice, although the conduits come to within 100 m of each other 250 m below the crater floor.

Both upper and lower point sources illustrated in Fig. 9 feature a dominant crack sustaining the largest volume change (colored red),

and a subdominant crack undergoing a smaller volume change (shaded gray). Both cracks in Fig. 9a display a similar sequence of inflation-deflation-inflation. The dominant crack in the lower source displays a volumetric response similar to that seen in the dominant crack at the upper source, but delayed by about 1 s with respect to the upper source. This implies a propagation speed of roughly 500 m/s between the two sources, consistent with the slow speed expected for a crack wave (see Section 4.1). A striking aspect of the mechanisms imaged for the two sources is the presence of dominantly vertical single-force components with similar time histories, except for a polarity reversal in one source compared to the other. The upper source (Fig. 9a) shows an initially downward force followed by an upward force, while an upward force followed by a downward force is manifest in the lower source

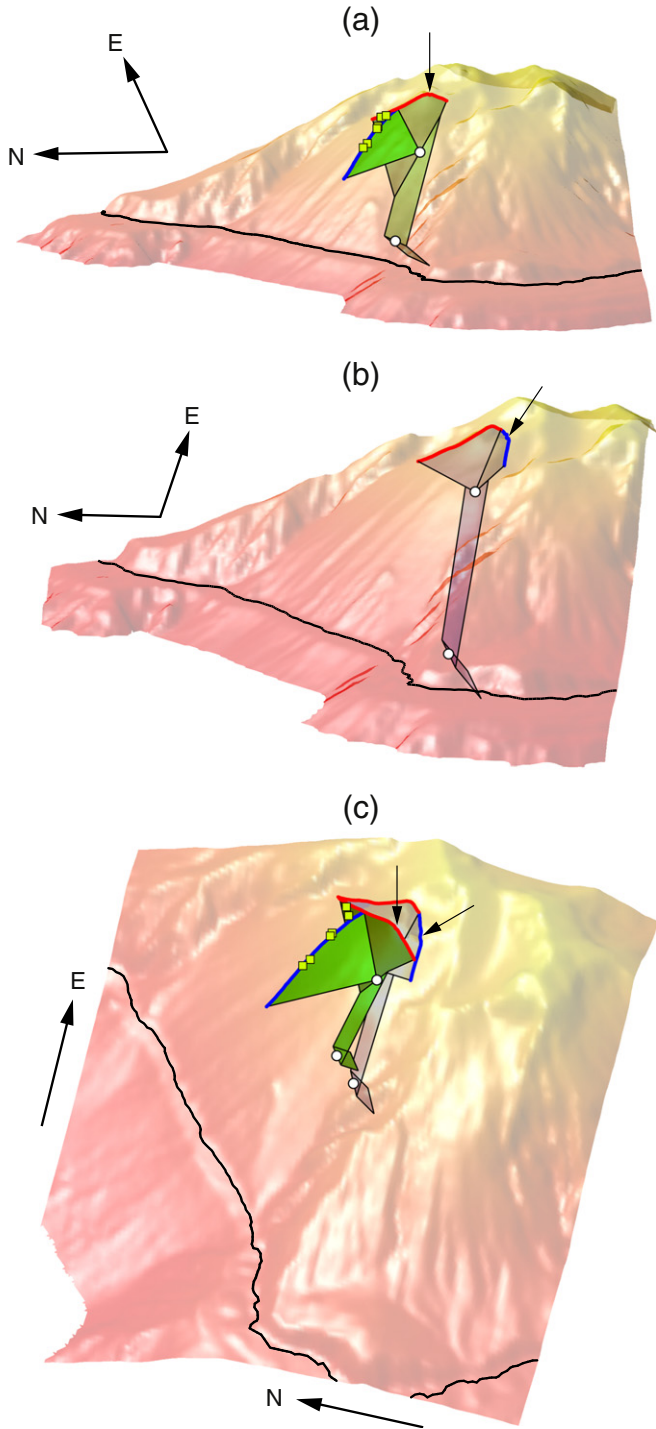


Fig. 10. (a) Geometry of the uppermost 1 km of conduit underlying the northern vent area of Stromboli (after Chouet et al., 2008). A semi-transparent view of the northwest quadrant of the edifice including the sector graben of the Sciara Del Fuoco, provides the reference for the location and geometry of the conduit, which is derived from the seismic source mechanisms obtained from inversions of VLP signals associated with explosions. A black line indicates sea level. The summit of the volcano is 924 m above sea level (no vertical exaggeration). The two flow disruption sites that are sources of VLP elastic radiation are indicated by white dots. The irregular red and blue lines, respectively, mark the surface traces of the dominant and subdominant dike segments constituting the shallowest portions of the conduit system. The eruptive vent is marked by a vertical arrow, and temporary vents active during the flank eruption in 2002–2003 are indicated by green squares. The lateral extents of individual dike segments are unknown and are shown for illustrative purpose only. (b) Same as (a) for conduit underlying the southern vent area. A slanted arrow points to the southern vent. (c) Plunging view of the Sciara Del Fuoco showing the two dike systems underlying the summit crater. The conduit structure underlying the northern vent (marked by a vertical arrow) is shaded green and that underlying the southern vent (marked by a slanted arrow) is colored gray (see (a) for details).

(Fig. 9b). In contrast to the delay of ~1 s in the volumetric components, no significant delay is apparent in the onsets of the vertical forces at the two sources, suggesting that transmission of the force between the two sources occurred via the faster speed (3.5 km/s) of the compressional wave in the rock matrix (Chouet et al., 2003).

The temporal features of the upper point source in Fig. 9a reflect a sequence of pressurization, depressurization, and repressurization, which may be viewed as the expression of a funnel-like flow disturbance induced by the transit of a gas slug through the shallow bifurcation in the conduit. Support for this view is provided by laboratory simulations (James et al., 2006) investigating the ascent of a slug of gas in a vertical liquid-filled tube featuring a sharp flare (see Fig. 4). The pressure pulse in the liquid and downward force on the apparatus holding the tube observed as the slug clears the flare are both consistent with the mechanism imaged for the upper source at Stromboli (compare volume changes and vertical force F_z in Fig. 9a with pressure and vertical tube displacement in Fig. 4b).

At the lower source (Fig. 9b), the start of the vertical force signal is synchronous with the onset of deflation of the lower dike segment (see arrows above F_z trace and above volume change signature of gray dike in left panels in Fig. 9b). As the amplitude of the upward force increases, the lower dike segment continuously deflates. During the same interval, the dominant dike (red-colored trace in Fig. 9b) remains in a slightly deflated state. This picture is consistent with a compression of the lower dike synchronous with a downward acceleration of the liquid mass, both of which may be viewed as reflecting increasing external pressure on the conduit wall induced by the elastic radiation from the downward vertical force at the upper source. Compression of the lower dike proceeds unimpeded until this process is overprinted by the arrival of the much slower volumetric expansion signal from the upper source. These temporal features of the lower point source suggest a passive response of the conduit to the action of the upper source.

Although not shown here, a similar slug disruption mechanism was imaged in the dike system underlying the southern vent (Chouet et al., 2003, 2008). However, Chouet et al. (2008) noted a marked difference in the source time functions of volume change and vertical force obtained for this eruption compared to that imaged under the northern vent (Fig. 9a). Under the southern vent, the time history of volume change in the dominant dike at the upper source begins with 15 s of accelerating deflation synchronous with a clear upward force (Chouet et al., 2008), both of which suggest that the slug was undergoing rapid expansion prior to clearing the upper conduit bifurcation. The higher elevation (by 80 m) of this bifurcation compared to that imaged under the northern vent indicates a shorter distance to the magma surface. This eruption at the southern vent was also noted to last twice as long as that observed at the northern vent (Chouet et al., 2008). Put together, these observations are consistent with the idea of a larger slug undergoing rapid expansion through this bifurcation, and clearing it a short distance below the liquid surface. This scenario combines the two effects illustrated in Figs. 4 and 5.

The picture emerging from the dynamics documented by Chouet et al. (2008) is that of an upper source representing an active fluid phase and passive solid phase, and a lower source representing an active solid phase and passive fluid phase. Thus, each discontinuity in the conduit provides a site where pressure and momentum changes resulting from flow processes associated with the passage of a gas slug through the discontinuity are coupled to the Earth, or where the elastic response of the conduit can couple back into pressure and momentum changes in the fluid. The repeatability of recorded pressure data and dependence of the magnitude of the pressure transient on slug size seen in the experiments of James et al. (2006) are in harmony with the spatio-temporal properties of VLP signals at Stromboli (Chouet et al., 2003, 2008). Collectively, these laboratory results suggest that such transients represent strong candidates for VLP sources at Stromboli. Volume estimates inferred by Chouet et al. (2008) are approximately

300 m³ and 100 m³, respectively, for the upper and lower sources under the northern vent (Fig. 9), and about 200 m³ for each source under the southern vent. The magnitudes of the forces imaged under both vents suggest pressure changes on the order of 10 MPa (Chouet et al., 2003, 2008).

The other classic example of a basaltic system is Kilauea Volcano, Hawaii. Eruptive activity at the summit of Kilauea, beginning in March, 2008 and continuing to February 2009, was characterized by episodic explosive bursts of gas and ash from a vent within Halemaumau pit crater. This activity was monitored from its onset by a network of 10 three-component broadband (0.02–60 s) seismometers deployed in the summit caldera (Fig. 11). This tight network coverage of the source under Halemaumau afforded a unique opportunity to image shallow magmatic processes under the Kilauea summit (Chouet et al., 2010).

Fig. 12a shows a typical signal obtained in the 0.02–10 Hz band at station NPB (Fig. 11) for a degassing burst on 27 August 2008. The event signature shows a burst of short-period energy followed by decaying oscillations with LP and VLP components. Fig. 12b shows the corresponding spectrum obtained in the 0–1 Hz band. The spectrum is dominated by spectral peaks at frequencies near 0.04, 0.22, 0.41, and 0.49 Hz. These spectral peaks are common to all bursts originating from this vent.

Chouet et al. (2010) carried out waveform inversions for fifteen bursts, including the initial vent-clearing event on March 19 and the bursts that occurred between 9 April 2008 and 4 February 2009. They restricted their attention to the 0.02–0.1 Hz (10–50 s) band and imaged a point source at a depth of ~1 km below the east side of Halemaumau, ~250 m east and ~500 m north of the degassing vent (Fig. 11). The source mechanism they obtained for all the bursts includes a volumetric component and a single force. For the volumetric component, Chouet et al. (2010) found several source geometries which equally satisfy the observed waveforms in that band. These geometries include a single pipe, a pipe elbow, an elbow connecting an inclined dike to a pipe, and two interlocking sub-vertical dikes.

Chouet et al. (2010) interpreted this source as a discontinuity in the conduit, where pressure and momentum changes in the magma induced during the terminal ascent stage and burst of a large slug of gas are effectively coupled to the Earth. The slug burst triggers oscillations in the magma column and attendant volumetric and force oscillations due to mass advection.

Consideration of fluid dynamic arguments lead Chouet et al. (2010) to select the dual-dike model as the preferred VLP source geometry, as this was found to be the only model capable of producing plausible values of length scales and pressure changes consistent with the magnitudes of the imaged single force component. The model features an east striking dike dipping 80° to the north, intersecting a north striking dike dipping 65° to the east (Fig. 13). Fig. 14 illustrates the VLP source behavior during a degassing burst on 27 August 2008. Fig. 14a shows the volume changes in the two dikes and related pressure change, and Fig. 14b shows the accompanying vertical force. Fig. 14c shows amplitude envelopes of the vertical component of ground velocity recorded at NPB, roughly 1 km away from the vent (see Fig. 11). Drawn in blue is the signal filtered in the 0.1–0.3 s band emphasizing the short-period (SP) contents of the burst, and in red is the corresponding signal in the 1–5 s band emphasizing the LP components of this event. The onset of deflation and simultaneous onset of the upward force occur at ~40 s (Fig. 14a,b). In Fig. 14c, the gray band marks the period of rapid increase in signal amplitude in the 0.1–0.3 s, interpreted by Chouet et al. (2010) as representing the onset of near-surface rapid slug expansion, with slug burst occurring at ~60 s.

The scenario envisioned by Chouet et al. (2010) involves the expansion and burst of a slug of gas in a vertical, pipe-like conduit extending between the vent and the VLP source. This scenario was introduced earlier in Section 2 and is illustrated in Fig. 5. In the 1-km-long elastic conduit envisioned at Kilauea, the pressure decrease associated with slug expansion propagates downward in the magma at the speed of the inhomogeneous interface wave (crack wave or tube wave) and is effectively coupled to the solid at the conduit

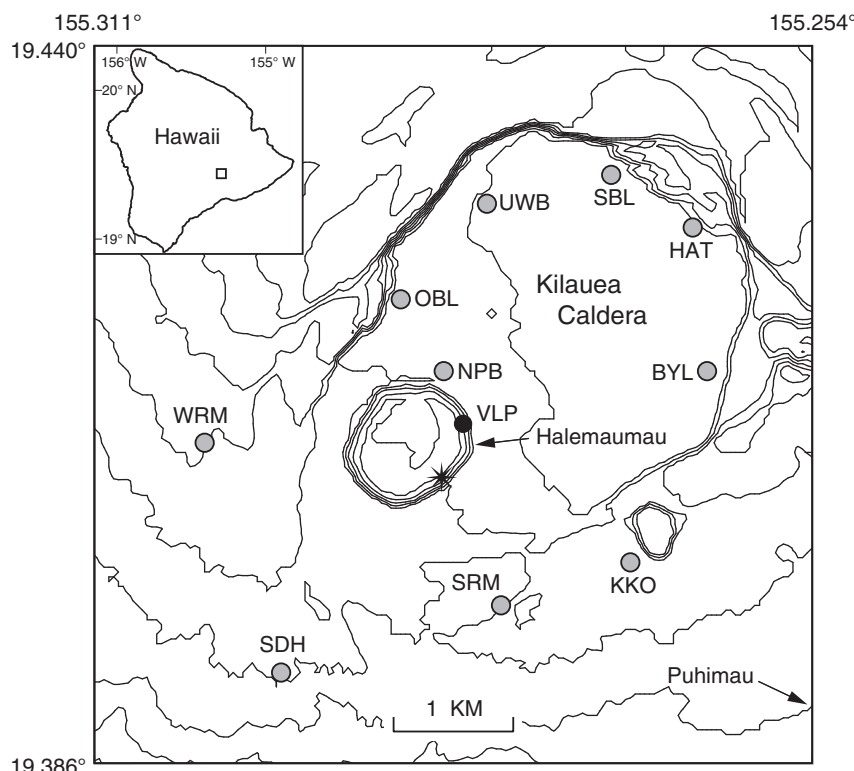


Fig. 11. Map of Kilauea Summit Caldera showing locations of three-component broadband stations (circles filled with gray). The star marks the position of the currently active vent in the Halemaumau pit crater and the black dot marks the epicenter of the VLP source centroid imaged by Chouet et al. (2010). Contour lines represent 20 m contour intervals. The inset shows the location of Kilauea Caldera on the Island of Hawaii.

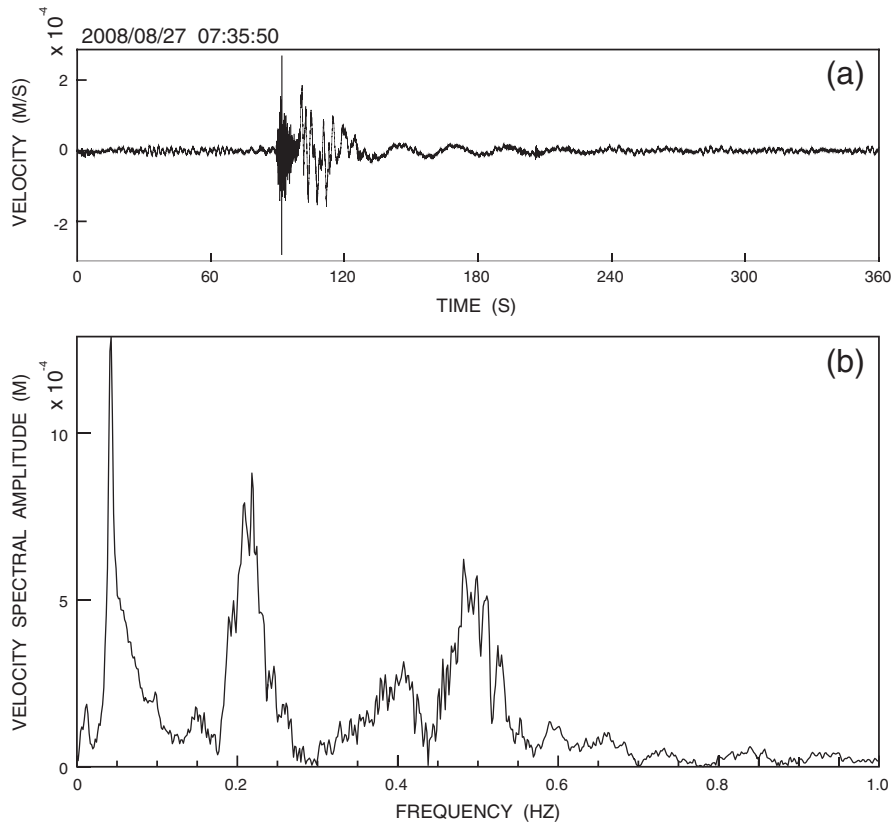


Fig. 12. (a) Record of the vertical component of velocity obtained at broadband station NPB (see Fig. 11) for a degassing burst on 27 August 2008. The record is representative of true ground motion after deconvolution for instrument response in the 0.1–50 s band. The date and time (LT) at the start of the record are indicated at the top left of the seismogram. (b) Vertical velocity spectrum obtained at station NPB in the 0–1 Hz band for the event in (a).

geometry change in the VLP centroid region. Chouet et al. (2010) interpreted the SP oscillations as a real-time indicator of the most dynamic stage of the fluid dynamic source mechanism, namely the

rapid expansion and burst in the last 3–4 s of slug ascent. VLP and LP oscillations are then stimulated by the pressure changes caused by slug expansion and burst. All degassing bursts during the year-long period of activity analyzed by Chouet et al. (2010) follow the same general pattern. Volume estimates and forces inferred by Chouet et al. (2010) from the dual-dike model range up to ~24,400 m³ and ~20 GN, respectively. Extrapolating from the results of James et al. (2009), in which force magnitudes scaled roughly in proportion to the square root of slug mass, Chouet et al. (2010) inferred slug masses ranging between 10⁴ and 10⁶ kg for the fifteen degassing bursts they quantified.

An alternate scenario for the triggering mechanism of VLP seismicity at Kilauea was proposed by Patrick et al. (2011) based on video observations of vent activity, the record of vertical ground motion at station NPT, and infrasound data. As in Chouet et al. (2010), their model of VLP source excitation is a top-down process in which a pressure disturbance occurring near the top of the liquid column propagates down the magma column and effectively couples to the surrounding rock at the VLP centroid location at 1 km depth. Patrick et al. (2011) do not assume that gas slugs are responsible for the observed degassing events. Rather, they infer that the observed gas-piston-like behavior is caused by the sudden overturning and degassing of near-surface magma triggered by large rockfalls. The gases are sourced from the top of the magma column where they accumulate due to a rheological barrier. We note that while some rockfalls are found to occur synchronously with VLP signals (Patrick et al., 2011), detailed analyses of two and one half years of broadband seismicity at Kilauea by Dawson et al. (2010) suggest that rockfalls are parts of random processes statistically disassociated from the degassing burst signals. Further insights into this issue of the triggering mechanism of degassing bursts will require additional observations of vent activity performed in concert with analyses of seismic source mechanisms.

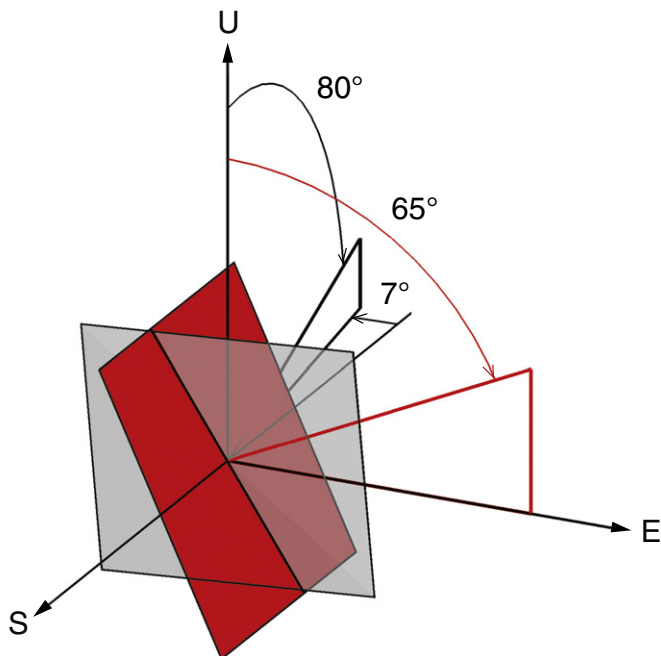


Fig. 13. Dual-dike model representative of the VLP point source under Kilauea's summit caldera. The dominant dike is colored red, and the sub-dominant dike is colored gray. Modified from Chouet et al. (2010, Fig. 8c).

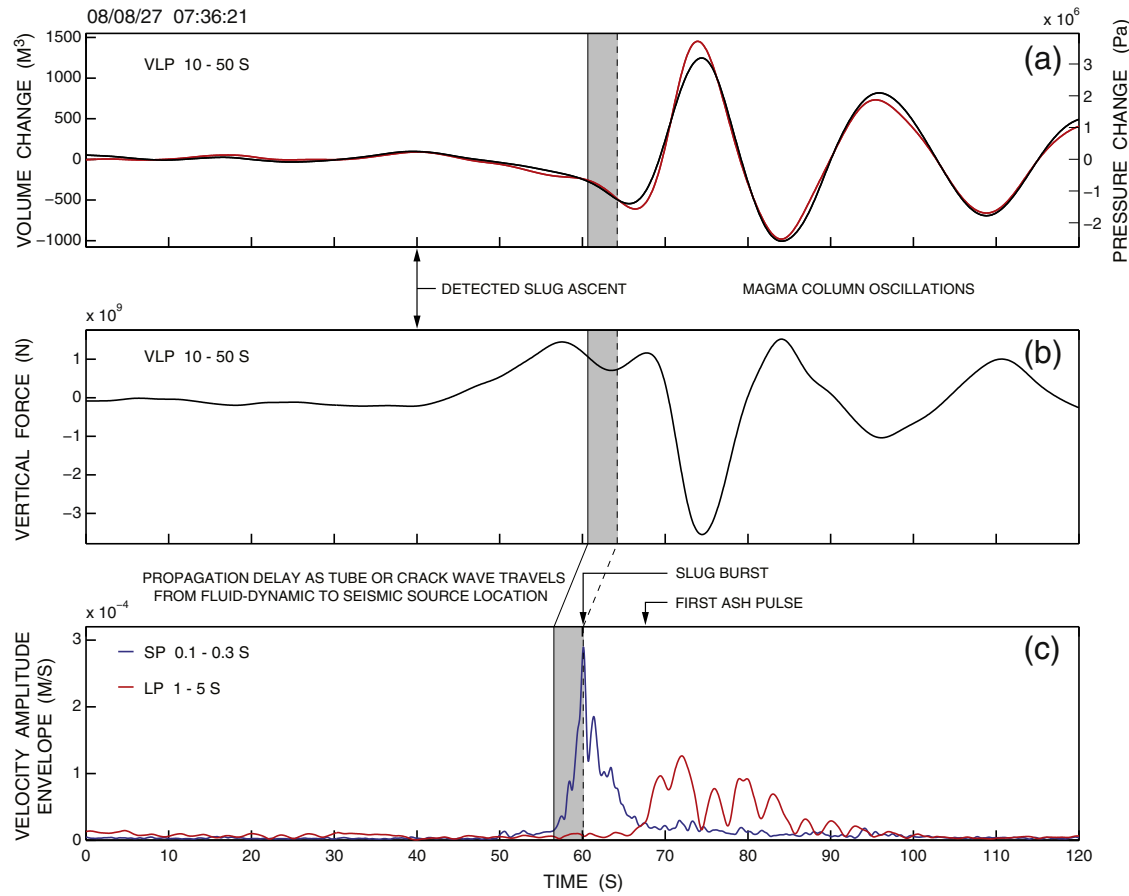


Fig. 14. Source behavior at the onset of the 27 August 2008 degassing burst at Kilauea (after Chouet et al., 2010). (a) Volume change (left scale) and related pressure change (right scale) in each dike in the dual-dike model illustrated in Fig. 13, color-coded with the same colors as the corresponding elements in that figure; the dominant dike is colored red. (b) Vertical force. Both (a) and (b) represent the same band of 10–50 s. (c) Amplitude envelopes of the vertical component of velocity at NPB, in which travel time (0.22 s) has been removed assuming a source located 200 m below the vent; blue and red represent the 0.1–0.3 s band, and 1–5 s band, respectively. The gray band represents the period of very rapid near-surface expansion of the gas-slug; a dashed line represents slug burst.

To resolve the dimensions and oscillation modes of the shallow conduit system inferred from VLP data, Chouet and Dawson (2011) carried out a more detailed analysis of the representative burst on 27 August 2008 in the 0.1–1 Hz (1–10 s) band. For this purpose, they considered an extended source consisting of a set of point sources distributed on a grid surrounding the source centroid, where the centroid position and source geometry are fixed from previous modeling of VLP data in the 10–50 s band (Chouet and Dawson, 2011). Each grid node is assigned a distinct source time function to represent inhomogeneous force/moment release (Nakano et al., 2007). The observed displacement field is made of the sum of the contributions from all point sources, expressed as (Nakano et al., 2007)

$$u_n(t) = \sum_{j=1}^{N_b} \sum_{i=1}^{N_m} m_i^{(j)}(t) * G_{ni}^{(j)}(t), \quad n = 1, \dots, N_t, \quad (8)$$

where $u_n(t)$ is the n component of seismic displacement at a receiver at time t , $m_i^{(j)}(t)$ is the amplitude of i -th component of single force or moment tensor from the j -th source, $G_{ni}^{(j)}(t)$ is the corresponding Green's functions or their spatial derivatives, and $*$ denotes convolution. N_b is the number of point sources representing the extended source, N_m is the number of source mechanism components, including single force and moment tensor, N_t is the number of seismic traces, and the subscript n stands for both receiver location and component of seismogram. The moment-tensor and single-force components associated with each point source represent the contributions from volume change

and mass advection at the source (Ohminato et al., 1998; Chouet et al., 2003, 2005, 2010).

Chouet and Dawson (2011) focused specifically on a representation of the source as an extended crack and further restricted their consideration to moment release only. In their analysis, the source time histories of all point sources are obtained simultaneously, and short-scale noisy fluctuations of the source time histories between adjacent sources are suppressed through the application of a smoothing constraint, whose strength is determined through a minimization of the Akaike Bayesian Information Criterion (ABIC) (Akaike, 1980; Nakano et al., 2007).

The analysis of Chouet and Dawson (2011) yielded estimates of the dimensions and oscillation characteristics of the dominant dike segment in the shallow magma plumbing under Kilauea Caldera. Sets of 3×3 sources were found to provide an optimum model of the oscillation signature of the dike along with a robust estimate of dike size. Their best model features an east trending dike extending 2.9 km along strike and spanning the depth range of 0.2–3.1 km (Fig. 15). The dike extends ~2 km west and ~0.9 km east of the VLP centroid where it bends from a strike E 27° N with northern dip of 85° to the west, to a strike E 7° N with northern dip of 80° to the east of the centroid. This model fits both the orientation of southwest rift fractures west of Halemaumau and the VLP solution to the east (compare with Fig. 13) and is also in rough agreement with the strike azimuth of an old eruptive fissure extending eastward from the eastern edge of Halemaumau (Neal and Lockwood, 2003). The oscillation signature of the dike is dominated by harmonic motions in the fundamental mode and first degenerate mode with respective frequencies

of ~ 0.2 Hz and ~ 0.5 Hz. These modes correspond to the two dominant spectral peaks seen in the 0.1–1 Hz band (Fig. 12b).

The modeling by Chouet and Dawson (2011) also provides evidence for another north trending dike segment. Although not strongly supported by data in the 1–10 s band, this dike is required for enhanced compatibility with the model elaborated in the 10–50 s band (Fig. 15) and provides connectivity between the east trending dike and the vent within Halemaumau pit crater. Waveform inversions carried out with a dual-dike model suggest dimensions of 0.7×0.7 km to 2.6×2.6 km for this segment (Chouet and Dawson, 2011). Consideration of the hinged model of east dike, along with clues from the dual-dike model, suggests that the VLP centroid lies at a triple junction made by the intersection of the north dike with the hinged east dike (Chouet and Dawson, 2011). The location of the VLP

centroid at this juncture thus appears readily explained as the natural expression of the efficient coupling of pressure and momentum to the Earth favored at this geometrical discontinuity.

Fuego Volcano, Guatemala, provides an end-member perspective of the range of behaviors in basaltic systems. Fuego magmas, like many other arc basalts, are characterized by high water contents (2.1–6.1 wt.% H₂O) (Sisson and Lane, 1993; Roggensack, 2001), and the precipitous loss of water as magma nears the surface leads to stiffer basalts that seem to behave more like silicic magmas (Lyons and Waite, 2011). Undercooling of magmas and crystallization induced by degassing results in a drastic increase in melt viscosity, producing basalts with high yield strengths (Sparks and Pinkerton, 1978).

Activity at Fuego in recent years has been characterized by persistent degassing from the summit crater, frequent explosions, and intermittent production of lava (Lyons et al., 2010). Lyons and Waite (2011) investigated eruption dynamics at Fuego by analyzing VLP signals produced during an explosion on 19 January 2009. They modeled the source mechanism in the 10–30 s band using data recorded with a six-station broadband network, including five seismometers on the north flank and one seismometer on the southwest flank of the edifice, ranging in distances between 1 and 2 km from the summit. The limited azimuthal coverage of the source under the Fuego summit precluded a detailed interpretation of the source mechanism based on moment and force components, hence the mechanism resolved by Lyons and Waite (2011) is restricted to moment only. The best fit VLP source centroid they obtained is offset 300 m west and 300 m below of the summit crater.

The moment tensor solution obtained by Lyons and Waite (2011) is best represented by a volumetric source composed of a near-vertical dike feeding a sill dipping 35° to the southwest. The dip of the sill is the same as the slope of the upper cone of Fuego, and its projection to the surface nearly bisects the summit crater. In light of this geometry, Lyons and Waite (2011) suggest that the magma pathway near the surface may have been controlled by the presence of a resistant layer, such as a lava flow or series of flows. They inferred that as the intruding feeder dike neared the surface, it encountered this strong layer, which was easier to follow to the summit than to break through and open a new vent on the west flank.

Volume changes estimated by Lyons and Waite (2011) are 1570 m³ in the dominant sill component, and 84 m³ in the subdominant dike component. The source time history of the sill begins with inflation, followed by deflation and reinflation, and is similar in shape to the source time function inferred for a Vulcanian explosion at Augustine Volcano (Dawson et al., 2011). Lyons and Waite (2011) interpreted the main features of the source as an initial pressurization, followed by a depressurization and repressurization. The dominant explosion driver in their model is an overpressurization of the uppermost conduit due to crystallization-induced degassing and rheological stiffening, which creates a pressurized plug that resists magma flow from below. When overpressure exceeds the tensile strength of the magma plug, brittle failure of the plug occurs, causing the eruption of gases and pyroclasts and depressurizing the sill. The resulting pressure drop allows the flow of fresh magma into the sill, which leads to its reinflation and starts a new phase of crystallization and pressurization. This mechanism is an extension of the diffusion pumping model proposed by Nishimura (2004) and extended to Popocatépetl by Chouet et al. (2005, 2006), which considered repeated pressurization/explosive degassing cycles without the injection of fresh magma into the shallow conduit.

Other explosions sampled by Lyons and Waite (2011) during their 2009 monitoring campaign produced VLP signals that were highly similar (cross-correlation coefficients larger than 0.85) to the well-studied event from 19 January. Using the latter event as reference, Lyons and Waite (2011) estimated volume changes ranging from 192 m³ to 2062 m³ for 52 explosions that occurred over 19 days.

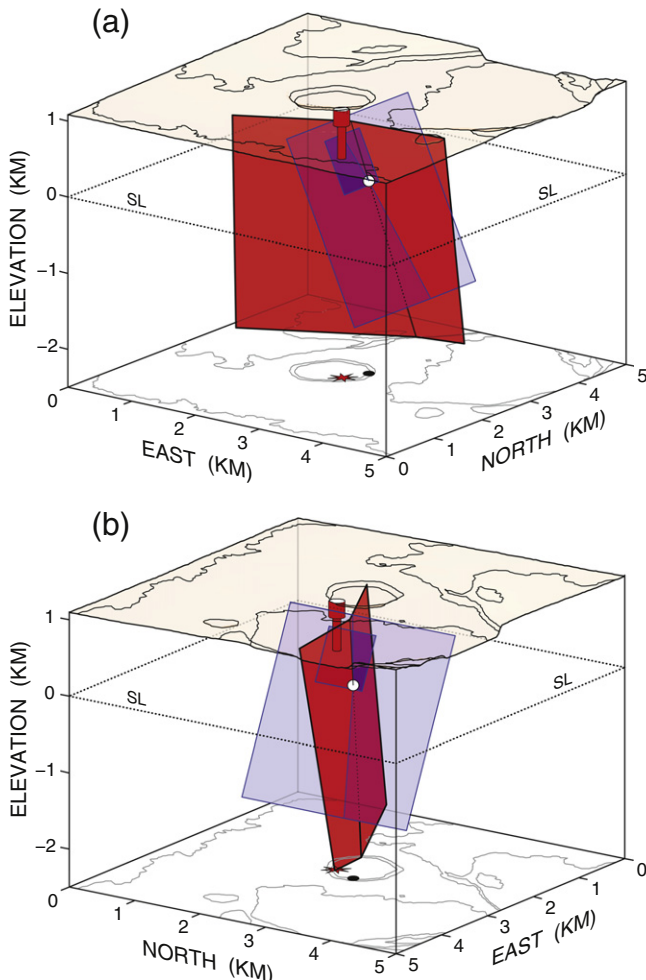


Fig. 15. Dike system imaged by Chouet and Dawson (2011) for the 27 August 2008 degassing burst at Kilauea. (a) A northwest-looking cutaway view of the Kilauea Caldera floor provides the reference for the location of the two dikes in relation to the vent (red star) in the Halemaumau pit crater. Sea level (SL) is indicated by a dotted line. The east trending dike is colored red, and the north striking dike is colored blue, with two shades of blue representing two possible sizes inferred for the latter. The white dot is the point source solution obtained by Chouet et al. (2010) in the 10–50 s band for a dual-crack mechanism plus three forces. The point source lies at a triple junction made by the intersection of the west and east branches of the east dike with the slanted north dike. This point is located near the bottom north corner of the short north dike and about a third of the way down the intersection of the longer north dike with the two branches of the east dike. The degassing pit is shown in red, where the wider upper segment is relatively well constrained by lidar measurements but narrower lower segment is unknown and shown for illustrative purpose only. This bottom segment provides communication to the north striking dike pictured in blue. Topographic contours in the bottom plane are shown to better picture the location of the VLP source centroid location with respect to the vent (red star) projected vertically downward from the surface. (b) Southwest looking view of the dike system.

The tilt signals extracted from the horizontal broadband record at the station closest to the summit, SO₂ emission and infrasound data, and visual observations all provide supporting evidence for the model of repeated degassing-driven crystallization and brittle failure in the uppermost conduit as the source of explosive activity. Undercooling of the magma due to water loss during ascent induces the growth of phenocrysts, further enhancing volatile exsolution and leading to a rheological stiffening of the magma (Lyons and Waite, 2011). Sealing of the conduit by this highly viscous plug of magma is evidenced by a decrease in SO₂ emissions and inflation reflected in the tilt data minutes prior to explosions (Lyons and Waite, 2011). The observations made by Lyons and Waite (2011) at Fuego suggest that the process operating in this stiff basaltic system is similar to that driving Vulcanian explosions at more silicic volcanoes.

3.3. Source mechanisms representative of magma–hydrothermal interactions

VLP signals, inferred to be related to hydrothermal processes, have been observed and analyzed at a few volcanoes, including Aso (Kaneshima et al., 1996; Yamamoto et al., 1999; Kawakatsu et al., 2000; Legrand et al., 2000), Satsuma-Iwojima (Ohminato, 2006), Ontake (Nakamichi et al., 2009), and Asama (Maeda and Takeo, 2011) in Japan, and Mount St. Helens, Washington (Waite et al., 2008).

Historical activity at Aso has been characterized by Strombolian and phreatomagmatic eruptions recurring at intervals of 5–10 years. Most of the recent activity has been limited to the main crater of Naka-dake, the northernmost of a 1-km-long chain of seven craters trending northwest–southeast across the youngest central cone of the volcano. A remarkable aspect of Aso's seismic activity has been the repeated occurrence of VLP tremor with period of 7.5 s, first noted by Sassa (1935) and sampled more recently with modern broadband seismometers by Kaneshima et al. (1996) and Kawakatsu et al. (2000), who discovered that this tremor is actually composed of modes with periods of 15, 7.5, 5, and 4 s, and is often accompanied by shorter-period tremor.

Kaneshima et al. (1996) and Kawakatsu et al. (2000) deployed a 12-station broadband seismic network at Aso to analyze VLP signals associated with phreatic eruptions in 1994 (Fig. 16). Eight stations were set surrounding the main crater of Naka-dake within a range of 2.5 km, providing good azimuthal coverage of the shallow source under Naka-dake (Kawakatsu et al., 2000). They located the VLP source centroid a few hundred meters southwest and 1–1.5 km below the main crater. Legrand et al. (2000) performed waveform inversions of these signals and imaged a volumetric source mechanism composed of an isotropic component and a sub-vertical crack. Details of the crack-like conduit were further investigated by Yamamoto et al. (1999), who determined that the strike and width of this conduit match the orientation and spread of the chain of craters and that the conduit extends between the depths of 0.3 km and 2.5 km below the craters. Kaneshima et al. (1996) and Kawakatsu et al. (2000) interpreted this VLP source as activity in a hydrothermal reservoir induced by hot gases leaking from a deep-seated magma chamber. Pressure in the hydrothermal reservoir is sustained by heat flow from below and lost through the sporadic release of batches of hydrothermal fluids in the fracture extending above the reservoir. The loss of pressure seals the hydrothermal reservoir shut, allowing recharge of the source region and starting a new cycle of activity.

Activity at Satsuma-Iwojima mainly consists of sustained fumarolic gas emissions from a central vent in the summit crater of Iwo-dake, a rhyolitic cone occupying the eastern half of the island (Ohminato, 2006). Besides the central vent, fumarolic activity also occurs at many smaller vents in and around the summit area of Iwo-dake (Ohminato, 2006). Monitoring of this activity was carried out by Ohminato (2006) in April 1997 using a network composed of 3 three-component

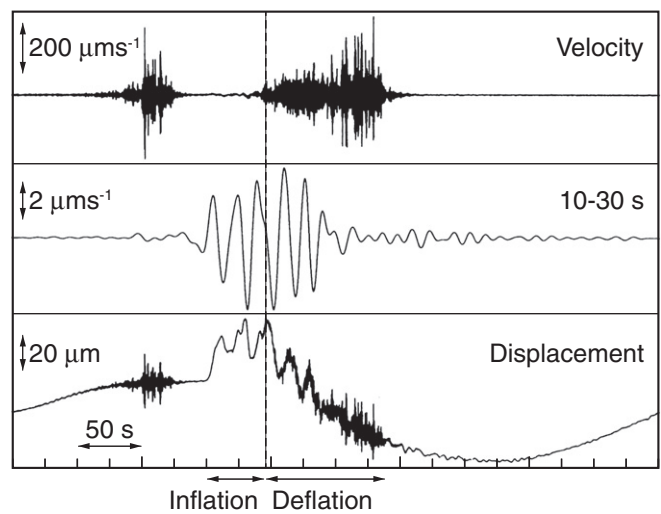


Fig. 16. Broadband waveforms of phreatic eruption at Aso Volcano. The top panel shows the raw velocity seismogram (vertical component) recorded at a receiver positioned ~1.5 km east of the crater of Naka-dake. The middle panel shows the same velocity seismogram after bandpass filtering between 10 and 30 s; the VLP signal is clear in this period band. The bottom panel shows the displacement obtained from integration of the velocity record in the top panel, in which the instrument response has been removed. The broken vertical line marks the time of the eruption. The ultra-long-period trend of several hundred seconds is due to noise.

After Kawakatsu and Yamamoto (2007, Fig. 6).

broadband sensors and 5 vertical-component short-period sensors deployed around Iwo-dake within 1.4 km of the summit crater.

A characteristic feature of the broadband data recorded by Ohminato (2006) is a regular amplitude modulation of tremor. The modulation occurs with a period of 46–50 min and is strongly frequency dependent. At frequencies above 40 Hz, the modulation cycle begins with a sharp increase in signal amplitude lasting about 1 min, followed by gradual decay lasting ~10–12 min, and ending with a rapid decay back to background noise over an interval of a few minutes; the overall duration of high amplitudes is about 15 min at these frequencies. In the frequency range of 1–40 Hz, the amplitude modulation features two stages, the first showing a gradual amplitude increase with an upward convex envelope lasting about 15 min, and the second a decreasing amplitude with concave-shaped envelope lasting 30–35 min. At frequencies below 0.2 Hz, the velocity record features repeating VLP pulses with almost identical shapes from event to event. The pulses have typical widths of 3–4 s and are perfectly synchronized with the abrupt onset of high-frequency (>40 Hz) tremor (Ohminato, 2006).

Ohminato (2006) performed waveform inversions of the VLP pulses and imaged a volumetric source mechanism in the form of a northeast dipping sub-vertical crack at a depth of 100 m below the summit crater of Iwo-dake. The source time history of the crack points to a step-like inflation, indicative of a sudden pressurization. No significant contribution from a single force was found in the inferred mechanism. The hydrothermal process hypothesized by Ohminato (2006) to explain both the periodic amplitude modulation of tremor and associated VLP signals involves a water-filled crack connected to a network of gas pockets separated by narrow constricted pathways. Water is supplied to the crack from the surrounding shallow aquifer through permeable rock. The water is heated by hot volcanic gases streaming upward from an underlying magma body. At a critical level of superheating the water in the crack suddenly vaporizes, causing a pressure surge and triggering the release of steam from the crack into the network of interconnected gas pockets. The pressure surge is the source of the VLP signal and drives the passive part of the system consisting of a dendritic set of gas pathways to individual fumarolic vents. In this interpretation, the pressurized gas flow through the narrow constricted paths

between gas pockets is choked and generates high-frequency tremor (Morrissey and Chouet, 1997). Ohminato (2006) used a simple model of tremor generating system composed of a pressure source and a gas-filled chamber with narrow inlet and outlet, to demonstrate that the temporal characteristics of the inlet and outlet flow rates are compatible with the observed pattern of amplitude modulation of tremor above 1 Hz. Such a distributed network of gas pockets is also compatible with source and path effects observed in the tremor spectra at individual sites around Iwo-dake (Ohminato, 2006).

With an altitude of over 3000 m, Mount Ontake is the second highest stratovolcano of Japan. The first historic eruption of this volcano occurred on 28 October 1979 and produced ash and steam concurrent with the opening of several vents southwest of the summit (Nakamichi et al., 2009). A new crater with steaming fumaroles was observed ~400 m south of the summit in late May 1991. A year and a half later, seismic activity beneath the summit was followed by the emission of a plume of steam rising 100 m above the crater (Nakamichi et al., 2009).

In late December 2006, renewed VT activity started below the Ontake summit, accompanied by LP events, tremor and a single VLP event on January 25, 2007 (Nakamichi et al., 2009). Approximately 1 cm of east–west extension was measured concurrently with the seismic activity (Nakamichi et al., 2009). This was followed by a small phreatic eruption in the fumarole region south of the crater in late March 2007.

The VLP event, featuring a period longer than 20 s, was well recorded by a network of 9 broadband seismometers set around the edifice at ranges of 7 to 25 km from the summit (Nakamichi et al., 2009). Nakamichi et al. (2009) inverted the VLP signals in the 20–50 s band, assuming either a crack or isotropic source as possible mechanisms. Their best fit solution is a northwest striking crack dipping 60°–90° northeast, located 0.6 km above sea level beneath the Ontake summit. The source time history of the crack has the form of a triangular pulse, suggesting inflation followed by deflation. Nakamichi et al. (2009) interpreted the overall seismic activity at Ontake as the result of a magma intrusion beneath the volcano. They viewed the swarm of VT events as the brittle response of the edifice to the intrusion. Concurrently, hot gases released from the intruding body impacted the shallow hydrothermal system, heating and pressurizing this system and triggering LP events and tremor. During this stage of activity, sudden vaporization of ground water opened a hydrothermal crack, producing the VLP event (Nakamichi et al., 2009). Sustained pressurization of the hydrothermal system eventually lead to a small phreatic eruption in late March. This model of VLP event generation under Ontake is similar to that proposed by Ohminato (2006) for the VLP source under Satsuma-Iwojima.

Recent activity at Asama Volcano, Japan, has been marked by moderate-sized Vulcanian eruptions in 2004 (Ohminato et al., 2006), three small ash eruptions in August 2008, and another small-scale eruption in early February 2009. The 2009 activity produced a vent several tens of meters in diameter in the summit crater, which has since been a source of passive gas emissions (Maeda and Takeo, 2011).

VLP pulses were observed at Asama before the first of the 2004 eruptions and after the re-installation of the summit stations in 2007. No VLP data is available for the period September 2004–October 2007 following the destruction of the summit network during the explosive activity in 2004. When observed, the rate of occurrence of VLP events has been relatively stable, averaging approximately 10 events per day (Maeda and Takeo, 2011). Concurrent with activity in 2008, the daily frequency of VLP pulses was noted to increase before eruptions. Of particular interest were VLP pulses with durations of ~50 s seen to occur ~3 min before each of the three eruptions in 2008 (Maeda and Takeo, 2011). VLP pulses observed since May 2009 have preceded distinct slow gas emissions by 30–60 s, suggesting these pulses are related to gas movement at shallow depths below the summit (Maeda and Takeo, 2011).

The source mechanism of VLP events at Asama was analyzed by Maeda and Takeo (2011) using data from a dense network of 14 broadband seismometers deployed within 1 km of the summit crater. This network remained in operation for three and one half months in late 2008. The VLP events considered by Maeda and Takeo (2011) consist of one-sided velocity pulses with durations of 5–30 s. A superficial source is implied by the shallow dipping VLP particle motions. Also of note are the horizontal seismograms recorded for this event, whose signatures typically display much longer transient signals indicative of a contamination by ground tilt. Accordingly, Maeda and Takeo (2011) performed their analyses of these events by using Green's functions that account for both translational and tilt motions (see Section 2.1). They did not consider a single force in their source mechanism as the recorded pulses were inferred to be associated with gentle movements of non-viscous gases with minimal exchange of momentum.

The best fitting sources inferred by Maeda and Takeo (2011) are located under the northern perimeter of the summit crater, at depths of 100–150 m below the crater floor. Their inferred source mechanism is composed of a crack and a pipe, where the strike and dip of the crack are both 70°, and the pipe axis is tilted 30° from vertical and rotated 60° counterclockwise from east (Maeda and Takeo, 2011). The source time histories indicate an initial source pressurization lasting ~10 s, followed by more gradual depressurization lasting on the order of 100 s. These source features were attributed by Maeda and Takeo (2011) to an inflow of gases into the VLP-source cavity from a deeper magma source or from boiling ground water, resulting in a rapid pressurization of the VLP cavity. Upon reaching a critical pressure threshold, gentle escape of this gas toward the surface induced a gradual depressurization of the source.

The dome-building eruption of Mount St. Helens in 2004–2008 was distinguished by the extrusion of a stiff plug of dacitic magma accompanied by shallow, repetitive LP earthquakes that were termed drumbeats by scientists monitoring Mount St. Helens (Moran et al., 2008a). VLP signals commonly accompanied the LP events, but were detected only in the immediate vicinity of the crater (Waite et al., 2008). Using data from a temporary network of 19 broadband seismometers surrounding the crater at ranges of 1.2 to 6.3 km, Waite et al. (2008) modeled the source mechanisms of LP and VLP events in the 0.5–4 s and 8–40 s bands, respectively. Their waveform inversions point to the perturbation of a common crack system linking the magma conduit and shallow water-saturated region of the volcano.

A scenario consistent with the source mechanisms imaged by Waite et al. (2008) involves the repeated pressurization of a subhorizontal steam-filled crack located directly beneath the growing lava dome in the southern part of the crater (see Section 4.5). Steam produced by the vaporization of ground water by magmatic heat, and exsolved steam from the magma, feed into the crack and pressurize it. Upon reaching a critical pressure threshold, steam is vented out of the crack through fractures leading to the surface. The drop of pressure triggers a partial collapse of the crack, which resonates for 5 to 10 s of seconds (Waite et al., 2008). The collapse of the crack induces sagging of the overlying dome and triggers a passive response in the magma conduit that is observed in the VLP band. Waveform inversion of the VLP event revealed a volumetric source component plus a single force. The volumetric source is composed of a north-dipping sill and a near-vertical dike or pipe (Waite et al., 2008). The VLP source sill is roughly co-planar with the LP source crack, but is offset deeper and to the north beneath the 1980s lava dome. The main VLP signal is dominated by the deflation–inflation of the sill and near simultaneous inflation–deflation of the dike. Large, sub-horizontal force components that accompany the volume changes were viewed by Waite et al. (2008) as reaction forces on the Earth resulting from transient mass advection in the conduit.

The observed forces and volumetric components of the VLP response modeled by Waite et al. (2008) are both consistently

explained as the result of a perturbation in an otherwise smooth steady flow of magma upward through a dike and into a sill underlying the old dome. In this model, the dike represents the top of the old conduit that fed the 1980s dome-building eruptions, and the sill represents a bypass below the old dome (Waite et al., 2008). According to this interpretation, at the start of renewed activity in September 2004, magma moving up the conduit found an easier pathway to the surface by breaking out of the conduit near the surface and pushing sub-horizontally to the south rather than intruding the 1980s dome. The imaged sill represents this segment of conduit, and the hydrothermal crack may represent a branch of this fracture extending into the water-soaked region beneath the crater floor. This picture of Mount St. Helens as a steam engine is quite distinct from an earlier model in which the drumbeats were assumed to represent stick-slip motion between the extruding lava and conduit walls (Iverson et al., 2006) (see further discussion of this issue in Section 4.8). A sustained supply of heat and fluid from the magmatic system is necessary to keep the LP crack pressurized and keep the drumbeats beating in the model of Waite et al. (2008). This model provides a counterpoint to models derived for Aso, Satsuma-Iwojima, Ontake, and Asama volcanoes and testifies to the richness of processes associated with magma–hydrothermal interactions.

4. LP Seismicity

Long-period (0.5–5 Hz) seismicity includes individual LP events and tremor. LP events are transient, volumetric signals consisting of a brief broadband onset, followed by a coda of decaying harmonic oscillations containing pronounced spectral peaks that are independent of azimuth and distance to the source (Chouet, 1996a) (Fig. 17). This is commonly interpreted as a broadband, time-localized pressure excitation mechanism (or trigger mechanism), followed by the response of a fluid-filled resonator. Tremor is a more continuous vibration of the ground, which may last from minutes up to years in duration (McNutt, 1992). In some instances, inter-event time spacing between discrete,

repetitive LP events decreases, and the individual LP events merge to form tremor (e.g., Latter, 1979; Fehler, 1983; Neuberg, 2011; Hotovec et al., 2012). This particular type of tremor clearly has a common origin with the preceding LP events, and these LP events have been interpreted as the impulse response of the resonant, tremor-generating system (Chouet, 1985). However, worldwide observations of volcanic tremor show a wide variability in temporal durations, signal amplitudes, and frequency contents. This large variety indicates that volcanic tremor probably results from a number of different processes. For example, “eruption tremor” is used to describe broadband tremor directly associated with sustained explosions (Scandone and Malone, 1985; McNutt and Nishimura, 2008); this contrasts markedly with harmonic tremor (McNutt, 1992).

4.1. Fluid resonance and crack waves

Interpretations of the oscillating characteristics of LP codas have mostly relied on the model of a fluid-driven crack (Chouet, 1986, 1988, 1992). This geometry is the most natural geometry satisfying mass transport conditions at depth in a volcano, and is supported by results from inversions of LP waveforms recorded on several volcanoes (Kumagai et al., 2002a; Nakano et al., 2003; Kumagai et al., 2005; Waite et al., 2008; Arciniega-Ceballos et al., 2012). The fluid-driven crack model evolved from an initial treatment of volcanic tremor by Aki et al. (1977a), who proposed a mechanism for volcanic tremor at Kilauea, Hawaii consisting of the jerky extension of dry and fluid-filled tensile cracks. Although this simplified two-dimensional model considered both the driving excitation and geometry appropriate for transport, the fluid inside the crack was only treated as a passive cushion that did not support the acoustic propagation of the pressure disturbance caused by the motion of the crack wall.

The 1980–86 eruptions of Mount St. Helens provided new observations of LPs and tremor at a time when understanding of LP events was very limited (Fehler and Chouet, 1982; Fehler, 1983; Qamar et al., 1983). Fehler and Chouet (1982) reported LP events with durations of

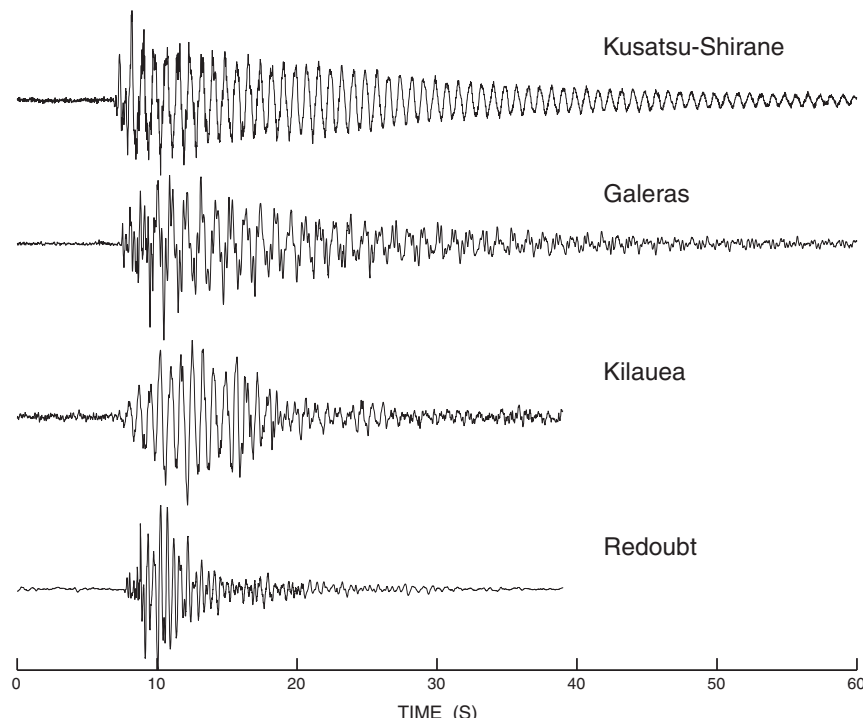


Fig. 17. Typical signatures of long-period events observed at Kusatsu-Shirane, Galeras, Kilauea, and Redoubt Volcanoes. The signatures are all characterized by a harmonic coda following a signal onset enriched in higher-frequencies.
After Chouet (2003).

~30 s, spectra peaked in the range 1.7–2.3 Hz, and depths between 0 and 5 km. Fehler and Chouet (1982) proposed that the peaked spectra originated from excitation of a fixed cavity under the active crater. These observations rejuvenated interest in LP and tremor models in which the fluid plays an active role (e.g., St. Lawrence and Qamar, 1979; Ferrick et al., 1982; Chouet, 1985; Bame and Fehler, 1986). Accordingly, an extension of the crack model including active fluid participation was proposed by Chouet and Julian (1985), who considered a simultaneous solution of the elastodynamics and fluid dynamics equations for a two-dimensional crack. This model was later extended to three dimensions by Chouet (1986) and was extensively studied by Chouet (1988, 1992).

The most significant feature of these models was the presence of an interface wave propagating through the fluid and reflecting back and forth at the crack tips (Fig. 18). The asymptotic behavior of this “crack wave” was investigated by Ferrazzini and Aki (1987) by analyzing the normal modes trapped in a liquid layer sandwiched between two elastic half spaces. The excitation of modes in the crack model depends on the position of the pressure transient, the extent of crack surface affected by the transient, the temporal characteristics of the transient, and crack stiffness $C = (b/\mu)(L/d)$, where b is the bulk modulus of the fluid, μ is the rigidity of the rock, L is the crack length, and d is the crack aperture (Aki et al., 1977a; Chouet, 1986). The crack wave velocity is slower than the acoustic velocity of the fluid at all wavelengths, and is inversely dispersive (velocity decreases with increasing wavelength and crack stiffness); this is a result of the elasticity of the crack wall, whose effect is to decrease the effective bulk modulus of the fluid. The deformation of the crack wall is such that it is easier for the fluid to expand and contract compared to the situation in a perfectly rigid crack or conduit. The motion of the fluid is out of phase with the solid motion for the crack wave. The crack wave is an inhomogeneous wave. This implies that the crack wave is only detectable close to the fracture due to its exponential decay away from the fracture wall. However, upon reflection at the fracture tip, part of the wave energy is transferred to the surrounding elastic solid in the form of body waves that are observable in the far field from the fracture (Chouet, 1986, 1988). The properties of the crack wave are analogous to those of tube waves propagating in a fluid-filled borehole (Biot, 1952). However, unlike the tube wave, as the wavelength increases to infinity, the velocity of the crack wave approaches zero in inverse proportion to the square root of wavelength (Ferrazzini and Aki, 1987). In the short wavelength limit, the crack wave reduces to the Stoneley wave propagating along a fluid-solid interface.

Fig. 18 shows an example of a calculation with the model of Chouet (1986). This figure shows the normal component of velocity at the wall of a fluid-filled crack embedded in an infinite elastic solid at eight snapshot times in the finite-difference simulation. The crack is excited by an arbitrary step function in pressure applied at a small patch located in this example at the center of one tip of the crack (snapshot 1). As time progresses in the calculation, the lateral and longitudinal resonant modes of the crack are excited (snapshot 5), and crack waves propagate up and down the crack, reflecting at the crack tips (snapshots 7, 8). The fluid-filled crack is specified by the parameters α/a , b/μ , W/L , and the crack stiffness C , where α is the P-wave velocity of the elastic solid, a is the sound speed of the fluid in the crack, and W is the width of the crack (Chouet, 1986).

The slow characteristics of the crack wave lead to more realistic estimates of resonator dimensions compared to estimates based on the sound speed of a fluid embedded in a resonator with perfectly rigid walls. For instance, Kubotera (1974) determined the source of 3.5–7 s period tremor at Mount Aso to be a resonating spherical magma chamber of 4–6 km radius. By considering crack waves, this same tremor signal can be modeled by a modest-sized magma body ~500 m long and a few meters thick (Ferrazzini and Aki, 1987; Chouet, 1988). Source dimensions estimated from LP data based on

the crack model typically range from tens to several hundreds of meters for hydrothermal cracks (Saccorotti et al., 2001; Kumagai et al., 2002a, 2005). As formulated, the crack model accounts for radiation and viscous drag losses only. Intrinsic losses due to dissipation mechanisms within the fluid were treated separately by Kumagai and Chouet (2000), and systematic investigations of LP signatures based on their results underscore the importance of dusty gases or bubbly basalt as fluids for generating LP events of magmatic origin (Chouet, 1996a; Gil Cruz and Chouet, 1997; Kumagai and Chouet, 1999), and misty gases, steam, and bubbly water in generating LP events of hydrothermal origin (Saccorotti et al., 2001; Kumagai et al., 2002b) (see Section 4.5 for more details).

In the model of Chouet (1986), a simultaneous solution of the equations of motion of the fluid inside the crack and the surrounding elastic solid is obtained numerically by using a 3D time-domain finite-difference scheme. Another approach to numerically simulate the dynamic response of a fluid-filled crack is to formulate this problem using the frequency-domain boundary integral method (Yamamoto and Kawakatsu, 2009). The boundary integral method relies on a formulation of governing equations in terms of integrals on boundaries, which can be solved by using a point collocation method (Yamamoto and Kawakatsu, 2009). This approach appears particularly well-suited to address the frequency-dependent properties of materials (i.e., bubbly liquids) found in volcanic and hydrothermal processes.

Neuberg et al. (2000) and Jousset et al. (2003) investigated seismic-acoustic wave conversion and coupling in a shallow rectangular conduit embedded in a homogeneous elastic half space. They used a 2D finite-difference scheme to model major features of the LP seismic wave field and study the behavior of single LP events as well as tremor. In their model, seismic propagation in the elastic solid and acoustic propagation in the fluid-filled conduit are solved simultaneously using a single velocity-stress computational scheme. The fluid is defined by a zero shear-velocity (rigidity $\mu=0$), and appropriate values for the density and sound speed (compressional wave velocity, α). This approach does not require explicit boundary conditions at the conduit wall to define the coupling between the fluid and solid. Acoustic-seismic conversion results from energy transmission controlled by effective material properties at the fluid-solid interface. Using a 2D finite-difference scheme and rectangular conduit model, Jousset et al. (2004) further investigated the effects of viscoelasticity and topography on the amplitudes and spectra of LP events. Their study indicates that the effects of anelastic attenuation and topography can induce significant distortion in LP spectra. Their results also suggest that the rheological properties of magmas may be constrained from detailed analyses of LP seismograms.

4.2. Excitation mechanism of LP seismicity

None of these models address the excitation (trigger) mechanism of LP events or tremor. For example, in the model of Chouet (1986) the spatiotemporal properties of the pressure transient triggering the crack resonance are preset as kinematic conditions in the model (e.g., an arbitrary step function in pressure applied to a small patch of the crack wall, see Fig. 18). The utility of this model is thus restricted to a quantification of the crack resonance and properties of the fluids at the source of LP events.

A wide variety of volcanological processes could conceivably produce the excitation mechanism of LP seismicity. For example, LP seismicity has been observed in relation to lava dome growth and solid extrusion processes in summit craters of andesitic-dacitic stratovolcanoes (e.g., Gil Cruz and Chouet, 1997; Yamasato, 1998; Neuberg et al., 2000; Moran et al., 2008a). However, water is also frequently abundant in stratovolcanoes, with brine and steam exsolved from magma accumulating in horizontal lenses and forming tree-like distributions of hydrothermal alteration around a central magma conduit and around dikes; these features are interpreted from

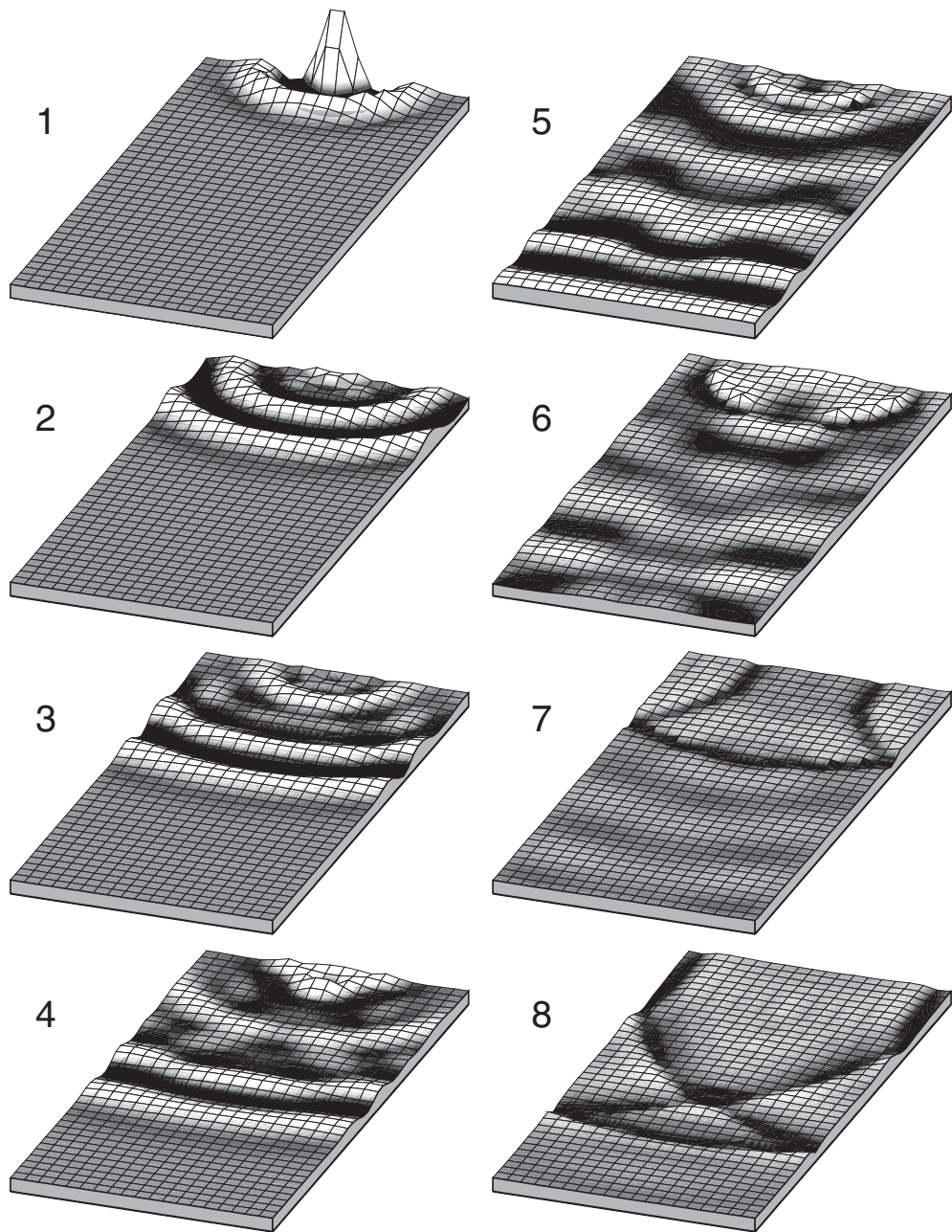


Fig. 18. Normal component of velocity at the wall of a fluid-filled crack with $\alpha/a = 17.5$, $b/\mu = 0.0018$, $W/L = 0.5$, and $C = 7.5$ calculated with the model of Chouet (1986). See text for explanation of symbols. Numbers 1–8 represent different snapshot times in the finite-difference calculation. The time step has scale $dt = 0.00625L/\alpha$ and the snapshots shown correspond to N time steps where: (1) $N = 50$, (2) $N = 100$, (3) $N = 150$, (4) $N = 200$, (5) $N = 300$, (6) $N = 500$, (7) $N = 1000$, and (8) $N = 2000$. Figure reproduced from Matoza (2009).

outcrops of partially collapsed or fossil stratovolcanoes (Branch, 1976; Wohletz and Heiken, 1992; Fournier, 1999; John et al., 2008). Hydrothermal processes are also evident in surface manifestations such as fumaroles, hot springs and seeps, and sulfur deposits in active volcanoes (Shevenell and Goff, 1993). Meteoric water from rainfall, snow melt, and glacier melt may circulate or reside in perched aquifers within the upper region of the volcanic edifice, generating phreatic and phreato-magmatic processes (Wohletz and Heiken, 1992; Fournier, 1999). LP seismicity is also commonly observed in direct relation to magmatic fragmentation, degassing, and explosions (e.g., Arciniega-Ceballos et al., 2003, 2008; Molina et al., 2004; Chouet and Dawson, 2011), and may be related to brittle failure of melt itself in the conduit (Goto, 1999; Neuberg et al., 2006), or to self-sustained oscillations within magma flow channels (Julian, 1994).

In order to understand the excitation mechanism of LP seismicity within this wide array of potential (and not necessarily mutually exclusive) candidates, observations of the source over a broad band of frequencies are necessary, along with an adequate sampling of the evolutionary characteristics of volcanic seismicity. Understanding the fundamental processes leading to LP seismicity, and understanding which processes are pertinent to a particular volcanic system and eruption, are critical for volcanic eruption forecasting decisions and hazard mitigation. In Sections 4.4–4.8, we address five broad families of processes that have been widely invoked for the source origin of LP seismicity: (1) self-sustained fluid oscillations, (2) magma-hydrothermal interactions, (3) magmatic degassing, (4) brittle fracture of melt, and (5) solid extrusion dynamics and plug stick-slip. We preface this discussion with a comment about hybrid events

(Section 4.3), and conclude this section with a brief review of deep LP seismicity observed beneath active volcanic centers (Section 4.9).

4.3. Hybrid events

An important extension to the fluid-filled resonator model for LP events is the concept of a *hybrid* event. Lahr et al. (1994) coined the term *hybrid* to describe a group of events observed during the 1989–1990 eruptions of Redoubt that had decaying harmonic codas characteristic of an LP event, but with more pronounced high-frequencies in the onsets and mixed first-motions, which are characteristic of VT events. Hybrid events were interpreted as arising from, for instance, brittle faulting in zones of weakness intersecting a fluid-filled crack (Lahr et al., 1994). A hybrid is therefore defined as an event with characteristics of both shear-failure (e.g., mixed first-motions) and resonance (harmonic coda). In other words, a hybrid event is an LP event for which the trigger mechanism is a shear-failure. The mixed first-motions are thus far more critical in classifying an event as a hybrid than are pronounced high frequencies in the onset. Mixed first-motions or some shear-faulting source component (e.g., Foulger et al., 2004) should be viewed as a necessary condition in the definition of a hybrid. However, the term *hybrid* has subsequently been applied much more loosely to seismic signals observed at other volcanoes throughout the literature. In this second usage, a hybrid is defined simply as an LP event with a pronounced high-frequency onset; the requirement of mixed first-motions being dropped. This is unfortunate because the observed frequency content of the onset of an LP event is dependent on several factors unrelated to the initial trigger mechanism.

As discussed above, the response of a fluid-filled crack to a broadband excitation consists of a broad range of frequencies or crack modes. Chouet (1985) showed that seismic energy radiated per unit time by a pipe is proportional to the 4th power of frequency (the same is expected for a crack). This implies that higher modes are quickly dissipated away from the source and that their signature is observable only for a short time interval at the onset of the LP signal (Fig. 19). Broadband onsets (including high-frequencies) are therefore predicted by the standard fluid-filled crack model (Fig. 19). In addition, the observed frequency content in the onset of an LP event will vary with the source depth, epicentral distance of the seismometer, and attenuation and scattering properties of the volcanic edifice. Therefore, the presence of high frequencies at the signal onset does not necessarily imply a hybrid source process. A good example of events that could be mistakenly classified as hybrids on the basis of high-frequencies in the onsets are degassing bursts at Kilauea (Chouet and Dawson, 2011); there is no double-couple involved in these bursts (see Fig. 12). Neuberg et al. (2000) investigated the fraction of energy <2 Hz in the trigger onset of LP/“hybrid” seismicity at Soufrière Hills Volcano, Montserrat. Rather than a bimodal distribution that would enable separation of LPs and “hybrids” based on frequency content of the onset, a smooth distribution was observed (Fig. 20). This highlights the problem of defining a hybrid based solely on the frequency content of the event onset.

A true hybrid source process could be identified through source inversions (Section 2). For instance, Foulger et al. (2004) present source inversion results of microearthquakes at Long Valley Caldera, California. These non-double-couple earthquakes had source types (Hudson et al., 1989) consistent with mixed shear and tensile faulting combined with an additional volume-compensating process, perhaps representing fluid flow into opening tensile cracks. Such a source mechanism, combined with an oscillatory LP coda, would indicate a true hybrid source process.

4.4. Self-sustained oscillations

Analyses of the dynamics of magma fluid flow have suggested that volcanic tremor may be generated by self-sustained oscillations. Julian (1994) proposed a nonlinear excitation mechanism of tremor

using a simple lumped-parameter model. In the model of Julian (1994), elastic coupling of the fluid and solid produces self-excited oscillations in a viscous incompressible liquid flowing through a channel with compliant walls. In this model, an increase in flow velocity leads to a decrease of fluid pressure via the Bernoulli effect. As a result, the channel walls move inward and constrict the flow, causing an increase in fluid pressure and forcing the channel open again. The cyclic repetition of this process results in the self-sustained oscillations, somewhat analogous to the mechanism of tone production in musical reed instruments such as the clarinet. Julian (1994) demonstrated that with increasing driving pressure, the model can exhibit various types of oscillatory behavior resembling tremor.

Balmforth et al. (2005) further investigated Julian's model, exploring the stability of fluid flow through a thin channel bounded by two semi-infinite elastic solids. Treating the fluid as viscous and incompressible, they demonstrated the occurrence of shock-like flow disturbances propagating in the direction of flow with phase speed similar to the background flow speed. This type of instability is analogous to what fluid dynamicists call roll waves (e.g., Balmforth and Mandre, 2004). Assuming periodic inlet-outlet flow conditions, and considering flow speeds much slower than the shear and compressional wave speeds in the solid, Balmforth et al. (2005) obtained the critical flow speed, $V_{crit\ roll}$, required for the generation of roll wave instability:

$$V_{crit\ roll} \approx \beta \sqrt{\frac{\rho_s}{\rho_f}} \varepsilon, \quad (9)$$

where $\beta = \sqrt{\mu/\rho_s}$ is the shear wave velocity in the solid, ρ_s/ρ_f is the rock-to-fluid density ratio, and ε is the channel aspect ratio (thickness/length) with $\varepsilon \ll 1$. Eq. (9) shows that the roll wave instability can only occur for fast flow of dense fluid through long, thin channels. For example, for flow through a channel with aspect ratio $\varepsilon = 10^{-4}$ in a solid with shear wave speed $\beta = 2 \text{ km s}^{-1}$ and $\rho_s = \rho_f$, Eq. (9) suggests that flow speeds of tens of meters per second are required for instability.

Rust et al. (2008) discussed the conditions for roll wave instability and concluded that roll waves are unlikely to explain most volcanic tremor, but could possibly occur in the flow of hot, high-pressure H₂O- and CO₂-rich fluids at sustained flow speeds on the order of 10 m/s. The wave speed of roll waves in the model of Balmforth et al. (2005) represents the long-wavelength limit of the dispersion relation of Ferrazzini and Aki (1987) for crack waves when the elastic and acoustic wave speeds are relatively large (Rust et al., 2008). Note, however, that the crack stiffness parameter is not the proper parameter to describe these slow waves in this limit because the fluid is incompressible in the model of Balmforth et al. (2005).

This problem has been further analyzed by Dunham and Ogden (2012), who extend the work of Balmforth et al. (2005) to include compressible flow and crack waves. Similar to Balmforth et al.

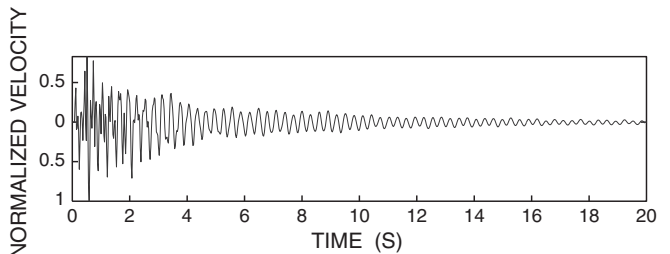


Fig. 19. Synthetic velocity waveform observed at an epicentral distance of 500 m and azimuth of 45° from the crack trace for a vertical crack (vertical extent $L = 150$ m and horizontal extent $W = 75$ m) buried at a depth of 500 m in a homogeneous half space. The aspect ratio is $L/d = 10^4$, and the parameters of the fluid and solid are $a = 300 \text{ m/s}$, $\rho_f = 2120 \text{ kg/m}^3$, and $\alpha = 4500 \text{ m/s}$, $\rho_s = 2650 \text{ kg/m}^3$. Figure reproduced from Kumagai and Chouet (2000).

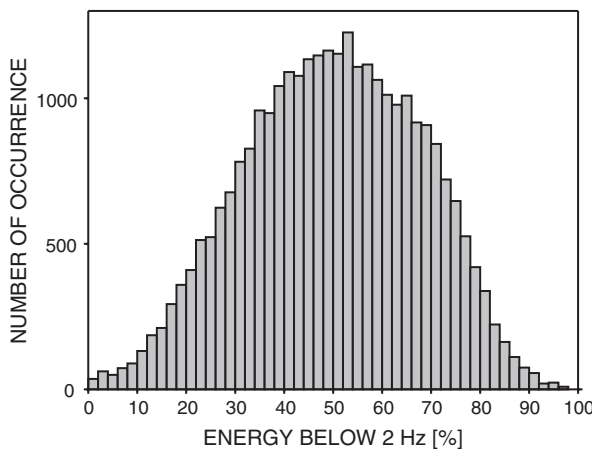


Fig. 20. Distribution of long-period/“hybrid” events according to their fraction of energy below 2 Hz. The histogram is based on the analysis of velocity seismograms at one station. The distribution demonstrates a continuum between LPs and events identified on Montserrat as “hybrids”. For distinct event types one would expect a bimodal distribution. Figure reproduced from Neuberg et al. (2000).

(2005), Dunham and Ogden (2012) identify an instability associated with certain wave modes when the fluid velocity exceeds a certain threshold. However, the parameter space of this instability does not appear to overlap with realistic magma flow conditions. For example, the velocities required at depth are more than an order of magnitude larger than those typically inferred in fissure eruptions, while closer to the surface, the fluid compressibility is likely too high. Similar to Rust et al. (2008), Dunham and Ogden (2012) tentatively conclude that self-excited oscillations are unlikely to generate volcanic tremor in magma flow channels. They underscore the importance of crack waves in generating LP seismicity and highlight the necessity, in the absence of self-sustained oscillations, of other excitation mechanisms as described in Sections 4.5–4.8.

4.5. Magmatic–hydrothermal interactions

Interactions between magma and water (either juvenile, meteoric, or a mixture of both) have for a long time been suspected as important in the generation of shallow volcanic seismicity (e.g., Latter, 1981; Havskov et al., 1983), and represent one of the first impulsive trigger mechanisms suggested for LP events during the development of the fluid-driven crack model (Chouet, 1985). Shallow LP seismicity arising from the pressure-induced disruption of a shallow hydrothermal region is believed to play a pivotal role in eruption forecasting (Chouet, 1996a). Magmatic–hydrothermal interactions may give rise to shallow LP seismicity via boiling and depressurization of groundwater (Leet, 1988; Matoza and Chouet, 2010), cyclic collapse and recharge of pressurized hydrothermal cracks (Nakano and Kumagai, 2005; Ohminato, 2006; Waite et al., 2008; Matoza et al., 2009a; Matoza and Chouet, 2010; Arciniega-Ceballos et al., 2012), or unsteady choking of a supersonic flow of magmatic steam (Chouet et al., 1994; Morrissey and Chouet, 1997).

Links between magmatic–hydrothermal interactions and LP seismicity are postulated at Kusatsu-Shirane Volcano, central Japan based on a variety of evidence. Kusatsu-Shirane is an andesitic stratovolcano with three crater lakes in its summit (Yugama, Mizugama, and Karagama). Numerous hot springs are found in the area, making this one of the major hot spring regions in Japan, and geochemical studies provide further evidence of hydrothermal activity resulting from the interaction of hot volcanic gases with groundwater (Hirabayashi, 1999; Ohba et al., 2000; Kumagai et al., 2002a). LP events with nearly monochromatic codas have frequently been observed at Kusatsu-Shirane (Hamada et al., 1976; Fujita et al., 1995). Analyses of the coda of LP events at Kusatsu-Shirane indicate fluid-

resonance with attenuation characteristics of hydrothermal fluids (Nakano et al., 1998; Kumagai et al., 2002a).

By treating the coda of the LP event as a decaying harmonic oscillation, it is possible to determine the complex frequencies using the Sompi method (Kumazawa et al., 1990; Nakano et al., 1998). The complex frequencies $f - ig$, where f is the frequency, g is the growth rate, and $i = \sqrt{-1}$, are related to the quality factor Q by

$$Q^{-1} = -2g/f. \quad (10)$$

Sompi utilizes an autoregressive (AR) equation in the complex frequency domain, equivalent to the linear differential equation of a linear dynamic system (Kumazawa et al., 1990; Nakano et al., 1998). Sompi can be applied to observed LP waveforms to recover the effective excitation function or trigger source-time function initiating resonance (Nakano et al., 1998) and to determine the Q of the resonator. The observed Q is composed of two components:

$$Q^{-1} = Q_r^{-1} + Q_i^{-1}, \quad (11)$$

where Q_r^{-1} and Q_i^{-1} are the radiation and intrinsic losses respectively. Q_r^{-1} is a function of the resonator geometry and sound speed and density of the fluid, and can be evaluated using the fluid-filled crack model (Kumagai and Chouet, 1999, 2000; Kumagai and Chouet, 2001; Morrissey and Chouet, 2001). The intrinsic attenuation Q_i^{-1} corresponds to intrinsic losses in the fluid, e.g., viscous, thermal and acoustic damping. Calculation of Q_i^{-1} requires knowledge of the thermodynamic equations of state for multiphase fluids (e.g., Commander and Prosperetti, 1989). Kumagai and Chouet (2000, 2001) evaluated Q_r^{-1} and Q_i^{-1} for various gas–gas mixtures, ash–gas mixtures and liquid–gas mixtures. They found that Q_r^{-1} is negligible compared to Q_i^{-1} for gas–gas mixtures, but that Q_i^{-1} can be important in bubbly liquids when the bubble radius is larger than 1 mm, and in dusty and misty gases where particles larger than 10 μm are considered. Furthermore, they found that the high Q values of dusty and misty gases with small particles ($\sim 1 \mu\text{m}$) were consistent with the values of Q observed for long-lasting LP codas observed at several volcanoes, highlighting the importance of these fluids in sustaining LP events.

By performing a systematic study of the temporal evolution of Q in a sequence of 35 LP events at Kusatsu-Shirane as a function of time between August 1992 and January 1993, Kumagai et al. (2002b) were able to infer possible changes in the fluid composition of the LP resonator. They interpret these changes in Q to an initially wet misty gas becoming progressively drier with time in response to drying out of the hydrothermal system in response to magmatic heating.

Waveform inversion of Kusatsu-Shirane LPs applied to both the full LP waveform (Kumagai et al., 2002a; Nakano and Kumagai, 2005) and to the effective excitation function of the LP event (Nakano et al., 2003) point to the repeated excitation of a fixed sub-horizontal crack near ~300 m under the Yugama crater lake. Based on the derived source mechanisms, Nakano et al. (2003) proposed a conceptual model for the source process of LP seismicity at Kusatsu-Shirane (Fig. 21). In this model, magmatic heating causes a gradual build up of steam pressure in a hydrothermal crack, which causes repeated discharges of steam from the crack. The rapid discharge of fluid causes the collapse of the fluid-filled crack, which excites resonance and leads to the LP coda.

Similar observations, source mechanisms, and reasoning have linked shallow LP events to magmatic–hydrothermal interactions at a variety of volcanoes, including Kilauea (Almendros et al., 2001a,b; Saccorotti et al., 2001; Kumagai et al., 2005); Redoubt (Chouet et al., 1994; Morrissey and Chouet, 1997; Stephens and Chouet, 2001); Mount St. Helens (Waite et al., 2008; Matoza et al., 2009a; Matoza and Chouet, 2010); Popocatépetl (Arciniega-Ceballos et al., 2012); Satsuma-Iwojima (Ohminato, 2006); Ontake (Nakamichi et al., 2009); Aso (Kaneshima et al., 1996; Kawakatsu et al., 2000); Pinatubo

(Harlow et al., 1996); Campi Flegrei (D'Auria et al., 2011); and La Fossa, Vulcano (Alparone et al., 2010).

At Kilauea Volcano, Hawaii, Almendros et al. (2001b) applied frequency-slowness methods using three small-aperture seismic arrays deployed in the summit caldera to image the source volume of LP events and tremor. LP events and tremor located in the same source region with dimensions $\sim 0.6 \times 1.0 \times 0.5$ km along the east flank of Halemaumau pit crater. Located within the top 500 m below the caldera floor, this source volume was interpreted as a shallow hydrothermal reservoir perched above the shallowest segment of magma conduit inferred by VLP source inversions (Ohminato et al., 1998). Waveform inversion of an LP recorded on a dense temporary seismic network pointed to the resonance of a horizontal crack at depth ~ 150 m (Kumagai et al., 2005), immediately above the conduit imaged by Ohminato et al. (1998). The observed frequencies and attenuation properties of the LP event were consistent with a crack filled with either bubbly water or steam (Kumagai et al., 2005). The overall inferred picture is similar to that proposed at Kusatsu-Shirane, involving the boiling of groundwater by rising magmatic gases, which produces steam and raises the overall pressure of hydrothermal fluids in a distributed network of fractures. Impulsive discharges of steam and collapse of these hydrothermal fractures give rise to impulsive excitation and resonance, which results in LP events.

The eruption of Redoubt Volcano, Alaska on 14 December 1989, following 23 years of quiescence, was preceded by a rapidly accelerating swarm of repetitive LP events that merged into sustained tremor a few hours before the eruption onset (Chouet et al., 1994; Stephens and Chouet, 2001). Chouet et al. (1994) interpreted these LP events as the resonant excitation of a crack linking a shallow, low-pressure hydrothermal system and a deeper supercharged magma-dominated reservoir. The initiation of the swarm was attributed to the failure of a barrier separating the two reservoirs. The LP trigger mechanism in this model consists of shocks resulting from unsteady choking of a supersonic flow of magmatic steam driven by the pressure gradient existing between the two reservoirs. Unsteady choking is the result of fluctuations in crack outlet pressure associated with the reaction of the hydrothermal system to the injection of mass and heat from below. The emergence of sustained tremor late in the swarm is interpreted as a change in choked-flow regime related to a gradual weakening of the pressure gradient driving the flow.

Morrissey and Chouet (1997) performed numerical simulations of transonic flow through a crack featuring a nozzle-like constriction using the Navier-Stokes equations representing a mixture of gas

and suspended solid particles. In these simulations, shock waves develop immediately downstream from the nozzle-like constriction, and the flow acts as an energy transducer that converts smooth low-amplitude fluctuations of outlet flow pressure into strongly-amplified and repetitive step-like pressure transients applied to the crack wall immediately downstream from the nozzle. The magnitude of the pressure transient at the walls is fixed by the pressure of the supplying reservoir and the geometry of the nozzle aperture, presumably remaining constant as long as these conditions prevail. The temporal pattern of outlet pressure fluctuations controls the areal extent of the crack wall impacted by shock waves and, given a roughly constant shock magnitude, fixes the amplitude of the force applied to the wall by the fluid. This variable force applied at a fixed location along the crack wall is viewed as the force responsible for the scaling of amplitudes and the similarity of waveforms observed in the LP swarm at Redoubt (Chouet et al., 1994).

Seismicity associated with both the 1980–1986 and 2004–2008 eruptions of Mount St. Helens (MSH), Washington has been interpreted in different ways. The onset of the 2004–2008 eruption of MSH began after a month of abnormally high rainfall (Scott et al., 2008) and was marked by an initial vent-clearing phase consisting of a swarm of VT earthquakes followed by intensified seismic unrest and four small (VEI~1) phreatic explosions. However, the majority of the 2004–2008 eruption consisted of solid lava spine extrusion or dome-building marked by a sustained sequence of millions of repetitive seismic events with long-period coda and slowly evolving waveforms (Moran et al., 2008a; Thelen et al., 2008). At times during 2004–2008, the events occurred with very high regularity (near-constant interevent time spacing) and were termed drumbeats (Moran et al., 2008a). Only two phreatic explosions occurred during this prolonged dome building phase despite the sustained seismic activity. Because the seismicity occurred during solid lava-spine extrusion, friction-controlled stick-slip and brittle fracture were proposed as potential seismic source processes (discussed in detail in Section 4.8).

Waite et al. (2008) analyzed the drumbeat seismic events using a dense temporary network of 19 three-component broadband seismometers, and showed that the events had all-dilatational first-motions where visible (Fig. 22). A stick-slip source mechanism associated with lava spine extrusion (Section 4.8) would be represented by a combination of a double-couple moment-tensor associated with shearing of highly viscous magma at the conduit wall, and a reaction force resulting from sudden acceleration of the lava spine. If a near-vertical single-force were to dominate the proposed stick-slip mechanism (assuming near-

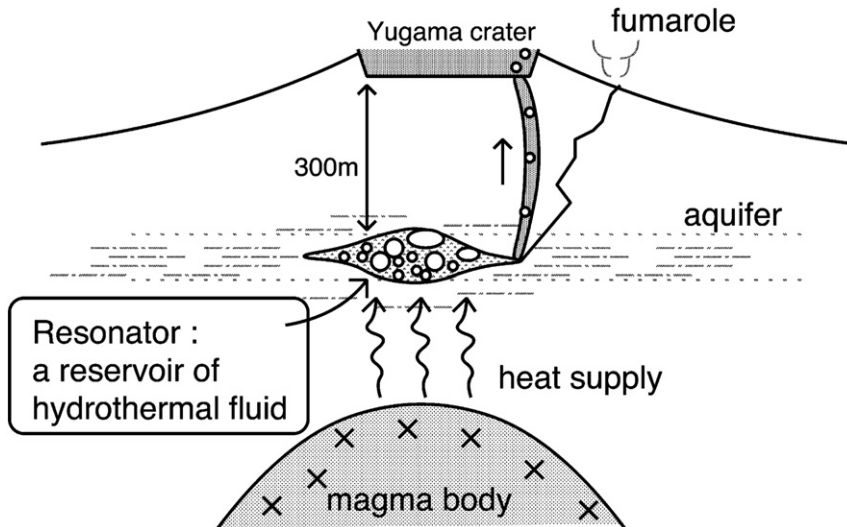


Fig. 21. Schematic view of the source process of LP events at Kusatsu-Shirane Volcano inferred from the results of waveform inversion. Similar mechanisms have been proposed at Kilauea, Satsuma-Iwojima, and Mount St. Helens. Figure reproduced from Nakano et al. (2003).

vertical acceleration of the spine), an upward acceleration of the spine could result in downward first-motions everywhere on the network.

However, Waite et al. (2008) also performed full waveform inversion and obtained a source mechanism consisting of a volume change combined with a vertical single-force component (Fig. 23). Both of these components had long-duration and oscillatory source-time functions (Fig. 23). The seismic events were also found to have common spectral peaks observed on stations at multiple azimuths and ranges from the source, which is indicative of source rather than path resonance (Chouet et al., 1994; Chouet, 1996a). These are all defining characteristics of LP events. For these reasons, and following the classification system of Lahr et al. (1994), Waite et al. (2008) identified the drumbeat events as ordinary LP events. Application of the Sompi method (Nakano et al., 1998) to MSH LPs by Waite et al. (2008) determined Q to be $\sim 10\text{--}20$, which can be attributed to bubbly magma, bubbly water, or steam (Kumagai and Chouet, 2000; Kumagai et al., 2005).

Atmospheric infrasound observations were also consistent with a source process for the seismic events involving fluids (Matoza et al., 2009a). Matoza et al. (2009a) showed that MSH LP events during 2004–2005 were at times accompanied by impulsive, broadband infrasound signals, and found that these signals could not be explained by simple seismic-acoustic wave conversion. They proposed rapid fluid expansions into loosely consolidated shallow subsurface rock layers as an explanation for the infrasound signals.

Waite et al. (2008) proposed that a sub-horizontal crack imaged in the LP moment-tensor inversions at $\sim 200\text{ m} \pm 200\text{ m}$ depth consists of a water- or steam-filled crack, maintained at high heat and pressure by magmatic activity. The source mechanism proposed is very similar to that proposed by Nakano et al. (2003) and Ohminato (2006) (note that Ohminato, 2006 was considering VLP events rather than LP events). Intermittently, pressure in the crack exceeds the containment pressure of a “valve” sealing the crack, leading to rapid collapse of the crack (the trigger of the LP event) and resonance of the remaining fluid (the coda of the LP event). To explain the all-dilatational first-motions, the initial rupture of the valve sealing the crack must be considered a relatively aseismic process in comparison to the coincident volumetric collapse. This model can also explain the impulsive infrasonic signals associated with the LP events, where the sudden failure of the valve results in a rapid fluid expansion, propagating the trigger signal into the

atmosphere through shallow porous and permeable weathered material overlying the source (Matoza et al., 2009a). In this model, the regular inter-event time spacing between individual LP events corresponds to the time taken for fluid pressure and temperature conditions in the crack to recharge back to the critical conditions for valve failure.

These constraints from seismic waveform inversion and seismo-acoustic modeling run counter to the idea of the drumbeats being directly generated by solid plug extrusion processes (Section 4.8). The interpretation is that the LP events are generated in a shallow hydrothermal region underlying the solid extrusion observed at the surface. An active hydrothermal system is indicated at MSH by the emergence of hot water, rich in minerals and magmatic volatiles, from springs and seeps in the vicinity of Loowit Creek and Step Creek in The Breach (Shevenell and Goff, 1993; Bergfeld et al., 2008), which is the area to the north of the MSH crater exposed by the 18 May 1980 lateral blast (e.g., Kieffer, 1981). These springs and seeps, present since 1983, are believed to represent limited discharge of water from beneath the crater area, from both juvenile and meteoric sources (Shevenell and Goff, 1993). Until at least 1998, continuous fumarolic activity also occurred at the 1980–86 lava dome, but by 2002 only diffuse steam was observed from this area (Bergfeld et al., 2008).

Self-potential (SP) and time-domain electromagnetic (TEM) data have also pointed to a stable hydrothermal system within a few hundred meters of the 1980s crater floor, which was persistent throughout the 2004–2008 MSH eruption, and was not boiled off by magmatic heating (Bedrosian et al., 2007, 2008; Hotovec, 2009). This is qualitatively consistent with the LP source process envisioned by Waite et al. (2008). Additional water may have been added to this system via partial melting of the $\sim 80 \times 10^6\text{ m}^3$ Crater Glacier, which accumulated in the crater of MSH between 1986 and 2004 and was present throughout the 2004–2008 eruption. Walder et al. (2008) showed that Crater Glacier decreased in volume by $\sim 6.7 \times 10^6\text{ m}^3$ between October 2004 and October 2005. The dynamics of this glacier were different from those of typical alpine glaciers, in that the glacier showed no evidence of slip along its bed, indicating a lack of glacier meltwater accumulated at the glacier bed. Walder et al. (2008) concluded that the meltwater likely drained down through the crater bedrock and into the volcano's groundwater system.

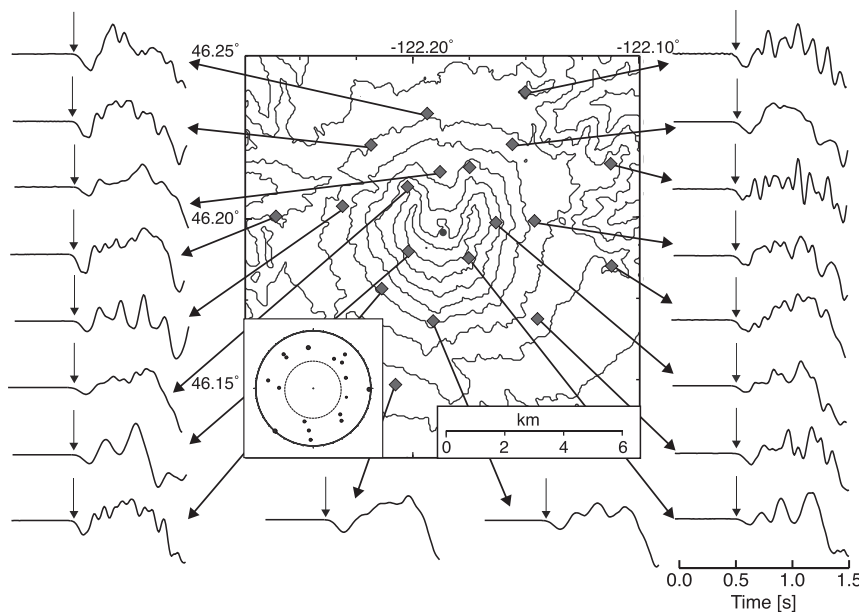


Fig. 22. First motions recorded for a sample LP event (black dot in crater) from 31 July 2005 at Mount St. Helens. Dilatational onsets are clear at all the broadband stations (diamonds filled with gray). The focal sphere in the inset shows the distribution of the first motion recordings for the network receivers, with the dotted circle in the middle outlining the region where there are no receivers.

Figure reproduced from Waite et al. (2008).

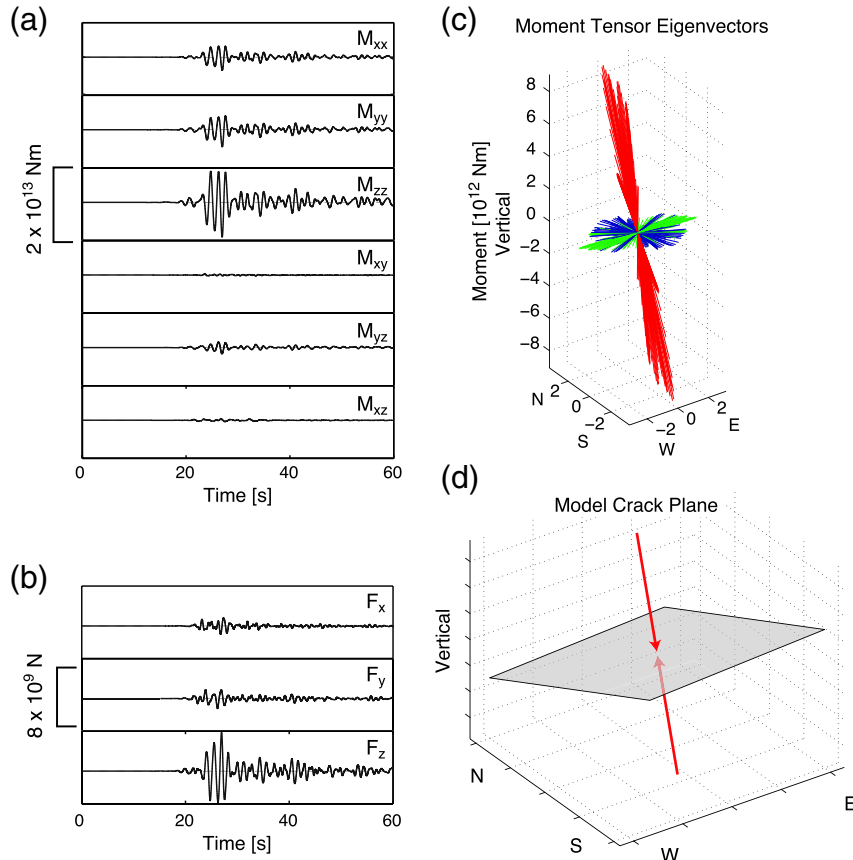


Fig. 23. Source mechanism of sample LP event at Mount St. Helens on 2 July 2005. The source mechanism is dominated by the dipole components of the moment tensor, indicative of a volumetric source (a), and a vertical single force (b). (c) Point by point eigenvector analysis of the moment tensor source time function. Maximum (red), intermediate (blue), and minimum (green) eigenvectors, scaled by the eigenvalues, showing a consistent relationship between the three eigenvectors with a ratio near 3:1:1, indicative of a crack geometry. (d) Crack model consistent with the data in (c), assuming a Poisson solid; the crack is plotted normal to the maximum eigenvector (red) (see Fig. 2b). Figure reproduced from Waite et al. (2008).

The trigger mechanism of shallow LP seismicity via magmatic-hydrothermal interactions can be better illuminated by considering the explosive properties of water (Wohletz, 1986; Thiéry and Mercury, 2009a,b; Matoza and Chouet, 2010). In the shallow region of a volcanic system, phase changes between liquid water and vapor may produce a rich variety of potential seismo-acoustic source processes, including via boiling (Leet, 1988), cavitation (Leighton, 1994), intermittent collapse of a steam film blanketing magma (Wohletz, 1986; Zimanowski et al., 1991), and perhaps more explosive transitions known as spinodal decompositions (Thiéry and Mercury, 2009a).

As reviewed by Matoza and Chouet (2010), water can exist in stable solid, liquid, and vapor phases, with these phases coexisting under certain pressure P , temperature T , and volume V conditions (Collier and Thome, 1996). The regions of stability of these various phases in P - V - T space are described by the thermodynamic equations of state. In addition, water can be brought into metastable or unstable states (e.g., Reid, 1978a,b,c; Debenedetti, 1996; Thiéry and Mercury, 2009a). Fig. 24 shows the regions of stability and metastability of water in P - T space according to the Wagner and Pruss (2002) IAPWS-95 equations of state for pure water (after Thiéry and Mercury, 2009a). The saturation curve (blue) in Fig. 24a separates the stable regions for liquid and gas phases. Adjacent to the saturation curve are the two metastable regions of water. The superheated liquid (SHL) field represents a metastable liquid that has been brought into P - T conditions beyond the stability limits of liquid water, i.e., to a P and T at which vapor is the stable phase. Conversely, the supercooled gas field (SCG) represents a metastable gas that has been brought into P - T conditions at which liquid is the stable phase.

Metastable states relax back to stable states via nucleation and phase growth, e.g., cavitation in a superheated liquid. However, rapid temperature or pressure changes may perturb a system beyond a metastable state and into an unstable state. The red curves are the liquid and gas spinodals, $Sp(L)$ and $Sp(G)$, respectively (Thiéry and Mercury, 2009a). These curves are the theoretical limits for the metastable fields, i.e., they are the boundaries between the metastable and unstable regions. For example, a liquid heated at constant pressure from a temperature on the left-hand-side of the curve $Sp(L)$ in Fig. 24a, towards a temperature on the right-hand-side of $Sp(L)$, would undergo a sudden and violent spinodal decomposition back to a more stable biphasic liquid-gas mixture upon intersection of $Sp(L)$ (e.g., Reid, 1978a,b,c; Favvas and Mitropoulos, 2008; Thiéry and Mercury, 2009a). Spinodal decomposition is a spontaneous and explosive phase separation that occurs throughout the fluid (e.g., Favvas and Mitropoulos, 2008; Thiéry and Mercury, 2009a).

The generation of LP seismicity within a shallow hydrothermal system as proposed by Nakano et al. (2003) or Waite et al. (2008) can be examined in this framework. The sudden loss of pressure in the crack from opening the “valve” causes it to collapse and resonate. Ohminato (2006) also proposed that superheated liquid water in a hydrothermal crack may suddenly vaporize, causing a rapid fluid expansion and causing a valve rupture. These scenarios can be represented by various trajectories in the P - T space of Fig. 24a.

The sudden opening of a valve sealing a crack (Nakano et al., 2003; Waite et al., 2008) can be approximated by an isothermal decompression (i.e., a vertical fall in pressure along a line of constant temperature in Fig. 24a). Following the definitions above, liquid decompressions can

be classified as either subspinodal or superspinodal. In a subspinodal liquid decompression, the pressure drop brings the system only into the metastable region. In a superspinodal liquid decompression the pressure drop brings the system beyond the liquid spinodal, leading to spinodal decomposition. Superspinodal decompressions have been hypothesized as the cause of BLEVEs (Boiling Liquid Expanding Vapor Explosions), a particularly destructive and dangerous type of explosion that can occur in chemical plants or tanks containing pressurized liquids (Reid, 1979; Abbasi and Abbasi, 2007). Alternatively, a liquid heated rapidly into the metastable or unstable field (Ohminato, 2006) represents some trajectory from left to right in Fig. 24a. If this trajectory crosses $Sp(L)$, explosive boiling will result.

However, the above considerations are for a pure H_2O system. The explosive potential of the system increases significantly by the addition of even a small mole fraction of dissolved volatiles, e.g., CO_2 (Thiéry and Mercury, 2009b). Fig. 24b shows the same pure H_2O curves in $P-T$ space as Fig. 24a. However, the liquid spinodals for the binary H_2O-CO_2 system with different values of CO_2 mole fraction are also shown as orange dashed curves (Thiéry and Mercury, 2009b). Note that as the mole fraction of CO_2 increases from 0.05 to 0.12, the position of the liquid spinodal (orange dashed curves) shifts to lower and lower temperatures for pressures between 0 and ~ 30 MPa. Therefore, as more CO_2 is added to the system, smaller pressure drops can lead to violent superspinodal phase changes, and the potential of the system to generate seismic energy seems to be increased (Matoza and Chouet, 2010). The addition of salts to the system, however, has the opposite effect on the spinodal curves and reduces the explosivity (Thiéry and Mercury, 2009b).

4.6. Magmatic degassing

Long-period seismicity is widely observed in relation to magmatic degassing, including (but not limited to) Hawaiian effusive degassing (e.g., Chouet and Shaw, 1991; Chouet, 1996b; Patrick et al., 2011), passive rhythmic degassing (e.g., Gil Cruz and Chouet, 1997; Lesage et al., 2006), low-intensity explosions (e.g., Johnson et al., 2008), degassing bursts (Arciniega-Ceballos et al., 2008; Chouet and Dawson, 2011), and Strombolian (e.g., Neuberg et al., 1994; Chouet et al., 2003) and Vulcanian explosions (e.g., Kawakatsu et al., 1992; Palo et al., 2009; Buurman and West, 2010; Traversa et al., 2011). Long-period seismicity could also arise from repetitive injections of ash-laden gas, or opening and closing of voids, within or at the boundaries of a magma conduit (Heiken et al., 1988; Molina et al.,

2004; Rowe et al., 2004). As outlined in Section 4.5, long-lasting LP oscillations in the fluid-filled crack model (e.g., Chouet, 1988) require a large velocity contrast between the surrounding solid rock and the fluid. This points to the importance of bubbly basaltic magma, misty water–steam mixtures, or dusty ash–gas mixtures in generating LP seismicity (Kumagai and Chouet, 2000, 2001). In this section we focus on observational constraints on LP events and tremor source mechanisms at several volcanoes exemplifying a range of magmatic degassing styles in systems with widely differing magma viscosities. Discussion of magmatic degassing interpreted as resulting from brittle failure of magma (e.g., Varley et al., 2010a; Traversa et al., 2011) is deferred to Section 4.7.

Long-period seismicity is associated with shallow magma transport and eruption at low-viscosity basaltic volcanoes such as Kilauea, Hawaii; Piton de la Fournaise, Réunion; and Stromboli, Aeolian Islands. Aki and Ferrazzini (2000) analyzed ~800 LP events from 28 eruptions at Piton de la Fournaise from 1981 to 1992. They found that most eruptions were preceded by a swarm of VT events beneath the central cone, that summit eruptions themselves were characterized by continuous tremor, and that LP events tended to occur following summit eruptions rather than preceding them. However, they found that LP events did occur prior to flank eruptions near the caldera rim. Based on these observations, Aki and Ferrazzini (2000) concluded that the LP events were associated with the lateral path of magma towards the rift zones and not with magma movement along a separate vertical path to the summit. In addition, during a period of declining volcanic activity following an eruption in August 1992, LPs with 1 Hz dominant frequency were found to disappear before LPs with 2 Hz dominant frequency. Aki and Ferrazzini (2000) interpreted this as progressive draining of a reservoir in which the 1 Hz LP source is located above the separate 2 Hz LP source.

Observations at Kilauea and Stromboli indicate that LP seismicity may be generated as part of a broadband source process associated with the unsteady transport of magma and gases through conduits as described in Section 3.2 (Ohminato et al., 1998; Chouet et al., 2003, 2008; Chouet and Dawson, 2011). For example, LP signals are found within sawtooth-like VLP waveforms at Kilauea (Fig. 25) (Dawson et al., 1998; Ohminato et al., 1998). The source mechanism of the sawtooth VLPs is consistent with a model involving injection of a large slug of gas into a subhorizontal crack featuring a narrow constriction (Ohminato et al., 1998). The LPs in this case can be explained by acoustic oscillations of the fluid–gas mixture excited by shocks associated with compound choking of the flow. Similarly, explosions at Stromboli

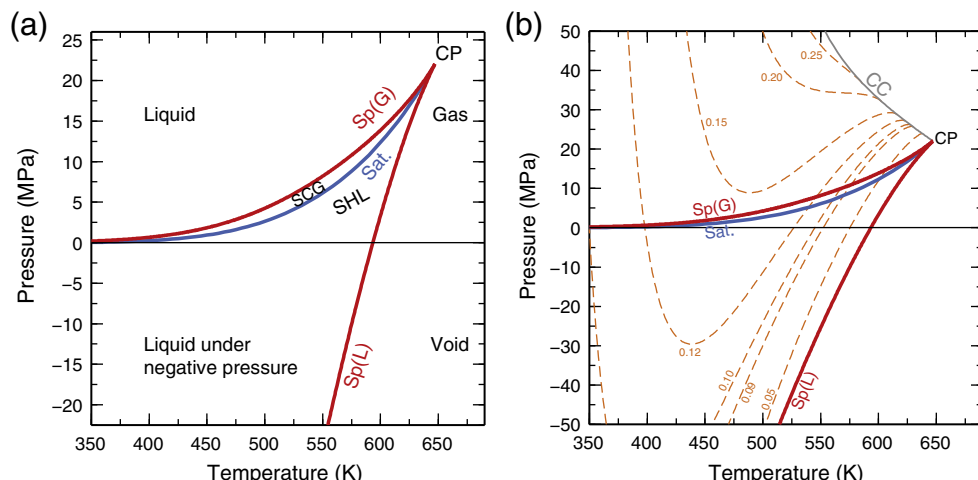


Fig. 24. Stable, metastable, and unstable regions of water in $P-T$ space according to the IAPWS-95 equations of state (Wagner and Pruss, 2002). In (a) and (b) the blue line is the vapor-pressure curve or saturation curve (Sat.) while the red lines are the spinodals. $Sp(G)$ is the gas spinodal, $Sp(L)$ is the liquid spinodal. All three lines meet at the critical point (CP). SCG denotes supercooled gas, while SHL denotes superheated liquid. In (b) the orange dashed curves represent the liquid spinodals for the H_2O-CO_2 binary system (numbers indicate mole fraction of CO_2). The gray line is the H_2O-CO_2 critical curve (CC) (Thiéry and Mercury, 2009b). After Thiéry and Mercury (2009a) and Thiéry and Mercury (2009b) and modified from Matoza and Chouet (2010).

generate broadband seismic signals including both VLP and LP components (see Section 3.2). The LP signal in this case is attributed to the oscillatory response of the shallowest segment of the fluid-filled conduit associated with the rapid expansion and ejection of the slug (Chouet et al., 1997). Relationships between VLP seismicity and LP seismicity are also observed in more silicic systems (e.g., Arciniega-Ceballos et al., 2003, 2008).

Long-period seismicity is well-documented at Mount Etna, Sicily in relation to effusive and weakly explosive eruptions at this basaltic stratovolcano (Falsaperla et al., 2002; Saccorotti et al., 2007; Patanè et al., 2008). The geometry of the shallow feeding system at Etna is illuminated by tremor locations using spatial amplitude decay methods (Patanè et al., 2008). Time variations of tremor, LP, and VLP signals are explained by the transport and discharge of gas-rich magma (Patanè et al., 2008). Q values of LP events are consistent with resonance in cracks filled with bubbly basalt or water-vapor mixtures (Saccorotti et al., 2007; Lokmer et al., 2008; Patanè et al., 2008). Possible interactions with a shallow hydrothermal system were discussed by Saccorotti et al. (2007) and Lokmer et al. (2008). De Barros et al. (2011) performed moment-tensor inversion of LP events at Mount Etna using an exceptionally dense network of 50 broadband seismometers, 30 of which were located in the source near field (Fig. 26a, middle). De Barros et al. (2011) focus on observations from an eruptive period beginning with energetic lava fountaining activity 10 May 2008 and ending on 6 July 2009. An eruptive fissure opened on 13 May 2008 on the east flank of the volcano and the seismic network was deployed between 18 June 2008 and 3 July 2008. LP events at Etna during this time period had frequencies of 0.2–1.3 Hz and were grouped into two waveform families based on cross-correlation (De Barros et al., 2009). Using the time-delays determined from waveform cross-correlation, De Barros et al. (2009) located 129 selected events belonging to these

two families into a dike-like structure and 2 pipe-shaped bodies at shallow depth (20–700 m) below the summit craters. Migration of these hypocenters was observed during a 96-hour period. The geometry of the dike-like structure was consistent with previous waveform inversions using a sparser seismic network (Lokmer et al., 2007).

After a series of numerical tests investigating the stability and reliability of the source inversions, De Barros et al. (2011) found that both waveform families are well-explained by highly volumetric sources, likely crack-like geometries (Fig. 26b and c). These cracks both strike in the SW–NE direction, with orientations not necessarily the same as the structures along which the event hypocenters are located (De Barros et al., 2009), or with locations of tremor sources found in previous studies (Patanè et al., 2008). De Barros et al. (2011) conclude that the LP events are likely related to gases, rather than magma movement, in this shallow part of the volcanic edifice. The orientation of the cracks determined by source inversion is consistent with weaknesses oriented SW–NE associated with gravitational sliding of the east flank of the volcano.

Galeras, Colombia is an andesitic stratovolcano, which reactivated in 1988 and underwent a series of explosive eruptions in 1989, 1992, and 1993. Gil Cruz and Chouet (1997) analyzed LP events and both spasmodic and harmonic tremors associated with this activity. In particular they focussed on LP events accompanying the emplacement, extrusion, and ultimate destruction of a lava dome in the crater of Galeras between 1991 and 1992. Repetitive LP events with dominant frequencies in the range of 1–5 Hz characterizing this dome emplacement and extrusion were each accompanied by weaker precursory signals with frequencies in the range of 10–20 Hz and preceding the main LP by ~7 s. Gil Cruz and Chouet (1997) document remarkable photograph and field observations made during two visits to the crater on 11 and 20 November 1991 (Fig. 27). These photographs

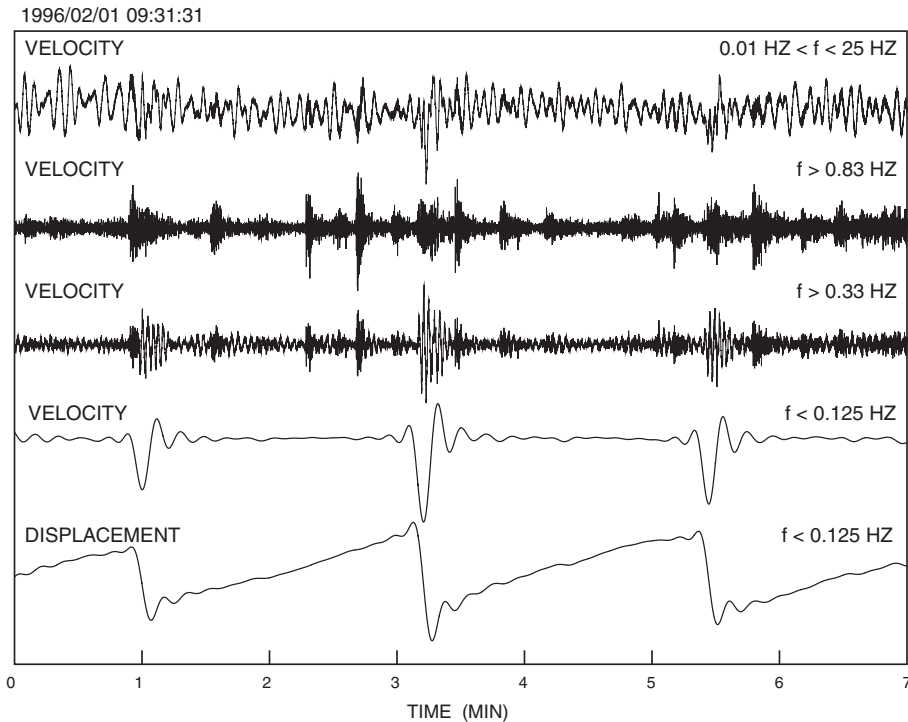


Fig. 25. Broadband record and associated filtered signals obtained at Kilauea Volcano during a volcanic event on February 1, 1996. The broadband signal represents ground velocity and is filtered in various frequency bands to produce five records for the same 7-min time interval. The top trace shows the broadband signal ($0.01 < f < 25$ Hz), which is dominated by the oceanic wave-action microseism with dominant periods in the range of 3 to 7 s. The second trace shows the signal obtained after application of a high-pass filter ($f > 0.83$ Hz). The result is equivalent to a typical short-period record and shows a series of events superimposed on a background of tremor. The third trace also has a high-pass filter applied but with a lower corner frequency ($f > 0.33$ Hz); LP signals with a dominant period of about 2.5 s are enhanced in this record. The fourth trace shows the signal obtained after application of a low-pass filter ($f < 0.125$ Hz); a repetitive VLP signal consisting of pulses with period of about 20 s is observed. The fifth trace is the corresponding displacement record obtained with the same low-pass filter ($f < 0.125$ Hz), showing a repetitive sawtooth pattern with rise time of 2–3 min and drop time of 5–10 s. Notice that the onset of the LP signal seen above coincides with the onset of the down drop in the VLP displacement. Figure reproduced from Dawson et al. (1998).

capture sporadic explosive pulses of gas venting through a transitory crack bisecting the dome. The explosive releases were temporally correlated with the occurrence of the LP events, and each launched a few rocks and produced a distinctive audible jet noise (Gil Cruz and Chouet, 1997). This crack was visually estimated to have a length of 120–150 m and an aperture of a few millimeters. These observations provided convincing evidence of a link between LP events and fluid pressurization and degassing (Gil Cruz and Chouet, 1997). No surficial activity was correlated with the precursor events.

Although the seismic instrumentation at Galeras at this time consisted of a relatively sparse network of short-period seismometers, constraints on the LP source were made by forward spectral modeling with the fluid-filled crack model (Gil Cruz and Chouet, 1997). The LPs and their small precursory signals were modeled by two distinct cracks. For the LP source, values of 240–360 m, 130–150 m, and 0.5–3.4 mm were determined for the crack length, width, and aperture, respectively. For the precursory signals, values of 20–30 m, 15–25 m, and 2.3–8.7 mm were determined for the crack length, width, and aperture, respectively.

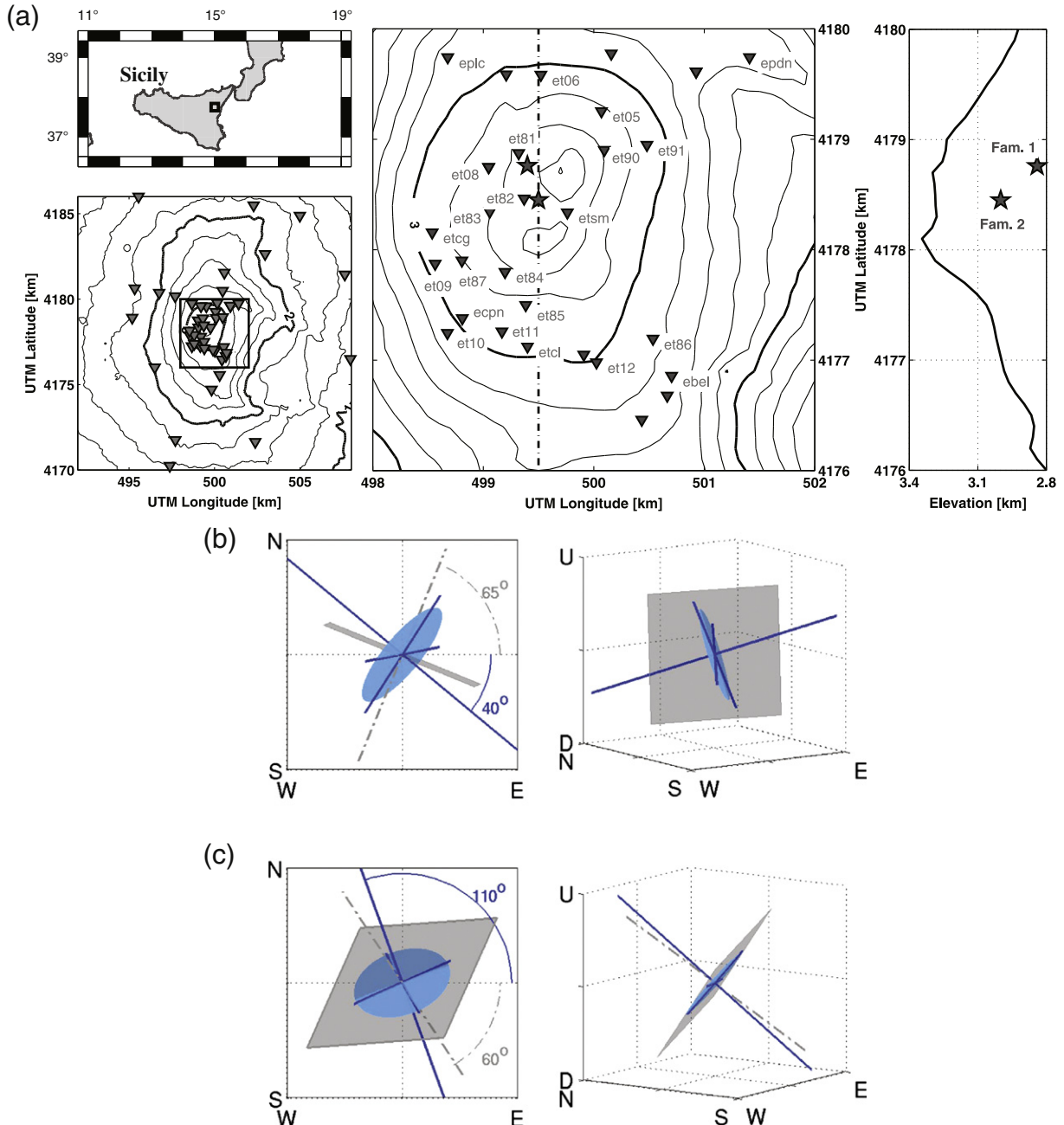


Fig. 26. Seismic network deployed on Mount Etna between 18 June and 3 July 2008, and source mechanisms of LP events obtained by De Barros et al. (2011). (a) Location of Etna Volcano (square) in Sicily (upper left) and map of Etna showing locations of three-component broadband stations (inverted triangles) on Etna (lower left). Contour interval is 250 m. (middle) Summit area of the volcano (indicated by square in lower left panel) with stations (inverted triangles) and epicenters (stars) of the two LP sources investigated by De Barros et al. (2011); the dashed line marks the position of the vertical cross section illustrated at the right. Contour interval is 100 m. (right) North-south cross section at UTM longitude of 499.5 km (marked by dashed line in panel a, middle) showing hypocenters (stars) of the two LP sources. (b, c) Source mechanisms obtained for (b) the deeper LP source (Fam. 1 in panel a, right) and (c) the shallower LP source (Fam. 2 in panel a, right) for a crack constrained inversion including both moment and force. (left) Map view and (right) 3-D view. The ellipses with blue shading represent the cracks and the solid blue lines represent the normalized eigenvectors. Crack orientation is provided by the dominant dipole normal to the crack plane. The light gray squares show the location structures obtained by De Barros et al. (2009) from high-resolution locations of individual LP events; the dashed lines represent axes perpendicular to these structures. The azimuths of the normal dipoles are given in the map views; Figure reproduced from De Barros et al. (2011).

Following the laboratory experiments of [Jaupart and Vergniolle \(1989\)](#), [Gil Cruz and Chouet \(1997\)](#) present a conceptual model for the generation of the LP signals at Galeras. In this model, periodic collapse of a foam layer atop a magma conduit beneath the solid lava dome induces a rapid ascent of a gas slug. This gas ascends to the surface via a preexisting crack in the overlying dome, and vents to the atmosphere resulting in the documented explosive releases. The crack corresponding to the main LP event is interpreted as the primary escape pathway; the small precursory signal is interpreted as resulting from a smaller crack or nozzle connecting this main LP crack to the top of the magma conduit. Prior to the eventual destruction of the lava dome in 1992, this characteristic shallow LP seismicity essentially stopped (dropped to a few events per month) and was replaced by deeper LP seismicity. This was viewed by [Gil Cruz and Chouet \(1997\)](#) as the result of progressive crystallization which sealed the shallow gas escape pathway shut, and led to pressurization of the shallow system. The deeper LPs were interpreted as discrete pumping events which incrementally raised the pore pressure in the dome, eventually leading to its destruction once a critical pressure was reached.

Arenal, Costa Rica is a small basaltic-andesitic stratovolcano, which since a Plinian eruption in 1968 has exhibited persistent magmatic degassing activity in addition to lava flows, lava dome building and rockfalls, and occasional pyroclastic flows ([Hagerty et al., 1997](#); [Lesage et al., 2006](#)). The degassing is characterized by passive rhythmic gas emissions, Strombolian-Vulcanian explosions, audible rhythmic sounds and infrasound, and long-period events and tremor ([Benoit and McNutt, 1997](#); [Garcés et al., 1998](#); [Hagerty et al., 2000](#); [Métaxian et al., 2002](#); [Lesage et al., 2006](#); [Davi et al., 2012](#)). Tremor at Arenal includes both spasmodic and harmonic tremors ([Benoit and McNutt, 1997](#); [Garcés et al., 1998](#); [Hagerty et al., 2000](#); [Lesage et al., 2006](#); [Davi et al., 2012](#)). Harmonic tremor at Arenal is characterized by long-lasting (typically several hours per day) oscillations having sharp spectral peaks and forming multiple harmonic overtone sequences (fundamental frequency ~0.9–2 Hz), which glide as a function of time and also exhibit discontinuous frequency jumps (Fig. 28a and b) ([Benoit and McNutt, 1997](#); [Lesage et al., 2006](#); [Davi et al., 2012](#); [Valade et al., 2012](#)). In some cases, two simultaneous systems of spectral peaks are observed with independent gliding behavior (Fig. 28c and d), which can be linked to two simultaneously active vents probably fed by distinct conduit branches ([Lesage et al., 2006](#)). The harmonic properties are observed in both seismic and infrasonic data; together with the gliding phenomenon ([Benoit and McNutt, 1997](#)), this gives very strong evidence that this harmonic spectrum originates from a source rather than a seismic propagation (path) effect ([Garcés et al., 1998](#); [Hagerty et al., 2000](#)). This type of tremor is similar to that observed at several other volcanoes, including Lascar, Langila, Semeru, and Galeras (e.g., [Gil Cruz, 1999](#); [Gil Cruz and Chouet, 1997](#); [Hellweg, 2000](#); [Mori et al., 1989](#); [Schlindwein et al., 1995](#)). Harmonic tremor at Arenal is often found in the coda of explosion events, and it is considered that the source mechanism of the shallow explosions and LP events are fundamentally similar and related ([Benoit and McNutt, 1997](#); [Garcés et al., 1998](#); [Lesage et al., 2006](#)).

Both harmonic and spasmodic tremor are thought to result from intermittent flow of gas through fractures in a dome-like cap atop the conduit ([Lesage et al., 2006](#); [Valade et al., 2012](#)). Vulcanian explosions are commonly interpreted as a sudden release of pressure, which has accumulated below a plug capping the conduit. The capping obstruction impedes the release of gas, so that gas escape to the surface is accommodated by fractures opening and closing within the lava dome ([Gil Cruz and Chouet, 1997](#)). The escape mechanism of pressurized gas through these fractures ([Johnson and Lees, 2000](#); [Lesage et al., 2006](#); [Valade et al., 2012](#)), as well as resonance of the upper conduit section ([Benoit and McNutt, 1997](#); [Garcés et al., 1998](#); [Hagerty et al., 2000](#)) have been proposed as components in the source origin of harmonic tremor at Arenal. [Lesage et al. \(2006\)](#) considered a tremor source process in which intermittent gas flow through

fractures produces repetitive pressure pulses. When these repetitive pulses are regular enough, they produce harmonic tremor via a Dirac comb effect ([Lesage et al., 2006](#)). [Lesage et al. \(2006\)](#) also proposed that resonant modes of the upper conduit have a controlling influence on the intermittent gas flow through the fractures, analogous to the mechanism of tone production in a clarinet. We note that the comb effect was also investigated as a source of harmonic tremor at Arenal by [Hagerty et al. \(2000\)](#) using synthetic tests. These synthetics indicate that the impulse repeat time must be exceedingly regular to produce Arenal's harmonic tremor. [Hagerty et al. \(2000\)](#) conclude that this, together with the absence of explosion spectral envelopes in the harmonic tremor spectra, suggests that sustained harmonic tremor is not likely generated by regularly repeating shallow gas explosions, although its mechanism is expected to be closely related.

[Valade et al. \(2012\)](#) further analyzed the explosion and degassing mechanisms at Arenal using Doppler radar. [Valade et al. \(2012\)](#) found that surface tephra emissions are actually poorly correlated in both time and energy with the seismic activity, indicating that there is no simple relation between the two. In addition, [Valade et al. \(2012\)](#) found no clear relationship between the explosion repose time and the exit velocity of solid particles or mass loading of the plume. [Valade et al. \(2012\)](#) propose that the dominant mechanism consists of pressure build-up under a viscous degassed cap, which is crosscut by fractures. Similar to [Lesage et al. \(2006\)](#) and following [Rust et al. \(2008\)](#), [Valade et al. \(2012\)](#) consider that harmonic tremor results from periodic opening and closure of fractures triggered by pressure oscillations associated with standing waves in the conduit. Explosions are generated in the same system by a more sudden high-velocity gas escape following pressure build-up. Poor correlation between tephra emissions as measured with radar, and seismic signals, is explained by variable entrainment of ash by gas as it escapes through the fractures.

Source mechanism inversions appear to support these inferences ([Davi et al., 2010, 2012](#)). [Davi et al. \(2010, 2012\)](#) performed inversions for both moment-tensor and moment-tensor plus single-force vector source representations using data from a temporary network of 9 broadband seismometers at Arenal. Because of the non-ideal network geometry and poorly constrained velocity structure, [Davi et al. \(2010\)](#) conclude using synthetic tests that inversions including single-force components are unreliable. Mislocated sources and noisy data lead to spurious single-force components appearing in the inversion results. However, inversion of seismic signals accompanying an explosion (the inversion was applied to the explosion onset and excluded a harmonic coda) recovered a moment-tensor with dominantly isotropic components, as would be expected for an explosive source. The source centroid is placed at ~200 m below the summit crater and the moment corresponds to an estimated volume change of 68 m³ assuming a shear modulus of 10 GPa ([Davi et al., 2010](#)). This study was followed by [Davi et al. \(2012\)](#), who applied the waveform inversion to 15 harmonic tremor sequences at Arenal. Synthetic tests demonstrated the stability of the moment-tensor inversion results even when applied to the full duration of a long-lasting tremor signal, and inversions on sliding time windows of data were performed to analyze time-variability of the source. The retrieved mechanisms point to a crack dipping around 20° to the north-northeast with a strike of 110°. Comparing inversion results of the 15 separate tremor events reveals a non-destructive source process, which is relatively stable with time. [Davi et al. \(2012\)](#), following [Lesage et al. \(2006\)](#), interpret the crack as a fracture in the plug that opens and closes periodically, and whose intermittent pressure oscillations are somehow controlled by resonant oscillations of an underlying conduit.

Long-period seismicity is connected with Vulcanian explosions and water-rich ash-free explosions at Volcán de Colima, Mexico, an andesitic stratovolcano ([Zobin et al., 2008](#); [Palo et al., 2009](#); [Varley et al., 2010b](#)). However, this connection has been observed and interpreted in different ways. [Varley et al. \(2010a\)](#) and [Varley et al. \(2010b\)](#) discuss LP swarms associated with Vulcanian explosions at

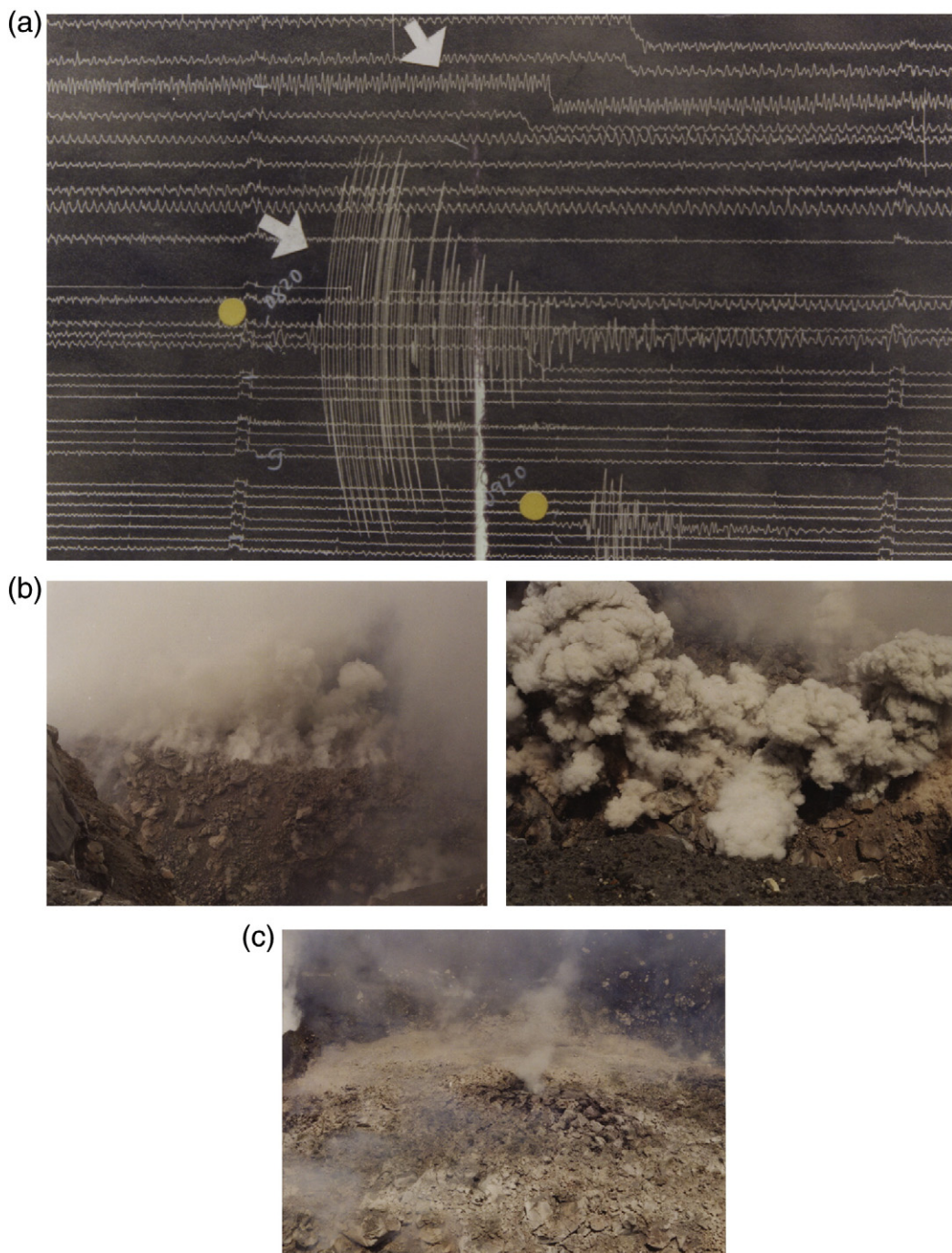


Fig. 27. Correlation between seismic signals and strong degassing activity at Galeras Volcano in November 1991. (a) Portion of vertical velocity seismogram obtained at a receiver located 1.6 km east of the crater between 07:00 and 09:30 on November 11. The harmonic tremor marked by an arrow near the top of the record was correlated with steady degassing from two small vents at the top of the lava dome (see steady steam plume in (c)). The LP event indicated by the lower arrow occurred at 08:20 and was associated with the explosive gas emission shown in the two snapshots in (b). (b) Sequential snapshots taken 2 s apart of explosive gas release along a NNE-SSW-trending crack bisecting the lava dome. (c) Steam plume produced by steady degassing from two small closely spaced vents located at the top of the lava dome. Figure reproduced from Gil Cruz and Chouet (1997).

Colima, while Palo et al. (2009) and Zobin et al. (2008, 2009) analyzed actual explosion signals. Comparison of seismograms and video data by Palo et al. (2009) indicates that a small LP seismic precursor (30–60 s long) is observed prior to Vulcanian and ash-free explosions. No increase in ash or steam emissions is observed during the precursory LP; the emissions are synchronous with a later higher frequency signal lasting from a few to tens of minutes in duration (Palo et al., 2009). The amplitude of the secondary high-frequency signal was greater in explosions producing ash than those which were ash-free (Palo et al., 2009). Using array analysis this was

interpreted by Palo et al. (2009) as a pressure step acting at depth in the conduit, which excites the conduit into resonance (precursory LP), followed by an upward migration of the source to the surface manifestation of the explosion (higher frequency signal). De Lauro et al. (2012) analyzed 20 LP events associated with explosions using Independent Component Analysis and interpreted the results as evidence for self-sustained oscillations of a conduit in relation to the explosions. LP events also occur at Volcán de Colima in relation to lava dome growth, and small magnitude LPs often occur in repetitive families and in swarms associated with large Vulcanian explosions

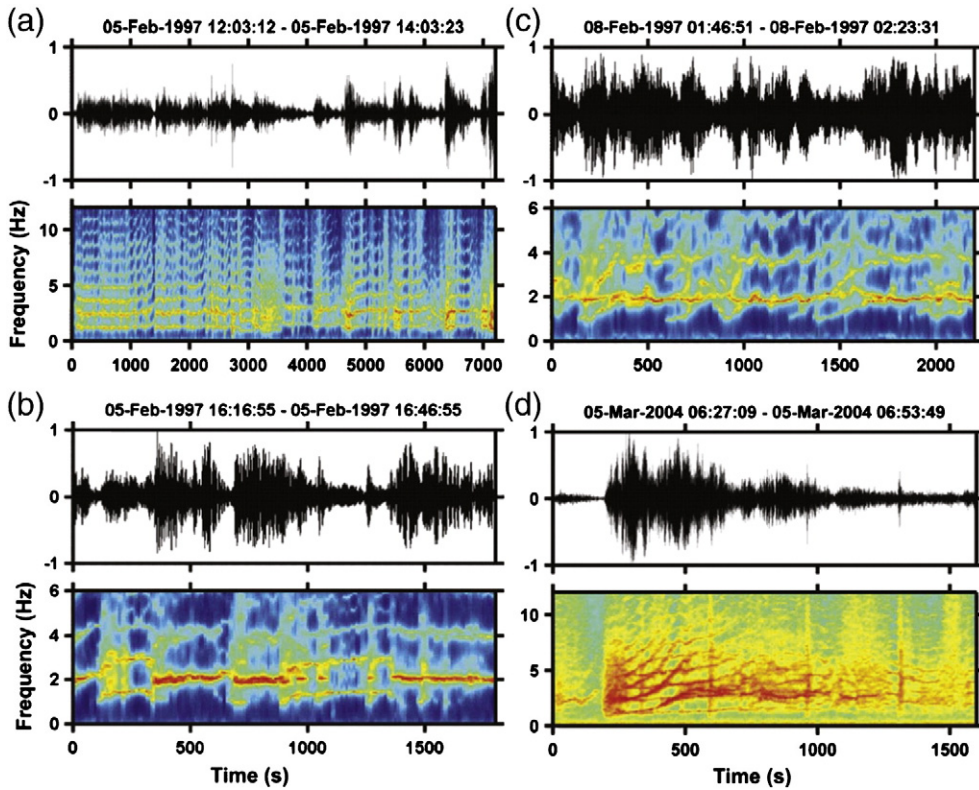


Fig. 28. Vertical-component velocity records and associated spectrograms of volcanic tremor at Arenal Volcano. The date and time for each record are indicated above each panel. (a) Two-hour-long record of tremor featuring nine regularly-spaced spectral peaks. (b) Tremor featuring sharp transitions between two states with fundamental frequencies near 1.5 and 2 Hz. (c, d) Tremor featuring two sets of spectral peaks with independent gliding behaviors.

Figure reproduced from Lesage et al. (2006).

(Varley et al., 2010a; Arámbula-Mendoza et al., 2011). Poor correlation between swarm metrics (e.g., duration, magnitude, occurrence frequency of LPs) was found with the magnitude of the Vulcanian explosions, and swarms were found to continue after explosions, suggesting that the source origin of these LPs is not related in a simple way to the explosion mechanism (Varley et al., 2010b). It has been suggested that these LP events represent brittle failure events in magma associated with high strain rates (see Section 4.7), while more monochromatic LPs with Q values of about 100–150 were interpreted as fractures filled with water vapor or gas and ash, perhaps within the conduit walls (Varley et al., 2010a; Arámbula-Mendoza et al., 2011). However, source inversions have not yet been performed at Colima of which we are aware.

As at Volcán de Colima, long-period seismicity at Soufrière Hills Volcano, Montserrat (also an andesitic stratovolcano) has been interpreted in different ways (see Section 4.7). Rowe et al. (2004) analyzed 3914 events in 36 swarms at Soufrière Hills from July 1995 to February 1996 using waveform cross-correlation-based phase repicking and cluster analysis. Their results show that the sources in individual swarms occurred within restricted, stable regions, often extending less than 100 m in radius. Swarm centroids were found to be located very near each other, with the largest separation being no more than 500 m. The overall source volume for the swarms is confined laterally to an area no greater than the footprint of the summit dome complex (750 m), and is limited in depth to the range ~1.3–1.6 km. Each swarm occurred within a time span of several hours to several days. There is a clearly preferred event size in each swarm, which is inconsistent with the magnitude–frequency relationship typically associated with double-couple type events. Rowe et al. (2004) conclude that shear failure is an unlikely mechanism for the events. Swarm activity showed an approximate correspondence with visual estimates of dome growth at the vent. Rowe et al.

(2004) attribute the events to a repetitive, non-destructive source process in the form of rapid gas bubble formation or the repeated opening and closure of cavities or cracks in the extruding magma caused by localized elevations in volatile pressure related to the onset of plug flow.

At Tungurahua volcano, Ecuador (an andesitic stratovolcano) LP seismicity is also associated with explosive eruptive activity. Molina et al. (2004) analyzed a swarm of LP events preceding heightened eruptive activity in December 2001. Their analysis points to LP source depths of 1–3 km and resonant coda Q values corresponding to a dusty ash–gas mixture. Using the fluid-filled crack model and the results of Kumagai and Chouet (2001), Molina et al. (2004) modeled an observed systematic temporal increase in Q and a corresponding decrease in dominant frequency f as resulting from an increasing ash content in a crack. Similar to Gil Cruz and Chouet (1997) and Rowe et al. (2004), Molina et al. (2004) proposed a model whereby decompression-induced degassing and volatile growth raise the pressure as magma ascends. Consequently, ash-laden gas is injected into a pre-existing crack in the conduit. As this process occurs repeatedly, ash accumulates in the crack, resulting in the observed variations in Q and f . The swarm analyzed by Molina et al. (2004) lasted from 5 to 11 December 2001, and was subsequently followed by a pause in seismicity from 11 to 18 December prior to the explosive activity. Molina et al. (2004) interpreted the pause in LP activity as resulting from the crack being nearly filled by ash particles and therefore no longer able to sustain LP resonance.

4.7. Brittle failure of melt

New ideas about volcano-seismic source processes (e.g., Goto, 1999; Neuberg et al., 2006) have emerged from experimental and numerical studies showing that highly viscous silicic melts (liquids)

can exhibit solid-like brittle behavior (e.g., Alidibirov and Dingwell, 1996; Dingwell, 1996; Ichihara and Rubin, 2010; Webb and Dingwell, 1990) in conditions realizable in magma conduits (e.g., Papale, 1999; Collier and Neuberg, 2006; Gonnermann and Manga, 2007; Hale, 2007; Thomas and Neuberg, 2012).

Experiments have investigated the viscoelastic rheology of silicate melts at a large range of stress and strain-rates (Webb and Dingwell, 1990; Alidibirov and Dingwell, 1996). At low strain-rates, the melts behave as Newtonian fluids (stress directly proportional to strain-rate). As strain rate increases, non-Newtonian shear-thinning behavior or pseudoplasticity (viscosity decreasing with increasing shear stress) is observed. The strain rates at which the non-Newtonian behavior occurs can be estimated using the Maxwell relation for a viscoelastic material and the relaxed, Newtonian shear viscosity of the liquid (Webb and Dingwell, 1990; Ichihara and Rubin, 2010). Non-Newtonian behavior occurs at time-scales three orders of magnitude smaller than the Maxwell relaxation time of the melt for a wide range of melt compositions and temperatures (Webb and Dingwell, 1990; Gonnermann and Manga, 2007). At higher strain rates, silicate melts exhibit brittle behavior. This transition from viscous-fluid-like to solid-like mechanical behavior is known as the brittle-ductile or glass transition (Dingwell and Webb, 1989; Webb and Dingwell, 1990). The temperature and strain rate at which the glass transition occurs are strongly affected by variations in melt composition and water content. For example, water degassing leads to sharp increases in melt viscosity (Shaw, 1972), increasing the likelihood of non-Newtonian and brittle behavior during magma ascent. The rheology of magma (melt, crystals, and bubbles) differs from that of the pure melt phase; crystal formation and bubbles have a substantial effect on magma viscosity and rheology (e.g., Gonnermann and Manga, 2007; Petford, 2003). These effects are only beginning to be explored (e.g., Lavallée et al., 2007; Kameda et al., 2008).

Ichihara and Rubin (2010) reviewed the notion of brittleness in magma. They addressed confusion in the literature about the relationship between shear-thinning and brittle behavior, and proposed a new parameter to quantify brittleness in magma more fundamentally by the extent to which the material response is dominated by elasticity rather than inelasticity. The implications of the study by Ichihara and Rubin (2010) are that increased strain rate and shear thinning do not necessarily cause brittleness, and that magma fracture is unlikely to occur at steady creep. However, they conclude that if the stress associated with steady creep is close to the critical stress for fracture, small fluctuations with sufficiently high frequencies (or sufficiently rapid transitions) can satisfy the conditions for brittle fracture.

Evidence for brittle failure and faulting in magma conduits has come from studying microtexture and structure in exposed fossil conduits (Heiken et al., 1988; Stasiuk et al., 1996; Tuffen et al., 2003; Tuffen and Dingwell, 2005). Due to intense hydrothermal alteration, fault textures in volcanic conduits are rarely preserved (Tuffen and Dingwell, 2005). However, Tuffen et al. (2003) and Tuffen and Dingwell (2005) report two well-preserved young-rhyolitic conduits at Torfajökull, Iceland exposed by partial collapse. The conduits record multiple generations of anastomosing tuffisite veins filled by fragments of magma and broken phenocrysts. The observed textures point towards repeated shear fracture and welding of magma. Tuffen et al. (2003) and Tuffen and Dingwell (2005) proposed a link between this textural evidence for conduit faulting and volcanic seismicity.

Brittle failure of melt in the conduit has been invoked as a volcano-seismic source process at, e.g., Unzen, Japan (Goto, 1999), and Soufrière Hills, Montserrat (Neuberg et al., 2006). The notion of brittle failure occurring within certain regions of fluid magma plumbing systems is compatible with the concept of hybrid LP seismicity (Lahr et al., 1994) (see Section 4.3). Neuberg et al. (2006) proposed that brittle behavior of magma near the glass transition results in shear-failure, which acts as the trigger mechanism of the hybrid event and excites resonance in the fluid magma conduit (resulting

in the LP coda). Numerical conduit flow modeling suggests that glass transition conditions are realized within a certain depth window and within the thermal boundary layer near the conduit walls, which experience gas-loss (hence increased viscosity gradients) and high strain rates (Collier and Neuberg, 2006; Neuberg et al., 2006). In this model, relatively fixed seismic source locations are attributed to relatively localized regions within the conduit where conditions are met for brittle, potentially seismogenic behavior.

Repeated fracture and healing (RFH) of magma (e.g., Gonnermann and Manga, 2003; Tuffen et al., 2003; Rust et al., 2004; Gonnermann and Manga, 2005) is proposed as a rechargeable, non-destructive source process to permit highly repetitive waveforms occurring within relatively fixed seismic source volumes, i.e., waveform families, clones, or multiplets (Green and Neuberg, 2006; Hammer and Neuberg, 2009; De Angelis and Henton, 2011). Therefore, rapid healing of magma following fracture (i.e., complete recovery of mechanical strength of preexisting interfaces) is required to explain the inter-event time-scales of LP/hybrid multiplets and swarms. Tuffen et al. (2003) considered the healing or welding process to consist of two processes: (1) viscous deformation, whereby pore space between imperfectly packed particles is removed, and (2) a diffusion-related process (sintering), which establishes cohesion between surfaces of adjacent particles. The total RFH cycle time T_t (Fig. 29) is the sum of the fracture time t_f , the diffusion process time-scale t_d , and the viscous process time-scale t_v :

$$T_t = t_f + t_d + t_v. \quad (12)$$

This time T_t corresponds to the inter-event time between individual seismic events, assuming that one fracture represents one seismic event and that only one fracture forms at a time (Tuffen et al., 2003). Tuffen et al. (2003) estimated theoretically that the total RFH cycle time T_t can plausibly range from about 10^2 to 10^6 s for magma viscosities of 10^9 to 10^{14} Pa s (Fig. 29).

Yoshimura and Nakamura (2010) subsequently investigated the fracture healing process experimentally. They determined healing times at the contact interface between rhyolitic obsidian melts at temperatures of 850°–1000 °C and pressures of 1.6–3.2 MPa. Yoshimura and Nakamura (2010) found the healing time to depend strongly on the temperature and roughness of the contact interface. They conclude that interface roughness results in fracture-healing times much longer than those predicted with the theoretical formulation of Tuffen et al. (2003). The shortest healing time ($t_d + t_v$) observed by Yoshimura and Nakamura (2010) was 0.36 h for a nonpolished surface at 950°. Considering cracks in tuffisite veins filled with fine ash, roughness is likely to be important and therefore the estimates of Tuffen et al. (2003) would be underestimates.

Yoshimura and Nakamura (2010) use their experimentally derived healing times ($t_d + t_v$) to suggest times T_t of 10^4 – 10^6 s (~2.6 h to 11.6 days) for the total RFH cycle. These time-scales are much longer than frequently observed inter-event times of highly repetitive LP and hybrid events. Yoshimura and Nakamura (2010) state that the time-scale of 10^4 – 10^6 s is consistent with seismic swarm observations at Soufrière Hills, Montserrat (Voight et al., 1999). However, time-scales of 10^4 – 10^6 s in the observations of Voight et al. (1999) correspond to the period of tilt deformation cycles and the repose time between swarms (i.e., the repose time between large sets of individual seismic events, rather than the inter-event time between individual seismic events). Voight et al. (1999) show event rates of ~32 triggers/h, corresponding to an inter-event time of ~2 min. Similarly, Hammer and Neuberg (2009) determined event rates of ~40 events per 10 min bin, or ~1 event every 15 s for Soufrière Hills. Furthermore, the inter-event time spacing between LP or hybrid events can reduce to very short time-scales (tending towards zero) when individual events merge to form volcanic tremor (e.g., Neuberg et al., 2000; Powell and Neuberg, 2003;

Hotovec et al., 2012). Therefore, the time-scales of the RFH process seem to be far too long to generate volcanic swarms and tremor.

This said, the relatively small confining pressures used by Yoshimura and Nakamura (2010), as well as the strong observed temperature dependence, leave open the possibility of shorter healing time-scales at depth in a conduit. In addition, Neuberg et al. (2006) proposed an extension to the RFH process to enable seismicity with inter-event times shorter than the fracture healing time. Following Goto (1999), they proposed that seismic sources are confined to a fixed depth range in the conduit, where the stress and strain rate conditions for brittle magma failure are met. Above this “seismogenic window”, magma ascends via aseismic plug flow. Rapid magma ascent through the seismogenic window provides a continuous supply of unruptured melt, and permits new events to be triggered at the same location at time-scales shorter than the crack healing time. A geometrical discontinuity in the conduit (e.g., an elbow, constriction, or bend) may also provide a fixed source location (Thomas and Neuberg, 2012).

Another important consideration for volcano-seismic source models involving brittle melt rupture is the seismic attenuation in high-viscosity magma. Fluids that can easily support LP resonance are bubbly basaltic magmas, bubbly water and steam, and dusty and misty gas-particle mixtures (Kumagai and Chouet, 2000). Models invoking brittle failure of melt combined with conduit resonance (e.g., Neuberg et al., 2006) must address whether the viscoelastic, gas-charged magma can sustain LP resonance and generate the LP coda (Ichihara and Kameda, 2004; Ichihara et al., 2004; Collier et al., 2006; Kurzon et al., 2008, 2011). Damping is likely to be high in magma conditions that support brittle melt failure (Webb and Dingwell, 1990). Consequently, Neuberg et al. (2006) considered that strong viscosity gradients across a conduit permit brittle failure near the conduit walls, simultaneous with lower attenuation conditions in the conduit center that support conduit resonance or interface waves.

Ichihara et al. (2004) and Ichihara and Kameda (2004) investigated the effects of liquid viscosity and volatile diffusion on bubble oscillation and attenuation in magma, building on the theory of attenuation in low-viscosity bubbly liquids (Commander and Prosperetti, 1989). Ichihara and Kameda (2004) concluded that attenuation and dispersion are severe in magma for frequencies lower than the characteristic frequency of mass transfer into and out of the bubbles by volatile diffusion, and for frequencies close to the characteristic frequency of viscous response of the bubbles within the melt. Collier et al. (2006) further considered attenuation in saturated bubbly magma and the effects of mass transfer

between bubbles and melt by diffusion and exsolution. Bubble growth by diffusion results in increased attenuation in comparison to bubble growth by expansion alone, and Collier et al. (2006) concluded that conduit resonance is confined to a limited depth range of a few hundred meters; multiple reverberations within a conduit over length-scales greater than this would be too severely damped. However, Collier et al. (2006) did not take into account the effects of melt viscoelasticity. By incorporating the effects of viscoelasticity and a compressible melt in a saturated bubbly magma, Kurzon et al. (2008) obtained a significant reduction in attenuation, especially at high-frequencies (≥ 1 Hz). Kurzon et al. (2008) also point out that a reduction in shear modulus may lead to a further decrease in attenuation. This leads to a significant improvement in the resonating properties of a magma-filled conduit, widening the possible conduit propagation lengths and frequency ranges. We note that Kurzon et al. (2011) have further considered the effect of a supersaturated bubbly magma, in which chemical energy released during bubble growth may lead to amplification of pressure waves. Kurzon et al. (2011) propose a conceptual model for cyclic LP generation and amplification via cyclic sudden collapse of a pressurized magma-filled crack, similar to mechanisms proposed for LP generation in hydrothermal cracks (see Section 4.5).

A further important consideration is whether brittle melt failure is seismogenic, and can explain both the amplitude (magnitude) and frequency content of observed volcanic seismicity (Tuffen et al., 2008). The Torfajökull conduits (10 m and 15–20 m wide) reported by Tuffen et al. (2003) and Tuffen and Dingwell (2005) contain fractures indicating slips on the order of a few millimeters or centimeters, combined with source dimensions of a few meters. The scalar seismic moment is defined as $M_0 = \mu D A$, with μ the shear modulus, D the mean slip, and A the fault area. Assuming $\mu \sim 10$ GPa and using $D = 0.13$ m and $A = 25$ m 2 (corresponding to the largest observed fracture; Tuffen and Dingwell, 2005), M_0 is $\sim 3 \times 10^{10}$ N m. The Torfajökull fracture dimensions imply moment magnitudes between about –1 and 1, which is consistent with smaller LP events, but not with the full range of observed LP magnitudes. These relatively small fault dimensions imply source frequency radiation in the kHz frequency range (see, for example, Kwiatek et al., 2011). The lengths and widths of the Torfajökull fractures are more than one order of magnitude smaller than those required by the fluid-filled crack model to explain LP frequency radiation (0.5–5 Hz). Therefore, either larger fractures, or connection of these smaller triggering fractures to a larger seismic resonator is required to explain LP/hybrid seismicity (Tuffen and Dingwell, 2005).

The seismogenic nature of non-Newtonian magma behavior has also been investigated with laboratory acoustic emission (AE) experiments on high-temperature, high-pressure silicic melt samples (Lavallée et al., 2008; Tuffen et al., 2008). Swarms of AE events are recorded during the non-Newtonian regime of sample deformation, until the sample breaks (Lavallée et al., 2008; Tuffen et al., 2008). The occurrence of these AE events is taken as an indication that melt fracture can produce measurable seismic events (Tuffen et al., 2008). However, because AE event amplitudes are typically reported in non-physical units (voltages), it currently remains unclear how to scale AE event amplitudes to compare with seismic observations, i.e., it is not known if the melt failure is seismogenic enough. Furthermore, the time-scales of the AE process and their relation to seismic swarm time-scales have not yet been addressed.

Despite all of these complexities, the general framework of brittle melt fracture as a source of LP/hybrid seismicity holds appeal because it potentially offers a link between melt fracture at depth; magma movement and conduit flow; extrusion dynamics; ground deformation and tilt cyclicity; and magma fragmentation and explosivity (Voight et al., 1999; Green and Neuberg, 2006; Green et al., 2006; Hammer and Neuberg, 2009; Neuberg, 2011). Material failure forecasting methods (Voight, 1988) applied to melt fracture and volcanic seismicity have consequently been proposed as a means to forecast

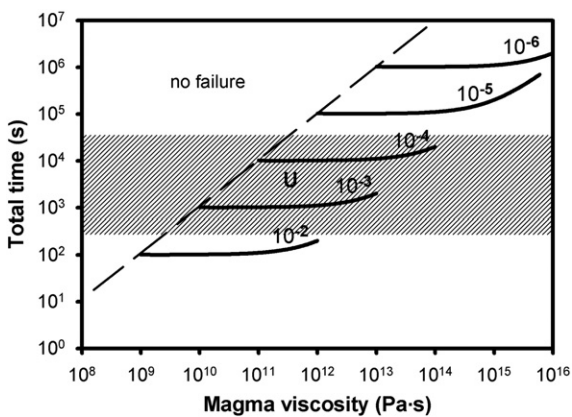


Fig. 29. Calculated total time T_r for the RFH (repeated fracture and healing) cycle during conduit flow according to the formulation of Tuffen et al. (2003). Curves are for different strain rates, indicated in units of s^{-1} . No fracture occurs to the left of the dashed line. Shaded area is intended to indicate the repeat time of hybrid and long-period earthquakes during silicic dome eruptions (note that repeat times during swarms may be shorter than this). U indicates inferred viscosity and strain rate of magma undergoing shear fracture at Unzen (Goto, 1999). Figure reproduced from Tuffen et al. (2003).

runaway conduit processes and volcanic eruptions (Lavallée et al., 2008; Hammer and Neuberg, 2009; Arámbula-Mendoza et al., 2011; Neuberg, 2011; Traversa et al., 2011).

An alternative but related mechanism is brittle failure near conduit margins resulting in significant degassing and the formation of gas-rich cracks or degassing pathways (Fig. 30a) (Gonnermann and Manga, 2003; Tuffen et al., 2003; Rust et al., 2004; Tuffen et al., 2008). The explosivity of silicic eruptions is determined in great part by how easily gas can escape from rising magma, and there seem to be two general ways this can occur: (1) via a gas-rich shear zone at the conduit wall (Fig. 30a) (Tuffen et al., 2003; Tuffen and Dingwell, 2005), and/or (2) via propped hydraulic fractures extending from the conduit into the country rock (Fig. 30b) (Heiken et al., 1988; Stasiuk et al., 1996). Stasiuk et al. (1996) reported on structures and textures of the rhyolitic feeder conduit and vent of the 19–21 Ma Mule Creek vent (NM, USA). These observations indicate: (1) local channeling of gas in the central part of the vent in steep syn-eruptive tuffisite veins cutting across the rhyolite, and (2) local channeling of gas in sub-horizontal syn-eruptive rhyolitic tuffisite veins departing from the vent margin and extending into the country rock by about 5–10 m. Similar but larger sub-horizontal cracks were observed in a 600 ya feeder dike beneath the rhyolitic Inyo Domes (CA, USA) extending ~100–150 m into the country rock (Fig. 30b) (Heiken et al., 1988). The presence, orientation, and texture of the Inyo Domes fracture fillings were found to strongly resemble man-made hydrofractures. Heiken et al. (1988) proposed that these natural hydrofractures may result either from vapor exsolution from decompressed magma, or rapid heating of groundwater (see also Section 4.5). Gas-rich, dusty and/or misty cracks with lengths ~100–200 m near the conduit/vent margins or extending from the magma conduit/vent into the country rock are good candidates for supporting LP resonance and LP-coda generation (e.g., Kumagai and Chouet, 2000; Molina et al., 2004). We note that degassing that extends to the surface associated with LP seismicity has been suggested by some co-eruptive observations. Visual observations of discrete impulsive degassing bursts at, e.g., Galeras (Gil Cruz and Chouet, 1997) and Soufrière Hills (Neuberg et al., 2000); as well as impulsive infrasonic signals (Yamasato, 1998; Johnson et al., 2008; Matoza et al., 2009b) associated with LP seismicity have been well documented.

4.8. Solid extrusion dynamics and near-vent plug stick-slip

On the end of the spectrum of the mechanical behavior of silicic systems, solid lava dome extrusion and plug flow have been linked to shallow LP/hybrid seismicity. Although in Section 4.2 we introduced solid extrusion dynamics in the context of the unknown excitation mechanism of LP seismicity, we point out that several of the studies referenced in this section consider the generation of volcano-seismic events without reference to a fluid-filled resonator model (e.g., Chouet, 1986). Plug stick-slip, taken on its own, does not satisfy the characteristics of LP seismicity as defined in Section 4. From this point of view, plug stick-slip should be viewed not as an excitation mechanism of LP seismicity, but as an entirely different process invoked to explain the phenomenon of volcanic earthquakes.

As described in Section 4.5, the onset of the 2004–2008 eruption of Mount St. Helens was marked by an initial vent-clearing phase consisting of a swarm of VT earthquakes followed by intensified seismic unrest and four small (VEI~1) phreatic explosions. However, the majority of the 2004–2008 eruption was characterized by near-continuous solid extrusion of a sequence of seven crystal-rich dacite spines mantled by gouge zones consisting of cataclasite, breccia and unconsolidated gouge, which were marked by multiple slickensides aligned in the direction of plug motion (Fig. 31) (Dzurisin et al., 2005; Cashman et al., 2008; Pallister et al., 2008; Scott et al., 2008; Vallance et al., 2008). This long (>3 years) and sustained dome-building phase of the 2004–2008 Mount St. Helens eruption was accompanied by a sustained

sequence of highly repetitive seismic events occurring at shallow depth (<1 km) with slowly evolving waveforms (Moran et al., 2008a; Thelen et al., 2008). At times during 2004–2008, the events occurred with very high regularity (near-constant interevent time spacing) and were termed *drumbeats* (Moran et al., 2008a). Petrological evidence indicates a plug solidification depth of <1 km, which is within the depth range of the observed repetitive seismicity (Iverson, 2008; Pallister et al., 2008; Thelen et al., 2008).

The spine extrusion features, including brittle deformation and granular flow (Cashman et al., 2008; Pallister et al., 2008), are reminiscent of shallow fault zones and suggest a shear-faulting source process. The fracturing on the lava spines is evident at multiple scales, ranging from meter-scale Riedel shears to micron-scale fractures within the fault gouge. The gouge layer was observed to be ~1–3 m thick on spines extruded earlier in the eruption when extrusion rates were higher (Cashman et al., 2008; Pallister et al., 2008).

The compelling link between near-steady-state spine extrusion and highly regular seismicity naturally led to the hypothesis that the drumbeat seismic source process involved shear failure and/or plug stick-slip motion (Fig. 32) (Iverson et al., 2006; Iverson, 2008). Iverson et al. (2006) and Iverson (2008) formalized this hypothesis with a mechanical model whereby the regular and repetitive nature of the drumbeat events is related to extrusion dynamics of the solid plug forced upward by a constant flux of more molten and compliant (bubbly) magma at depth in the conduit (Fig. 32). In this model, each drumbeat event corresponds to an individual stick-slip motion of the solid lava plug. These oscillations result from interactions between the plug momentum, upward force from the magma below, and downward force due to plug weight; they are damped by friction at the plug boundary (Iverson, 2008). Iverson (2008) concludes that stick-slip oscillations are almost inevitable during an eruption in which steady ascent of compressible magma drives upward extrusion of a solidified lava plug with margins that exhibit rate-weakening friction.

Moore et al. (2008) evaluated the frictional properties of gouge samples from Mount St. Helens in laboratory ring-shear experiments. Stick-slip motion as formulated by Iverson (2008) can occur if two conditions are met by the gouge (Iverson, 2008; Moore et al., 2008): (1) the gouge exhibits rate-weakening behavior, and (2) the gouge has higher stiffness than the compliant magma driving the plug upwards (otherwise the gouge can shear irreversibly before significant elastic strain accumulates). The experiments conducted by Moore et al. (2008) indicate that the gouge collected from Mount St. Helens lava spines does satisfy both of these criteria, and indeed unstable sliding or stick-slip behavior was observed in some of their laboratory configurations. Therefore, it was concluded that stick-slip is a plausible process within the ascending solid lava spines during the 2004–2008 eruptions of Mount St. Helens. However, whether the stick-slip oscillations would be large enough and rapid enough to produce the dominant drumbeat seismic events is dependent on several model parameters, particularly the elasticity of the magma driving the plug upwards and the gouge frictional properties (Iverson, 2008).

The observed gouge zone features (Cashman et al., 2008; Pallister et al., 2008) in isolation cannot be definitively linked to the seismic source process because they could have been generated aseismically by stable sliding during the extrusion. In contrast to the results of Moore et al. (2008), Kennedy and Russell (2012) observed only stable sliding and strain-hardening behavior in frictional experiments on Mount St. Helens dacite. Kennedy and Russell (2012) proposed an alternative mechanism to stick-slip for the formation of gouge and drumbeat seismicity. They proposed that a continual supply of undeformed dacite magma at ~1 km depth permits a “fracture-slip” mechanism rather than a stick-slip mechanism. Following rock fracture and generation of a drumbeat, the dacite plug continues upwards via stable sliding within the newly developed shear zones (Kennedy and Russell, 2012). We note that Cashman et al. (2008) reported

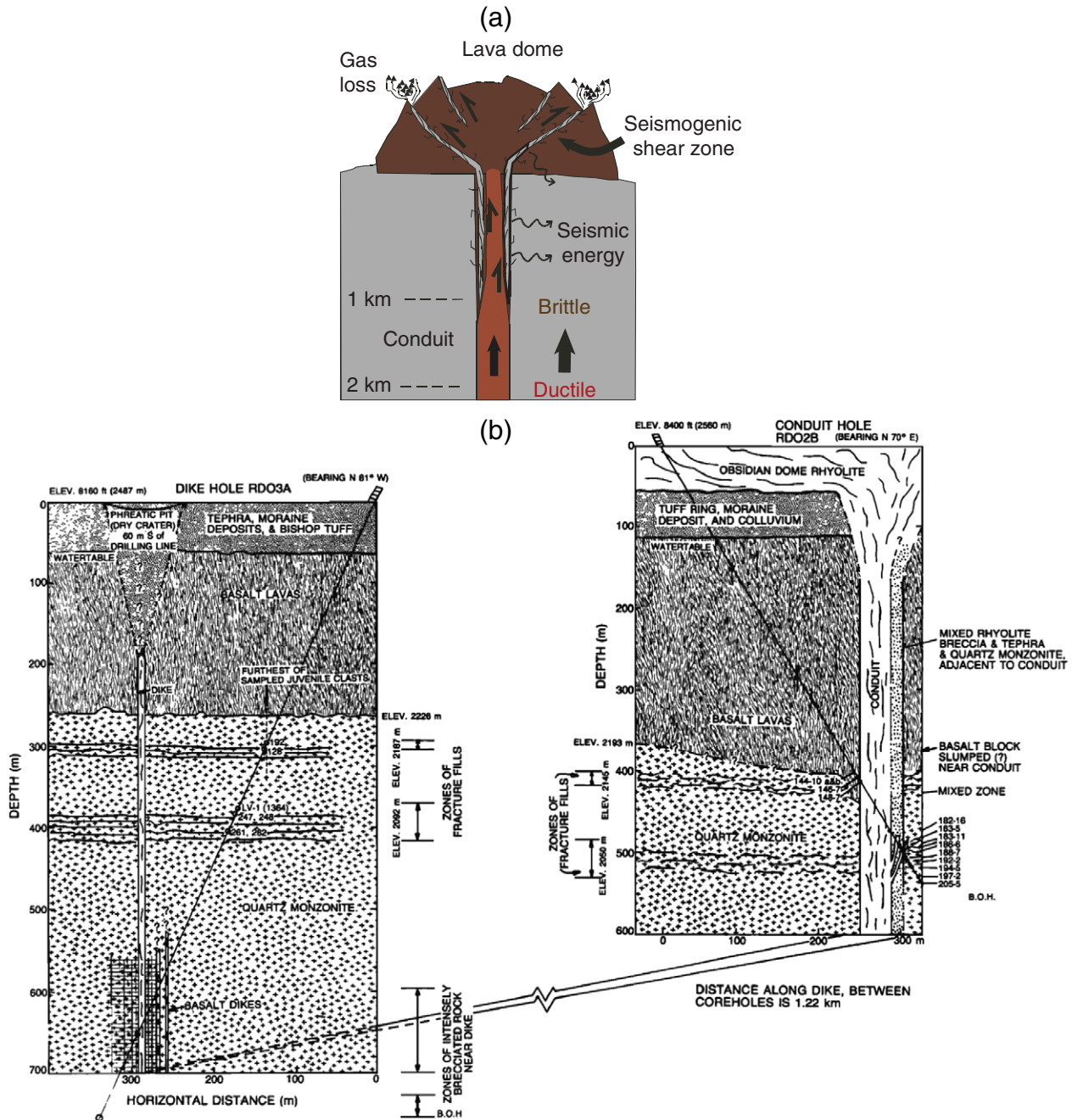


Fig. 30. Degassing pathways associated with lava dome formation in silicic magma eruption. (a) Cartoon illustrating degassing pathways in shear zones at conduit walls and within lava domes. (b) Hydraulic fractures extending horizontally from a dike (left panel) and from the Obsidian Dome conduit (right panel) at Inyo Domes, California. The fractures containing juvenile pyroclastic materials were intersected by boreholes drilled through the conduit of Obsidian Dome and through an unvented portion of the intrusion dike 1 km to the south (Heiken et al., 1988).

Panel a: Figure reproduced from Tuffen et al. (2008). Panel b: Figure reproduced from Heiken et al. (1988).

lack of evidence for annealing as is observed in tuffisite veins (Tuffen et al., 2003; Tuffen and Dingwell, 2005). Therefore, repeated fracture and healing (RFH) of the same material (see Section 4.7) is not a plausible process in the shallow extrusion of crystalline dacite lava domes at Mount St. Helens (Cashman et al., 2008).

Kendrick et al. (2012) describe a field study and laboratory analysis of samples collected from Spine 7, which is inferred to have been extruded during September–November 2006, later in the eruption than the spines considered by Pallister et al. (2008) and Cashman et al. (2008). Kendrick et al. (2012) identify four structurally distinct layers (L1–L4) across the margin of Spine 7. L1 represents the gouge layer documented by Pallister et al. (2008) and Cashman et al. (2008).

On Spine 7, this L1 gouge layer is observed to be much thinner (<3 cm) than that of ~1–3 m observed on spines extruded earlier in the eruption (Cashman et al., 2008; Pallister et al., 2008). Kendrick et al. (2012) interpret layer L2 as melt or pseudotachylite (representing plastic deformation) on the basis of grain size, circularity, remanence magnetization, variable Curie Temperatures, and DSC analysis (differential scanning calorimetry). L4 represents marginally deformed bulk dome material, while L3 represents a transitional layer between L2 and L4. The boundary between L1 and L2 is unconformable. Kendrick et al. (2012) propose that the L2 layer represents frictional melting associated with seismic slip and attribute this in particular to two large seismic events that occurred during the time of extrusion of this spine. The

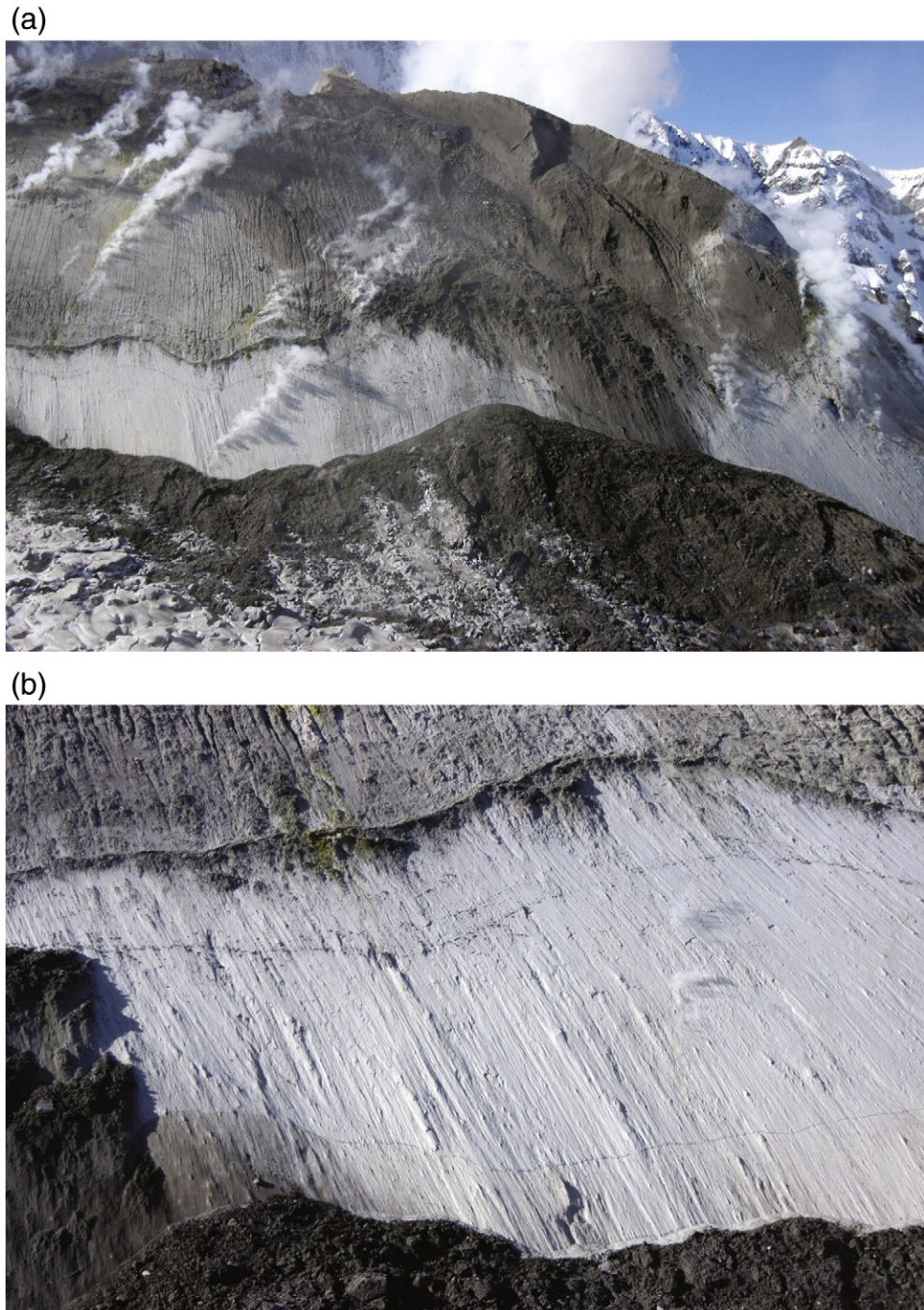


Fig. 31. Mount St. Helens Spine 3 on November 4, 2004 (USGS photographs by J. S. Pallister). (a) West-looking view showing, from the base upward: an apron of sandy debris, snow, and glacial ice; a 10–15-m-high wall of white slickenside-bearing gouge with “bathtub rings” marking former contact levels between gouge surface and debris apron; a dark tan (weathered) gouge or cataclasite with steeply dipping erosional furrows; and blocky outcrops (uppermost spine rough-weathering area near center-frame) consisting of uplifted material from the debris apron (after Cashman et al., 2008). Steam is venting from fractures in gouge caparace. (b) Close-up photograph of gouge outcrop showing slickensides and “bathtub” rings that parallel contact between the gouge and the debris apron (Cashman et al., 2008).

ambient temperature in the conduit ~860 °C is inferred to inhibit signature pseudotachylite characteristics by causing slow recrystallization following melting and localized plastic deformation during continued ascent. They did not discuss whether slower, stable aseismic sliding could generate the melt in these high ambient temperature conditions.

Several geophysical observations run counter to the hypothesis that rapid stick-slip motions of the lava spines generated the drumbeat seismicity at Mount St. Helens. For example, the correlation between spine extrusion rate and seismicity was at times poor

(Moran et al., 2008a), and although there were periods of time when larger drumbeat events were followed by longer inter-event (repose) times, there were also many instances when larger events were followed by smaller inter-event times, and smaller events were followed by larger inter-event times (Moran et al., 2008a). A tiltmeter network was deployed at Mount St. Helens with one aim being to capture episodic ground tilt related to lurching of the solid plug in the conduit (Anderson et al., 2010). Such tilt transients associated with the drumbeat seismic events were not identified (Anderson et al., 2010).

However, Anderson et al. (2010) do identify and model longer-period tilt signals (durations of minutes to hours) associated with slower extrusional processes, which are not directly related to the seismicity.

The brittle faulting hypothesis for the drumbeat source was also advanced in work by Harrington and Brodsky (2007) using empirical Green's function analysis. Harrington and Brodsky (2007) used corner frequency/seismic moment scaling arguments and concluded that the drumbeat events could be explained by brittle failure combined with low rupture velocities and path effects such as scattering and reverberation in loosely consolidated near-surface geology. However, a repetitive LP coda and its spectral properties may be removed during the empirical Green's function (eGf) procedure (Harrington and Brodsky, 2007), which assumes that the event used to compute the eGf has a flat source displacement spectrum up to a well-defined corner frequency (Harrington and Benson, 2011). In addition, stations NED and MIDE used in the work by Harrington and Brodsky (2007) were short-period piezoelectric accelerometer seismic "spider" stations designed for rapid deployment (LaHusen et al., 2008). These instruments have a limited frequency response in the band 0.5–5 Hz of the LP coda (LaHusen et al., 2008). We note that the role of source vs. path effects in generating the LP coda has been discussed extensively in the literature (e.g., Chouet, 1996a; Goldstein and Chouet, 1994; Malone, 1983). For example, VT or local tectonic earthquakes (Fehler and Chouet, 1982) and chemical explosives detonated within a volcanic edifice (Chouet et al., 1994) recorded by the same seismic network as LPs

can be used to evaluate site and path effects and to discriminate them from source resonance. Furthermore, stacking of LP spectra at a range of azimuths and distances from the source is commonly employed to emphasize source vs. path/site resonances (Chouet, 1996a; Waite et al., 2008).

As discussed in Section 4.5, waveform inversion using a network of 19 broadband seismometers indicated a volumetric moment-tensor plus vertical single-force source process for a large multiplet of drumbeats at Mount St. Helens (Fig. 23). Waite et al. (2008) concluded that drumbeats are ordinary LP events generated in a sub-horizontal crack, perhaps representing repetitive collapse of a hydrothermal crack pressurized and replenished by magmatic activity. The implication of the study by Waite et al. (2008) is that spine extrusion is not directly linked to the dominant seismic source process at Mount St. Helens during 2004–2008. The seismic source process is proposed to be the shallow hydrothermal system underlying the solid extrusion processes observed at the surface. Note that this does not preclude an indirect link between LP seismicity and dome extrusion, for instance, water degassing from the solidifying upper conduit could enter a shallow hydrothermal system. Indeed, some petrologic evidence suggests that about 2 wt.% water was exsolved on solidification of the spine at shallow (<2 km) levels (Pallister et al., 2008).

Nevertheless, millions of seismic events occurred during the 2004–2008 eruption of Mount St. Helens, and source mechanism inversions have only been performed on a selection of events (Waite et al., 2008). Similar source mechanisms can be inferred for events that have similar waveforms to (i.e., belong to the same multiplet as) the events for which source inversions were performed. Matoza and Chouet (2010) analyzed a class of smaller seismic events or "subevents" accompanying the dominant LP class of events. Unlike the cyclic drumbeat events, the subevents occur randomly in time (Moran et al., 2008a; Matoza and Chouet, 2010). Many of these subevents have similar waveforms to the dominant LP class, indicating a similar source mechanism to that derived by Waite et al. (2008). Temporal association and triggering of both LP events and subevents in relation to a phreatic explosion on 8 March 2005 further suggest a link between LP seismicity and the shallow groundwater system (Matoza and Chouet, 2010). However, several subevent multiplets were identified that did not correlate with the dominant LP class. Some of these subevents may be explained by shear-faulting processes (Matoza and Chouet, 2010).

We also note that drumbeat-style seismicity similar to that observed at Mount St. Helens was also recorded during the 1986 and 2006 eruptions of Augustine, Alaska (Power and Lalla, 2010). Drumbeats at Augustine were associated with periods of active lava extrusion during an initial dome-building phase of the 1986 eruption, and during an effusive phase of the 2006 eruption (Power and Lalla, 2010). The rate of magma extrusion and drumbeat seismicity were greater during the effusive phase of the 2006 Augustine eruption than at Mount St. Helens. However, at least one dome was emplaced without the occurrence of drumbeats. In addition, fault gouge or peleean spines were not observed during the Augustine 2006 effusive phase, and best estimates of hypocentral depths place the drumbeat source within the cone of Augustine at ~0.2 to 0.5 km a.s.l., which is below the summit (~1.2 km a.s.l.). Power and Lalla (2010) conclude that drumbeat seismicity at Augustine is related to the shallow movement of magma and the formation of lava domes, but is not likely directly caused by the emplacement of lava domes at the volcano's summit.

What is clear is that the 2004–2008 eruption of Mount St. Helens has generated interest and debate about the concept of brittle failure and friction associated with solid lava spine extrusion as a volcano-seismic source process. The development of gouge-mantled spines at Mount St. Helens was unusual but not unique, being observed at, e.g., Mount Usu, Japan; Mount Pelée, Martinique; and Soufrière Hills, Montserrat (Pallister et al., 2008). We note that Jellineck and Bercovici (2011)

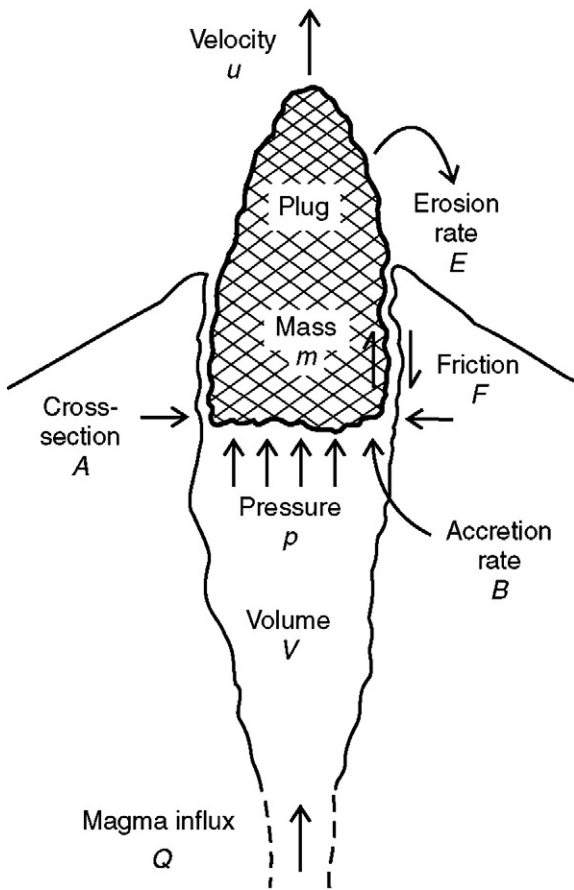


Fig. 32. Cartoon illustrating the conceptual stick-slip model of Iverson et al. (2006) and Iverson (2008). A constant flux of magma pushes on a rigid plug of solidified magma occupying the upper ~0.5 km of conduit. Extrusion is resisted by the frictional force at the conduit wall, and plug weight. Earthquakes result from incremental slip along the plug margins (see Iverson et al., 2006 for details). Figure reproduced from Iverson et al. (2006).

have also proposed a volcano-seismic source process in the framework of plug flow. They propose that oscillations (or “wagging”) of a stiff columnar magma plug flowing within a highly vesicular annulus of sheared bubbles result in harmonic tremor.

4.9. Deep Long-Period (DLP) seismicity

Deep Long-Period (DLP) seismicity has been observed at depths of 10–60 km beneath volcanoes in a range of tectonic settings and has generally been attributed to magma transport in the mid-to-lower crust and uppermost mantle (e.g., Aki and Koyanagi, 1981; Shaw and Chouet, 1989, 1991; Hasegawa et al., 1991; Pitt and Hill, 1994; White, 1996; Pitt et al., 2002; Nakamichi et al., 2003; Power et al., 2004; Hill and Prejean, 2005; Ukawa, 2005; Nichols et al., 2011). However, the connection between deep magma transport and seismic radiation remains poorly understood. Deep harmonic tremor and LP events at depths of 40–60 km have been recorded for decades at Kilauea (Eaton and Murata, 1960; Aki and Koyanagi, 1981; Koyanagi et al., 1987; Shaw and Chouet, 1989, 1991). Aki and Koyanagi (1981) examined 200 example records of Kilauea's deep tremor from 1973 to 1977 with durations longer than 10 min. The tremor frequencies in the range of 1.5–3 Hz were found to be uniform across the seismic network, and independent of distance and station. Furthermore, the frequency content was observed to change with time but remain uniform across the network, demonstrating conclusively that the frequencies of the DLP tremor at Kilauea are primarily controlled by source rather than path or near-station effects. Aki and Koyanagi (1981) then performed a systematic search for deep tremor from 1962 to 1979 and interpreted the tremor observations using a kinematic model linking fluid flow and tremor amplitude. They found that the total magma flow estimated from the cumulative reduced displacement underestimated, by an order of magnitude, the cumulative volume of lava erupted at the surface over the period. They therefore concluded that magma transport through the lithosphere may be mostly aseismic, and that only a small number of channels with strong barriers generate tremor when magma is forced through them.

Analyses of the durations and onset intervals of deep tremor episodes under Kilauea were carried out by Shaw and Chouet (1989) and Shaw and Chouet (1991), who viewed such activity as the relaxation oscillations of a percolation network of coupled magma-filled fractures. In their interpretation, each individual fracture in the network acts as a source of LP events, and sets of fractures give rise to multiple LP events and episodes of tremor. The aggregate nature of fracture propagation and vibration then leads to the existence of universal scaling laws that give rise to the long-recognized frequency invariance of LP events (Shaw and Chouet, 1989, 1991).

Okubo and Wolfe (2008) present observations of two swarms of DLPs in the mantle beneath Mauna Loa which occurred in 2002 (31 events) and 2004–2005 (~2000 events) associated with a geodetically observed intrusion. Okubo and Wolfe (2008) performed waveform cross-correlation and double-difference relocations of the weakly repetitive events. In the 2004–2005 swarm, about 50% of events were relocated and collapsed to a compact point source (~1 km spatial extent) beneath Mauna Loa at a depth of ~44–45 km. The 2002 sequence of events relocated to a similar compact source at ~36 km depth. Similar to Aki and Koyanagi (1981), Okubo and Wolfe (2008) attribute the DLPs to resonating cracks of magma but conclude that most of the deep magma transport beneath Mauna Loa during the 2002–2005 intrusion occurred aseismically and that the DLP locations illuminate only a tiny portion of Mauna Loa's deep magma system.

The 1996 eruption of Pinatubo produced an unprecedented quantity of energetic DLP events (about 600 between late May and early June 1991, one of which had a magnitude of ~3.7), as well as DLP

tremor lasting 25 h in one case (White, 1996). The DLPs at Pinatubo had frequencies of ~2 Hz, located at depths of 28–40 km at the base of the crust and directly below the volcano's summit, and were temporally correlated with geological and seismicity changes at the surface. DLP seismicity was found to be followed, 1–4 h later, by shallow LP events, tremor and steam emissions. DLP seismicity accompanied by inflation of the summit area was also found to precede by a few days the extrusion of an andesitic dome containing inclusions of freshly quenched olivine basalt, interpreted as arriving only recently from the deep crust. The DLPs occurred in swarms implying a repetitive, nondestructive source process of fixed length-scale. White (1996) concludes that the DLPs at Pinatubo resulted from flow of basaltic fluids near the base of the crust upward into the magma chamber (the basaltic inclusions in the andesite dome are explained as preserved remnants of these fluids). Since major explosive silicic eruptive activity is thought to be triggered by deep basaltic fluid injections, White (1996) concludes that monitoring DLPs may be important for predicting the timing and size of destructive eruptions.

Systematic analyses of DLPs beneath Northern California (Pitt et al., 2002), Aleutian (Power et al., 2004), and Cascades (Nichols et al., 2011) volcanoes indicate that DLPs are probably not as rare as once thought. In Northern California, the Aleutians, and the Cascades, DLP hypocenters correspond to mid-to-lower crustal depths. The horizontal offset of the DLP epicenters from the volcanic summit is generally less than the average focal depth (Pitt et al., 2002; Power et al., 2004; Nichols et al., 2011). Pitt et al. (2002) describe occurrences of DLPs beneath each of the major volcanic centers in Northern California, including the Mount Shasta-Medicine Lake complex, Lassen Peak, Clear Lake, and the Mammoth Mountain-Mono Craters complex, as well as beneath the central Sierra Nevada. Pitt et al. (2002) point out that standard network processing techniques and automatic event detection algorithms may overlook and underreport DLP activity. Power et al. (2004) report 162 DLPs beneath 11 volcanic centers in the Aleutian arc between 1989 and 2002. Most Aleutian DLPs occur at depths of 10–35 km but some are as deep as 52 km. The DLPs occur both in isolation and as sequences of events lasting from 1 to 30 min (Power et al., 2004). The sequences are often accompanied by deep volcanic tremor with a similar spectral character to the DLPs, and sometimes contain VT events with similar hypocenter locations (Fig. 33). Most of the Aleutian DLPs occur as a relatively stable background seismic process, but the 1992 eruption of Mount Spurr initiated DLP activity and the 1999 eruption of Shishaldin was preceded and accompanied by DLPs (Power et al., 2004). Nichols et al. (2011) identified >60 DLPs at >10 km depth beneath 6 Cascades volcanic centers occurring between 1980 and 2009. None of these were directly related with volcanic activity and more than half were located near Mount Baker, which is characterized by higher background flux of magmatic gases than other Cascades volcanoes. In some cases, DLPs did not occur directly beneath volcanoes but were associated with large actively slipping structural faults extending into the deep crust, which may provide pathways for fluid movement (Nichols et al., 2011). Collectively these studies indicate that systematic detection and monitoring of DLP seismicity beneath active volcanic centers may provide information on magma flow in the mid-to-lower crust and uppermost mantle, and in some cases DLPs may be early indicators of an eruption. Source mechanism inversions of DLPs at Iwate volcano, Japan produced variable moment-tensors with a mix of double-couple, compensated linear-vector dipole, and volumetric components, suggesting a complex magma system at the source region (Nakamichi et al., 2003).

5. VT Seismicity

Volcano tectonic (VT) earthquakes are ordinary earthquakes in the brittle rock within a volcanic edifice or in the crust beneath it. They are characterized by sharp, mostly impulsive onsets of P- and

S-waves, with typically broad spectra extending up to 15 Hz (Lahr et al., 1994). They are named VT earthquakes due to their close similarity to tectonic earthquakes, although the stresses that drive them are derived from magmatic processes rather than large-scale tectonic movements (Chouet et al., 1994). Similar to tectonic earthquakes, VT earthquakes result from abrupt frictional slip on opposing rock surfaces with a double-couple source mechanism (Aki and Richards, 1980). More rarely, they may also result from tensile failure (crack opening) due to cooling and solidification of magma (Chouet, 1979). The latter feature a non-double couple source mechanism that includes a positive volumetric component. VT earthquakes may occur as single events or as rapid-fire sequences of earthquakes with overlapping coda called spasmodic bursts (Hill and Prejean, 2005).

5.1. Intrusive geometry and related seismicity

Magma transport in the crust is intimately related to the magnitude and orientation of crustal stresses. The ambient stress field affects the position and orientation of magma conduits (Nakamura et al., 1977), while local stresses near the conduit may in turn be influenced by conduit pressurization or depressurization resulting from magma movement (Roman et al., 2004). The resulting stress field made of the superposition of the ambient stress and stress perturbation due to magmatic intrusion induces VT seismicity, which manifests as slip along suitably aligned preexisting fractures in the rock matrix (Rubin and Gillard, 1998). The spatial distribution of VT seismicity reflects the distribution of stresses near the failure threshold (Okada and Yamamoto, 1991; Hayashi and Morita, 2003; Morita et al., 2006). Knowledge of the state of the stress field can be inferred from the focal mechanisms of VT earthquakes, and provides constraints on the geometry of the magma pathway and physical processes occurring in a volcano.

Dikes represent the most natural geometry for fluid transport at depth in the Earth. Dike intrusion is governed by the balance between magma pressure and the ambient stress state, defined by three principal compressive stresses $\sigma_1 > \sigma_2 > \sigma_3$. A necessary condition for dike intrusion is that magma pressure exceeds the ambient compression perpendicular to the dike. Dike intrusion then occurs perpendicular to the least compressive stress σ_3 (Rubin, 1995). This condition generally applies to dikes producing their own fracture. The situation may be different if preexisting joints or fractures are present in the host rock. Under such conditions a dike may locally intrude an existing fracture at any orientation if magma pressure exceeds the largest compressive stress σ_1 (Rubin, 1995). Magma intrusion into fractures that are not aligned with the principal stresses induces a shear stress concentration at the dike tip that may cause the rock to break in tension along oblique fractures, similar to the tensile wing cracks formed at fault tips (Rubin, 1995). However, if the magma pressure barely exceeds the least compressive stress, then only fractures that are nearly perpendicular to the least compressive stress can be dilated. Other factors may affect the injection pathway. For example, under mixed Mode I, II (in-plane) loading (shear perpendicular to the local crack front), the crack propagates perpendicular to the local tension direction, resulting in rotation of the crack tip consistent with the applied shear couple (Fig. 34b) (Rubin, 1995). Under mixed Mode I, III (out-of-plane) loading (shear parallel to the local crack front), the crack front breaks down into en-echelon segments (Fig. 34c) (Rubin, 1995). The latter process is responsible for the common en-echelon segmentation of dikes and fissure eruptions, and is believed to result when a Mode-I dike propagates into a region where the least compressive stress is rotated slightly about an axis parallel to the propagation direction (Rubin, 1995).

For propagating dikes, the near-tip stress field is dominated by the large suction generated by viscous fluid flow within the dike (Rubin, 1995). The perturbation of the ambient stress is on the order of the

tip suction and extends over a region on the scale of the cavity length (Rubin, 1995). Elastic dilation of the host rock produces a drop in pore pressure near the dike tip that depends upon the dike propagation speed and poroelastic properties of the host rock (Rubin, 1995). Both tensile and shear failure of the dike plane are possible and dike-parallel joints may form near the tip cavity (Rubin, 1995).

Gravitational loading and failure can affect the intrusive process. A relevant example is Kilauea, where southeastward displacement of the south flank of the volcano decreases the least compressive stress and increases the differential stress within Kilauea's rift zones, raising the potential for a large excess magma pressure during rift intrusion and hence large stress perturbation (Rubin and Gillard, 1998). Mechanical heterogeneity naturally plays a critical role in governing the path of intrusions. Abrupt changes in mechanical stiffness between alternating layers of soft pyroclastic deposits and stiff solidified lava flows can lead to stress discontinuities and barriers that can arrest dike propagation at such boundaries (Gudmundsson, 2002).

For large enough ambient differential stress, VT earthquakes larger than magnitude 1 or 2 may be produced with focal mechanisms consistent with the ambient stress field, that is with greatest compression aligned parallel to the dike (Rubin, 1995). If the ambient differential tension is so large that preexisting faults are near failure, then the stress perturbation due to the intrusion can induce failure over distances that scale with the dike length (Rubin, 1995). The focal mechanisms of induced earthquakes may be normal or strike slip faults depending on the direction of the maximum principal stress (Fig. 35) (Ukawa and Tsukahara, 1996). For slip on an existing fault near the tip of a propagating dike, the optimal fault lies at an angle of ~30° from the direction of maximum compression assuming a coefficient of friction of 0.6 (Rubin and Gillard, 1998). A model of earthquake swarms accompanying dike intrusion that is consistent with this picture was originally proposed by Hill (1977). In this model, a cluster of magma-filled dikes oriented parallel to the direction of regional maximum principal stress is linked by a system of conjugate shear faults joining en echelon offset dike tips at oblique angles, and dike expansion is transferred through the mesh by right- and left-lateral faulting on such conjugate faults (Fig. 36). The model can apply to either swarms dominated by strike-slip faulting (σ_1 in horizontal direction) or swarms dominated by normal or perhaps reverse faulting (σ_1 in vertical direction). The buildup of pressure within a dike induces compression in the wall rock, which may also cause slip along pre-existing fractures in the dike flanks (Roman, 2005; Roman and Cashman, 2006; Roman and Heron, 2007; Roman et al., 2008; Vargas-Bracamontes and Neuberg, 2012) (see Section 5.5 below).

5.2. Large-scale dike intrusions

An earthquake swarm in 2000 under the Izu volcanic islands, Japan, provides a spectacular example of VT seismicity accompanying dike intrusion (Fig. 37) (Toda et al., 2002). This swarm featured 7000 earthquakes with magnitude $M \geq 3$, and five $M \geq 6$ earthquakes, with total seismic energy release of 1.5×10^4 J (Toda et al., 2002). The seismicity and deformation data are both consistent with lateral (horizontal) propagation of a vertical dike during a week-long episode, followed by dike inflation during the next seven weeks. Toda et al. (2002) inferred 20 m of expansion over a depth extent of 8–13 km, and associated volume increase of ~1.5 km³, with a corresponding geodetic moment of $\sim 5 \times 10^{19}$ N m. Using a dike expansion model, Toda et al. (2002) estimated stressing rates of up to 150 bar yr⁻¹ during this intrusion. Relative to a background stressing rate of ~0.1 bar yr⁻¹ inferred from crustal deformation, this implies a 1500-fold increase in the shear stressing rate near the dike (Toda et al., 2002). The stressing rate change calculated by Toda et al. (2002) correlates with the observed seismicity rate change, supporting a stress transfer model incorporating rate/state friction, for which the seismicity rate should be linearly related to the swarm stressing rate.

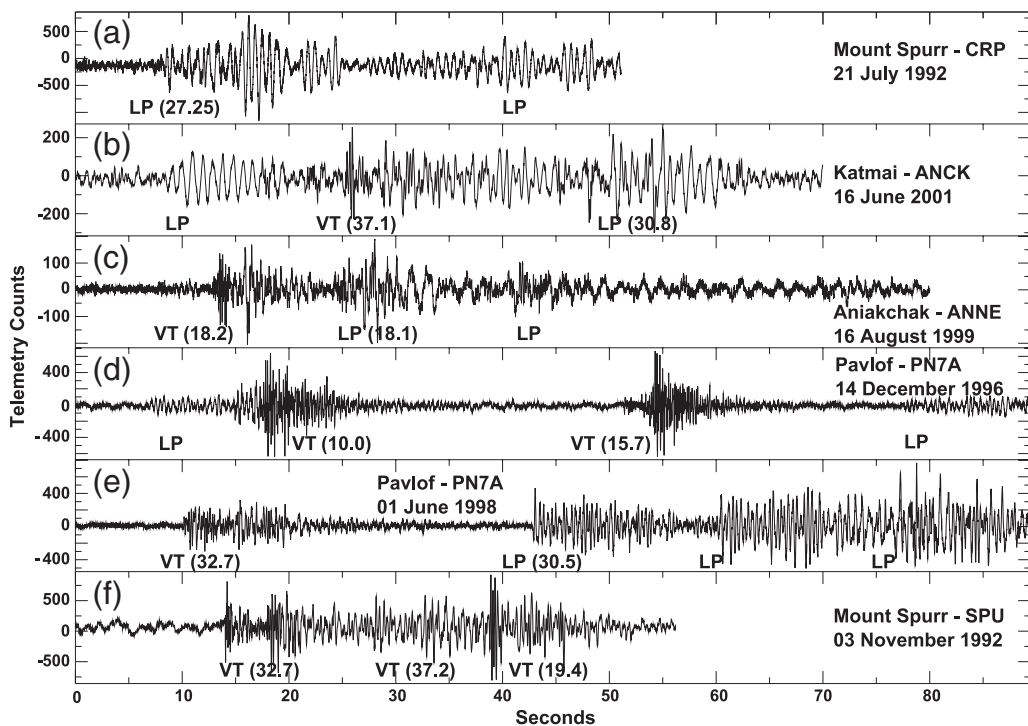


Fig. 33. Waveforms of DLP events beneath several Aleutian arc volcanoes. DLP sequences typically include several DLP events occurring during intervals of 1–30 min; these often feature a mix of DLP and VT events that locate at similar depths and sometimes occur with bursts of tremor. The volcano name, station code and record date are indicated next to each seismogram (see Power et al., 2004 for details). The event type (LP or VT) and estimated hypocentral depth (between parentheses for locatable events) are noted below each signal.

Figure reproduced from Power et al. (2004).

The ‘dog-bone’ pattern of seismicity observed at Izu (Fig. 37d) can be explained by the transfer of shear stress from an expanding dike to vertical faults in the surrounding crust, where stress is relieved through right- and left-lateral faulting. This behavior is reminiscent of that expected for the Hill mesh (see Fig. 36), however seismicity at Izu occurs in these lobes whether or not connecting faults are present (Toda et al., 2002).

The September 2005 rifting episode in the Manda-Harraro rift zone of the Afar depression of Ethiopia provides a perspective on strain accommodation associated with a mega-dike intrusion (Wright et al., 2006; Rowland et al., 2007; Ebinger et al., 2008; Ayele et al., 2009; Coté et al., 2010). The spatial pattern of deformation and accompanying distribution of seismicity are well explained by the intrusion of a dike up to 8 m wide between depths of 2 and 9 km along the ~60-km-long Dabbahu magmatic segment of the rift (Wright et al., 2006). Subsidence within the central rift and shoulder uplift observed along the entire rift segment are also compatible with the vertical displacement field expected for a large-scale vertical dike intrusion (Chouet, 1981). Wright et al. (2006) estimate that 2.4–2.6 km³ of magma was intruded along this segment during the ~2 week episode. The intrusion was heralded by 163 earthquakes with magnitudes of 3.9–5.5 between

September 14 and October 4. The total seismic moment release during this period is 6.7×10^{18} N m, more than one order of magnitude smaller than the estimated geodetic moment release ($\sim 8.0 \times 10^{19}$ N m), suggesting that most of the deformation occurred aseismically. Earthquake focal depths lie between 10 km depth and the surface along the entire Dabbahu segment, and focal mechanisms show dominantly normal faulting associated with rift opening (Rowland et al., 2007; Ebinger et al., 2008). Field observations of fresh ground breaks and the pattern of seismicity are largely consistent with the spatial pattern of strain produced by dike intrusion to depths <2.5 km along this segment, as predicted from 3-D models of satellite radar data (Wright et al., 2006). Vertical and horizontal offsets accrued on faults and associated fissures within a ~5 km swath extending along strike over most of the 60 km length of the segment can be explained by shear failure coupled with extensional opening of preexisting cooling joints near the surface. Normal faulting was initiated ahead of and above the laterally propagating dike in response to a reduction in horizontal compression above the dike (Pollard et al., 1983; Rubin and Pollard, 1988; Chadwick and Embley, 1998). Upon reaching shallower crustal levels, these faults reactivated preexisting columnar joints as opening mode fissures to form vertical faults with opening displacements (Rowland et al.,

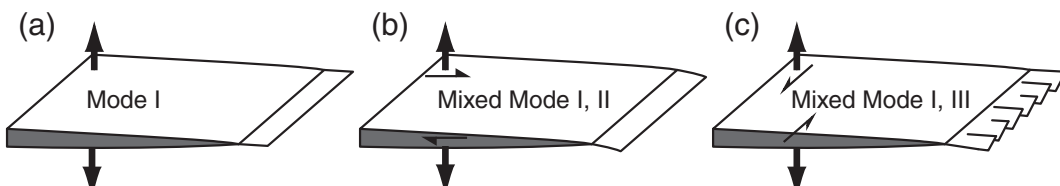


Fig. 34. Crack propagation under mixed mode loading. (a) In Mode I, the tensile mode, the crack opens normal to the crack propagation direction. The other two modes (Mode II and Mode III, which are not shown in this figure) include shear displacements. Mode II has displacements in the plane of the crack and in the direction of propagation (sliding mode). Mode III has displacements in the plane of the crack but normal to the crack propagation direction (tearing mode). (b) Under mixed Mode I, II loading, the crack front propagates perpendicular to the local tension direction. (c) Under mixed Mode I, III loading, the crack front breaks down into en-echelon segments (Rubin, 1995).

Figure reproduced from Rubin (1995).

2007). LP and hybrid events, indicative of the resonant excitation of a fluid-filled fracture, were found to accompany VT earthquakes during this rifting episode (Coté et al., 2010; Belachew et al., 2011). Sporadic tremor and ULP signals with periods of ~500 s were also recorded during the most intense VT crisis from September 24 to 26 (Ayele et al., 2009).

The 2009 dike intrusion and associated seismic crisis at Harrat Lunayyir, northwest Saudi Arabia, is another example of an energetic rifting episode (Pallister et al., 2010) similar to that seen in the Afar in 2005. The deformation field imaged by InSAR satellite data is best modeled by the intrusion of a ~10-km-long NW-trending dike, shallowing to less than 2 km depth, with volume of about 0.13 km³. Faulting on graben-bounding normal faults is also required to obtain adequate fit to the InSAR model (Pallister et al., 2010). The results of Pallister et al. (2010) imply that during intrusion the dike progressively migrated to shallow crustal levels and triggered meter-scale fault slip on western graben-bounding faults. The accompanying earthquake swarm includes VT earthquakes, VLP signals, and tremor (Pallister et al., 2010). Focal mechanisms for selected VT earthquakes ($M > 3.5$) point to double-couple mechanisms with average tensional axes oriented ENE–WSW, consistent with tensional opening across the rift (Pallister et al., 2010). The VLP signals accompanying the VT earthquakes are suggestive of a combined shear and tensile response of the crust induced by pulses of magma injection, where brittle rock fracture triggers VLP dike oscillations (Pallister et al., 2010).

5.3. Lower-crustal dike injections

Over a period of one year (March 2007–March 2008), over 10,000 microearthquakes (up to magnitude 2.2) occurred below Mount Upptyppingar in the Kverkfjöll volcanic system in Iceland (White et al., 2011). This seismicity was attributed to melt injection along a southward dipping dike (Jakobsdóttir et al., 2008). Starting from a depth of ~18 km below sea level, the deep seismicity migrated in both up- and down-dip directions as well as laterally before stopping at ~13 km depth, where the melt apparently froze without eruption (White et al., 2011). The brittle–ductile boundary in the vicinity of Mount Upptyppingar is evidenced by a termination of upper crustal seismicity at 6–7 km depth, hence the earthquakes at 13–18 km depth are well below the brittle zone, in a normally aseismic region (White et al., 2011). White et al. (2011) postulated that the high strain rates produced locally by magma movement generated the seismicity. Hypocentral locations obtained by White et al. (2011) using the double-difference scheme of Waldhauser (2001) have relative location uncertainties less than 60 m. The inferred fault planes from microearthquakes were found to align precisely with the overall plane of the dike delineated by earthquake hypocenters. Moment tensor solutions obtained by White et al. (2011) show dominantly shear failure with source mechanisms sometimes flipping between normal and reverse in essentially the same location on faults with the same orientation. White et al. (2011) proposed several possible explanations for the flipping fault mechanisms: (1) shear failure of dike-parallel joints near the dike tip or near constrictions in the dike (Rubin, 1995); (2) shear failure of solidified plugs of basalt within the dike itself in response to melt intrusion; and (3) movement of fractures between en echelon dike segments.

Smith et al. (2004) presented evidence for magma intrusion in the lower crust under north Lake Tahoe, California in late 2003. Their inference of magma intrusion is based on the character and on the spatial and temporal evolution of a swarm of 1600 microearthquakes ($M < 2.2$) located between 25- and 30-km depth, contemporaneous with outward horizontal and vertical displacements of 6 and 8 mm, respectively, recorded at a GPS receiver 18 km to the northeast. Hypocentral depths define a planar structure of approximately 35 km², dipping to the northeast at an angle of roughly 40° (von Seggern et al., 2008). The swarm lasted about 6 months, with

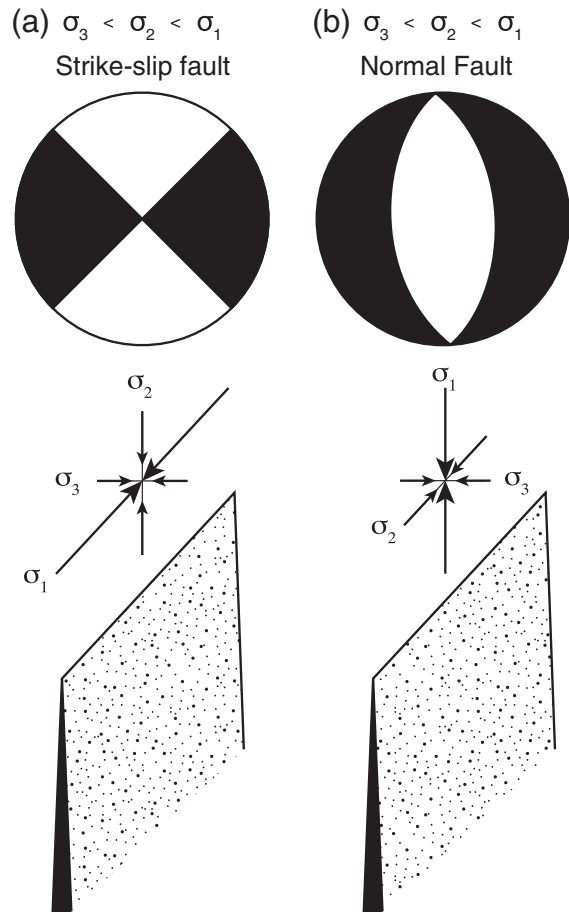


Fig. 35. Relationship between crustal stress and fault type induced by dike intrusion. The ambient stress state is defined by the three principal compressive stresses $\sigma_1 > \sigma_2 > \sigma_3$. (a) The maximum principal stress is horizontal and the expected fault type is a strike slip fault. (b) The maximum principal stress is vertical and the expected fault type is a normal fault.

After Ukawa and Tsukahara (1996).

hypocenters migrating upwards from 33 to 29 km at an average rate of 8.5 m/h during the first 23 days (Smith et al., 2004; von Seggern et al., 2008). Shear failure with reverse faulting component provides a reasonable explanation for the largest earthquakes in the sequence ($M > 1.5$). Overall, however, focal mechanisms exhibit a wide range of orientations that do not reflect the known regional stress field and are also generally inconsistent with the dike plane inferred from the distribution of hypocenters (von Seggern et al., 2008). Two months after the deep swarm, a shallower swarm of 1100 microearthquakes began at 10–12 km depths almost immediately above the deep swarm and continued through 2005. Hypocenters for the shallow swarm are concentrated in a narrow pipe-like volume, with event depths gradually becoming shallower. The focal mechanisms in this swarm are generally more consistent with the regional stress field than those of the deep swarm. The shallow swarm appears consistent with stress triggering from the deep magma intrusion (von Seggern et al., 2008).

VT earthquakes in the lower crust, where high pressures and temperatures would typically promote ductile deformation, are relatively rare but have been occasionally observed under other active volcanic centers. Other reported swarms include the deep swarms at Kilauea, Hawaii (Wright and Klein, 2006), the northern volcanic zone in Iceland (Soosalu et al., 2010; Key et al., 2011), the Taupo Volcanic Zone in New Zealand (Reyners et al., 2007), and Long Valley Caldera in California (Shelly and Hill, 2011) (see Section 5.4).

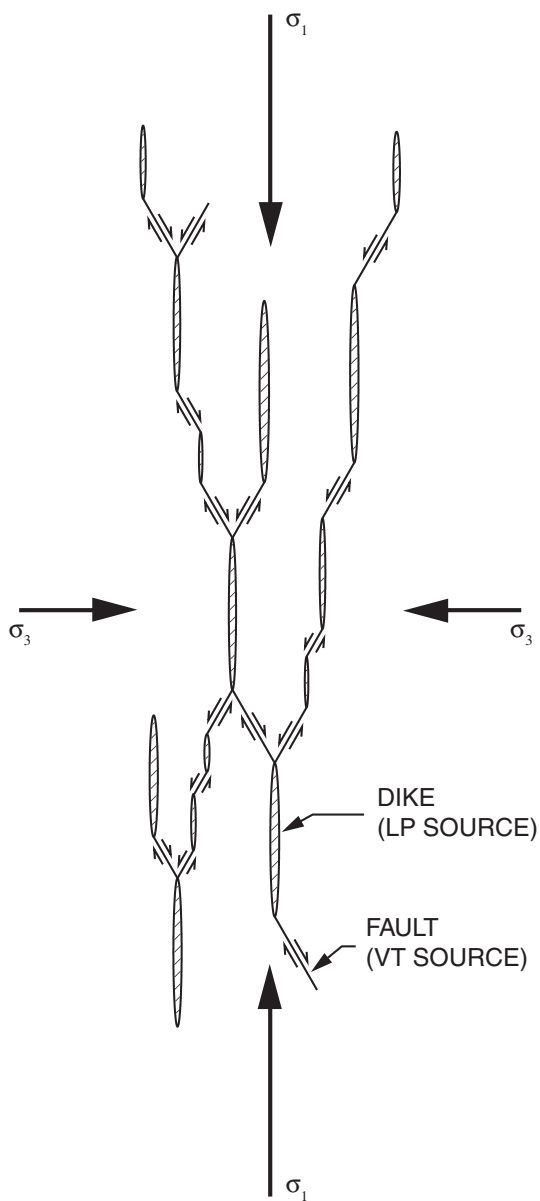


Fig. 36. Conceptual model of a fracture mesh and conjugate fault planes with respect to the greatest and least principal stresses σ_1 and σ_3 . Fluid intrusion into the fracture mesh produces both VT and LP earthquakes.

After Hill (1977).

5.4. Gas-driven intrusions

An earthquake swarm under Mammoth Mountain, California, provides evidence for a magmatic intrusion in the upper crust beneath the mountain (Hill, 1996). This swarm started on 2 May 1989, lasted eleven months, and included nearly 1000 earthquakes with magnitudes $M > 2$ and three $M > 3$ earthquakes (Hill and Prejean, 2005). Earthquake hypocenters in the 7–9 km depth range define a north-northeast trending vertical, blade-like structure with dimensions of 2×0.5 km (Prejean et al., 2003). Focal mechanisms for these earthquakes display tension axes that are predominantly oriented perpendicular to the slab, consistent with fluid intrusion in an opening dike (Hill et al., 1990; Prejean et al., 2003). Activity in the slab-like structure coincides with the initial interval of accelerating swarm activity that persisted over the first three months of the swarm. Contemporaneously, activity developed into a ring-like pattern beneath the southern and western flanks of Mammoth Mountain with the seismicity front

migrating circumferentially away from its initiation point directly over the seismicity keel (Hill and Prejean, 2005). One month after initiation of the swarm, seismicity began migrating to progressively shallower depths at a rate of 1–2 km/month defining more diffuse, ring-like structures at depths of 3–5 km and <3 km, each with diameters of ~3 km (Prejean et al., 2003). High-resolution hypocentral locations indicate that the lower seismicity ring has the form of a conical section over the depth interval of 5–6 km with a diameter of ~2.5 km concentric with the summit of Mammoth Mountain and with the conical surface dipping away from the summit at an angle of ~60° (Prejean et al., 2003). Focal mechanisms for earthquakes defining the outward-dipping conical surface of this seismicity ring show normal slip with tension axes radial to the summit, suggesting uplift of Mammoth Mountain with respect to the surrounding basement (Hill and Prejean, 2005).

Frequent spasmodic bursts, indicative of rapid fire brittle failure driven by transient surges in local fluid pressure were observed during the 1989 swarm (Hill et al., 1990). This swarm also coincided with the onset of a continuing sequence of mid-crustal LP events below the southwest flank of Mammoth Mountain, which continues to this day (Hill and Prejean, 2005). Following the 1989 earthquake swarm, areas of dead trees began to appear on the flanks of Mammoth Mountain in 1990. A close correlation between the tree kills and elevated soil concentrations of carbon dioxide (CO_2) in the tree-kill areas points to a link between elevated CO_2 flux, the 1989 swarm and onset of deep LP events (Hill, 1996). Accordingly, Hill (1996) hypothesized that this swarm may have been driven by the release of a volume of CO_2 -rich, hydrous fluids from the upper reaches of the mid-crustal source region of LP seismicity. As the clear seismicity keel is restricted to the ductile portion of the crust beneath Mammoth Mountain (Hill and Prejean, 2005), this suggests that intrusion to depths shallower than 7 km may have been partly aseismic. The lack of slab-like seismicity at depths shallower than the brittle–ductile transition could reflect dike intrusion into a highly hydrothermally altered and fractured region, producing a more diffuse seismicity (Hughes, 2011).

Shelly and Hill (2011) analyzed a small swarm of earthquakes ($M < 1.4$) that occurred September 29–30, 2009 deep beneath the southwestern margin of Long Valley Caldera near Mammoth Mountain. This swarm is of particular interest in the context of the 1989 swarm under Mammoth Mountain in that it offers further clues about the dynamics of volcanic unrest at Long Valley and Mammoth Mountain. Shelly and Hill (2011) used waveforms of well recorded events in the swarm as template events in a matched-filter technique to search the seismic record systematically for events that strongly resemble the template events. Using these waveform templates, they scanned these through the continuous record and estimated correlation coefficients from all stations/components in a 2.5-s-long window sliding in 0.005-s increments across the record. They recorded a detection when the sum of the absolute correlation coefficients at all stations exceeded a threshold value. The strength of this matched-filter technique derives from a simultaneous consideration of waveforms recorded at all receivers, which dramatically increases the detection power.

For each detected event, Shelly and Hill (2011) proceeded to measure the differential times at each seismic channel between the template event and events detected in the continuous data. These differential times were then used as input in a double-difference relocation algorithm (Waldhauser and Ellsworth, 2000) to obtain high-resolution event locations. The event hypocenters determined by Shelly and Hill (2011) exhibit systematically decelerating upward migration from 21 to 19 km over approximately 12 h. The relatively high migration rate of ~250 m/h during the first 4 h and modest magnitudes of events in this swarm suggest that the trigger could be ascending magmatic volatiles, perhaps in the form of CO_2 -rich hydrous fluids (Shelly and Hill, 2011) similar to those assumed to have triggered the 1989 swarm (Hill and Prejean, 2005). Lower crustal swarms occurred in June 2006 and January 2008 in the same region

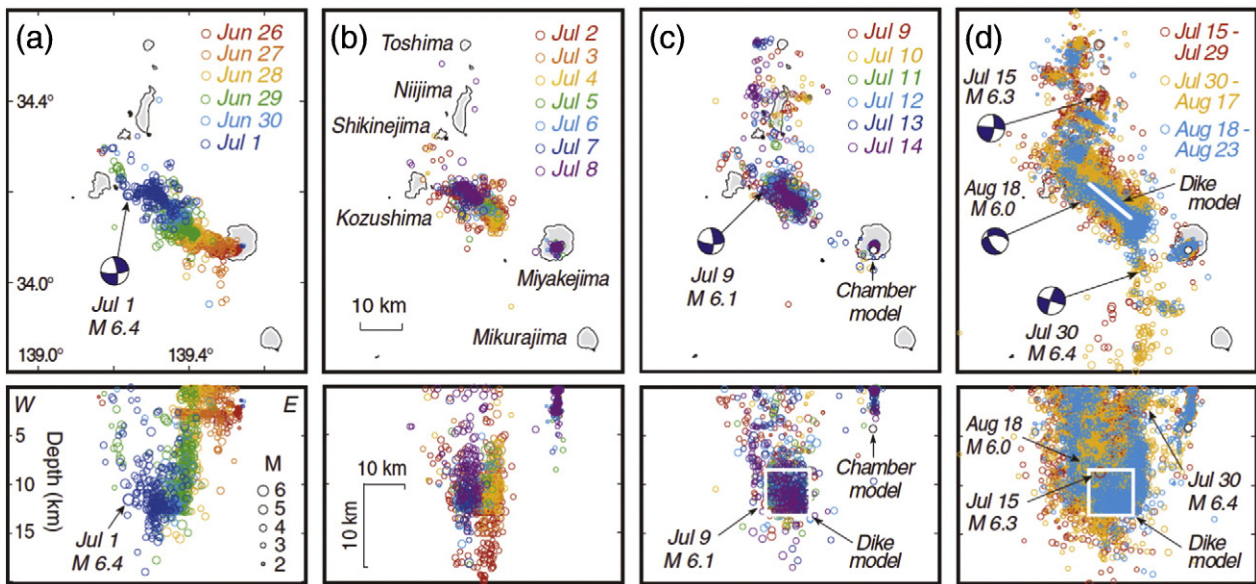


Fig. 37. Temporal evolution of the Izu swarm in map view (top panels) and cross section (bottom panels). The geometry of the inferred dike and magma chamber is shown in (c,d). Off-dike seismicity starts within three days (a) and expands substantially after two weeks (c,d). The 'dog-bone' pattern of seismicity in (d) can be explained by the transfer of shear stress from the expanding dike to vertical faults in the surrounding crust. Figure reproduced from Toda et al. (2002).

3–6 km SW of the Mammoth Mountain summit. Each swarm was short-lived, with the vast majority of events occurring within less than 24 h. Focal depths in the 2006 swarm ranged from 26 to 31 km, and those in the 2008 swarm spanned 19 to 22 km. The Mammoth swarms are characterized by a diversity of source mechanisms, a feature shared with the Lake Tahoe (von Seggern et al., 2008) and northern Iceland (White et al., 2011) swarms.

5.5. Local-regional stress interactions

Battaglia et al. (2004) documented the seismicity that followed the 15 June 1991 climactic eruption of Mount Pinatubo, Philippines. Unlike the pre-eruptive seismicity, which remained concentrated in two clusters 5 km to the northwest and directly below the summit, the post-eruptive seismicity was widely distributed below and around the volcano and was marked by the presence of several large multiplets. Away from the summit, earthquake hypocenters define planes oriented predominantly southwest–northeast, and also occur along several northwest–southeast conjugate structures. Composite focal mechanisms, obtained for all events in a multiplet, point to predominantly strike-slip, right-lateral faulting. Most of the seismicity that occurred after the June 15 eruption is related to the east–west regional compressional stress field associated with subduction (Battaglia et al., 2004). Surprisingly, the seismicity analyzed by Battaglia et al. (2004) shows no clear evidence of earthquakes associated with the formation of a 2.5-km-wide caldera at Pinatubo. Battaglia et al. (2004) attribute this absence of caldera-related seismicity to the lack of network coverage during the first two weeks following the eruption of June 15, when most of the collapse is expected to have occurred.

Moran (2003) studied VT earthquakes at Katmai National Park, Alaska, and attributed these to a wide range of processes associated with both regional and local stress states. Some earthquake clusters were found to primarily reflect tectonic forces, while others were inferred to be related directly or indirectly to volcanic processes (Moran, 2003). Earthquakes several kilometers away from the volcanic axis reflect a stress field characterized by horizontally-oriented σ_1 and σ_3 axes, with σ_1 rotated 12° relative to the subduction vector, indicating that these earthquakes occurred in response to regional tectonic forces. In contrast, stress tensors for earthquake clusters

beneath several Katmai volcanoes have vertically-oriented σ_1 axes, indicating that these events occurred in response to local, not regional, processes (Moran, 2003). At Martin-Mageik, a vertically-oriented σ_1 is most consistent with failure under edifice loading in conjunction with localized pore pressure increase associated with hydrothermal circulation. At Trident-Novarupta, it appears consistent with a number of possible models, including fractures formed during the 1912 eruption now serving as horizontal pathways for migrating fluids from nearby degassing and cooling magma bodies. At Mount Katmai, it is most consistent with continued seismicity along ring-fracture systems created during the 1912 eruption, possibly enhanced by circulation of hydrothermal fluids and/or seepage from the caldera-filling lake.

Systematic changes in the orientations of fault plane solutions of VT events related to episodes of magmatic activity have been documented at several volcanoes (Roman and Cashman, 2006). For instance, the pressure axis of VT fault-plane solutions has been observed to be orthogonal to the dominant regional stress orientation in some cases, indicating that these earthquakes may result from dike inflation in the direction of minimum compressive stress (Roman and Cashman, 2006). Temporal changes in VT hypocenter locations and the orientation of fault-plane solutions have also been attributed to pressurization of the mid-level conduit system prior to eruption at Soufrière Hills, Montserrat (Roman et al., 2006; Roman et al., 2008). In this case, most of the VT events are located within a limited depth range of 1–3 km below sea level and exhibit pure strike-slip or oblique strike-slip (P -axis dip $\leq 45^\circ$) mechanisms (Roman et al., 2008). For strike-slip mechanism on a fault with fixed orientation, a 90° rotation of the P -axis is equivalent to slip in opposite directions on the same fault. In other words, right-lateral faulting and left-lateral faulting may occur on the same fault depending on the relative magnitudes of local and regional stresses.

Within the tight cluster of VT earthquakes at Soufrière Hills documented by Roman et al. (2008), events with rotated fault plane solutions were found to dominate in the weeks to months prior to each eruptive phase and also prior to a major change in eruptive style. The rotated events ceased to occur shortly after the start of each eruption. Given the limited depth range of hypocenters, it seems possible that slip reversal could have occurred repeatedly on the same set of faults at Soufrière Hills. Similar examples of variability in focal

mechanisms during periods preceding or accompanying eruptive activity have been noted at Mount Etna, Sicily (Cocina et al., 1996; Patanè and Privitera, 2001), Mount Unzen, Japan (Umakoshi et al., 2001), Guagua Pichincha, Ecuador (Legrand et al., 2002), Mount Spurr, Alaska (Roman et al., 2004), Popocatépetl, Mexico (Arámbula-Mendoza et al., 2010), and Mount St. Helens, Washington (Lehto et al., 2010). Stress changes resulting from magma withdrawal have also been proposed to explain post-eruptive earthquakes reflecting a stress regime that is inconsistent with the regional stress field (Barker and Malone, 1991).

The likelihood of a particular fault to slip in response to a particular state of stress can be assessed from the Coulomb failure stress change, $\Delta\sigma_f$ (also called ΔCFS or ΔCFF), defined as (Stein, 1999)

$$\Delta\sigma_f = \Delta\tau + \mu(\Delta\sigma_n + \Delta P), \quad (13)$$

where $\Delta\tau$ is the shear stress change on the fault (positive in the direction of fault slip), $\Delta\sigma_n$ is the normal stress change (positive if the fault is unclamped, i.e., positive for tension), ΔP is the pore pressure change in the fault zone (positive in compression), and μ is the friction coefficient (range 0–1). Failure is promoted if $\Delta\sigma_f > 0$ and inhibited if $\Delta\sigma_f < 0$. Both increased shear and unclamping of faults encourage failure.

Roman and Heron (2007) assessed the effects of interacting regional and volcanically-induced stress fields on patterns of VT seismicity by calculating Coulomb stress changes on faults optimally oriented for failure. Their 2-D calculations, carried out for a specified instantaneous 1-m inflation of a 1-km-long dike, demonstrate that the patterns of fault slip induced by dike inflation are strongly dependent on the relative strength and orientation of tectonic stresses. Their model represents a best-case scenario where the orientation of the optimal faults receiving a maximum Coulomb stress change is actually determined by the two interacting stress fields and stresses acting on these faults are represented solely by magma-induced stress changes. In reality, such ideal faults may not be present in a volcanic system and are unlikely to arise from stress perturbations due to magma injection (Rubin and Gillard, 1998).

Further analyses of the interaction between a regional stress field and local stress field due to magma intrusion were carried out by Vargas-Bracamontes and Neuberg (2012), who specifically addressed Coulomb stress changes on pre-existing faults of fixed orientations. Their calculations performed for dike- or pipe-like intrusions, show that in the presence of a dominant regional stress field, faulting along pre-existing faults surrounding the conduit will be mostly in a direction consistent with the background regional stress field. Failure on these faults with an opposite slip direction is highly unlikely. As magma pressure starts counteracting regional stresses, the likelihood of faults to slip with either a regional or opposite slip direction relative to regional maximum compression increases, allowing the co-existence of possible failure with both slip tendencies in several regions surrounding the conduit. With increasing magma pressure, slip motion reflecting the regional stress field is inhibited along the flanks of a dike, leading to the development of aseismic zones there. With further increase of magma pressure the stress patterns approach those produced in the absence of a regional stress field. Earthquakes with slip direction consistent with the regional stress may occur in dog-bone-shaped regions extending from the dike tips, whereas earthquakes with slip direction opposite to that expected for regional stress may occur either along the dike flanks, or in regions adjacent to the dog-bone distribution of regional stress faulting extending from the dike tip.

The analyses of Vargas-Bracamontes and Neuberg (2012) suggest that low levels of magma pressure may be sufficient to promote failure on regional faults in broad areas surrounding a conduit and demonstrate that patterns in $\Delta\sigma_f$ are sensitive to small increments of applied pressure. In contrast, magma pressures that are significantly

larger than the regional maximum compression (σ_1) are necessary to promote zones where VT earthquakes with reverse slip may occur. This is in harmony with the observation that such earthquakes are ephemeral and suggests that they probably reflect major but short-lived stress perturbations. Vargas-Bracamontes and Neuberg (2012) conclude that the occurrence of VT events with rotated mechanisms may be indicative of a high state of pressurization and that as such these may be critical to eruption forecasting.

Finally, we note that a handful of papers have investigated possible "distal" VT events, i.e., VT-like events which are suggested to be related to magmatic stresses but are located at some distance from the volcanic edifice. A study by Fisher et al. (2010) mentions a cluster of earthquakes that occurred 25 km northeast of Augustine starting about 8 months before the Augustine eruption in 2006; this increase in distal seismicity was contemporaneous with an increase in seismicity directly below the crater of Augustine, although the connection between the proposed distal VTs and the volcanic activity remains problematic. Distal clusters have also been suggested at Pinatubo (Harlow et al., 1996) and Soufrière Hills (Aspinall et al., 1998). At Pinatubo, Harlow et al. (1996) report that most of the seismic energy release from April 5 up to May 31, 1991 (roughly one week prior to the start of the dome-building phase on or about June 8) occurred in a cluster 5 km northwest of the summit. Seismic activity shifted to a region under the summit in early June. The northwest cluster was located 2–6 km below sea level and the pre-dome cluster was centered at a depth of 3 km below sea level. The NW cluster was located under an area of geologically young fault traces, suggesting that these earthquakes may have occurred in response to small regional stress changes due to rising magma. The seismic data from Montserrat show features that are similar to what was seen at Pinatubo, with two clusters, one under St. George's Hill (about 5 km NW of the summit) and another under Soufrière Hills; a third elongated cluster appears to have moved southwestward with time from near the east coast of the island toward Soufrière Hills. The mechanisms and evidence for distal VTs appear to remain unclear at this time.

5.6. Changes in seismic anisotropy related to volcanic activity

Pressurization of a magmatic system affects the stress state of the crust around a volcanic edifice, which in turn may affect the alignment of fluid-filled microcracks and pore space, causing seismic anisotropy. The result of this anisotropy is a direction-dependent speed of elastic waves. Specifically, this anisotropy may induce the splitting of near-vertically propagating shear waves into two nearly perpendicular components with distinct velocities. The polarization direction of the faster S wave observed at the surface (fast direction, Φ) is sub-parallel to the predominant crack alignment and the orientation of maximum principal horizontal stress, σ_H . Observations of Φ and the delay time, δt , between the fast and slow S wavelets provide estimates of the direction and relative strength of σ_H . Unlike the stress-monitoring method based on inversions of earthquake source mechanisms, in which an estimate of stress is obtained at earthquake depths, the measurement of anisotropy yields an estimate of the average stress state in a region surrounding the ray path, with the probed area being mainly a function of receiver coverage (Gerst and Savage, 2004). Another advantage of using anisotropy over earthquake source mechanisms to quantify the state of stress in the crust is that it is free of artifacts caused by changing source conditions.

Gerst and Savage (2004) investigated seismic anisotropy beneath Ruapehu Volcano, New Zealand, to assess the state of stress in the crust under this volcano. They used earthquake data recorded during three seismometer deployments in 1994, 1998, and 2002. The first two deployments bracketed the two largest historical eruptions of Ruapehu in 1995 and 1996 and were used to investigate changes in anisotropy specifically related to pre- and post-eruptive states of

the volcano. The instruments deployed in 2002 covered all but one of the previously occupied sites and were used to provide a baseline comparison for the assessment of temporal anisotropy changes observed in the first two deployments. For this investigation, Gerst and Savage (2004) used waveforms of local and regional tectonic earthquakes originating at depths between 5 and 250 km and distances of up to 250 km from Ruapehu.

The data recorded at Ruapehu show a clear change in anisotropy between 1994 and 1998, marked by a rotation of the mean Φ for deep earthquakes (depths > 55 km) of 80°, from a perpendicular to a parallel alignment relative to the direction of regional σ_H (Fig. 38a and b). The mean Φ for shallow earthquakes (depths < 35 km) also changed by 42° between 1994 and 1998. Another change occurred for shallow earthquakes between 1998 and 2002, which essentially erased the change that occurred between 1994 and 1998, so that the mean Φ for shallow events observed in 2002 is similar to that seen on 1994 (perpendicular to the regional σ_H , Fig. 38c). In contrast, the mean Φ for deep events remained almost constant between 1998 and 2002.

The alignment of Φ for deep events is controlled by mantle anisotropy, so that shear waves from deep events must have acquired their first splitting in the mantle. There is no known processes that could have changed the fast direction of propagation over a large (> 300 × 300 km) region of the mantle over the observed time scale of 4 years, hence Gerst and Savage (2004) concluded that during their three deployments the fast direction of anisotropy beneath the crust must have remained constant and sub-parallel to the commonly documented NNE–SSW-aligned Φ for deep events. This suggests that the fast direction must have been altered during transit of the waves through the upper crust, and implies that there are two distinct layers of anisotropy, one in the mantle, and one in the upper crust (Gerst and Savage, 2004). While the mantle layer remained temporally stable, the crustal layer changed with time.

Based on their data, Gerst and Savage (2004) inferred a footprint of approximately 10 km for the anomalous region, and proposed that the only plausible mechanism for rapid temporal changes in anisotropy was a stress change in the medium in response to volcanic activity at Ruapehu. Under the known regional stress conditions $\sigma_V \gg \sigma_H > \sigma_h$, where σ_h and σ_V are the minimum horizontal stress and vertical principal stress, respectively, the expected shape of the magma intrusion is a vertical dike or set of dikes aligned with σ_H (NNE–SSW). The stresses in the direction perpendicular to the dike are mainly oriented perpendicular to the strike axis, that is parallel to σ_h . With strong pressurization of the dike, the stress field locally reorients the principal stresses as well as the local alignment of fluid-filled microcracks and pore space, effectively swapping σ_H and σ_h , so that in the anomalous region along the dike flanks, the direction of σ_H and Φ become nearly perpendicular to the dike (Fig. 38a). Gerst and Savage (2004) suggest that, before the eruption, the dike system became highly pressurized by fresh magma ascending from a deeper reservoir, rotating σ_H and the microcrack alignment (and therefore Φ) in this region, and eventually overwhelming the rock strength and triggering an eruption. The time scale for these changes in anisotropy is controlled by fluid movement between cracks and depends on rock permeabilities but is on the order of several minutes or less even for low permeabilities of 10^{-9} to 10^{-10} Darcy under an applied differential stress of 10 MPa (Gerst and Savage, 2004).

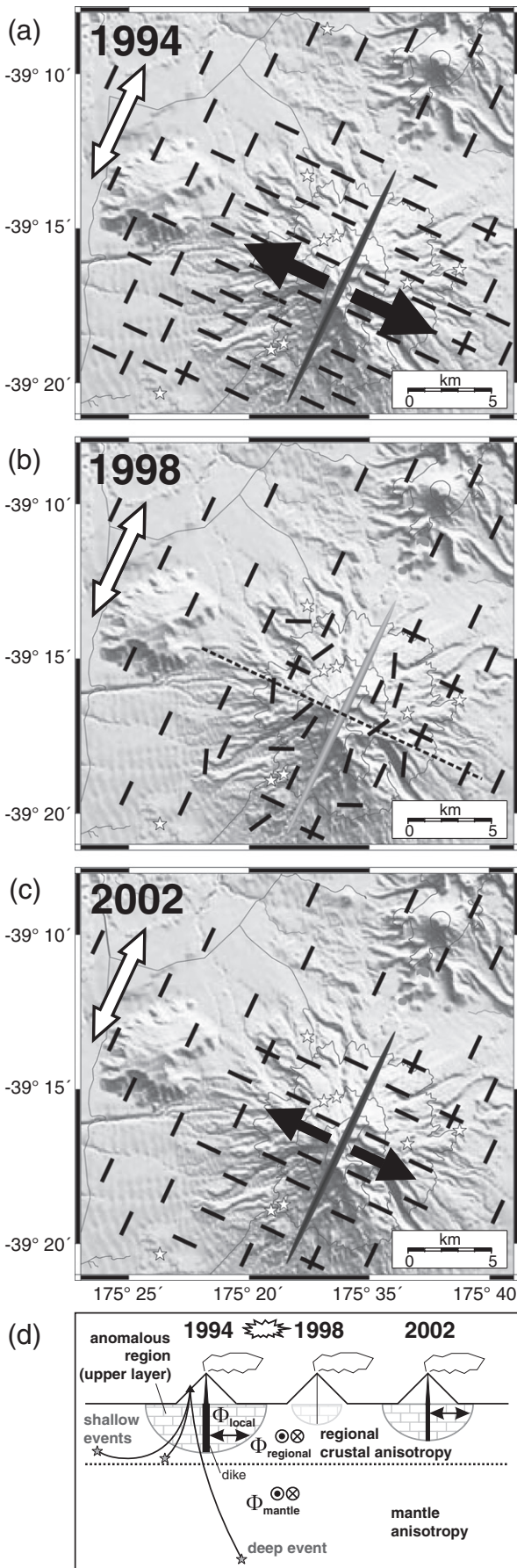
The analysis by Gerst and Savage (2004) suggests that microcracks can act as indicators of stresses in the crust. Eruptive activity at Ruapehu in 1995–1996 caused the pressure to drop, leading to the eventual disappearance of the anomalous region by 1998 when the second set of measurement was made (Fig. 38b). Measurements made in 2002 suggest that the system may have begun to repressurize, leading to the reappearance of the anomalous region, as reflected by the change in Φ for shallow earthquakes between 1998 and 2002 (Fig. 38c). The Φ for deep events did not change over this latter period, perhaps reflecting insufficient pressurization inducing weaker anisotropy and/or a smaller

anomalous region than in 1994, which may have remained undetected by the longer wavelengths associated with deep events (Gerst and Savage, 2004).

The precise interpretation of changes in seismic anisotropy depends critically on the availability of benchmark data allowing an examination of spatial anisotropy variations and their relationship to regional stresses and structures. Johnson et al. (2011) used a dense network of 34 broadband and short-period three-component seismometers deployed on and around Ruapehu to improve the resolution of spatial variations in anisotropy below the edifice. They used the automatic shear wave splitting method of Savage et al. (2010) to measure anisotropy parameters for shallow (< 30 km) and deep (> 50 km) earthquakes that occurred throughout 2008 near Ruapehu. Their analysis points to a strong azimuthal dependence of Φ , highly dependent upon the ray path from the source. This non-uniformity in anisotropy suggests that a simple averaging of Φ over the entire region may not be appropriate. To locate regions with different anisotropy, Johnson et al. (2011) used spatial averages of Φ as a first-order approximation to the heterogeneous anisotropic structure (Audoine et al., 2004). When all results are combined, they exhibit a mean azimuth of N13°E, sub-parallel to the trench caused by subduction of the Pacific Plate beneath the Australian Plate, and the strike of regional volcanic structures in the Taupo Volcanic Zone. At smaller scales, however, the overall distribution of Φ is heterogeneous and shows that the NNE–SSW regional trend is dominant only in regions to the south-east and north-east of Ruapehu. South of the volcano the trend of Φ is more north-south, and to the north-west the orientation of the fast polarization is more east–west. The anisotropy pattern can be broadly divided into regions in which Φ agrees with stress estimates obtained from focal mechanism inversions, consistent with stress-induced anisotropy, and those in which Φ is aligned with structural features such as fractures and faults, indicative of structural heterogeneity (Johnson et al., 2011). Johnson et al. (2011) demonstrated that Coulomb modeling with a dike-like conduit cannot fully match the anisotropy pattern inferred to be stress related. They suggested that major effects from other stresses due to topographic loading of the edifice and those related to the Taranki-Ruapehu lithospheric discontinuity should be accounted for to enable a more accurate interpretation of anisotropy changes.

6. Classic and new methodologies

In the following, we present a selection of classic and promising new approaches to imaging volcanic structures, tracking the temporal evolution of these structures, and assessing the source locations of magmatic and hydrothermal energy. Included in this list are seismic interferometry, tomography, muon radiography, the frequency-slowness method, the spatial auto-correlation method, and techniques for the automatic detection and classification of volcanic signals. Among these methods, ambient noise seismic interferometry is a new (less than a decade old) and growing field that has been successfully employed for a number of purposes including tomography of the shallow crust (Brenguier et al., 2007), seismic hazard analysis (Prieto and Beroza, 2008), volcano deformation, and temporal monitoring of active volcanoes and fault zones (Brenguier et al., 2008a; Brenguier et al., 2008b). The basic idea of ambient noise seismology exploits the fact that the cross correlation of seismic noise recordings at two stations separated by some distance reproduces the impulse response of the medium to a source located at one station with the other station being the receiver (Roux et al., 2005; Nakahara, 2006; Haney et al., 2012b). The method of inter-station correlation originates more than 50 years ago in a seminal paper by Aki (1957). Aki's spatial autocorrelation method (also known as the SPAC method) relies on correlations in the frequency domain, while ambient noise interferometry relies on correlations in the time domain. Thus, the two methods offer different but essentially equivalent ways to gain information about the structure of the subsurface from records of ambient noise (Chávez-García and Luzón, 2005).



Aki's SPAC method requires an azimuthal averaging of inter-station correlations, and as such has mainly been applied to the determination of superficial velocity structures (uppermost few 100 m) using data from small-aperture arrays with semi-circular geometries (Ferrazzini et al., 1991; Chouet et al., 1998). In contrast, ambient noise interferometry has mainly been directed toward imaging larger-scale structures (see Section 6.1). Although not a seismic method, muon radiography is included here because of the potential it offers to image shallow density structures in volcanoes at a resolution difficult to achieve with other geophysical techniques. Among the properties characterizing subsurface structures, density plays a special role because it is most readily interpreted in terms of composition and state.

6.1. Seismic interferometry

Seismic interferometry is the study of the interference phenomena between pairs of seismograms to obtain information about the medium properties from the differences between the recorded waveforms (Curtis et al., 2006). The principal mathematical tool used to study this interference is cross-correlation of the pairs of signals. Two different applications of seismic interferometry are commonly used: coda wave interferometry and ambient noise interferometry.

In coda wave interferometry, multiply scattered waves in the long duration signal that follows the main arrivals from earthquake multiplets or repeated explosions are used to detect temporal changes in the medium, which acts as an interferometer (Poupine et al., 1984; Ratdomopurbo and Poupine, 1995; Snieder et al., 2002; Wegler et al., 2006; Haney et al., 2009). The original application of this technique was carried out by Poupine et al. (1984), who used waveforms from two earthquakes with the same hypocenters and magnitudes recorded before and after the Coyote Lake, California, earthquake of August 6, 1979 to estimate time shifts between pairs of earthquake traces from a cross-correlation of signals in a short sliding window spanning the coda waves. Assuming that the entire volume of crust between the source and stations sampled by scattered waves was modified, they obtained the relative velocity change $\delta v/v$ from the measured relative travel time changes $\delta t/t$ from the relation

$$\delta t/t = -\delta v/v. \quad (14)$$

They inferred a temporal decrease in shear wave velocity of 0.2% in a small area 5–10 km wide at the southern end of the aftershock zone of the Coyote Lake earthquake, which they attributed to stress relaxation and/or seasonal variations in groundwater conditions. Ratdomopurbo and Poupine (1995) applied the same methodology to shallow multiplet earthquakes recorded at Merapi and found an increase of ~1.2% in shear wave velocity under Merapi prior to its 1992 eruption. They interpreted this increase as a medium response to a pressurization, in harmony with the relationship between pressure changes and elastic wave velocity noted in laboratory experiments (Nur, 1971; Grêt et al., 2006). In another study at Merapi, Wegler et al. (2006) analyzed

Fig. 38. Stress and anisotropy model of Gerst and Savage (2004) for Ruapehu Volcano. The thick white arrow in (a–c) shows the direction of the regional maximum principal horizontal stress σ_H obtained from geodetic measurements. Black bars in (a–c) represent fluid-filled microcracks and pore spaces distributed throughout the medium. (a) In 1994, a pressurized dike under Ruapehu generated a local stress field with σ_H (thick black arrow) oriented perpendicular to the regional σ_H (white arrow). The local stress field effectively realigned the microcracks and pore spaces in the vicinity of the dike along the direction of the local σ_H . (b) In 1998, following the eruption of Ruapehu, the dike depressurized and the orientation of σ_H and microcrack alignment in the vicinity of the dike partly returned to the original regional trend. (c) In 2002, the dike repressurized and the local stress field near the dike realigned normal to the dike. (d) Schematic cross section along dashed line in (b). The fast directions Φ_{mantle} and $\Phi_{regional}$ (crustal), and the dike strike are perpendicular to the plane of the figure, and Φ_{local} (anomalous region) is within the plane. The extent of the anomalous region within the gray half circle (<10 km) is exaggerated with respect to the depth of the deepest earthquakes (~250 km). Figure reproduced from Gerst and Savage (2004).

scattered waves from repeated airgun shots on the flanks of the edifice to infer a relative shear wave velocity increase $\delta v/v = (0.08 \pm 0.02)\%$ over a 10-day interval prior to the 1998 eruption of Merapi. This pre-eruptive increase in wave speed occurred synchronously with pre-eruptive seismicity and dome growth, consistent with a pressurization of the magmatic system. Haney et al. (2009) examined records of repeating explosions from Pavlov Volcano during its 2007 eruption and estimated an increase of 0.3% in relative travel time change for late-arriving seismic waves over the course of the last two weeks of the eruption. A dominance of source effects in the records obtained at Pavlov argues against changes related to path effects as the primary cause for the late-arriving waves at Pavlov. Rather, Haney et al. (2009) suggested that their results could be explained by a decrease in wave speed in the feeder conduit, possibly related to conduit deflation in response to decreasing pressure during the late stage of the eruption. Such a decrease in wave speed may be expected in a crack-like conduit due to the increase in crack stiffness associated with conduit deflation (Aki et al., 1977a; Chouet, 1986; Chouet, 1988). At Asama Volcano, Nagaoka et al. (2010) used cross-correlations of coda waves from regional earthquakes to infer a reduction of 1.5% in relative velocity during the latter half of 2007, followed by recovery before an eruption in 2008. Battaglia et al. (2012) used repeating LP events to infer time dependent changes in the volcanic structure at Yasur Volcano (Vanuatu) following a magnitude 7.3 earthquake that occurred 80 km from its summit. They attributed the cause of this change to a weakening and healing of the volcanic subsurface in response to this earthquake.

Unlike coda wave interferometry, which relies on the coda of earthquakes or explosions to obtain information on the average statistical properties of the Earth, ambient noise interferometry relies on the ambient seismic noise excited by shallow sources such as ocean microseisms (Friedrich et al., 1998) and atmospheric perturbations (Logonne et al., 1998; Tanimoto, 1999). Over long periods of time, the distribution of noise sources tends to randomize and noise is further randomized by scattering from heterogeneities within the Earth, hence the ambient noise may be viewed as a random diffuse field (Shapiro et al., 2005). Using ambient noise instead of the coda has the advantage that the noise does not depend on earthquake occurrence and can be recorded almost continuously at any location.

The method of ambient noise interferometry is based on the idea that ambient noise recorded at two stations separated by some distance can be cross-correlated for some period of time and what emerges from this cross-correlation is the impulse response (the Green's function) of the medium to a seismic source located at one station with the other station being the receiver (Curtis et al., 2006; Wapenaar and Fokkema, 2006; Fan and Snieder, 2009; Snieder et al., 2009; Wapenaar et al., 2011). Surface waves are most easily extracted from the ambient noise because their contribution dominates the Green's function between receivers located at the surface of the Earth and also because ambient noise is excited preferentially by superficial sources such as oceanic microseisms and atmospheric disturbances (Campillo and Paul, 2003; Shapiro and Campillo, 2004; Sabra et al., 2005a; Sabra et al., 2005b; Shapiro et al., 2005; Gerstoft et al., 2006; Larose et al., 2006; Yao et al., 2006; Bensen et al., 2007; Bensen et al., 2008; Liang and Langston, 2008; Lin et al., 2008; Ma et al., 2008; Yao et al., 2008; Lin et al., 2009; Picozzi et al., 2009). The most commonly studied phase arising from noise correlation studies is the Rayleigh wave at periods shorter than ~50 s for continental-scale studies (inter-station spacing up to ~500 km) (Bensen et al., 2007), or periods <20 s for regional-scale and local-scale studies (inter-station spacing < 100 km) (Shapiro et al., 2005; Brenguier et al., 2007). The existence of this phase at such short periods is the reason for the popularity of this method. While surface wave studies based on earthquake data have typically focused on longer-period data providing a view of the lower crust and upper mantle, our growing ability to use shorter-period data via noise correlation studies enhances our picture of the upper and middle crust, thereby improving our understanding of

processes occurring at depths shallower than the Moho. This newfound ability is particularly relevant to our understanding of volcanic processes.

A key requirement for a reliable reconstruction of the impulse response of the Earth between two receivers by cross-correlation is that the noise distribution be uniform in space and time (Fan and Snieder, 2009). This means that the energy flow must be equipartitioned for a successful extraction of the Green's function from noise. Provided this equipartition condition is satisfied the Green's function can be retrieved by stacking (to satisfy a required integration over all actual sources) the cross-correlation functions obtained for successive records of noise. The resulting cross-correlation functions are two-sided functions with positive and negative time coordinates representing the Green's function and time-reversed Green's function that describe waves traveling in opposite directions between the receivers. When the noise is equipartitioned, the Green's function and time-reversed Green's function have equal strength. In most seismological applications, however, the noise being correlated is incompletely equipartitioned and the causal Green's function and its time-reversed counterpart have different strengths. The reason for this stems from the spatial distribution of oceans and localization of storm disturbances generating ocean waves, which all contribute to a noise distribution that is far from uniform. One solution to remedy such limitation in the actual noise source distribution is to cross-correlate the coda of the cross-correlation of ambient seismic noise (Stehly et al., 2008). This procedure provides a better sampling of the field fluctuations because coda waves propagate in more directions than the direct surface waves.

To guarantee accuracy, the cross-correlation operation is carried over a window sufficiently long for the correlation to stabilize. To minimize the effect of short-lived noise bursts that may dominate the noise cross-correlation function it is best to normalize the noise before cross-correlation. The simplest form of normalization is to replace the recorded noise by its sign bit (Larose et al., 2004). In this normalization method, only the sign of the raw signal is retained by replacing all positive amplitudes by +1 and all negative amplitudes by -1. This procedure has been shown to increase the signal-to-noise ratio (Campillo and Paul, 2003; Larose et al., 2004; Shapiro and Campillo, 2004). Other useful normalization schemes have been described by Bensen et al. (2007). Spectral whitening, performed by inversely weighting the complex spectrum of ambient seismic noise by a smoothed version of the raw amplitude noise spectrum, can also be applied to broaden the band of ambient noise signal used in cross-correlation (Bensen et al., 2007). The noise correlation function obtained by this method represents the impulse response filtered by the bandwidth of the noise spectrum. In other words, the noise spectrum fixes the bandwidth over which the impulse response can be retrieved.

An application of ambient noise seismology to image volcanic structure was carried out by Brenguier et al. (2007), who used Rayleigh waves obtained from cross-correlations of noise recorded on short-period vertical-component receivers at Piton de la Fournaise Volcano, Reunion Island, to obtain group velocity dispersion curves at periods of 1.5 to 4.5 s. They used the shear velocity profiles derived from Rayleigh group velocity measurements to obtain a three-dimensional shear wave velocity model of Piton de la Fournaise for the depth range +2 to -1 km above sea level. Their model points to an intrusive high-velocity body underlying the active 10-km wide caldera and bounded laterally within the caldera perimeter. Surrounding this high-velocity body is a lower-velocity region, which was attributed by Brenguier et al. (2007) to the accumulation of effusive products from the volcano. A westward trend of the high-velocity anomaly is suggested in the deeper reaches of the model, and a preferential orientation of this anomaly along the NE and SE rift zones is also apparent at depth, suggesting a preferred magma transport aligned with the rift zones.

Ambient noise tomography was also used to obtain an image of the magma chamber beneath Lake Toba Caldera, north Sumatra (Stankiewicz et al., 2010). For this study, Stankiewicz et al. (2010) used data from 40 temporary short-period seismic stations deployed

around Lake Toba to extract the fundamental-mode Rayleigh wave by stacking daily cross-correlations of the seismic signals in the 2.5–12 s period band. Arrival times of the surface waves were picked for available station pairs for six periods in this range and these travel times were then used in a tomographic inversion to estimate surface wave velocities at these periods. The resultant three-dimensional velocity models show a low-velocity zone that correlates well with the location of Samosir Island. The volume of this low-velocity anomaly is estimated to be at least $34 \times 10^3 \text{ km}^3$, in general agreement with estimates based on the volume of erupted magma.

A study by [Masterlark et al. \(2010\)](#) is another example of ambient noise tomography imaging a molten and active magma reservoir at Okmok Volcano, Alaska. [Masterlark et al. \(2010\)](#) used 40 days of continuous data from a network of 12 seismometers deployed on Okmok in late 2005 to derive a tomographic model from group velocities of Rayleigh waves in the frequency band of 0.2–0.7 Hz. Their 3-D model clearly images two distinct low velocity zones subjacent to the caldera of Okmok. A low-velocity zone in the uppermost ~2 km below the caldera floor corresponds to a region of weak, fluid-saturated caldera materials, while a deeper low-velocity zone is indicative of the presence of a magma reservoir whose main part lies at depths greater than 4 km below the caldera floor. Their model also images a thinner conduit-like structure connecting this reservoir to the shallow low velocity zone.

In a groundbreaking study, [Brenguier et al. \(2008a\)](#) used ambient noise to probe temporal changes in the interior of Piton de la Fournaise. Their approach relied on measurements of very small time delays in the coda of noise cross-correlations. They considered 18 months (July 1999–December 2000) of continuous seismic records in the frequency band of 0.1–0.9 Hz and computed cross-correlation functions corresponding to all possible receiver pairs in the 21-station network of Piton de la Fournaise. Taking the cross-correlation function obtained by stacking 18 months of cross-correlations as reference function, they measured travel time shifts by comparing the reference function with current cross-correlation functions obtained from 10-day stacks of cross-correlations. The resulting time series of relative velocity derived from these measurements with Eq. (14) shows changes in the volcano interior occurring over time scales ranging from a few days to a few months ([Fig. 39a](#)). After removing long-term variations from the raw relative velocity changes, they observed systematic precursors to eruptions marked by small (0.1%) edifice-wide decreases in seismic velocity beginning roughly 20 days prior to eruptions ([Fig. 39b](#)). They attributed the precursory velocity decreases to the opening of cracks in response to edifice inflation associated with magma pressurization. Using the same approach, [Duputel et al. \(2009\)](#) analyzed ambient noise at Piton de la Fournaise during an 18-month interval from January 2006 to June 2007. Their analyses of data in the 0.1–0.5 Hz band point to relative velocity changes of a few tenth of 1% that correlate with volcanic activity. They ascribed these changes to an edifice dilation or compression in response to pressure variations in the magmatic system. The observed velocity changes were found to be mostly restricted to a region a few kilometers wide near the central cone of the volcano.

[Sens-Schönfelder and Wegler \(2006\)](#) retrieved Green's functions from ambient seismic noise at Merapi and resolved velocity variations with an accuracy of 0.1% with a temporal resolution of one day. Green's functions were retrieved from records high-pass filtered at 0.5 Hz. Contrasting the results at Piton de la Fournaise, the relative velocity variations at Merapi show a strong seasonal influence and correlate better with precipitation than with eruptive activity. Such outcome is not totally unexpected since the Green's function extracted from short-period noise is dominated by waves propagating near the surface.

6.2. Tomography

The course of volcano seismology was fundamentally altered in the late 1970s with the publication of a landmark paper by [Aki et al.](#)

(1977b), in which Aki and his colleagues developed a method for the determination of the three-dimensional seismic structure of the lithosphere based on an inversion of earthquake travel-time data. Tomography techniques have since become the most diagnostic approaches to image complex heterogeneous volcanic structures and map magma reservoirs.

The three-dimensional velocity structure of a volcanic edifice can be imaged through inversion of first-arrival times from local earthquakes. The technique uses crisscrossing ray paths to separate the integrated effects of slowness (the reciprocal of velocity) on travel times and derive an image of the velocity structure. The arrival time of a seismic wave from an earthquake at a receiver is expressed by the nonlinear relationship

$$t = \tau + \int_{\mathcal{L}[u(\vec{r})]} u(\vec{r}) d\mathcal{L}, \quad (15)$$

where t is the arrival time, τ is the earthquake origin time, $u(\vec{r})$ is the slowness, $d\mathcal{L}$ is the differential length along the ray, and $\mathcal{L}[u(\vec{r})]$ is the ray path, a function of the earthquake location and velocity structure. Linearization of Eq. (15) about a starting reference model and earthquake location then yields the relation ([Hole, 1992; Benz et al., 1996](#))

$$r_{ij} = \sum_{k=1}^3 \frac{\partial T_{ij}}{\partial x_k} \Delta x_k + \Delta \tau_i + \int_{\text{raypath}} \delta u(\vec{r}) d\mathcal{L}, \quad (16)$$

where r_{ij} is the arrival time residual for the i -th earthquake at the j -th receiver, T_{ij} is the travel time from the i -th earthquake to the j -th receiver, $\partial T_{ij}/\partial x_k$ are the partial derivatives of travel time with respect to the spatial coordinates, x_k , Δx_k and $\Delta \tau_i$ are perturbations to the starting earthquake location and origin time, respectively, and $\delta u(\vec{r})$ is the slowness perturbation to the reference model. The arrival time residual is the difference between the observed and calculated travel times based on a starting earthquake location and reference slowness model.

In this approach, an initial reference slowness model is discretized by a uniformly spaced set of grid nodes in three dimensions and the first arrival times from a source location to each node in the model are calculated using finite-difference operators based on the Eikonal equation assuming a constant slowness within each cell ([Vidale, 1988; Podvin and Lecomte, 1991; Vidale, 1991](#)). Once the travel times are known everywhere in the model for a given source, rays are found by tracing from the receivers back to the source through the travel-time field. The ray within each cell is approximated by a straight segment and the ray direction is taken along the average travel-time gradient across the cell. Once a ray is traced, the length increments $d\mathcal{L}$ within all cells crossed by the ray are known, and the slowness and hypocenter perturbations are calculated by minimizing the differences between observed and calculated travel times. The model is then updated by the addition of the model perturbations, and the resulting new reference model is used for another linearized inversion. Iterations are stopped when the root-mean-square error in travel times between data and model reach a stable minimum value.

High-resolution velocity models (0.5 km resolution) of the Kilauea caldera region were obtained by [Dawson et al. \(1999\)](#) by tomographic inversion of P - and S -wave arrival times from local earthquakes ([Fig. 40](#)). The data used for their inversion were recorded on a network of 67 stations with average spacing of 650 m and include 4695 P -wave and 3195 S -wave arrivals from 206 earthquakes. Map views of the P and V_p/V_s models are illustrated for four depth intervals in [Fig. 40a–h](#). Their models show a low P wave velocity anomaly centered on the southeastern sector of the caldera at depths of 1 to 4 km. [Dawson et al. \(1999\)](#) also identified two zones of high V_p/V_s ratios at similar depths below the southern caldera rim and upper east rift. They attributed the latter anomalies to the presence of either highly fractured materials and/or a significant fraction of partial melt. A compact magma reservoir is not

required to satisfy the velocity constraints and is also inconsistent with the occurrences of VT earthquakes throughout these zones. Rather, Dawson et al. (1999) interpreted these regions as volumes of hot rock permeated by sills and dikes, whose orientations are likely controlled by the dominantly flat volcanic and primarily vertical tectonic structures observed at Kilauea. The anomalous zone centered at depth of 3 km under the southern caldera floor coincides with the summit magma reservoir inferred from long-term deformation of Kilauea, while the southeastern region underlies the Puhimau area, known to be a region of high heat flow. The latter region is near the source of LP seismicity originating under the eastern caldera perimeter. A shallow (<1 km depth) zone with low V_p velocity was also identified by Dawson et al. (1999) under the northeastern edge of Halemaumau. This zone overlaps the shallow hydrothermal system inferred by Almendros et al. (2001b), and reduced P wave velocities in this region were attributed by Dawson et al. (1999) to rock alteration in this acid-rich, hot aqueous environment.

In a similarly detailed investigation of the velocity structure of Redoubt Volcano, Benz et al. (1996) imaged perturbations of up to 12% in P -wave velocities and up to 20% in S -wave velocities. The most prominent feature observed at Redoubt in both the P - and S -wave velocity models is a relatively low-velocity, near-vertical, pipe-like anomaly approximately 1 km in diameter that extends

from 1 to 6 km below sea level. This pipe-like structure is consistent with the magma pathway inferred by Lahr et al. (1994) from the seismicity associated with the 1989 eruption and was attributed by Benz et al. (1996) to a highly fractured or altered zone surrounding a magma conduit. No large low-velocity body suggestive of a magma source was identified in the upper 7–8 km of the crust. However, a small volume with V_p/V_s near 1.85 associated with low S -wave velocities was imaged 2.5 km below the crater and 1–2 km north of the eruptive vent. This 2–3 km³ volume is located immediately below and to the north of the source of long-period events that preceded the December 14, 1989 eruption and may represent a perched magma chamber or the top of a vertical pipe roofing just below the LP source (Benz et al., 1996).

Applications of tomographic inversions to volcanoes are multifarious and feature several ray tracing schemes that are distinct from that described above (Aki and Lee, 1976; Thurber, 1983; Eberhart-Phillips, 1986; Um and Thurber, 1987; Thurber, 1993; Thurber et al., 1995; Zhang and Thurber, 2003; Hansen et al., 2004; Koulakov, 2009). The resolution of structural details is contingent upon adequate receiver coverage, good illumination of the structure by well-distributed earthquake sources, and precise timing of arrival times. The latter depends on the signal-to-noise ratio and is constrained by the shortest measurable wavelength, which itself is conditioned by anelastic dissipation

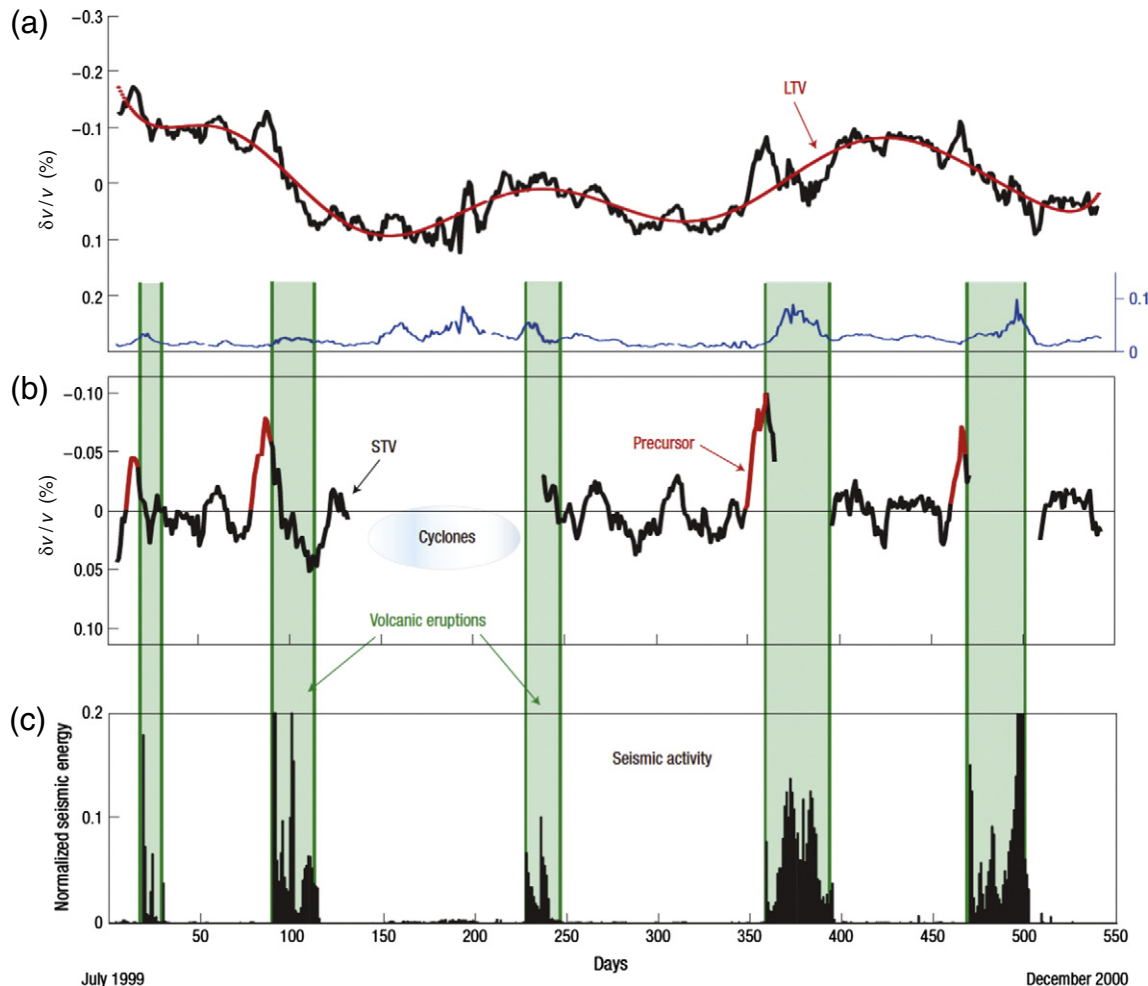


Fig. 39. Temporal evolution of relative velocity changes at Piton de la Fournaise Volcano over 18 months. (a) Raw relative velocity changes. The red curve is a fit to the long-term variation (LTV) of relative velocity. The blue error curve represents the uncertainty (scale shown at right) in the estimation of relative velocity change; measurements with uncertainties larger than 0.04% are excluded from the analysis (Brenguier et al., 2008a). (b) Short-term variation (STV) of relative velocity changes after removal of LTV (red curve in a) from the raw relative velocity changes in (a). Colored red are clear precursors to eruptions (green-shaded intervals). No data is available for days 135–229, a period marked by tropical cyclone activity. (c) Daily seismic energy recorded at a receiver near the Dolomieu crater. Figure reproduced from Brenguier et al. (2008a).

and scattering. Given such constraints, the spatial resolution of three-dimensional volcanic structures achievable by tomography is commonly a few km. A more comprehensive review of seismic tomography applied to various magmatic systems, with an evaluation of its current achievements and limitations, may be found in Lees (2007).

6.3. Muon radiography

Muon radiography is a new technique used for imaging the shallow density structures of volcanoes and detecting magma conduits. The method is based on the observation of the absorption of muons in matter and is the same in principle as ordinary medical X-ray radiography, except for the substitution of highly-penetrating muons in lieu of X-rays (Tanaka et al., 2007b). Muons are produced in the Earth's atmosphere as the result of collisions of cosmic rays with the nuclei of atoms in the atmosphere. Muons continuously bombard the Earth's surface from above, arriving at angles ranging from vertical to horizontal (Tanaka et al., 2007b). They are not hindered much by matter and can penetrate it to great depths. For example, a typical horizontally-arriving muon with an energy of 1 TeV can penetrate 2.6 km of water (Tanaka et al., 2007b). This means that muon radiography can be applied to image kilometer-size objects positioned above a muon detector. This property of muons makes this technique particularly attractive for scanning the shallow structures of volcanoes. Moreover, given the steady muon stream produced in the atmosphere, muon radiography can be performed everywhere at any time on the Earth's surface.

Muons transmitted through matter are differentially absorbed, depending on the thickness of matter crossed and density distribution of matter encountered along the path. The attenuation of muon flux through matter increases proportional to the product $\text{density} \times \text{path length}$, called "density length" (Tanaka et al., 2007b). In muon radiography, a detector with area of $\sim 1 \text{ m}^2$ is placed at shallow depth underground to capture an image of the volume of Earth above the detector. The intensity of an image pixel in the detector is fixed by the attenuation of incident muons due to absorption along the path and provides a measure of density length that is completely independent of the geophysical model. In muon radiography applied to volcanoes, a detector placed on the flank of a volcano is used to obtain a two-dimensional image of the volcano interior projected onto the plane of the detector. The muon tracks reconstructed from the detector are analyzed to determine the absorption along different ray paths through the volcano. From the path lengths determined from topographic data, the measurement provides the average density $\langle \rho \rangle$ along the path lines of muons through the Earth. The energy loss of muons through matter is calculated from the Standard Model of muon-initiated interactions, which is sufficiently well known for the purpose of radiography (Tanaka et al., 2007b). The required observation time is inversely proportional to the area of the detector. For example, two months of observations with a detector area of 1000 cm^2 are necessary for the detection of density contrasts of 3% in a 1-km thick layer of rock with an angular resolution of 10 mrad (Tanaka et al., 2007a, 2007b). This angular resolution corresponds to about 10 m in spatial resolution, which far exceeds what can be achieved with conventional geophysical techniques. Muon radiography has been used to obtain images of conduit shapes under several volcanoes, including Asama (Tanaka et al., 2007b, 2008, 2009a), Usu (Tanaka et al., 2007a, 2008), and Satsuma-Iwojima (Fig. 41) (Tanaka et al., 2009b).

Unidirectional radiography only resolves the average density distribution along muon paths. To obtain a three-dimensional picture of the shape and size of a magma body, two or more detectors need to be used. Provided adequate muon illumination of the structure is available, an image of this structure can be obtained by discretizing the volume under study and applying a tomographic inversion to determine the average density in each cell (Tanaka et al., 2010).

6.4. Frequency-slowness method

Small-aperture seismic arrays (seismic antennas) are useful for tracking the spatio-temporal properties of LP seismicity. LP earthquakes and tremor are difficult to locate by conventional means because of the general lack of impulsive phases in their records. The standard procedure is to compute frequency-slowness power spectra over short moving windows spanning the signal. Assuming a finite number of plane waves are incident on the antenna, frequency-slowness spectra yield estimates of the directional properties of these plane waves, from which the locations of the strongest sources of seismic energy can be inferred using an appropriate structure model. Time-dependent changes in signal properties detected by the antenna are thus converted into time-dependent changes in source locations. Each plane wave traveling across the antenna is defined by its ray parameter, P , where

$$P = \sqrt{S_x^2 + S_y^2}, \quad (17)$$

and azimuth ϕ , where

$$\phi = \pi/2 - \arctan(S_y/S_x), \quad (18)$$

and S_x and S_y are the x and y components of slowness, respectively.

Goldstein and Chouet (1994) used the multiple signal classification (MUSIC) frequency-slowness method (Schmidt, 1986; Goldstein and Archuleta, 1987; Goldstein and Archuleta, 1991) to investigate sources of tremor at the Puu Oo crater on Kilauea. They used short-period vertical-component records obtained with two dense arrays with respective apertures of 800 and 120 m deployed at a distance of 1 km from Puu Oo. They found the tremor to be composed of body and surface waves originating from the direction of Puu Oo. Based on a comparison of measured ray parameters with theoretical ray parameters estimated as a function of source depth for a model of the local velocity structure (Ferrazzini et al., 1991) they inferred a maximum source depth of 250 m for P waves, and 1 km for S waves composing the wave field. Based on uncertainties in slowness at the large array, they estimated the uncertainties in maximum source depth to be approximately 100 m for P waves and 300 m for S waves. These results clearly show that the source of tremor observed at Puu Oo at the time was close to or within the upper kilometer of crust.

Similar analyses of slowness spectra using the MUSIC algorithm were carried out by Chouet et al. (1997) for tremor and explosions at Stromboli. Their measurements of ray parameters and azimuths, obtained with a dense array of short-period seismometers with aperture of 300 m deployed on the north flank of Stromboli at a distance of 1.7 km from the active crater, point to sources localized below the summit crater at depths shallower than 200 m with occasional bursts of energy from sources extending to a depth of 3 km. Their slowness, azimuth, and particle motion analyses revealed a complex composition of body and surface waves associated with topography, structure, and source properties. Body waves originating at depths shallower than 200 m were found to dominate the wave field at frequencies of 0.5–2.5 Hz, and surface waves generated by sources nearest to the surface and by scattering sources distributed around the island were found to dominate at frequencies above 2.5 Hz.

Almendros et al. (2001a,b) used the MUSIC algorithm to track LP events and tremor originating below Kilauea Caldera. They used vertical-component data recorded simultaneously with three dense arrays of short-period seismometers with apertures of 300, 400, and 600 m to estimate ray parameters and azimuths for first arrivals for 1129 LP events and 149 samples of tremor that occurred during a 23-hour period of swarm activity. With the exception of a few more distant events, this activity was found to originate from a region beneath and to the northeast of the Halemaumau pit crater (Almendros et al., 2001b). To estimate the spatial extent of the source region of LP

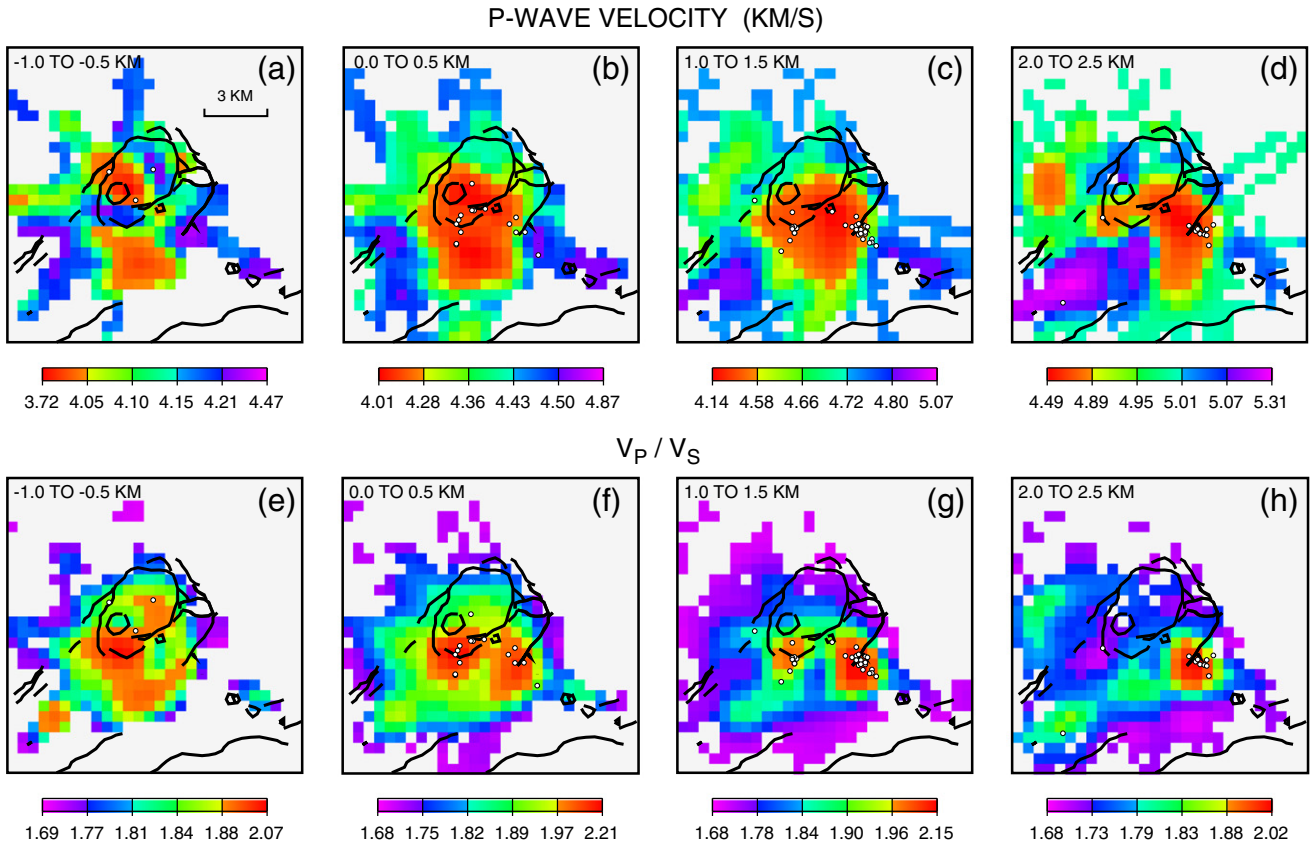


Fig. 40. Map views of the P -wave velocity (*a*–*d*) and V_p/V_s ratio (*e*–*h*) models elaborated by Dawson et al. (1999) for the Kilauea Caldera region. The maps sample four depth intervals from 1 km above, down to 2.5 km below sea level. Lines indicate ring fractures, faults, and pit craters. White circles mark earthquake locations within each layer. Figure reproduced from Dawson et al. (1999).

seismicity, Almendros et al. (2001b) used synthetic slowness results obtained for a medium including both topography and three-dimensional velocity structure. The results from forward modeling of the wave field were then used to invert slowness data obtained with the three arrays. The procedure used by Almendros et al. (2001b) consists in a discretization of the source region using a uniformly spaced set of grid points in three dimensions, and computation of the free-surface responses produced by isotropic sources located at each grid node. Synthetic seismograms are calculated at three synthetic antennas that simulate the three arrays, and frequency-slowness analyses of the synthetic data yield estimates of ray parameters and azimuths for the three arrays for each point source. In this manner, a three-dimensional slowness vector model is generated at each array from the grid of source positions.

Using this forward model, Almendros et al. (2001b) obtained probabilistic estimates of the source locations of LP events and tremor. First, a probability was assigned to every point in the source domain by comparing the results from frequency-slowness analyses to the slowness vector model obtained for the domain. The statistical distributions of slownesses observed at each array for each individual event and tremor sample determine the shape of the probability functions. To each value in the slowness vector model corresponds, for each of the arrays, a given probability that can be mapped. The source location is obtained as the point corresponding to the maximum probability of the combined distributions for azimuths and ray parameters from the three arrays. As a final step, the source location probability distributions for individual events are stacked to obtain an overall spatial probability distribution for the ensemble of events analyzed (see Almendros et al., 2001a,b for details). The distributions of probabilities for the locations of the sources of LP events and tremor obtained by Almendros et al. (2001b) are shown in Fig. 42. The source regions of the two types of signals are

defined as the volumes contained within the surfaces corresponding to 5% of the maximum of the stacked source location probability. The choice of 5% is conservative enough to include all the located hypocenters and provides maximum constraints on the sizes of the source regions. The data illustrated in Fig. 42 represent 83% of the total activity recorded during the 23 h considered, hence these results provide a good representation of the overall behavior of the LP swarm. Fig. 42a–c illustrates the source region of LP events and Fig. 42d–e shows the source region of tremor. The dimensions of the source regions in the east–west, north–south, and depth directions are roughly $0.6 \times 1.0 \times 0.5$ km for LP events and $0.2 \times 0.5 \times 0.2$ km for tremor, with volumes of 0.09 and 0.01 km^3 , respectively. The locations, depths, and sizes of the source regions imaged in Fig. 42 point to a hydrothermal origin for all the analyzed LP seismicity (Almendros et al., 2001b).

Inza et al. (2011) adapted the MUSIC algorithm for use with three-component seismometer arrays. They used triaxial broadband data from two cross-shaped antennas deployed on the north and west flanks of Ubinas Volcano, Peru, to estimate the source locations of an explosion and LP event. Based on three-component array analyses, they estimated source depths of 1000 ± 660 m and 3000 ± 730 m below the summit crater for the explosion and LP event, respectively.

In the earthquake seismology field, the MUSIC algorithm is nowadays used to image the rupture of large global earthquakes (Meng et al., 2011, 2012).

6.5. Spatial auto-correlation method

The array correlation method, due to Aki (1957), is aimed at a characterization of shallow velocity structure from analyses of noise records obtained with a small array of seismometers. The method is

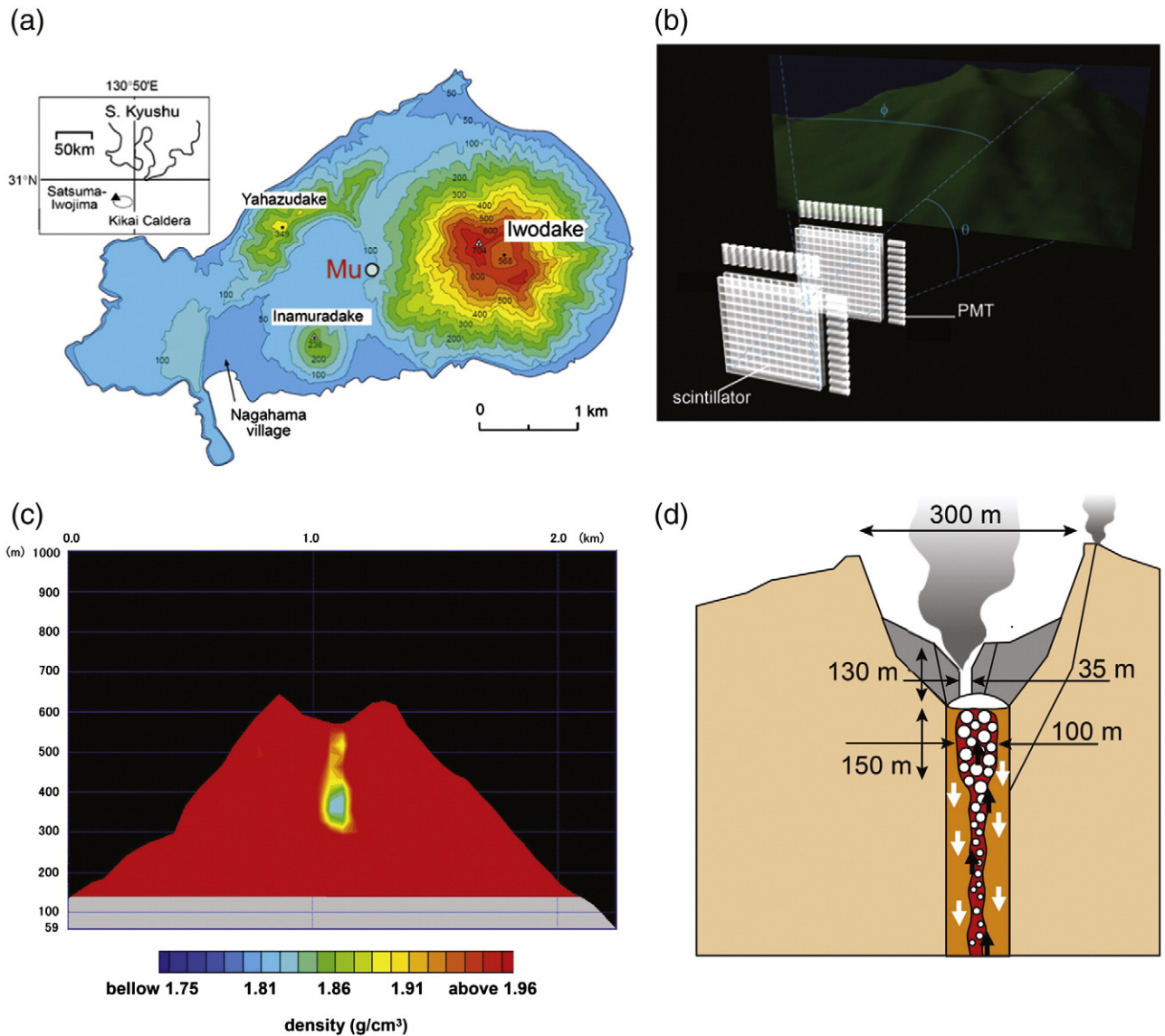


Fig. 41. Shallow density structure imaged by cosmic-ray muon radiography of Mount Iwo-dake at Satsuma-Iwojima Volcano. (a) Map of Satsuma-Iwojima showing the location of the Muon detector (Mu) below the west flank of Iwo-dake. The inset shows the position of Satsuma-Iwojima offshore of southern Kyushu. (b) Muon detector consisting of 48 modules arranged to make two segmented scintillation detector planes to track muon trails; each module includes a scintillator and power-effective photomultiplier tube (PMT). Muons are detected by the brief flash of light emitted as the particles pass through a scintillator; a straight line connecting the Muon intersect positions at two scintillator planes determines the Muon trail (Tanaka et al., 2009b). (c) Average density distribution at Iwo-dake, projected on a plane parallel to the detector plane; density anomalies that are less than 3.6% of the average density are not included in the map. Two low-density zones are imaged below the crater: (1) a 30–50-m wide zone in the uppermost 130 m below the crater floor (pictured in yellow), representing a porous high-temperature fumarolic area; and (2) a 100-m wide zone extending from 130 to 280 m below the crater floor (pictured in light blue), representing low-density degassed magma (Tanaka et al., 2009b). (d) Model of shallow conduit structure and magma convection under Iwo-dake (after Kazahaya et al., 2002).

Figure reproduced from Tanaka et al. (2009b).

specifically designed for use with a circular pattern of sensors. The basic assumption underlying the method is that the wave field is stochastic and stationary in time and space. Aki assumed from the start that the stochastic waves comprise only surface waves. Accordingly, this method is well-suited for the analysis of shallow sources of tremor or where surface waves dominate the scattered wave field. The method consists in filtering the records through a narrow-band filter centered at the frequency ω_0 , and calculations of the spatial correlation functions for individual receiver pairs in a circular array, where one receiver is located at the hub and the other receivers are distributed at fixed azimuthal increments along a circle centered on the hub station. Correlation coefficients are estimated for each azimuth by

using the hub as reference station, and these correlation coefficients are then averaged over azimuth. For vertical components of motion, the azimuthally averaged correlation coefficient, $\bar{\rho}_z(r, \omega_0)$, is obtained as (Aki, 1957)

$$\bar{\rho}_z(r, \omega_0) = J_0 \left[\frac{\omega_0}{c_R(\omega_0)} r \right], \quad (19)$$

where r is the distance between receivers, and $c_R(\omega_0)$ is the phase velocity of Rayleigh waves measured at the frequency ω_0 . This equation shows that the phase velocity $c_R(\omega_0)$ of the Rayleigh waves can be derived by matching the Bessel function J_0 to the azimuthal

average of the correlation coefficients calculated for a series of receivers set in a circular pattern around a central reference receiver. Repeating the procedure as a function of frequency ω yields the dispersion characteristics of $c_R(\omega)$.

A similar procedure is followed for polarized waves recorded on the horizontal components of motion. In this case, spatial correlation functions are defined for the radial and azimuthal horizontal components. The radial and azimuthal components are defined here as parallel and normal to the radii extending from the hub to each individual receiver on the periphery of the circular array. For single-mode vector waves with horizontal component polarized parallel to the direction of wave propagation (e.g., Rayleigh waves), the azimuthally averaged correlation coefficients for the radial and azimuthal components are obtained as (Aki, 1957)

$$\bar{\rho}_r^{\parallel}(r, \omega_0) = J_0\left[\frac{\omega_0}{c_R(\omega_0)} r\right] - J_2\left[\frac{\omega_0}{c_R(\omega_0)} r\right], \quad (20)$$

$$\bar{\rho}_{\phi}^{\parallel}(r, \omega_0) = J_0\left[\frac{\omega_0}{c_R(\omega_0)} r\right] + J_2\left[\frac{\omega_0}{c_R(\omega_0)} r\right], \quad (21)$$

whereas for single-mode vector waves with horizontal component polarized in the direction normal to that of wave propagation (e.g., Love waves), the corresponding averaged correlation coefficients are given by (Aki, 1957)

$$\bar{\rho}_r^{\perp}(r, \omega_0) = J_0\left[\frac{\omega_0}{c_L(\omega_0)} r\right] + J_2\left[\frac{\omega_0}{c_L(\omega_0)} r\right], \quad (22)$$

$$\bar{\rho}_{\phi}^{\perp}(r, \omega_0) = J_0\left[\frac{\omega_0}{c_L(\omega_0)} r\right] - J_2\left[\frac{\omega_0}{c_L(\omega_0)} r\right], \quad (23)$$

in which $C_L(\omega_0)$ is the phase velocity of Love waves, and J_2 is the Bessel function of second order. The type of polarization of the wave field is identified by matching these correlation coefficients to the data. When two or more modes coexist in the wave field, the resulting correlation functions are represented by the sum of the functions due to individual contributions under the assumption that these are statistically independent (Chouet, 1996b). The depth to which the structure can be resolved with Aki's method is roughly comparable to the aperture of the array used.

Aki's correlation method was used by Ferrazzini et al. (1991) to describe the characteristics of the complex wave field of volcanic tremor at the Puu Oo crater on Kilauea. They used a semi-circular array with aperture of 120 m composed of a three-component geophone set at the center of the semicircle, 11 three-component geophones placed on the semicircle, and 36 vertical-component geophones distributed on seven radial lines. The spacing of 10 m between vertical-component geophones represents a distance over which good coherence between pairs of signals was consistently observed. The array radius of 60 m was selected to allow the sampling of roughly a half wavelength of Love wave at a frequency of 5 Hz, based on earlier observations (Aki et al., 1978). This array was set up at a distance of 1 km from the crater of Puu Oo over a flat expanse of densely cracked ponded lava flow.

The results obtained at Puu Oo by Ferrazzini et al. (1991) clearly depict dispersive waves propagating across the array from the direction of Puu Oo. They found the wave field to be composed of comparable amounts of Rayleigh and Love waves propagating with similar and extremely slow phase velocities ranging from 700 m/s at 2 Hz to 300 m/s at 8 Hz. They ascribed these slow velocities to the highly cracked solidified lava flow on which the array was deployed and subjacent structure of alternating lava and ash layers formed during repeated eruptions of Puu Oo. Their best structural model matching the observed phase velocities of Rayleigh and Love waves consists of a 30-m-thick surficial layer with P-wave velocity of 650 m/s and S-wave velocity of 350 m/s, and a second layer with thickness of 75 m, P-wave velocity of 1250 m/s, and S-wave velocity of 720 m/s,

underlain by a half space with P- and S-wave velocities of 2500 and 1440 m/s, respectively.

Chouet et al. (1998) applied the correlation method to quantify the contributions of surface waves in the tremor wave field at Stromboli. They used two semi-circular arrays with radii of 60 and 150 m and a linear array with length of 600 m deployed at a distance of 1.7 km from the active crater. The results they obtained are very similar to those obtained at Puu Oo by Ferrazzini et al. (1991). The correlation coefficients derived as a function of frequency for the three components of motion clearly define the dispersion characteristics for both Rayleigh and Love waves. Love and Rayleigh waves contribute 70% and 30%, respectively of the surface wave power. The phase velocities of Rayleigh waves range from 1000 m/s at 2 Hz to 350 m/s at 9 Hz, and those for Love waves range from 800 to 400 m/s over the same frequency band. Assuming that the phase velocities determined experimentally represent the fundamental modes of Love and Rayleigh waves, Chouet et al. (1998) obtained a structural model consisting of four layers with a combined thickness of 203 m, underlain by a homogeneous half space. The shallowest layer in their model has a thickness of 8 m with P- and S-wave velocities of 410 m/s and 270 m/s, respectively. Below this layer are three layers with thicknesses of 35, 70, and 90 m with respective P-wave velocities of 800, 1420, and 2000 m/s, and respective S-wave velocities of 520, 810, and 1140 m/s. The underlying half space has P- and S-wave velocities of 3500 and 2000 m/s, respectively. Based on the similarities in velocities observed at Stromboli and Puu Oo, Chouet et al. (1998) inferred that a high density of cracks may also characterize the shallow lava flows underlaying the surficial soil layer beneath the flank of Stromboli. The 8-m-thick top layer in their model may correspond to the layer of topsoil.

In another application of Aki's correlation method to volcanic tremor, Métaixian et al. (1997) obtained structural models for Masaya Volcano using data from three semi-circular arrays. Tremor at Masaya is composed of comparable amounts of Rayleigh and Love waves with phase velocities ranging from 730 to 1240 m/s at 2 Hz to 330 to 550 m/s at 6 Hz. The dispersion curves obtained by (Métaixian et al., 1997) extend down to 1 Hz, and the structures they derived are resolved to a depth of about 800 m. The Rayleigh dispersion at Masaya is similar to those observed at Puu Oo and Stromboli, but the frequency dependence of Love waves is much stronger at Masaya. Apart from the depth range of 40 to 110 m over which the P-wave velocities are significantly higher at Masaya, the shallow Masaya structure bears strong resemblance to the structures derived for Puu Oo and Stromboli. Métaixian et al. (1997) interpreted their structural model in terms of a top layer of poorly consolidated pyroclastic materials, underlain by lava flows interbedded with pyroclastic materials derived from postcaldera activity, underlain by the older caldera structure.

Saccorotti et al. (2003) used the correlation method to analyze the properties of the surface wave field in and around Kilauea Caldera. They used three semi-circular arrays with apertures of 300, 300, and 400 m, and a linear array with length of 1680 m to determine the phase velocities of both Rayleigh and Love waves. Within the caldera, the phase velocities of Rayleigh waves were found to range from 1400–1800 m/s at 1 Hz, down to 300–400 m/s at 10 Hz, while the phase velocities of Love waves were found in the range from 2600 to 400 m/s within the same frequency band. Outside the caldera, Rayleigh wave velocities were found to span the range of 1600–1800 m/s at 1 Hz, down to 260–360 m/s at 10 Hz, and Love wave velocities were found to range from 600 to 150 m/s within the same band. Saccorotti et al. (2003) inverted the experimentally derived dispersion curves for velocity structure beneath each array, assuming that these dispersions represent the fundamental modes of Rayleigh and Love waves. The velocity structures they inferred at the different sites are consistent with results obtained by Dawson et al. (1999) from three-dimensional traveltome tomography of the caldera region, and point to a marked velocity discontinuity associated with the southern caldera boundary.

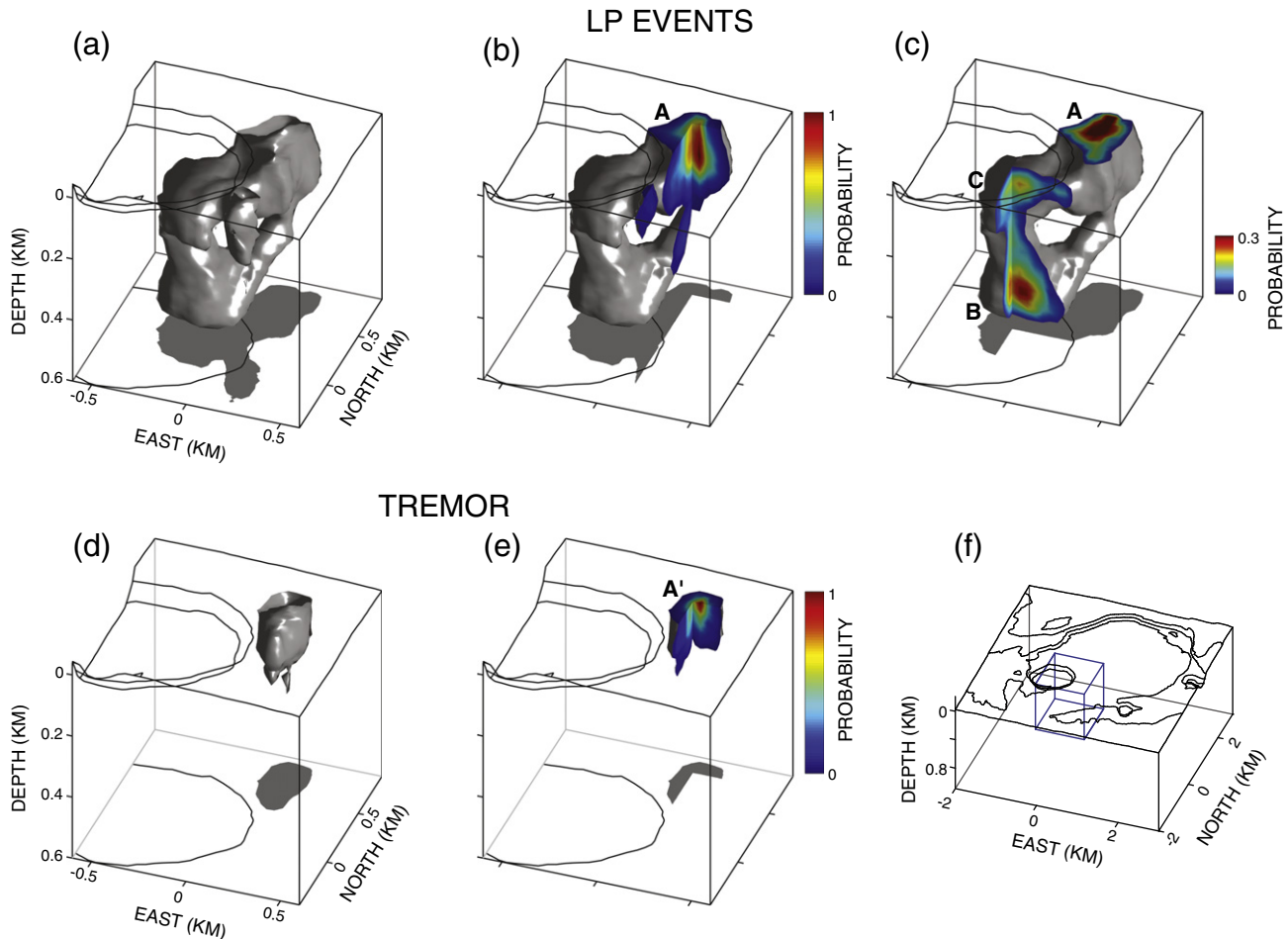


Fig. 42. Location and extent of the source region of long-period seismicity recorded at Kilauea Volcano in February 1997. (a) 3-D view of the source region of LP events. The horizontal projection of the source region and rim of the Halemaumau pit crater shown on the bottom of the cube provide additional information about the horizontal extent of this seismicity. (b) Cutaway view of the source region showing the most active source zone (A) located northeast of Halemaumau. (c) Secondary clusters of hypocenters (B, C) are also present at two depths below the crater; the maximum of the color scale is 0.3 in this panel, hence the probability is saturated in the main source region (A) illustrated in (b). (d) 3-D view of the source region of tremor. (e) Cutaway view of the source region of tremor showing that there are no subregions and that the maximum probability occurs in region A' coincident with the most active zone of LP event generation (Almendros et al., 2001b). (f) General view of the Kilauea Caldera region. The blue cube shows the boundaries of the region extracted in (a–e). Figure reproduced from Almendros et al. (2001b).

Haney et al. (2012b) developed an extension of Aki's spatial autocorrelation method for multicomponent recordings of surface waves. Their analysis includes the full 3×3 matrix of correlation coefficients that exists between all pairs of three-component motions. They demonstrated that the inclusion of vertical-radial and radial-vertical correlations offers additional ways to measure Rayleigh dispersion within the spatial autocorrelation framework. The values of phase velocity estimated from vertical-radial correlations naturally interpolate the estimates obtained from vertical-vertical correlations, thus providing a finer sampling of the dispersion characteristics of $c_R(\omega)$. Haney et al. (2012b) also demonstrated theoretically that the vertical-radial and radial-vertical correlations have advantageous properties compared to the vertical–vertical correlation in the presence of anisotropic ambient noise.

6.6. Automatic detection and classification of volcanic signals

Volcanic unrest is often accompanied by swarms of seismic events characterized by highly repetitive waveforms, indicating the repeated action of a nondestructive source process (Stephens and Chouet, 2001; Matsubara and Yomogida, 2004; Rowe et al., 2004; Green and Neuberg, 2006; Petersen, 2007; Moran et al., 2008a; Ottemoller, 2008; Waite et

al., 2008; Matoza et al., 2009b; Buurman and West, 2010; Matoza and Chouet, 2010; Thelen et al., 2010; D'Auria et al., 2011; De Barros et al., 2011). Recurring waveforms can be used for a high-resolution mapping of the source volume and to obtain information about the temporal properties of the source. A common approach to identifying and classifying event families relies on the use of waveform cross correlation to quantify the similarity of waveforms in an event catalog (Stephens and Chouet, 2001; Green and Neuberg, 2006). Event detection is based on locating peaks in the correlation function between a reference event and the time series of the swarm. A relatively short period is selected for data analysis, in which every single event is cross correlated with every other event in the time period considered. For n events in the time period, this forms an $n \times n$ matrix \mathbf{M} of maximum correlation coefficient (CC) values, where M_{ij} represents the maximum CC between events i and j . To sort the correlation matrix \mathbf{M} , a threshold CC value ψ is defined and the event with the largest number of repeat signatures correlated with it with $CC > \psi$ is identified (Green and Neuberg, 2006). All the events corresponding to this primary family of waveforms are then removed from \mathbf{M} and the procedure is repeated until all events are sorted into families. The choice of ψ is subjective, and affects both the number of defined event families and the number of unclassified events. Unclassified events are events that do not correlate with any other event with $CC > \psi$. Low

values of ψ result in a relatively coarse waveform classification, where only grossly dissimilar waveforms are grouped into distinct families. High values of ψ yield a finer classification, where waveforms with subtle differences are grouped into different waveform families.

Another approach to automatically identify repetitive events in a seismic record relies on the Hidden Markov Model (HMM) pattern recognition technique commonly applied in speech recognition systems (Granat and Donnellan, 2002; Benitez et al., 2007; Dawson et al., 2010, 2012). The HMM-based pattern recognition method provides a robust way to identify seismic events that do not correlate well to a master event and would require multiple families for their classification. This approach is particularly useful for recognizing volcanic and hydrothermal seismic events that have a common source process yet differ in temporal character due to the non-linear fluid dynamics involved in their generation and the presence of noise (Dawson et al., 2010). An HMM is a finite-state machine with several possible states, transition probabilities between states, and observation probability density functions associated with each state. The basic processing steps involved in an HMM-based pattern recognition system are training and decoding. In the training step, a portion of the seismic record is segmented into event types and the parameters describing each event type are determined using the well-known Baum–Welch algorithm (Rabiner and Juang, 1993). Using the HMM built in the training step, the continuous seismic signal is then analyzed using feature extraction and decoding based on the Viterbi algorithm (Rabiner and Juang, 1993). The decoding process is performed in real time and is run continuously over the seismic record without need of a previous segmentation or identification of the signal. The output is a sequence of recognized events with confidence measures and global accuracy scores.

Dawson et al. (2010) applied the HMM-based pattern recognition technique for the automatic identification of signals associated with degassing bursts at Kilauea. They considered two HMM models, one representing degassing bursts in the frequency band of 0.02–0.06 Hz, and the other representing noise in the same frequency band. They used three days of continuous data to train the recognition system by manually identifying bursts, possible bursts, and background noise. Events identified during the first two days were used to train the models with the Baum–Welch algorithm (Rabiner and Juang, 1993), and events for the third day were then decoded using the Viterbi algorithm (Rabiner and Juang, 1993) to verify the choice of parameters for the system. The time periods labeled as possible bursts were not used to train the system, but were classified as bursts or noise at the decoding step. After training, the recognition system identified 95% of the bursts and 98% of the noise segments for the manually selected events of the third day. Dawson et al. (2010) applied the decoding algorithm to a 2.5-year-long continuous record of VLP seismicity at Kilauea and were able to identify over 47,000 bursts, as well as document their temporal rate of occurrence.

Dawson et al. (2012) used the HMM technique to identify over five million high-frequency (> 15 Hz) events recorded at a temporary seismic station deployed in the Norris Geyser Basin in Yellowstone National Park in August–September 2003 in response to an unusual increase in hydrothermal activity. They observed a diurnal pattern in the rate of event occurrence, generally ranging between ~3500 and 5500 events/h. A diurnal pattern was also observed basin wide in air and hydrologic temperatures and outflow from the basin. Based on the close association of these patterns with solar thermal radiance, Dawson et al. (2012) interpreted this seismicity to be due to the collapse of small steam bubbles in the hydrothermal system, with rate of collapse being controlled by surface temperatures and daytime evaporation rates.

7. Future trends

Seismology alone cannot directly see into the conduit and resolve details of the actual fluid dynamics at the origin of the seismic source

mechanisms revealed by analyses of LP and VLP signals. To develop a better understanding of fluid behavior responsible for these signals, laboratory experiments are required to explore the links between known flow processes and the resulting pressure and momentum changes. The pressure and momentum changes generated under laboratory conditions may then be compared with the pressure and momentum changes estimated from the time-varying moment tensor and single force components imaged from seismic data, yielding clues about the physical flow processes linked to the seismic source mechanism.

Recent laboratory studies (Lane et al., 2001; James et al., 2004, 2006, 2008; Lane et al., 2008) have elucidated self-excitation mechanisms inherent to the fluid nonlinearity that are providing new insights into the mechanisms imaged from seismic data. For example, the results of experiments by James et al. (2006) with gas slugs ascending buoyantly in a liquid-filled tube featuring an upward widening in diameter, demonstrate that direct links between the moment tensor and single force seismic source mechanism are possible and could potentially provide a wealth of information not available from seismic data alone. The main physical process in these experiments (Fig. 4) is the deceleration of a volume of liquid falling under gravity as the slug clears the conduit flare. The downward forces and pressure surges generated by this process scale approximately to those measured at Stromboli (Chouet et al., 2003), suggesting that this is a potentially viable mechanism for the source of VLP signals observed at this volcano. James et al. (2008) also demonstrated that the rapid near-surface expansion of a decompressing gas slug induces a net upward force on the conduit due to the decrease in static pressure below the slug as more liquid becomes supported by the conduit wall (Fig. 5). The magnitude of the upward force scales roughly in proportion to the square of slug mass (James et al., 2009). When applied to Kilauea, this implies slug masses ranging between 10^4 and 10^6 kg for degassing bursts at this volcano (Chouet et al., 2010). The simulations by James et al. (2006) also indicate that the force does not necessarily couple into the conduit in the source region of fluid motion, but may do so at any upward-facing surface below the source. This points to the critical role played by conduit discontinuities in the generation of VLP and LP oscillations (Chouet et al., 2010; Chouet and Dawson, 2011).

The single forces evidenced in the modeling by James et al. (2006, 2008, 2009) may be operative in low-viscosity basaltic systems. As magma viscosity increases and rheology becomes more complex, the richness of oscillatory processes grows accordingly. In silicic systems, the formation of a rheologically stiffened plug due to the exsolution of water from the magma in the top few hundred meters of the conduit, may effectively seal the conduit (Sparks, 1997). This can inhibit further gas escape through the top of the conduit and favor escape through hydrofractures in the surrounding rock (Heiken et al., 1988; Stasiuk et al., 1996). Lane et al. (2008) used laboratory simulations to mimic the flow of high-viscosity fluids driven by an exsolving gas species. They observed the formation of a plug, leading to conduit pressurization below the plug, and demonstrated that instabilities may occur, in which the flow oscillates between Poiseuille flow and plug flow. The physical mechanisms driving the flow oscillation are diffusive pumping and margin decrepitation. The diffusive pumping, driven by gas diffusion into bubbles, pressurizes the system being sealed by the low-permeability plug. High strain rates at the flow margin then lead to the rupture of bubble walls at this boundary, resulting in margin decrepitation, which opens degassing pathways and initiates plug flow (Lane et al., 2008). This process may provide an explanation for tilt cycles observed at Soufrière Hills Volcano (Neuberg et al., 2006).

Together with these laboratory advances, numerical studies of multiphase flows are required to shed light on both the micro- and macrophysics of such flows (e.g., Badalassi et al., 2003), along with models exploring the coupled dynamics of fluid and solid (Nishimura and Chouet, 2003). Approaches include the phase-field method, also known as the diffuse-interface method (Anderson et al., 1998;

Lowengrub and Truskinovsky, 1998; Emmerich, 2003), the level set method (Kang et al., 2000; Osher and Fedkiw, 2003), and finite-volume method (James et al., 2008). The equations representing multiphase systems are analytically intractable and efforts have mainly been directed toward the development of robust, stable numerical schemes. Numerical implementations include the Lattice Boltzmann method (Rivet and Boon, 2001; Succi, 2001; Sukop and Thorne, 2006; O'Brien and Bean, 2008), and various finite-difference schemes based on an implicit-explicit discretization (Ascher et al., 1995), semi-implicit discretization (Badalassi et al., 2003; Yue et al., 2004), fully implicit discretization (Kim et al., 2004), or fully explicit central-differenced staggered-grid discretization (Jacqmin, 1999). Modeling volcanic fluid dynamics coupled with elastodynamics presents daunting challenges (D'Auria and Martini, 2009; Suckale et al., 2010a; Suckale et al., 2010b; James et al., 2011; Suckale et al., 2011), most of which have yet to be addressed.

The key to a better understanding of volcanic processes lies in a sustained effort aimed at cross-fertilization between increasingly realistic numerical and experimental models of the fluid dynamics and elastodynamics, spatially and temporally dense field measurements of diverse geophysical signals at all frequencies, and chemical and physical evidence recorded in the eruptive products. Among geophysical techniques, atmospheric infrasound (acoustic waves ~0.01–20 Hz) monitoring is emerging as a new and promising technique for capturing local and remote explosive volcanism, (e.g., Kamo et al., 1994; Vergniolle and Caplan-Auerbach, 2006; Johnson, 2007; Ripepe et al., 2007; Garcés et al., 2008; Fee et al., 2010a, 2010b; Cannata et al., 2011; Matoza et al., 2011a, 2011b), and for understanding the dynamics of shallow volcanic degassing and eruption columns (e.g., Johnson et al., 2008; Matoza et al., 2009b; Matoza et al., 2009a; Fee et al., 2010a; Matoza et al., 2010).

Volcano seismology and volcano acoustics are complementary methods for studying active volcanic processes. While volcano seismology is focussed on understanding volcanic processes occurring in the subsurface, volcano acoustics aims to understand shallow and subaerial volcanic processes, which radiate sound directly into the atmosphere. Although some coupling and wave conversion do occur (both ground-to-air and air-to-ground), these wave fields are mostly separated by the strong impedance contrast at the ground-air interface, and therefore contain separate information on volcanic processes. As with volcano seismology, volcano-acoustic signals are recorded from a full spectrum of volcanic processes ranging from persistent effusive degassing in shallow bubbly basaltic Hawaiian lava systems (Fee et al., 2010a; Matoza et al., 2010) to explosive Plinian eruption columns (Matoza et al., 2009a; Fee et al., 2010b). Across this spectrum, infrasound is generated, e.g., via Strombolian and Vulcanian explosions (Johnson, 2007; Ripepe et al., 2007; Marchetti et al., 2009); magmatic-hydrothermal interactions (Matoza et al., 2009b); shallow fluid oscillation and resonance (Garcés et al., 1998; Fee et al., 2010a; Matoza et al., 2010); rockfalls and dome collapses (Oshima and Maekawa, 2001; Green and Neuberg, 2005; Moran et al., 2008b); and pyroclastic flows (Yamasato, 1997; Ripepe et al., 2009). For more information, readers are referred to the recent reviews by Johnson and Ripepe (2011), Garcés et al. (in press), Zobin (2012), and Fee and Matoza (2013).

Infrasound is used to monitor the atmosphere for nuclear explosions, and rapid advances have recently been made in infrasound data acquisition, processing, and modeling techniques (Le Pichon et al., 2010). Broadband (flat response from ~0.01 to >20 Hz) and high-sensitivity (~0.1 mPa/count) infrasonic sensors are now commercially available, and can be digitized at the same sampling frequencies as seismometers. Infrasound sensors are often deployed in arrays to facilitate discrimination of signals of interest from other ambient infrasound sources, and a variety of techniques are employed to reduce wind noise, i.e., incoherent noise generated by wind flow (e.g., Walker and Hedlin, 2010).

Volcano-acoustic studies have an advantage over volcano-seismic studies, in that the source processes are often amenable to direct observation. Visual, infrared, or radar observations synchronized with acoustic instrumentation can therefore help to understand volcano-acoustic source processes (e.g., Gerst et al., 2008; Marchetti et al., 2009). For example, Moran et al. (2008b) used field geological observations and photographs to constrain the chronology and volcano-acoustic source model for an unusually large rockfall event at Mount St. Helens. A recent study by Fee et al. (2010a) highlights the potential for constraining near-surface degassing mechanisms by combining seismic, acoustic, and video datasets. The formation, evolution, collapse, and subsequent resurrection of a vent within Halemaumau Crater, Kilauea Volcano were captured on an infrasonic array between 2008 and 2009. Impulsive and energetic infrasonic signals accompanied degassing bursts (Chouet et al., 2010), while continuous oscillation of a cavity beneath Halemaumau vent produced near-continuous harmonic infrasonic tremor (Fee et al., 2010a). The infrasonic tremor contained a dominant spectral peak at ~0.55 Hz and a secondary peak at ~3 Hz. The dominant spectral peak is well explained by Helmholtz resonance of the cavity; this oscillation frequency is also clearly observed in “breathing” oscillations within gas emanating from the vent constrained by video data, and provides reasonable estimates of the cavity volume (Fee et al., 2010a). The secondary spectral peak and overtones were attributed by Fee et al. (2010a) to acoustic resonance.

Another study by Matoza et al. (2009a) provides an illustration of the potential for integrating seismic and acoustic datasets to understand shallow long-period seismicity. During the early stages of the 2004–2008 Mount St. Helens eruption, the sustained sequence of LP events (drumbeats) was intermittently accompanied by impulsive broadband infrasonic signals. During November 2005, USGS personnel working in the crater of Mount St. Helens reported hearing “booms” associated with the LPs, suggesting that at least some energy was also radiated in the audible acoustic frequency range (>20 Hz) (Matoza et al., 2007). To assess whether the signals could be generated simply by seismic-acoustic coupling from the shallow LP events, Matoza et al. (2009a) performed finite-difference simulations of the seismo-acoustic wave field, considering the effects of topography, near-surface seismic velocity structure, wind, and source configuration. Matoza et al. (2009a) conclude that the broadband infrasonic pulses were unlikely to be generated by simple seismo-acoustic coupling from a shallow-buried LP source. Instead they proposed a mechanism by which rapid venting of steam from a hydrothermal crack generates the acoustic signals and simultaneously triggers the collapse of the crack (the trigger mechanism of the LP event). The resulting resonance of the fluid remaining in the crack is well-coupled to the ground, leading to the seismic LP coda. However, these crack waves are not efficiently coupled to the air (the LP coda has a barely detectable amplitude in the infrasonic signals). The infrasonic signals are therefore interpreted as a record of the trigger mechanism initiating LP resonance. Denser seismo-acoustic deployments hold promise for providing more detailed observations and models of the seismo-acoustic phenomena accompanying magma movement and eruption.

8. Conclusions

Recent technological developments and improvements in the seismological instrumentation of volcanoes now allow the surface effects of subterranean volcanic processes to be imaged in unprecedented detail. Through careful analyses of the seismic wave fields radiated by volcanic activity, it has now become possible for volcano seismologists to make direct measurements of volcanic conduit responses to flow processes, thus opening the way for detailed modeling of such processes.

Unlike the description of seismic waves, which is based on the linear equations of elastodynamics, the description of the flow processes

underlying the observed seismic source mechanisms is governed by the nonlinear equations of fluid dynamics. In the classic Navier-Stokes equations of fluid mechanics, the nonlinearity resides in the convective acceleration terms in the equations of conservation of momentum. In volcanic fluids, further complexity arises from the strong nonlinear dependence of magma rheology on temperature, pressure, and water and crystal content, and nonlinear characteristics of the associated processes underlying the physico-chemical evolution of liquid–gas mixtures constituting magma. An example of nonlinearity in two-phase fluid mixtures is the changing boundary condition associated with the internal surfaces separating phases, a situation commonly encountered during the vesiculation, fragmentation, and collapse of bubble-rich suspensions to form separate melt and vapor in response to decreasing pressure along the ascent path of magma.

Bubble dynamics play a key role in the transport of magmatic and hydrothermal fluids, not only as sources of acoustic energy (Ichihara and Nishimura, 2009), but also in providing a sharp contrast in velocity between the fluid and encasing solid, which facilitates the entrainment of acoustic energy in the source region. This aspect of the source often manifests itself in the form of long-lasting, long-period oscillations produced by sustained resonance at the source.

Large gas slugs bursting at the liquid surface can act as active sources of acoustic and seismic radiation (Ripepe et al., 1996; Vergniolle et al., 1996; James et al., 2004; Chouet et al., 2010; Fee et al., 2010a). Gas slugs traversing discontinuities in conduit geometry can also cause transient liquid motions inducing pressure and momentum changes (James et al., 2006), which radiate elastic waves via their coupling to the conduit walls (Ohminato et al., 1998; Chouet et al., 2003; Chouet et al., 2008, 2010). In magmas, where a high fluid viscosity impedes flow, the diffusion of volatiles from a supersaturated melt may result in gradual pressurization of the melt and attendant deformation of the encasing rock matrix (Nishimura, 2004; Chouet et al., 2005, 2006; Shimomura et al., 2006). The fluid motions resulting from unsteady slug dynamics, large degassing bursts, and diffusion-dominated processes typically produce signals with characteristic periods longer than those commonly associated with acoustic resonance.

A diversity of behaviors also characterizes hydrothermal fluids. Heat transfer to the hydrothermal system from magmatic gases streaming through networks of fractures pervading the rock matrix may induce boiling in ground water, resulting in the formation of steam bubbles and attendant bubble oscillations and pressure fluctuations. The collapse of small vapor bubbles can be a source of pressure pulses and sustained tremor (Kieffer, 1977; Kedar et al., 1996; Ichihara and Nishimura, 2009; Cros et al., 2011; Dawson et al., 2012).

Refined understanding of magma and hydrothermal transport dynamics therefore requires multidisciplinary research involving detailed field measurements, laboratory experiments, and numerical modeling. The comprehensive breadth of seismology must be used to understand and interpret the wide variety of seismic signals encountered in various volcanic processes. This effort must then be complemented by laboratory simulations and numerical modeling to better understand the complex flow dynamics at the origin of the source mechanisms imaged from seismic data. Such research is fundamental to monitoring and interpreting the subsurface migration of magma that often leads to eruptions, and thus enhances our ability to forecast hazardous volcanic activity.

Recent studies also suggest that a range of novel seismic methods can shed light on dynamic processes occurring within active volcanoes and have potential as volcano monitoring tools. For example, ambient noise studies performed at Piton de la Fournaise Volcano have revealed small changes in seismic velocity ($\sim 0.1\%$) prior to eruptions, suggesting the utility of this technique for real-time monitoring of the state of a volcano (Brenguier et al., 2008a; Duputel et al., 2009). Changes in seismic anisotropy have also been observed in response to volcanic activity, indicating that anisotropy may be a robust indicator of stress changes associated with magma movement (Gerst and

Savage, 2004; Johnson et al., 2011). Systematic changes in the orientations of the pressure axis in fault plane solutions of VT earthquakes during eruptive episodes have been documented at several volcanoes (Roman and Cashman, 2006). For instance, the pressure axis of VT fault-plane solutions has been observed to be orthogonal to the dominant regional stress orientation in some cases, suggesting that these earthquakes were the result of dike inflation in the direction of minimum compressive stress (Roman and Cashman, 2006; Roman et al., 2006; Roman et al., 2008). Such temporal variations in source mechanisms of volcano tectonic earthquakes may provide yet another useful indicator of stress changes associated with magma intrusion.

Acknowledgments

We are grateful to Phil Dawson for his assistance in drafting figures. This manuscript has benefited from comments by Matt Haney, Hiroyuki Kumagai, and an anonymous reviewer. Robin Matoza gratefully acknowledges support from the Cecil H. and Ida M. Green Foundation at the Institute of Geophysics and Planetary Physics, Scripps Institution of Oceanography.

References

- Abbasi, T., Abbasi, S.A., 2007. The boiling liquid expanding vapour explosion (BLEVE): mechanism, consequence assessment, management. *Journal of Hazardous Materials* 141, 489–519.
- Acocella, V., Neri, M., Scarlato, P., 2006. Understanding shallow magma emplacement at volcanoes: orthogonal feeder dikes during the 2002–2003 Stromboli (Italy) eruption. *Geophysical Research Letters* 33, L17310. <http://dx.doi.org/10.1029/2006GL026862>.
- Akaike, H., 1974. A new look at the statistical model identification. *IEEE Transactions on Automatic Control* AC-9, 716–723.
- Akaike, H., 1980. Likelihood and the Bayes procedure. In: Bernardo, J.M., et al. (Ed.), *Bayesian Statistics*. Univ. Press, Valencia, Spain, pp. 143–166.
- Aki, K., 1957. Space and time spectra of stationary stochastic waves, with special reference to microtremors. *Bulletin of the Earthquake Research Institute*, Tokyo University 25, 415–457.
- Aki, K., Ferrazzini, V., 2000. Seismic monitoring and modeling of an active volcano for prediction. *Journal of Geophysical Research* 105 (B7), 16,617–16,640.
- Aki, K., Koyanagi, R., 1981. Deep volcanic tremor and magma ascent mechanism under Kilauea, Hawaii. *Journal of Geophysical Research* 86 (B8), 7095–7109.
- Aki, K., Lee, W.H.K., 1976. Determination of three-dimensional velocity anomalies under a seismic array using first *P* arrival times from local earthquakes 1. A homogeneous initial model, *it*. *Journal of Geophysical Research* 81, 4381–4399.
- Aki, K., Richards, P.G., 1980. *Quantitative Seismology*. W. H. Freeman, New York.
- Aki, K., Fehler, M., Das, S., 1977a. Source mechanism of volcanic tremor: fluid driven crack models and their application to the 1963 Kilauea eruption. *Journal of Volcanology and Geothermal Research* 2, 259–287.
- Aki, K., Christoffersson, A., Husebye, E.S., 1977b. Determination of the three-dimensional seismic structure of the lithosphere. *Journal of Geophysical Research* 82, 277–296.
- Aki, K., Chouet, B., Fehler, M., Zandt, G., Koyanagi, R., Colp, J., Hay, R.G., 1978. Seismic properties of a shallow magma reservoir in Kilauea Iki by active and passive experiments. *Journal of Geophysical Research* 83, 2273–2282.
- Alidibirov, M., Dingwell, D.B., 1996. Magma fragmentation by rapid decompression. *Nature* 380, 146–148.
- Almendros, J., Chouet, B., Dawson, P., 2001a. Spatial extent of a hydrothermal system at Kilauea Volcano, Hawaii, determined from array analyses of shallow long-period seismicity 1. Method. *Journal of Geophysical Research* 106, 13,565–13,580.
- Almendros, J., Chouet, B., Dawson, P., 2001b. Spatial extent of a hydrothermal system at Kilauea Volcano, Hawaii, determined from array analyses of shallow long-period seismicity 2. Results. *Journal of Geophysical Research* 106, 13,581–13,597.
- Almendros, J., Chouet, B., Dawson, P., Bond, T., 2002. Identifying elements of the plumbing system beneath Kilauea Volcano, Hawaii, from the source locations of very-long-period signals. *Geophysical Journal International* 148, 308–312.
- Alparone, S., Cannata, A., Gambino, S., Gresta, S., Milluzzo, V., Montalto, P., 2010. Time-space variation of volcano-seismic events at La Fossa (Vulcano, Aeolian Islands, Italy): new insights into seismic sources in a hydrothermal system. *Bulletin of Volcanology* 72, 803–816.
- Anderson, D.M., McFadden, G.B., Wheeler, A.A., 1998. Diffuse-interface methods in fluid mechanics. *Annual Review of Fluid Mechanics* 30, 139–165.
- Anderson, K., Lisowski, M., Segall, P., 2010. Cyclic ground tilt associated with the 2004–2008 eruption of Mount St. Helens. *Journal of Geophysical Research* 115, B11201. <http://dx.doi.org/10.1029/2009JB007102>.
- Arámbula-Mendoza, R., Váldez-González, C., Martínez-Bringas, A., 2010. Temporal and spatial variation of the stress state of Popocatépetl Volcano, Mexico. *Journal of Volcanology and Geothermal Research* 196, 156–168.
- Arámbula-Mendoza, R., Lesage, P., Valdés-González, C., Varley, N.R., Reyes-Davila, G., Navarro, C., 2011. Seismic activity that accompanied the effusive and explosive eruptions during the 2004–2005 period at Volcan de Colima, Mexico. *Journal of Volcanology and Geothermal Research* 205, 30–46.

- Arciniega-Ceballos, A., Chouet, B.A., Dawson, P., 1999. Very-long-period signals associated with Vulcanian explosions at Popocatepetl Volcano, Mexico. *Geophysical Research Letters* 26, 3013–3016.
- Arciniega-Ceballos, A., Chouet, B., Dawson, P., 2003. Long-period events and tremor at Popocatepetl Volcano (1994–2000) and their broadband characteristics. *Bulletin of Volcanology* 65, 124–135.
- Arciniega-Ceballos, A., Chouet, B., Dawson, P., Asch, G., 2008. Broadband seismic measurements of degassing activity associated with lava effusion at Popocatépetl Volcano, Mexico. *Journal of Volcanology and Geothermal Research* 170, 12–23.
- Arciniega-Ceballos, A., Dawson, P., Chouet, B.A., 2012. Long-period seismic source characterization at Popocatépetl Volcano, Mexico. *Geophysical Research Letters* 39, L20307. <http://dx.doi.org/10.1029/2012GL053494>.
- Ascher, U.M., Ruuth, S.J., Wetton, B.T.R., 1995. Implicit-explicit methods for time-dependent partial differential equations. *SIAM Journal on Numerical Analysis* 3, 797–823.
- Aspinall, W.P., Miller, A.D., Lynch, L.L., Latchman, J.L., Stewart, R.C., White, R.A., Power, J.A., 1998. Soufrière Hills eruption, Montserrat, 1995–1997: volcanic earthquake locations and fault plane solutions. *Geophysical Research Letters* 25 (18), 3397–3400.
- Aster, R., Mah, S., Kyle, P., McIntosh, W., Dunbar, N., Johnson, J., Ruiz, M., McNamara, S., 2003. Very long period oscillations of Mount Erebus Volcano. *Journal of Geophysical Research* 108 (B11). <http://dx.doi.org/10.1029/2002JB002101>.
- Aster, R., Zandomenighi, D., Mah, S., McNamara, S., Henderson, D., Knox, H., Jones, K., 2008. Moment tensor inversion of very long period seismic signals from Strombolian eruptions of Erebus Volcano. *Journal of Volcanology and Geothermal Research* 177, 635–647.
- Audoine, E., Savage, M.K., Gledhill, K., 2004. Anisotropic structure under a back arc spreading region, the Taupo Volcanic Zone, New Zealand. *Journal of Geophysical Research* 109, B11305. <http://dx.doi.org/10.1029/2003JB002932>.
- Auger, E., D'Auria, L., Martini, M., Chouet, B., Dawson, P., 2006. Real-time monitoring and massive inversion of source parameters of very long period seismic signals: an application to Stromboli Volcano, Italy. *Geophysical Research Letters* 33, L04301. <http://dx.doi.org/10.1029/2005GL024703>.
- Ayele, A., Keir, D., Ebinger, C., Wright, T.J., Stuart, G.W., Buck, W.R., Jacques, E., Ogubazghi, G., Sholan, J., 2009. September 2005 mega-dike emplacement in the Manda-Harraro nascent oceanic rift (Afar depression). *Geophysical Research Letters* 36, L20306. <http://dx.doi.org/10.1029/2009GL039605>.
- Badalassi, V.E., Ceniceros, H.D., Banerjee, S., 2003. Computation of multiphase systems with phase field models. *Journal of Computational Physics* 190, 371–397.
- Balmforth, N.J., Mandre, S., 2004. Dynamics of roll waves. *Journal of Fluid Mechanics* 514, 1–33.
- Balmforth, N.J., Craster, R.V., Rust, A.C., 2005. Instability in flow through elastic conduits and volcanic tremor. *Journal of Fluid Mechanics* 527, 353–377.
- Bame, D., Fehler, M., 1986. Observations of long period earthquakes accompanying hydraulic fracturing. *Geophysical Research Letters* 13, 149–152. <http://dx.doi.org/10.1029/GL013i002p00149>.
- Barker, S.E., Malone, S.D., 1991. Magmatic system geometry at Mount St. Helens modeled from the stress field associated with post-eruptive earthquakes. *Journal of Geophysical Research* 96, 11,883–11,894.
- Battaglia, J., Thurber, C.H., Got, J.-L., Rowe, C.A., White, R.A., 2004. Precise relocation of earthquakes following the 15 June 1991 eruption of Mount Pinatubo (Philippines). *Journal of Geophysical Research* 109, B07302. <http://dx.doi.org/10.1029/2003JB002959>.
- Battaglia, J., Métaxian, J.-P., Garaebiti, E., 2012. Earthquake–volcano interaction imaged by coda wave interferometry. *Geophysical Research Letters* 39, L11309. <http://dx.doi.org/10.1029/2012GL052003>.
- Bean, C., Lokmer, I., O'Brien, G., 2008. Influence of near-surface volcanic structure on long-period seismic signals and on moment tensor inversions: simulated examples from Mount Etna. *Journal of Geophysical Research* 113, B08308. <http://dx.doi.org/10.1029/2007JB005468>.
- Bedrosian, P.A., Unsworth, M.J., Johnston, M.J.S., 2007. Hydrothermal circulation at Mount St. Helens determined by self-potential measurements. *Journal of Volcanology and Geothermal Research* 160, 137–146.
- Bedrosian, P.A., Burgess, M., Hotovec, A., 2008. Groundwater hydrology within the crater of Mount St. Helens from geophysical constraints. *Eos, Transactions American Geophysical Union* 89 (53) (Fall Meet. Suppl., Abstract V43E-2191).
- Belachew, M., Ebinger, C., Coté, D., Keir, D., Rowland, J.W., Hammond, J.O.S., Ayele, A., 2011. Comparison of dike intrusions in an incipient seafloor-spreading segment of Afar, Ethiopia: seismicity perspectives. *Journal of Geophysical Research* 116, B06405. <http://dx.doi.org/10.1029/2010JB007908>.
- Benitez, C., Ramirez, J., Segura, J.C., Rubio, A., Ibañez, J.M., Almendros, J., García-Yeguas, A., Cortéz, G., 2007. Continuous HMM-based seismic event classification at Deception Island, Antarctica. *IEEE Transactions on Geoscience and Remote Sensing* 45 (1), 138–147.
- Benoit, J.P., McNutt, S.R., 1997. New constraints on source processes of volcanic tremor at Arenal Volcano, Costa Rica, using broadband seismic data. *Geophysical Research Letters* 24 (4), 449–452.
- Bensen, G.D., Ritzwoller, M.H., Barmin, M.P., Levshin, A.L., Lin, F., Moschetti, M.P., Shapiro, N.M., Yang, Y., 2007. Processing seismic ambient noise data to obtain reliable broad-band surface wave dispersion measurements. *Geophysical Journal International* 169, 1239–1260.
- Bensen, G.D., Ritzwoller, M.H., Shapiro, N.M., 2008. Broadband ambient noise surface wave tomography across the United States. *Journal of Geophysical Research* 113, B05306. <http://dx.doi.org/10.1029/2007JB005248>.
- Benz, H.M., Chouet, B.A., Dawson, P.B., Lahr, J.C., Page, R.A., Hole, J.A., 1996. Three-dimensional P and S wave velocity structure of Redoubt Volcano, Alaska. *Journal of Geophysical Research* 101 (B4), 8111–8128.
- Bergfeld, D., Evans, W.C., McGee, K.A., Spicer, K.R., 2008. Pre- and post-eruptive investigations of gas and water samples from Mount St. Helens, Washington, 2002 to 2005. In: Sherrod, D.R., Scott, W.E., Stauffer, P.H. (Eds.), *A Volcano Rekindled: The Renewed Eruption of Mount St. Helens, 2004–2006: U.S. Geological Survey Professional Paper*, 1750, pp. 523–542 (Chap. 25).
- Biot, M.A., 1952. Propagation of elastic waves in a cylindrical bore containing a fluid. *Journal of Applied Physics* 23, 997–1005.
- Branch, C.D., 1976. Development of porphyry copper and stratiform volcanogenic ore bodies during the life cycle of andesitic stratovolcanoes. In: Johnson, R.W. (Ed.), *Volcanism in Australasia*. Elsevier, Amsterdam, pp. 337–342.
- Brenguier, F., Shapiro, N.M., Campillo, M., Nercessian, A., Ferrazzini, V., 2007. 3-D surface wave tomography of the Piton de la Fournaise Volcano using seismic noise correlations. *Geophysical Research Letters* 34, L02305. <http://dx.doi.org/10.1029/2006GL028586>.
- Brenguier, F., Shapiro, N.M., Campillo, M., Ferrazzini, V., Duputel, Z., Coutant, O., Nercessian, A., 2008a. Towards forecasting volcanic eruptions using seismic noise. *Nature Geoscience* 1, 126–130.
- Brenguier, F., Campillo, M., Hadzioannou, C., Shapiro, N.M., Nadeau, R.M., Larose, E., 2008b. Postseismic relaxation along the San Andreas Fault at Parkfield from continuous seismological observations. *Science* 321, 1478–1481.
- Burman, H., West, M.E., 2010. Seismic precursors to volcanic explosions during the 2006 eruption of Augustine Volcano. In: Power, J.A., Coombs, M.L., Freymueller, J.T. (Eds.), *The 2006 Eruption of Augustine Volcano, Alaska: U. S. Geological Survey Prof. Pap.* 1769, pp. 41–57 (Ch. 2).
- Campillo, M., Paul, A., 2003. Long-range correlations in the diffuse seismic coda. *Science* 299, 547–549.
- Cannata, A., Sciotto, M., Spampinato, L., Spina, L., 2011. New insights into banded tremor from the 2008–2009 Mount Etna eruption. *Journal of Geophysical Research* 115, B12318. <http://dx.doi.org/10.1029/2009JB007120>.
- Cashman, K.V., Thornber, C.R., Pallister, J.S., 2008. From dome to dust: Shallow crystallization and fragmentation of conduit magma during the 2004–2006 dome extrusion at Mount St. Helens, Washington. In: Sherrod, D.R., Scott, W.E., Stauffer, P.H. (Eds.), *A Volcano Rekindled: The Renewed Eruption of Mount St. Helens, 2004–2006: U.S. Geological Survey Professional Paper* 1750, pp. 387–413 (Chap. 19).
- Chadwick Jr., W.W., Embley, R.W., 1998. Graben formation associated with recent dike intrusions and volcanic eruptions at the mid-ocean ridge. *Journal of Geophysical Research* 103, 9807–9825.
- Chávez-García, F.J., Luizón, F., 2005. On the correlation of seismic microtremors. *Journal of Geophysical Research* 110, B11313. <http://dx.doi.org/10.1029/2005JB003671>.
- Chouet, B., 1979. Sources of seismic events in the cooling lava lake of Kilauea Iki, Hawaii. *Journal of Geophysical Research* 84, 2315–2330.
- Chouet, B., 1981. Ground motion in the near field of a fluid-driven crack and its interpretation in the study of shallow volcanic tremor. *Journal of Geophysical Research* 86 (B7), 5985–6016.
- Chouet, B., 1985. Excitation of a buried magmatic pipe: a seismic source model for volcanic tremor. *Journal of Geophysical Research* 90, 1881–1893.
- Chouet, B., 1986. Dynamics of a fluid-driven crack in three dimensions by the finite difference method. *Journal of Geophysical Research* 91, 13,967–13,992.
- Chouet, B., 1988. Resonance of a fluid-driven crack: radiation properties and implications for the source of long-period events and harmonic tremor. *Journal of Geophysical Research* 93, 4375–4400.
- Chouet, B., 1992. A seismic model for the source of long-period events and harmonic tremor. In: Gasparini, P., Scarpa, R., Aki, K. (Eds.), *Volcanic Seismology*. Springer-Verlag, Berlin, pp. 133–156.
- Chouet, B., 1996a. Long-period volcano seismicity: its source and use in eruption forecasting. *Nature* 380, 309–316.
- Chouet, B., 1996b. New methods and future trends in seismological volcano monitoring. In: Scarpa, R., Tilling, R.I. (Eds.), *Monitoring and Mitigation of Volcano Hazards*. Springer-Verlag, New York, pp. 23–97.
- Chouet, B., 2003. Volcano seismology. *Pure and Applied Geophysics* 160, 739–788.
- Chouet, B., 2009. Non-linear processes in volcanoes, in: Meyers, R. A. (Editor-in-Chief), *Encyclopedia of Complexity and Systems Science*. Springer-Verlag, New York, pp. 9872–9899.
- Chouet, B., Dawson, P., 2011. Shallow conduit system at Kilauea Volcano, Hawaii, revealed by seismic signals associated with degassing bursts. *Journal of Geophysical Research* 116, B12317. <http://dx.doi.org/10.1029/2011JB008677>.
- Chouet, B., Julian, B.R., 1985. Dynamics of an expanding fluid-filled crack. *Journal of Geophysical Research* 90, 11187–11198.
- Chouet, B., Shaw, H.R., 1991. Fractal properties of tremor and gas piston events observed at Kilauea Volcano, Hawaii. *Journal of Geophysical Research* 96 (B6), 10,177–10,189.
- Chouet, B.A., Page, R.A., Stephens, C.D., Lahr, J.C., Power, J.A., 1994. Precursory swarms of long-period events at Redoubt Volcano (1989–1990), Alaska: their origin and use as a forecasting tool. *Journal of Volcanology and Geothermal Research* 62, 95–135.
- Chouet, B., Saccorotti, G., Martini, M., Dawson, P., De Luca, G., Milana, G., Scarpa, R., 1997. Source and path effects in the wave fields of tremor and explosions at Stromboli Volcano, Italy. *Journal of Geophysical Research* 102 (B7), 15,129–15,150.
- Chouet, B., De Luca, G., Milana, G., Dawson, P., Martini, M., Scarpa, R., 1998. Shallow velocity structure of Stromboli Volcano, Italy, derived from small-aperture array measurements of Strombolian tremor. *Bulletin of the Seismological Society of America* 88 (3), 653–666.
- Chouet, B., Saccorotti, G., Dawson, P., Martini, M., Scarpa, R., De Luca, G., Milana, G., Cattaneo, M., 1999. Broadband measurements of the sources of explosions at Stromboli Volcano, Italy. *Geophysical Research Letters* 26, 1937–1940.
- Chouet, B., Dawson, P., Ohminato, T., Martini, M., Saccorotti, G., Giudicepietro, F., De Luca, G., Milana, G., Scarpa, R., 2003. Source mechanisms of explosions at Stromboli Volcano, Italy, determined from moment-tensor inversions of very-long-period data. *Journal of Geophysical Research* 108 (B1), 2019. <http://dx.doi.org/10.1029/2002JB001919>.
- Chouet, B., Dawson, P., Arciniega-Ceballos, A., 2005. Source mechanism of Vulcanian degassing at Popocatepetl Volcano, Mexico, determined from waveform inversions

- of very long period signals. *Journal of Geophysical Research* 110, B07301. <http://dx.doi.org/10.1029/2004JB003524>.
- Chouet, B., Dawson, P., Nakano, M., 2006. Dynamics of diffusive bubble growth and pressure recovery in a bubbly rhyolitic melt embedded in an elastic solid. *Journal of Geophysical Research* 111, B07310. <http://dx.doi.org/10.1029/2005JB004174>.
- Chouet, B., Dawson, P., Martini, M., 2008. Shallow-conduit dynamics at Stromboli Volcano, Italy, imaged from waveform inversions. In: Lane, S.J., Gilbert, J.S. (Eds.), *Fluid Motions in Volcanic Conduits: A Source of Seismic and Acoustic Signals*: Geol. Soc., London, Special Publications, 307, pp. 57–84.
- Chouet, B.A., Dawson, P.B., James, M.R., Lane, S.J., 2010. Seismic source mechanism of degassing bursts at Kilauea Volcano, Hawaii: results from waveform inversion in the 10–50 s band. *Journal of Geophysical Research* 115, B09311. <http://dx.doi.org/10.1029/2009JB006661>.
- Cocina, O., Neri, G., Privitera, E., Spampinato, S., 1996. Earthquake and stress tensor space-time distribution at Mount Etna before the 1991–1993 volcanic eruption. *Acta Vulcanologica* 8, 15–22.
- Collier, L., Neuberg, J., 2006. Incorporating seismic observations into 2D conduit flow modeling. *Journal of Volcanology and Geothermal Research* 152, 331–346.
- Collier, J.G., Thome, J.R., 1996. Convective Boiling and Condensation, third ed. Oxford Engineering Science Series.
- Collier, L., Neuberg, J.W., Lensky, N., Lyakhovsky, V., Navon, O., 2006. Attenuation in gas-charged magma. *Journal of Volcanology and Geothermal Research* 153, 21–36.
- Commander, K.W., Prosperetti, A., 1989. Linear pressure waves in bubbly liquids: comparison between theory and experiments. *Journal of the Acoustical Society of America* 85, 732–746.
- Coté, D.M., Belachew, M., Quillen, A.C., Ebinger, C.J., Keir, D., Ayele, A., Wright, T., 2010. Low-frequency hybrid earthquakes near a magma chamber in Afar: quantifying path effects. *Bulletin of the Seismological Society of America* 100 (5A), 1892–1903.
- Cros, E., Roux, P., Vandemeulebrouck, J., Kedar, S., 2011. Locating hydrothermal acoustic sources at Old Faithful Geyser using Matched Field Processing. *Geophysical Journal International* 187, 385–393. <http://dx.doi.org/10.1111/j.1365-246X.2011.05147.x>.
- Curtis, A., Gerstoft, P., Sato, H., Snieder, R., Wapenaar, K., 2006. Seismic interferometry – turning noise into signal. *The Leading Edge* 25 (9), 1082–1092.
- D'Auria, L., Martini, M., 2009. Slug flow: modeling in a conduit and associated elastic radiation, in: Meyers, R.A. (Editor-in-Chief), *Encyclopedia of Complexity and System Science* Volume 10, Springer, New York, pp. 8153–8168.
- D'Auria, L., Giudicepietro, F., Aquino, I., Borriello, G., Del Gaudio, C., Lo Bascio, D., Martini, M., Ricciardi, G.P., Ricciolino, P., Ricco, C., 2011. Repeated fluid-transfer episodes as a mechanism for the recent dynamics of Campi Flegrei caldera (1989–2010). *Journal of Geophysical Research* 116, B04313. <http://dx.doi.org/10.1029/2010JB007837>.
- Davi, R., O'Brien, G.S., Lokmer, I., Bean, C.J., Lesage, P., Mora, M.M., 2010. Moment tensor inversion of explosive long period events recorded on Arenal volcano, Costa Rica, constrained by synthetic tests. *Journal of Volcanology and Geothermal Research* 194, 189–200.
- Davi, R., O'Brien, G.S., De Barros, L., Lokmer, I., Bean, C.J., Lesage, P., Mora, M.M., Soto, G.J., 2012. Seismic source mechanisms of tremor recorded on Arenal volcano, Costa Rica, retrieved by waveform inversion. *Journal of Volcanology and Geothermal Research* 213–214, 1–13.
- Dawson, P.B., Dietel, C., Chouet, B.A., Honma, K., Ohminato, T., Okubo, P., 1998. A digitally telemetered broadband seismic network at Kilauea Volcano, Hawaii. U.S. Geol. Surv. Open-File Rep., 98–108, pp. 1–121.
- Dawson, P.B., Chouet, B.A., Okubo, P.G., Villaseñor, A., Benz, H.M., 1999. Three-dimensional velocity structure of the Kilauea Caldera, Hawaii. *Geophysical Research Letters* 26, 2805–2808.
- Dawson, P., Whilldin, D., Chouet, B., 2004. Application of near real-time radial semblance to locate the shallow magmatic conduit at Kilauea Volcano, Hawaii. *Geophysical Research Letters* 31, L21606. <http://dx.doi.org/10.1029/2004GL021163>.
- Dawson, P.B., Benitez, M.C., Chouet, B.A., Wilson, D., Okubo, P.G., 2010. Monitoring very-long-period seismicity at Kilauea Volcano, Hawaii. *Geophysical Research Letters* 37, L18306. <http://dx.doi.org/10.1020/2010GL044418>.
- Dawson, P.B., Chouet, B.A., Power, J., 2011. Determining the seismic source mechanism and location for an explosive eruption with limited observational data: Augustine Volcano, Alaska. *Geophysical Research Letters* 38, L03302. <http://dx.doi.org/10.1029/2010GL045977>.
- Dawson, P.B., Benitez, M.C., Lowenstern, J.B., Chouet, B.A., 2012. Identifying bubble collapse in a hydrothermal system using hidden Markov models. *Geophysical Research Letters* 39, L01304. <http://dx.doi.org/10.1029/2011GL049901>.
- De Angelis, S., Henton, S.M., 2011. On the feasibility of magma fracture within volcanic conduits: constraints from earthquake data and empirical modeling of magma viscosity. *Geophysical Research Letters* 38, L19310. <http://dx.doi.org/10.1029/2011GL049297>.
- De Barros, L., Bean, C.J., Lockmer, I., Saccorotti, G., Zuccarello, L., O'Brien, G.S., Métaxian, J.-P., Patanè, D., 2009. Source geometry from exceptionally high resolution long period event observations at Mt Etna during the 2008 eruption. *Geophysical Research Letters* 36, L24305. <http://dx.doi.org/10.1029/2009GL041273>.
- De Barros, L., Lockmer, I., Bean, C.J., O'Brien, G.S., Saccorotti, G., Métaxian, J.-P., Zuccarello, L., Patanè, D., 2011. Source mechanism of long-period events recorded by a high-density seismic network during the 2008 eruption on Mount Etna. *Journal of Geophysical Research* 116, B01304. <http://dx.doi.org/10.1029/2010JB007629>.
- De Lauro, E., De Martino, S., Palo, M., Ibanez, J.M., 2012. Self-sustained oscillations at Volcan de Colima (Mexico) inferred by Independent Component Analysis. *Bulletin of Volcanology* 74, 279–292.
- De Benedictis, P.G., 1996. Metastable Liquids: Concepts and Principles. Princeton University Press.
- Dingwell, D.B., 1996. Volcanic dilemma: flow or blow? *Science* 273, 1054–1055.
- Dingwell, D.B., Webb, S.L., 1989. Structural relaxation in silicate melts and non-Newtonian melt rheology in geologic processes. *Physics and Chemistry of Minerals* 16, 508–516.
- Dunham, E.M., Ogden, D.E., 2012. Guided waves along fluid-filled cracks in elastic solids and instability at high flow rates. *Journal of Applied Mechanics* 79 (3), 031020. <http://dx.doi.org/10.1115/14005961>.
- Duputel, Z., Ferrazzini, V., Brenguier, F., Shapiro, N., Campillo, M., Nercessian, A., 2009. Real time monitoring of relative velocity changes using ambient seismic noise at the Piton de la Fournaise Volcano (La Réunion) from January 2006 to June 2007. *Journal of Volcanology and Geothermal Research* 184, 164–173.
- Durisic, D., Vallance, J., Gerlach, T., Moran, S., Malone, S., 2005. Mount St. Helens reawakens. *Eos* 86 (3), 25–29.
- Eaton, J.P., Murata, K.J., 1960. How volcanoes grow. *Science* 132, 925–938.
- Eberhart-Phillips, D., 1986. Three-dimensional velocity structure in northern California Coast Ranges from inversion of local earthquake arrival times. *Bulletin of the Seismological Society of America* 76, 1025–1052.
- Ebinger, C.J., Keir, D., Ayele, A., Calais, E., Wright, T.J., Belachew, M., Hammond, J.O.S., Campbell, E., Buck, W.R., 2008. Capturing magma intrusion and faulting processes during continental rupture: seismicity of the Dabbahu (Afar) rift. *Geophysical Journal International* 174, 1138–1152.
- Ekström, G., Nettles, M., Abers, G.A., 2003. Glacial earthquakes. *Science* 302, 622–624.
- Emmerich, H., 2003. The Diffuse Interface Approach in Materials Science – Thermodynamic Concepts and Applications of Phase-field Models. Springer, New York. (178 pp.).
- Falsaperla, S.E., Privitera, B., Chouet, Dawson, P., 2002. Analysis of long-period events recorded at Mount Etna (Italy) in 1992, and their relationship to eruptive activity. *Journal of Volcanology and Geothermal Research* 114, 419–440.
- Fan, Y., Snieder, R., 2009. Required source distribution for interferometry of waves and diffuse fields. *Geophysical Journal International* 179, 1232–1244.
- Favas, E.P., Mitropoulos, A.C., 2008. What is spinodal decomposition? *Journal of Engineering Science and Technology Review* 1, 25–27.
- Fee, D., Mattoza, R.S., 2013. An overview of volcano infrasound: from Hawaiian to Plinian, local to global. *Journal of Volcanology and Geothermal Research* 249, 123–139. <http://dx.doi.org/10.1016/j.jvolgeores.2012.09.002>.
- Fee, D., Garcés, M., Patrick, M., Chouet, B., Dawson, P., Swanson, D., 2010a. Infrasonic harmonic tremor and degassing bursts from Halema'uma'u Crater, Kilauea Volcano, Hawaii. *Journal of Geophysical Research* 115, B11316. <http://dx.doi.org/10.1029/2010JB007642>.
- Fee, D., Garcés, M., Steffke, A., 2010b. Infrasound from Tungurahua Volcano 2006–2008: Strombolian and Plinian eruptive activity. *Journal of Volcanology and Geothermal Research* 193, 67–81.
- Fehler, M., 1983. Observations of volcanic tremor at Mount St. Helens volcano. *Journal of Geophysical Research* 88, 3476–3484.
- Fehler, M., Chouet, B., 1982. Operation of a digital seismic network on Mount St. Helens volcano and observations of long period seismic events that originate under the volcano. *Geophysical Research Letters* 9, 1017–1020.
- Ferrazzini, V., Aki, K., 1987. Slow waves trapped in a fluid-filled infinite crack: implication for volcanic tremor. *Journal of Geophysical Research* 92 (B9), 9215–9223.
- Ferrazzini, V., Aki, K., Chouet, B., 1991. Characteristics of seismic waves composing Hawaiian volcanic tremor and gas-piston events observed by a near-source array. *Journal of Geophysical Research* 96 (B4), 6199–6209.
- Ferrick, M.G., Qamar, A., St. Lawrence, W.F., 1982. Source mechanism of volcanic tremor. *Journal of Geophysical Research* 87, 8675–8683.
- Fisher, M.A., Ruppert, N.A., White, R.A., Sliter, R.W., Young, F.L., 2010. Distal volcano-tectonic seismicity near Augustine Volcano. In: Power, J.A., Coombs, M.L., Freymueller, J.T. (Eds.), *The 2006 Eruption of Augustine Volcano, Alaska: U.S. Geological Survey Prof. Pap.* 1769, pp. 119–128 (Ch. 6).
- Foulger, G.R., Julian, B.R., Hill, D.P., Pitt, A.M., Malin, P.E., Shalev, E., 2004. Non-double-couple microearthquakes at Long Valley caldera, California, provide evidence for hydraulic fracturing. *California Journal of Volcanology and Geothermal Research* 132, 45–71.
- Fournier, R.O., 1999. Hydrothermal processes related to movement of fluid from plastic into brittle rock in the magmatic-epithermal environment. *Economic Geology* and the Bulletin of the Society of Economic Geologists 94, 1193–1211. <http://dx.doi.org/10.2113/sgcongeo.94.8.1193>.
- Friedrich, A., Kruger, F., Klinge, K., 1998. Ocean-generated microseismic noise located with the Grafenberg array. *Journal of Seismology* 2, 47–64.
- Fujita, E., Ida, Y., Oikawa, J., 1995. Eigen oscillation of a fluid sphere and source mechanism of harmonic volcanic tremor. *Journal of Volcanology and Geothermal Research* 69, 365–378.
- Fujita, E., Ukawa, M., Yamamoto, E., 2004. Subsurface cyclic magma sill expansions in the 2000 Miyakejima Volcano eruption: possibility of two-phase flow oscillation. *Journal of Geophysical Research* 109, B04205. <http://dx.doi.org/10.1029/2003JB002556>.
- Garcés, M.A., Hagerty, M.T., Schwartz, S.Y., 1998. Magma acoustics and time-varying melt properties at Arenal Volcano, Costa Rica. *Geophysical Research Letters* 25, 2293–2296.
- Garcés, M., Fee, D., McCormack, D., Servranckx, R., Bass, H., Hetzer, C., Hedlin, M., Mattoza, R., Yip, H., 2008. Prototype ASHE volcano monitoring system captures the acoustic fingerprint of stratospheric ash injection. *Eos, Transactions American Geophysical Union* 89 (40), 377–379.
- Garcés, M.A., Fee, D., Mattoza, R.S., in press. Volcano acoustics, in: Fagents, S.A., Gregg, T.K.P., Lopes, R.M.C. (Eds.), *Modeling Volcanic Processes: The Physics and Mathematics of Volcanism*. Cambridge University Press, Chap. 16.
- Gerst, A., Savage, M.K., 2004. Seismic anisotropy beneath Ruapehu Volcano: a possible eruption forecasting tool. *Science* 306, 1543–1547.
- Gerst, A., Hoft, M., Kyle, P.R., Voge, M., 2008. 4D velocity of Strombolian eruptions and man-made explosions derived from multiple Doppler radar instruments. *Journal of Volcanology and Geothermal Research* 177, 648–660.

- Gerstoft, P., Sabra, K.G., Roux, P., Kuperman, W.A., Fehler, M.C., 2006. Green's functions extraction and surface-wave tomography from microseisms in southern California. *Geophysics* 71 (4), S123–S131.
- Gil Cruz, F., 1999. Observations of two special kinds of tremor at Galeras volcano, Colombia (1989–1991). *Annali di Geofisica* 42 (3), 437–449.
- Gil Cruz, F., Chouet, B.A., 1997. Long-period events, the most characteristic seismicity accompanying the emplacement and extrusion of a lava dome in Galeras Volcano, Colombia, in 1991. *Journal of Volcanology and Geothermal Research* 77, 121–158.
- Goldstein, P., Archuleta, R.J., 1987. Array analysis of seismic signals. *Geophysical Research Letters* 14, 13–16.
- Goldstein, P., Archuleta, R.J., 1991. Deterministic frequency-wavenumber methods and direct measurements of rupture propagation during earthquakes using a dense array: theory and methods. *Journal of Geophysical Research* 96, 6173–6185.
- Goldstein, P., Chouet, B., 1994. Array measurements and modeling of sources of shallow volcanic tremor at Kilauea Volcano, Hawaii. *Journal of Geophysical Research* 99 (B2), 2637–2652.
- Gonnermann, H.M., Manga, M., 2003. Explosive volcanism may not be an inevitable consequence of magma fragmentation. *Nature* 39, 321–356.
- Gonnermann, H.M., Manga, M., 2005. Flow banding in obsidian: a record of evolving textural heterogeneity during magma deformation. *Earth and Planetary Science Letters* 236, 135–147.
- Gonnermann, H.M., Manga, M., 2007. The fluid mechanics inside a volcano. *Annual Review of Fluid Mechanics* 39, 321–356.
- Goto, A., 1999. A new model for volcanic earthquake at Unzen Volcano: melt rupture. *Geophysical Research Letters* 26 (16), 2541–2544.
- Graizer, V., 2006. Tilts in strong ground motion. *Bulletin of the Seismological Society of America* 96, 2090–2102.
- Granat, R., Donnellan, A., 2002. A hidden Markov model based tool for geophysical data exploration. *Pure and Applied Geophysics* 159 (10), 2271–2283. <http://dx.doi.org/10.1007/s00024-002-8735-6>.
- Green, D.N., Neuberg, J., 2005. Seismic and infrasonic signals associated with an unusual collapse event at the Soufrière Hills volcano, Montserrat. *Geophysical Research Letters* 32, L07308. <http://dx.doi.org/10.1029/2004GL022265>.
- Green, D.N., Neuberg, J., 2006. Waveform classification of volcanic low-frequency earthquake swarms and its implication at Soufrière Hills Volcano, Montserrat. *Journal of Volcanology and Geothermal Research* 153, 51–63.
- Green, D.N., Neuberg, J., Cayol, V., 2006. Shear stress along the conduit wall as a plausible source of tilt at Soufrière Hills Volcano, Montserrat. *Geophysical Research Letters* 33, L10306. <http://dx.doi.org/10.1029/2006GL025890>.
- Grêt, A., Snieder, R., Scales, J., 2006. Time-lapse monitoring of rock properties with coda wave interferometry. *Journal of Geophysical Research* 111, B03305. <http://dx.doi.org/10.1029/2004JB003354>.
- Gudmundsson, A., 2002. Emplacement and arrest of sheets and dikes in central volcanoes. *Journal of Volcanology and Geothermal Research* 116, 279–298.
- Hagerty, M., Schwartz, S.Y., Protti, M., Garces, M., Dixon, T., 1997. Observations at Costa Rican volcano offer clues to causes of eruptions. *Eos, Transactions American Geophysical Union* 78 (49), 565, 570–571.
- Hagerty, M.T., Schwartz, S.Y., Garces, M.A., Protti, M., 2000. Analysis of seismic and acoustic observations at Arenal Volcano, Costa Rica, 1995–1997. *Journal of Volcanology and Geothermal Research* 101, 27–65.
- Hale, A.J., 2007. Magma flow instabilities in a volcanic conduit: implications for long-period seismicity. *Physics of the Earth and Planetary Interiors* 163, 163–178.
- Hamada, N., Jingu, H., Ikumoto, K., 1976. On the volcanic earthquake with slowly decaying coda wave (in Japanese with English abstract). *Bulletin of the Volcanological Society of Japan* 21, 167–183.
- Hammer, C., Neuberg, J.W., 2009. On the dynamical behaviour of low-frequency earthquake swarms prior to dome collapse at Soufrière Hill volcano, Montserrat. *Geophysical Research Letters* 36, L06305. <http://dx.doi.org/10.1029/2008GL036837>.
- Haney, M.M., 2010. Location and mechanism of very long period tremor during the 2008 eruption of Okmok Volcano from interstation arrival times. *Journal of Geophysical Research* 115, B00B05. <http://dx.doi.org/10.1029/2010JB007440>.
- Haney, M.M., van Wijk, K., Preston, L.A., Aldridge, D.F., 2009. Observation and modeling of source effects in coda wave interferometry at Pavlov Volcano. *The Leading Edge* 28 (5), 554–560.
- Haney, M.M., Chouet, B.A., Dawson, P.B., Power, J.A., 2012a. Source characterization for an explosion during the 2009 eruption of Redoubt Volcano from very-long-period seismic waves. *Journal of Volcanology and Geothermal Research*. <http://dx.doi.org/10.1016/j.jvolgeores.2012.04.018>.
- Haney, M.M., Mikesell, T.D., van Wijk, K., Nakahara, H., 2012b. Extension of the spatial autocorrelation (SPAC) method to mixed-component correlations of surface waves. *Geophysical Journal International* 191 (1), 189–206. <http://dx.doi.org/10.1111/j.1365-246X.2012.05597.x>.
- Hansen, S., Thurber, C., Mandernach, M., Haslinger, F., Doran, C., 2004. Seismic velocity and attenuation structure of the East Rift Zone and South Flank of Kilauea Volcano, Hawaii. *Bulletin of the Seismological Society of America* 94 (4), 1430–1440.
- Harlow, D.H., Power, J.A., Laguerta, E.P., Ambubuyog, G., White, R.A., Hoblitt, R.P., 1996. Precursory seismicity and forecasting of the June 15, 1991, eruption of Mount Pinatubo. In: Newhall, C.G., Punongbayan, R.S. (Eds.), *Fire and Mud, Eruptions and Lahars of Mount Pinatubo, Philippines*. Univ. of Washington Press, Seattle, Washington, pp. 285–305.
- Harrington, R.M., Benson, P.M., 2011. Analysis of laboratory simulations of volcanic hybrid earthquakes using empirical Green's functions. *Journal of Geophysical Research* 116, B11303. <http://dx.doi.org/10.1029/2011JB008373>.
- Harrington, R.M., Brodsky, E.E., 2007. Volcanic hybrid earthquakes that are brittle-failure events. *Geophysical Research Letters* 34, L06308. <http://dx.doi.org/10.1029/2006GL028714>.
- Hasegawa, A., Zhao, D., Hori, S., Yamamoto, A., Horiuchi, S., 1991. Deep structure of the northeastern Japan arc and its relationship to seismic and volcanic activity. *Nature* 352, 683–689.
- Havskov, J., De la Cruz-Reyna, S., Singh, S.K., Medina, F., Gutierrez, C., 1983. Seismic activity related to the March–April, 1982 eruptions of El Chichón Volcano, Chiapas, Mexico. *Geophysical Research Letters* 10, 293–296.
- Hayashi, Y., Morita, Y., 2003. An image of a magma intrusion process inferred from precise hypocentral migrations of the earthquake swarm east of the Izu Peninsula. *Geophysical Journal International* 153, 159–174.
- Heiken, G., Wohletz, K., Eichelberger, J., 1988. Fracture fillings and intrusive pyroclasts, Inyo Domes, California. *Journal of Geophysical Research* 93 (B5), 4335–4350.
- Hellweg, M., 2000. Physical models for the source of Lascar's harmonic tremor. *Journal of Volcanology and Geothermal Research* 101, 183–198.
- Hess, K., Dingwell, D.B., 1996. Viscosities of hydrous leucogranitic melts: a non-Arrhenian model. *American Mineralogist* 81, 1297–1300.
- Hidayat, D., Voight, B., Langston, C., Ratdomopurbo, A., Ebeling, C., 2000. Broadband seismic experiment at Merapi Volcano, Java, Indonesia: very-long-period pulses embedded in multiphase earthquakes. *Journal of Volcanology and Geothermal Research* 100, 215–231.
- Hidayat, D., Chouet, B., Voight, B., Dawson, P., Ratdomopurbo, A., 2002. Source mechanism of very-long-period signals accompanying dome growth activity at Merapi Volcano, Indonesia. *Geophysical Research Letters* 29 (23), 2118. <http://dx.doi.org/10.1029/2002GL015013>.
- Hidayat, D., Chouet, B., Voight, B., Dawson, P., Ratdomopurbo, A., 2003. Correction to Source mechanism of very-long-period signals accompanying dome growth activity at Merapi Volcano, Indonesia. *Geophysical Research Letters* 30 (10), 2118. <http://dx.doi.org/10.1029/2003GL017211>.
- Hill, D.P., 1977. A model for earthquake swarms. *Journal of Geophysical Research* 82 (8), 1347–1352.
- Hill, D.P., 1996. Earthquakes and carbon dioxide beneath Mammoth Mountain, California. *Seismological Research Letters* 67 (1), 8–15.
- Hill, D.P., Prejean, S., 2005. Magmatic unrest beneath Mammoth Mountain, California. *Journal of Volcanology and Geothermal Research* 146, 257–283.
- Hill, D.P., Ellsworth, W.L., Johnston, M.J.S., Langbein, J.O., Oppenheimer, D.H., Pitt, A.M., Reasenberg, P.A., Sorey, M.L., McNutt, S.R., 1990. The 1989 earthquake swarm beneath Mammoth Mountain, California: an initial look at the 4 May through 30 September activity. *Bulletin of the Seismological Society of America* 80, 325–339.
- Hill, D.P., Dawson, P., Johnston, M.J.S., Pitt, A.M., Biasi, G., Smith, K., 2002. Very-long-period volcanic earthquakes beneath Mammoth Mountain, California. *Geophysical Research Letters* 29 (10), 1370. <http://dx.doi.org/10.1029/2002GL014833>.
- Hirabayashi, J., 1999. Formation of volcanic fluid reservoir and volcanic activity. *Journal of the Balneological Society of Japan* 49, 99–105.
- Hole, J.A., 1992. Nonlinear high-resolution three-dimensional seismic travel time tomography. *Journal of Geophysical Research* 97, 6553–6562.
- Hotovec, A.J., 2009. Hydrogeologic model of groundwater flow within Mount St. Helens Volcano determined from self-potential and time-domain electromagnetic measurements, Unpublished M.S. thesis, Colorado School of Mines.
- Hotovec, A.J., Prejean, S.G., Vidale, J.E., Gomberg, J., 2012. Strongly gliding harmonic tremor during the 2009 eruption of Redoubt Volcano. *Journal of Volcanology and Geothermal Research*. <http://dx.doi.org/10.1016/j.jvolgeores.2012.01.001>.
- Hudson, J.A., Pearce, R.G., Rogers, R.M., 1989. Source type plot for inversion of the moment tensor, California. *Journal of Geophysical Research* 94, 765–774.
- Hughes, G., 2011. Reinvestigation of the 1989 Mammoth Mountain, California seismic swarm and dike intrusion. *Journal of Volcanology and Geothermal Research* 207, 106–112.
- Ichihara, M., Kameda, M., 2004. Propagation of acoustic waves in a visco-elastic two-phase system: influences of the liquid viscosity and the internal diffusion. *Journal of Volcanology and Geothermal Research* 137, 73–91.
- Ichihara, M., Nishimura, T., 2009. Pressure impulses generated by bubbles interacting with ambient perturbation, in: Meyers, R. A. (Editor-in-Chief), *Encyclopedia of Complexity and Systems Science*. Springer, New York, pp. 6955–6977.
- Ichihara, M., Rubin, M.B., 2010. Brittleness of fracture in flowing magma. *Journal of Geophysical Research* 115, B12202. <http://dx.doi.org/10.1029/2010JB007820>.
- Ichihara, M., Ohkunitani, H., Iida, Y., Kameda, M., 2004. Dynamics of bubble oscillation and wave propagation in viscoelastic liquids. *Journal of Volcanology and Geothermal Research* 129, 37–60.
- Inza, L.A., Mars, J.I., Métxian, J.P., O'Brien, G.S., Macedo, O., 2011. Seismo-volcano source localization with triaxial broad-band seismic array. *Geophysical Journal International* 187, 371–384.
- Iverson, R.M., 2008. Dynamics of seismogenic volcanic extrusion resisted by a solid surface plug, Mount St. Helens, 2004–2005. In: Sherrod, D.R., Scott, W.E., Stauffer, P.H. (Eds.), *A Volcano Rekindled: The Renewed Eruption of Mount St. Helens, 2004–2006*. U.S. Geological Survey Professional Paper 1750, pp. 425–460 (Chap. 21).
- Iverson, R.M., Dzurisin, D., Gardner, C.A., Gerlach, T.M., LaHusen, R.G., Lisowski, M., Major, J.J., Malone, S.D., Messerich, J.A., Moran, S.C., Pallister, J.S., Qamar, A.I., Schilling, S.P., Vallance, J.W., 2006. Dynamics of seismogenic volcanic extrusion at Mount St. Helens in 2004–05. *Nature* 444, 439–443.
- Jacqmin, D., 1999. Calculation of two-phase Navier–Stokes Flows using phase-field modeling. *Journal of Computational Physics* 155, 96–127.
- Jakobsdóttir, S.S., Roberts, M.J., Gudmundsson, G.B., Geirsson, H., Slunga, R., 2008. Earthquake swarms at Upptyppingar, north-east Iceland: a sign of magma intrusion? *Studia Geophysica et Geodistica* 52, 513–528.
- James, M.R., Lane, S.J., Chouet, B., Gilbert, J.S., 2004. Pressure changes associated with the ascent and bursting of gas slugs in liquid-filled vertical and inclined conduits. *Journal of Volcanology and Geothermal Research* 129, 61–82.

- James, M.R., Lane, S.J., Chouet, B., 2006. Gas slug ascent through changes in conduit diameter: laboratory insights into a volcano-seismic source process in low-viscosity magmas. *Journal of Geophysical Research* 111, B05201. <http://dx.doi.org/10.1029/2005JB003718>.
- James, M.R., Lane, S.J., Corder, S.B., 2008. Modelling the rapid near-surface expansion of gas slugs in low-viscosity magmas. In: Lane, S.J., Gilbert, J.S. (Eds.), *Fluid Motions in Volcanic Conduits: A Source of Seismic and Acoustic Signals*: Geol. Soc., London, Spec. Publ., 307, pp. 147–167.
- James, M.R., Lane, S.J., Wilson, L., Corder, S.B., 2009. Degassing at low magma-viscosity volcanoes: quantifying the transition between passive bubble-burst and Strombolian eruption. *Journal of Volcanology and Geothermal Research* 180, 81–88.
- James, M.R., Llewellyn, E.W., Lane, S.J., 2011. Comment on "It takes three to tango: 2. Bubble dynamics in basaltic volcanoes and ramifications for modeling normal Strombolian activity" by J. Suckale, B. H. Hager, L. T. Elkins-Tanton, and J.-C. Nave. *Journal of Geophysical Research* 116, B06207. <http://dx.doi.org/10.1029/2010JB008167>.
- Jaupart, C., Vergniolle, S., 1989. The generation and collapse of a foam layer at the roof of a basaltic magma chamber. *Journal of Fluid Mechanics* 203, 347–380.
- Jellineck, A.M., Bercovici, D., 2011. Seismic tremors and magma wagging during explosive volcanism. *Nature* 470, 522–526.
- John, D.A., Sisson, T.W., Breit, G.N., Rye, R.O., Vallance, J.W., 2008. Characteristics, extent and origin of hydrothermal alteration at Mount Rainier Volcano, Cascades Arc, USA: implications for debris-flow hazards and mineral deposits. *Journal of Volcanology and Geothermal Research* 175, 289–314. <http://dx.doi.org/10.1016/j.jvolgeores.2008.04.004>.
- Johnson, J.B., 2007. On the relation between infrasound, seismicity, and small pyroclastic explosions at Karymsky volcano. *Journal of Geophysical Research* 112, B08203. <http://dx.doi.org/10.1029/2006JB004654>.
- Johnson, J.B., Lees, J.M., 2000. Plugs and chugs – seismic and acoustic observations of degassing explosions at Karymsky, Russia and Sangay, Ecuador. *Journal of Volcanology and Geothermal Research* 101, 67–82.
- Johnson, J.B., Ripepe, M., 2011. Volcano infrasound: a review. *Journal of Volcanology and Geothermal Research* 206, 61–69.
- Johnson, J.B., Lees, J.M., Gerst, A., Sahagian, D., Varley, N., 2008. Long-period earthquakes and co-eruptive dome inflation seen with particle image velocimetry. *Nature* 456, 377–381. <http://dx.doi.org/10.1038/nature07429>.
- Johnson, J.H., Savage, M.K., Townend, J., 2011. Distinguishing between stress-induced and structural anisotropy at Mount Ruapehu volcano, New Zealand. *Journal of Geophysical Research* 116, B12303. <http://dx.doi.org/10.1029/2011JB008308>.
- Jousser, P., Neuberg, J., Sturton, S., 2003. Modelling the time-dependent frequency content of low-frequency volcanic earthquakes. *Journal of Volcanology and Geothermal Research* 128, 201–223.
- Jousser, P., Neuberg, J., Jolly, A., 2004. Modelling low-frequency volcanic earthquakes in a viscoelastic medium with topography. *Geophysical Journal International* 159, 776–802.
- Julian, B.R., 1994. Volcanic tremor: nonlinear excitation by fluid flow. *Journal of Geophysical Research* 99, 11,859–11,877.
- Kameda, M., Kuribara, H., Ichihara, M., 2008. Dominant time scale for brittle fragmentation of vesicular magma by decompression. *Geophysical Research Letters* 35, L14302. <http://dx.doi.org/10.1029/2008GL034530>.
- Kamo, K., et al., 1994. Infrasonic and seismic detection of explosive eruptions at Sakurajima volcano, Japan, and the PEGASUS-VE early-warning system. In: Casadevall, T.J. (Ed.), *Volcanic Ash and Aviation Safety: Proceedings of the First International Symposium on Volcanic Ash and Aviation Safety*: U.S. Geol. Surv. Bull., 2047, pp. 357–365.
- Kanamori, H., Given, J.W., 1982. Analysis of long-period waves excited by the May 18, 1980, eruption of Mount St. Helens – a terrestrial monopole? *Journal of Geophysical Research* 87, 5422–5432.
- Kanamori, H., Mori, J., 1992. Harmonic excitation of Mantle Rayleigh waves by the 1991 eruption of Mount Pinatubo, Philippines. *Geophysical Research Letters* 19, 1856–1866.
- Kanamori, H., Given, J.W., Lay, T., 1984. Analysis of seismic body waves excited by the Mount St. Helens eruption of May 18, 1980. *Journal of Geophysical Research* 89, 1856–1866.
- Kaneshima, S., Kawakatsu, H., Matsubayashi, H., Sudo, Y., Tsutsui, T., Ohminato, T., Ito, H., Uhira, K., Yamasato, H., Oikawa, J., Takeo, M., Iidaka, T., 1996. Mechanism of phreatic eruptions at Aso Volcano inferred from near-field broadband seismic observations. *Science* 273, 642–645.
- Kang, M., Fedkiw, R.P., Liu, X.-D., 2000. A boundary condition capturing method for multiphase incompressible flow. *Journal of Scientific Computing* 15, 323–360.
- Kawakatsu, H., 1989. Centroid single force inversion of seismic waves generated by landslides. *Journal of Geophysical Research* 94, 12,363–12,374.
- Kawakatsu, H., Yamamoto, M., 2007. Volcano seismology. In: Kanamori, H., Schubert, G. (Eds.), *Treatise on Geophysics*. *Earthquake Seismology*, vol. 4. Elsevier, New York, pp. 389–420.
- Kawakatsu, H., Ohminato, T., Ito, H., Kuwahara, Y., 1992. Broadband seismic observation at Sakurajima Volcano, Japan. *Geophysical Research Letters* 19, 1959–1962.
- Kawakatsu, H., Ohminato, T., Ito, H., 1994. 10-s period volcanic tremors observed over a wide area in southwestern Japan. *Geophysical Research Letters* 21, 1963–1966.
- Kawakatsu, H., Kaneshima, S., Matsubayashi, H., Ohminato, T., Sudo, Y., Tsutsui, T., Uhira, K., Yamasato, H., Ito, H., Legrand, D., 2000. Aso94: Aso seismic observation with broadband instruments. *Journal of Volcanology and Geothermal Research* 101, 129–154.
- Kazahaya, K., Shinohara, H., Saito, G., 2002. Degassing process of Satsuma-Iwojima Volcano, Japan: supply of volatile components from a deep magma chamber. *Earth Planets Space* 54, 327–335.
- Kazahaya, R., Mori, T., Takeo, M., Ohminato, T., Urabe, T., Maeda, Y., 2011. Relation between single very-long-period pulses and volcanic gas emissions at Mt. Asama, Japan. *Geophysical Research Letters* 38, L11307. <http://dx.doi.org/10.1029/2011GL047555>.
- Kedar, S., Sturtevant, B., Kanamori, H., 1996. The origin of harmonic tremor at Old Faithful Geyser. *Nature* 379, 708–711.
- Kendrick, J.E., Lavallee, Y., Ferk, A., Perugini, D., Leonhardt, R., Dingwell, D.B., 2012. Extreme frictional processes in the volcanic conduit of Mount St. Helens (USA) during the 2004–2008 eruption. *Journal of Structural Geology* 38, 61–67. <http://dx.doi.org/10.1016/j.jsg.2011.10.003>.
- Kennedy, L.A., Russell, J.K., 2012. Cataclastic production of volcanic ash at Mount St. Helens. *Journal of Physics and Chemistry of the Earth* 45–46, 40–49. <http://dx.doi.org/10.1016/j.jpc.2011.07.052>.
- Key, J.R.S., White, H., Soosalu, Jakobsdóttir, S.S., 2011. Multiple melt injection along a spreading segment at Askja, Iceland. *Geophysical Research Letters* 38, L05301. <http://dx.doi.org/10.1029/2010GL046264>.
- Kieffer, S.W., 1977. Sound speed in liquid-gas mixtures: water-air and water-steam. *Journal of Geophysical Research* 82, 2895–2904.
- Kieffer, S., 1981. Blast dynamics at Mount St. Helens on 18 May 1980. *Nature* 291, 568–570.
- Kim, J., Kang, K., Lowengrub, J., 2004. Conservative multigrid methods for Cahn-Hilliard fluids. *Journal of Computational Physics* 193, 511–543.
- Koulakov, I., 2009. LOTOS Code for local earthquake tomographic inversion: benchmarks for testing tomographic algorithms. *Bulletin of the Seismological Society of America* 99 (1), 194–214.
- Koyanagi, R.Y., Chouet, B., Aki, K., 1987. Origin of volcanic tremor in Hawaii: Part I. Data from the Hawaiian Volcano Observatory 1969–1985. In: Decker, R.W., Wright, T.L., Stauffer, P.H. (Eds.), *Volcanism in Hawaii: U. S. Geol. Surv. Prof. Pap.*, 1350, pp. 1221–1257.
- Kubotera, A., 1974. Volcanic tremors at Aso volcano. In: Civetta, L., Gasparini, P., Luongo, G., Rapolla, A. (Eds.), *Physical Volcanology*. Elsevier, New York, pp. 29–48.
- Kumagai, H., 2006. Temporal evolution of a magmatic dike system inferred from the complex frequencies of very long period seismic signals. *Journal of Geophysical Research* 111, B06201. <http://dx.doi.org/10.1029/2005JB003881>.
- Kumagai, H., 2009. Source quantification of volcano seismic signals, in: Meyers, R. A. (Editor-in-Chief), *Encyclopedia of Complexity and Systems Science*. Springer-Verlag, New York, pp. 9899–9932.
- Kumagai, H., Chouet, B.A., 1999. The complex frequencies of long-period seismic events as probes of fluid composition beneath volcanoes. *Geophysical Journal International* 138, F7–F12.
- Kumagai, H., Chouet, B.A., 2000. Acoustic properties of a crack containing magmatic or hydrothermal fluids. *Journal of Geophysical Research* 105 (B11), 25,493–25,512.
- Kumagai, H., Chouet, B.A., 2001. The dependence of acoustic properties of a crack on the resonance mode and geometry. *Geophysical Research Letters* 28, 3325–3328.
- Kumagai, H., Ohminato, T., Nakano, M., Ooi, M., Kubo, A., Inoue, H., Oikawa, J., 2001. Very-long-period seismic signals and caldera formation at Miyake Island, Japan. *Science* 293, 687–690.
- Kumagai, H., Chouet, B.A., Nakano, M., 2002a. Waveform inversion of oscillatory signatures in long-period events beneath volcanoes. *Journal of Geophysical Research* 107 (B11), 2301. <http://dx.doi.org/10.1029/2001JB001704>.
- Kumagai, H., Chouet, B.A., Nakano, M., 2002b. Temporal evolution of a hydrothermal system in Kusatsu-Shirane Volcano, Japan, inferred from the complex frequencies of long-period events. *Journal of Geophysical Research* 107 (B10), 2236. <http://dx.doi.org/10.1029/2001JB000653>.
- Kumagai, H., Miyakawa, K., Negishi, H., Inoue, H., Obara, K., Suetzugu, D., 2003. Magmatic dyke resonances inferred from very-long-period seismic signals. *Science* 299, 2058–2061.
- Kumagai, H., Chouet, B.A., Dawson, P.B., 2005. Source process of a long-period event at Kilauea Volcano, Hawaii. *Geophysical Journal International* 161, 243–254.
- Kumagai, H., Yip, H., Vacca, M., Caceres, V., Nagai, T., Yokoe, K., Imai, T., Miyakawa, K., Yamashina, T., Arrais, S., Vasconez, F., Pinajota, E., Cisneros, C., Ramos, C., Paredes, M., Gomezjurado, L., Garcia-Aristizabal, A., Molina, I., Ramon, P., Segovia, M., Palacios, P., Troncoso, L., Alvarado, A., Aguilar, J., Pozo, J., Enriquez, W., Mothes, P., Hall, M., Inoue, I., Nakano, M., Inoue, H., 2007. Enhancing volcano-monitoring capabilities in Ecuador. *Eos Transactions American Geophysical Union* 88 (23), 245–246.
- Kumagai, H., Nakano, M., Maeda, T., Yip, H., Palacios, P., Ruiz, M., Arrais, S., Vacca, M., Molina, I., Yamashina, T., 2010. Broadband seismic monitoring of active volcanoes using deterministic and stochastic approaches. *Journal of Geophysical Research* 115, B08303. <http://dx.doi.org/10.1029/2009JB006889>.
- Kumagai, H., Placitos, P., Ruiz, M., Yip, H., Kozeno, T., 2011. Ascending seismic source during an explosive eruption of Tungurahua volcano, Ecuador. *Geophysical Research Letters* 38, L01306. <http://dx.doi.org/10.1029/2010GL045944>.
- Kumazawa, M., Imanishi, Y., Fukao, Y., Furumoto, M., Yamamoto, A., 1990. A theory of spectral analysis based on the characteristic property of a linear dynamic system. *Geophysical Journal International* 101, 613–630.
- Kurzon, I., Lyakhovsky, V., Navon, O., Lensky, N.G., 2008. Damping of pressure waves in visco-elastic, saturated bubbly magma. In: Lane, S.J., Gilbert, J.S. (Eds.), *Fluid Motions in Volcanic Conduits: A Source of Seismic and Acoustic Signals*: Geol. Soc., London, Special Publications, 307, pp. 11–31.
- Kurzon, I., Lyakhovsky, V., Navon, O., Chouet, B., 2011. Pressure waves in a supersaturated bubbly magma. *Geophysical Journal International* 187, 421–438.
- Kwiatek, G., Plenkers, K., Dresen, G., 2011. Source parameters of picoseismicity recorded at Mponeng Deep Gold Mine, South Africa: implications for scaling relations. *Bulletin of the Seismological Society of America* 101, 2592–2608. <http://dx.doi.org/10.1785/0120110094>.
- Lahr, J.C., Chouet, B.A., Stephens, C.D., Power, J.A., Page, R.A., 1994. Earthquake classification, location and error analysis in a volcanic environment: implications for the magmatic system of the 1989–1990 eruptions at Redoubt Volcano, Alaska. *Journal of Volcanology and Geothermal Research* 62, 137–151.

- LaHusen, R.G., Swinford, K.J., Logan, M., Lisowski, M., 2008. Instrumentation in remote and dangerous settings; examples using data from gps “spider” deployments during the 2004–2005 eruption of Mount St. Helens, Washington. In: Sherrod, D.R., Scott, W.E., Stauffer, P.H. (Eds.), A Volcano Rekindled: The Renewed Eruption of Mount St. Helens, 2004–2006: U.S. Geological Survey Professional Paper 1750, 1750, pp. 335–345 (Chap. 16).
- Lane, S.J., James, M.R., 2009. Explosive volcanic eruptions: experimental insights, in: Meyers, R. A. (Editor-in-Chief), Encyclopedia of Complexity and Systems Science, Springer-Verlag, New York, pp. 9784–9830.
- Lane, S.J., Chouet, B.A., Phillips, J.C., Dawson, P., Ryan, G.A., Hurst, E., 2001. Experimental observations of pressure oscillations and flow regimes in an analogue volcanic system. *Journal of Geophysical Research* 106 (B4), 6461–6476.
- Lane, S.J., Phillips, J.C., Ryan, G.A., 2008. Dome-building eruptions: insights from analogue experiments. In: Lane, S.J., Gilbert, J.S. (Eds.), Fluid Motions in Volcanic Conduits: A Source of Seismic and Acoustic Signals: Geol. Soc., London, Special Publications, 307, pp. 207–237.
- Larose, E., Derode, A., Campillo, M., Fink, M., 2004. Imaging from one-bit correlations of wideband diffuse wave fields. *Journal of Applied Physics* 95, 8393–8399.
- Larose, E., Margerin, L., Derode, A., van Tinggelen, B., Campillo, M., Shapiro, N., Paul, A., Stehly, L., Tanter, M., 2006. Correlation of random wavefields: an interdisciplinary view. *Geophysics* 71 (4), S111–S121.
- Latter, J.H., 1979. Volcanological observations at Tongariro National Park, 2, types and classification of volcanic earthquakes, 1976–1978. *New Zealand Dep. of Sci. and Ind. Res., Geophys. Div.*, Wellington, Rep., 150 . (60 pp.).
- Latter, J.H., 1981. Volcanic earthquakes, and their relationship to eruptions at Ruapehu and Ngauruhoe volcanoes. *Journal of Volcanology and Geothermal Research* 9, 293–309.
- Lavallée, Y., Hess, K.-U., Cordonnier, B., Dingwell, D.B., 2007. Non-Newtonian rheological law for highly crystalline dome lavas. *Geology* 35 (9), 843–846.
- Lavallée, Y., Meredith, P.G., Dingwell, D.B., Hess, K.-U., Wassermann, J., Cordonnier, B., Gerik, A., Kruhl, J.H., 2008. Seismogenic lavas and explosive eruption forecasting. *Nature* 453, 507–510.
- Le Pichon, A., Blanc, E., Hauchecorne, A., 2010. Infrasound Monitoring for Atmospheric Studies, First edition. Springer.
- Lees, J.M., 2007. Seismic tomography of magmatic systems. *Journal of Volcanology and Geothermal Research* 167, 37–56.
- Leet, R.C., 1988. Saturated and subcooled hydrothermal boiling in groundwater-flow channels as a source of harmonic tremor. *Journal of Geophysical Research* 93, 4835–4849.
- Legrand, D., Kaneshima, S., Kawakatsu, H., 2000. Moment tensor analysis of near-field broadband waveforms observed at Aso Volcano, Japan. *Journal of Volcanology and Geothermal Research* 101, 155–169.
- Legrand, D., Calahorrano, A., Guillier, B., Rivera, L., Ruiz, M., Villagómez, D., Yepes, H., 2002. Stress tensor analysis of the 1998–1999 tectonic swarm of northern Quito related to the volcanic swarm of Guagua Pichincha Volcano, Ecuador. *Tectonophysics* 344, 15–36.
- Lehto, H.L., Roman, D.C., Moran, S.C., 2010. Temporal changes in stress preceding the 2004–2008 eruption of Mount St. Helens, Washington. *Journal of Volcanology and Geothermal Research* 198, 129–142.
- Leighton, T.G., 1994. The Acoustic Bubble. Academic, New York.
- Lensky, N.G., Lyakhovsky, V., Navon, O., 2002. Expansion dynamics of volatile-saturated liquids and bulk viscosity of bubbly magmas. *Journal of Fluid Mechanics* 460, 39–56.
- Lensky, N.G., Navon, O., Lyakhovsky, V., 2004. Bubble growth during decompression of magma: experimental and theoretical investigation. *Journal of Volcanology and Geothermal Research* 129, 7–22.
- Lesage, P., Mora, M.M., Alvarado, G.E., Pacheco, J., Metaxian, J.P., 2006. Complex behavior and source model of the tremor at Arenal volcano, Costa Rica. *Journal of Volcanology and Geothermal Research* 157, 49–59.
- Liang, C., Langston, C.A., 2008. Ambient seismic noise tomography and structure of eastern North America. *Journal of Geophysical Research* 113, B03309. <http://dx.doi.org/10.1029/2007JB005350>.
- Lin, F.-C., Moschetti, M.P., Ritzwoller, M.H., 2008. Surface wave tomography of the western United States from ambient seismic noise: Rayleigh and Love wave phase velocity maps. *Geophysical Journal International* 173, 281–298.
- Lin, F.-C., Ritzwoller, M.H., Snieder, R., 2009. Eikonal tomography: surface wave tomography by phase front tracking across a regional broadband seismic array. *Geophysical Journal International* 177, 1091–1110.
- Linde, A.T., Agustsson, K., Selwyn Sacks, I., Stefansson, R., 1993. Mechanism of the 1991 eruption of Hekla from continuous borehole strain monitoring. *Nature* 365, 737–740.
- Logonne, P., Clevede, E., Kanamori, H., 1998. Computation of seismograms and atmospheric oscillations by normal-mode summation for a spherical Earth model with realistic atmosphere. *Geophysical Journal International* 135, 388–406.
- Lokmer, I., Bean, C.J., Saccorotti, G., Patane, D., 2007. Moment-tensor inversion of LP events recorded on Etna in 2004 using constraints obtained from wave simulation tests. *Geophysical Research Letters* 34, L22316. <http://dx.doi.org/10.1029/2007GL031902>.
- Lokmer, I., Saccorotti, G., Di Lieto, B., Bean, C.J., 2008. Temporal evolution of long-period seismicity at Etna Volcano, Italy, and its relationships with the 2004–2005 eruption. *Earth and Planetary Science Letters* 266, 205–220.
- Lowengrub, J., Truskinovsky, L., 1998. Quasi-incompressible Cahn-Hilliard fluids and topological transitions. *Proceedings of the Royal Society of London A* 454, 2617–2654.
- Lyakhovsky, V., Hurwitz, S., Navon, O., 1996. Bubble growth in rhyolitic melts: experimental and numerical investigation. *Bulletin of Volcanology* 58, 19–32.
- Lyons, J.J., Waite, G.P., 2011. Dynamics of explosive volcanism at Fuego volcano imaged with very long period seismicity. *Journal of Geophysical Research* 116, B09303. <http://dx.doi.org/10.1029/2011JB008521>.
- Lyons, J., Waite, G., Rose, W., Chigna, G., 2010. Patterns in open vent, Strombolian behavior at Fuego Volcano, Guatemala, 2005–2007. *Bulletin of Volcanology* 72 (1), 1–15.
- Ma, S., Prieto, G.A., Beroza, G.C., 2008. Testing community velocity models for Southern California using the ambient seismic field. *Bulletin of the Seismological Society of America* 98, 2694–2714.
- Maeda, Y., Takeo, M., 2011. Very-long-period pulses at Asama Volcano, central Japan, inferred from dense seismic observations. *Geophysical Journal International* 185, 265–282.
- Maeda, Y., Takeo, M., Ohminato, T., 2011. A waveform inversion including tilt: method and simple tests. *Geophysical Journal International* 184, 907–918.
- Malone, S.D., 1983. Volcanic Earthquakes: examples from Mount St. Helens. *Earthquakes: Observations, Theory and Interpretation*. Società Italiana di Fisica, Bologna, Italy, pp. 436–455.
- Marchetti, E., Ripepe, M., Harris, A.J.L., Delle Donne, D., 2009. Tracing the differences between Vulcanian and Strombolian explosions using infrasonic and thermal radiation energy. *Earth and Planetary Science Letters* 279 (3–4), 273–281.
- Masterlark, T., Haney, M., Dickinson, H., Fournier, T., Searcy, C., 2010. Rheologic and structural controls on the deformation of Okmok volcano, Alaska: FEMs, InSAR, and ambient noise tomography. *Geophysical Journal International* 115, B02409. <http://dx.doi.org/10.1029/2009JB006324>.
- Mattoza, R.S., 2009. Seismic and infrasonic source processes in volcanic fluid systems, Ph.D. Dissertation, University of California, San Diego.
- Mattoza, R.S., Chouet, B.A., 2010. Subevents of long-period seismicity: implications for hydrothermal dynamics during the 2004–2008 eruption of Mount St. Helens. *Journal of Geophysical Research* 115, B12206. <http://dx.doi.org/10.1029/2010JB007839>.
- Mattoza, R.S., Hedlin, M.A.H., Garcés, M.A., 2007. An infrasound study of Mount St. Helens. *Journal of Volcanology and Geothermal Research* 160, 249–262.
- Mattoza, R.S., Garcés, M.A., Chouet, B.A., D'Auria, L., Hedlin, M.A.H., De Groot-Hedlin, C., Waite, G.P., 2009a. The source of infrasound associated with long-period events at Mount St. Helens. *Journal of Geophysical Research* 114, B04305. <http://dx.doi.org/10.1029/2008JB006128>.
- Mattoza, R.S., Fee, D., Garcés, M.A., Seiner, J.M., Ramon, P.A., Hedlin, M.A.H., 2009b. Infrasonic jet noise from volcanic eruptions. *Geophysical Research Letters* 36, L08303. <http://dx.doi.org/10.1029/2008GL036486>.
- Mattoza, R.S., Fee, D., Garcés, M.A., 2010. Infrasonic tremor wavefield of the Pu'u 'O'o crater complex and lava tube system, Hawaii, in April 2007. *Journal of Geophysical Research* 115, B12312. <http://dx.doi.org/10.1029/2009JB007192>.
- Mattoza, R.S., Vergoz, J., Le Pichon, A., Ceranna, L., Green, D.N., Evers, L.G., Ripepe, M., Campus, P., Liszka, L., Kvaerna, T., Kjartansson, E., Hoskuldsson, A., 2011b. Long-range acoustic observations of the Eyjafjallajökull eruption, Iceland. *Geophysical Research Letters* 38, L06308.
- Matsubara, W., Yomogida, K., 2004. Source process of low-frequency earthquakes associated with the 2000 eruption of Mt. Usu. *Journal of Volcanology and Geothermal Research* 134, 223–240.
- McNutt, S.R., 1992. Volcanic tremor. In: Brekhovskikh, L., et al. (Ed.), Encyclopedia of Earth System Science, vol. 4. Academic, San Diego, Calif., pp. 417–425.
- McNutt, S.R., 2005. Volcanic seismology. *Annual Review of Earth and Planetary Sciences* 33, 461–491.
- McNutt, S.R., Nishimura, T., 2008. Volcanic tremor during eruptions: temporal characteristics, scaling and constraints on conduit size and processes. *Journal of Volcanology and Geothermal Research* 178, 10–18.
- Meng, L., Inbal, A., Ampuero, J.-P., 2011. A window into the complexity of the dynamic rupture of the 2011 Mw 9 Tohoku-Oki earthquake. *Geophysical Research Letters* 38, L00G07. <http://dx.doi.org/10.1029/2011GL048118>.
- Meng, L., Ampuero, J.-P., Sladen, A., Hendon, H., 2012. High-resolution backprojection at regional distances: application to the Haiti M7.0 earthquake and comparisons with finite source studies. *Journal of Geophysical Research* 117, B04313. <http://dx.doi.org/10.1029/2011JB008702>.
- Métaxian, J.-P., Lesage, P., Dorel, J., 1997. Permanent tremor at Masaya Volcano, Nicaragua: wave field analysis and source location. *Journal of Geophysical Research* 102, 22,529–22,545.
- Métaxian, J.-P., Lesage, P., Valette, B., 2002. Locating sources of volcanic tremor and emergent events by seismic triangulation: application to Arenal volcano, Costa Rica. *Journal of Geophysical Research* 107 (B10), 2243. <http://dx.doi.org/10.1029/2001JB000559>.
- Molina, I., Kumagai, H., Yepes, H., 2004. Resonances of volcanic conduit triggered by repeated injections of ash-laden gas. *Geophysical Research Letters* 31, L03603. <http://dx.doi.org/10.1029/2003GL018934>.
- Molina, I., Kumagai, H., García-Aristizábal, A., Nakano, M., Mothes, P., 2008. Source process of very-long-period events accompanying long-period signals at Cotopaxi Volcano, Ecuador. *Journal of Volcanology and Geothermal Research* 176, 119–133.
- Moore, P.L., Iverson, N.R., Iverson, R.M., 2008. Frictional properties of the Mount St. Helens gouge. In: Sherrod, D.R., Scott, W.E., Stauffer, P.H. (Eds.), A Volcano Rekindled: The Renewed Eruption of Mount St. Helens, 2004–2006: U.S. Geological Survey Professional Paper 1750, pp. 415–424 (Chap. 20).
- Moran, S.C., 2003. Multiple seismogenic processes for high-frequency earthquakes at Katmai National Park, Alaska: evidence from stress tensor inversions of fault-plane solutions. *Bulletin of the Seismological Society of America* 93, 94–108.
- Moran, S.C., Malone, S.D., Qamar, A.I., Thelen, W., Wright, A.K., Caplan-Auerbach, J., 2008a. 2004–2005 seismicity associated with the renewed dome-building eruption of Mount St. Helens. In: Sherrod, D.R., Scott, W.E., Stauffer, P.F. (Eds.), A Volcano Rekindled: The Renewed Eruption of Mount St. Helens, 2004–2006: U.S. Geological Survey Professional Paper 1750, pp. 27–60 (Chap. 2).

- Moran, S.C., Mattoza, R.S., Garces, M.A., Hedlin, M.A.H., Bowers, D., Scott, W.E., Sherrod, D.R., Vallance, J.W., 2008b. Seismic and acoustic recordings of an unusually large rockfall at Mount St. Helens, Washington. *Geophysical Research Letters* 35, L19302.
- Mori, J., Patia, H., McKee, C., Itikarai, I., Lowenstein, P., De Saint Ours, P., Talai, B., 1989. Seismicity associated with eruptive activity at Langila Volcano, Papua New Guinea. *Journal of Volcanology and Geothermal Research* 38, 243–255.
- Morita, Y., Nakao, S., Hayashi, Y., 2006. A quantitative approach to the dike intrusion process inferred from a joint analysis of geodetic and seismological data for the 1998 earthquake swarm off the east coast of Izu Peninsula, central Japan. *Journal of Geophysical Research* 111, B06208. <http://dx.doi.org/10.1029/2005JB003860>.
- Morrissey, M.M., Chouet, B.A., 1997. A numerical investigation of choked flow dynamics and its application to the triggering mechanism of long-period events at Redoubt Volcano, Alaska. *Journal of Geophysical Research* 102, 7965–7983.
- Morrissey, M.M., Chouet, B.A., 2001. Trends in long-period seismicity related to magmatic fluid compositions. *Journal of Volcanology and Geothermal Research* 108, 265–281.
- Nagaoka, Y., Nishida, K., Aoki, Y., Takeo, M., 2010. Temporal velocity change of phase velocity beneath Mt. Asama, Japan, inferred from coda wave interferometry. *Geophysical Research Letters* 37, L22311. <http://dx.doi.org/10.1029/2010GL045289>.
- Nakahara, H., 2006. A systematic study of theoretical relations between spatial correlation and Green's function in one-, two-, and three-dimensional random scalar wavefields. *Geophysical Journal International* 167, 1097–1105.
- Nakamichi, H., Hamaguchi, H., Tanaka, S., Ueki, S., Nishimura, T., Hasegawa, A., 2003. Source mechanisms of deep and intermediate-depth low-frequency earthquakes beneath Iwate volcano, northeastern Japan. *Geophysical Journal International* 154, 811–828.
- Nakamichi, H., Kumagai, H., Nakano, M., Okubo, M., Kimata, F., Ito, Y., Obara, K., 2009. Source mechanism of very-long-period event at Mt. Ontake, central Japan: response of a hydrothermal system to magma intrusion beneath the summit. *Journal of Volcanology and Geothermal Research* 187, 167–177.
- Nakamura, K., Jacob, K.H., Davies, J.N., 1977. Volcanoes as possible indicators of tectonic stress orientation: Aleutians and Alaska. *Pure and Applied Geophysics* 115, 87–112.
- Nakano, M., Kumagai, H., 2005. Response of a hydrothermal system to magmatic heat inferred from temporal variations in the complex frequencies of long-period events at Kusatsu-Shirane Volcano, Japan. *Journal of Volcanology and Geothermal Research* 147, 233–244.
- Nakano, M., Kumagai, H., Kumazawa, M., Yamaoka, K., Chouet, B.A., 1998. The excitation and characteristic frequency of the long-period volcanic event: an approach based on an inhomogeneous autoregressive model of a linear dynamic system. *Journal of Geophysical Research* 103, 10,031–10,046.
- Nakano, M., Kumagai, H., Chouet, B.A., 2003. Source mechanism of long-period events at Kusatsu-Shirane Volcano, Japan, inferred from waveform inversion of the effective excitation functions. *Journal of Volcanology and Geothermal Research* 122, 149–164.
- Nakano, M., Kumagai, H., Chouet, B., Dawson, P., 2007. Waveform inversion of volcano-seismic signals for an extended source. *Journal of Geophysical Research* 112, B02306. <http://dx.doi.org/10.1029/2006JB004490>.
- Neal, C.A., Lockwood, J.P., 2003. Geologic map of the summit region of Kilauea Volcano, Hawaii. U.S. Geol. Surv. Geol. Invest. Ser. I-2759.
- Neuberg, J.W., 2011. Earthquakes, volcanogenic. In: Gupta, H.K., et al. (Eds.), *Encyclopedia of Solid Earth Geophysics*. Springer, pp. 261–269.
- Neuberg, J., Luckett, R., 1996. Seismo-volcanic sources on Stromboli volcano. *Annali di Geofisica* 34 (2), 377–391.
- Neuberg, J., Luckett, R., Ripepe, M., Braun, T., 1994. Highlights from a seismic broadband array on Stromboli Volcano. *Geophysical Research Letters* 21, 749–752.
- Neuberg, J., Luckett, R., Baptie, B., Olsen, K., 2000. Models of tremor and low-frequency earthquake swarms onMontserrat. *Journal of Volcanology and Geothermal Research* 101, 83–104.
- Neuberg, J.W., Tuffen, H., Collier, L., Green, D., Powell, T., Dingwell, D., 2006. The trigger mechanism of low-frequency earthquakes on Montserrat. *Journal of Volcanology and Geothermal Research* 153, 37–50.
- Nichols, M.L., Malone, S.D., Moran, S.C., Thelen, W.A., Vidale, J.E., 2011. Deep long-period earthquakes beneath Washington and Oregon volcanoes. *Journal of Volcanology and Geothermal Research* 200, 116–128.
- Nishimura, T., 2004. Pressure recovery in magma due to bubble growth. *Geophysical Research Letters* 31, L12613. <http://dx.doi.org/10.1029/2004GL019810>.
- Nishimura, T., Chouet, B., 2003. A numerical simulation of magma motion, crustal deformation, and seismic radiation associated with volcanic eruptions. *Geophysical Journal International* 153, 699–718.
- Nishimura, T., Iguchi, M., 2011. *Volcanic Earthquakes and Tremor in Japan*. Kyoto University Press.
- Nishimura, T., Nakamichi, H., Tanaka, S., Sato, M., Kobayashi, T., Ueki, S., Hamaguchi, H., Ohtake, M., Sato, H., 2000. Source process of very long period seismic events associated with the 1998 activity of Iwate Volcano, northeastern Japan. *Journal of Geophysical Research* 105, 19,135–19,147.
- Nishimura, T., Ueki, S., Yamawaki, T., Tanaka, S., Hasino, H., Sato, M., Nakamichi, H., Hamaguchi, H., 2003. Broadband seismic signals associated with the 2000 volcanic unrest of Mount Bandai, northeastern Japan. *Journal of Volcanology and Geothermal Research* 119, 51–59.
- Nur, A., 1971. Effects of stress on velocity anisotropy in rocks with cracks. *Journal of Geophysical Research* 76, 2011–2034.
- O'Brien, G.S., 2008. Discrete visco-elastic lattice methods for seismic wave propagation. *Geophysical Research Letters* 35, L02302. <http://dx.doi.org/10.1029/2007GL032214>.
- O'Brien, G.S., Bean, C.J., 2004. A 3D discrete numerical elastic lattice method for seismic wave propagation in heterogeneous media with topography. *Geophysical Research Letters* 31, L14608. <http://dx.doi.org/10.1029/2004GL020069>.
- O'Brien, G.S., Bean, C.J., 2008. Seismicity on volcanoes generated by gas slug ascent. *Geophysical Research Letters* 35, L16308. <http://dx.doi.org/10.1029/2008GL035001>.
- Ochs, F.A., Lange, R.A., 1999. The density of hydrous magmatic liquids. *Science* 283, 1314–1317.
- Ohba, T., Hirabayashi, J., Nogami, K., 2000. D/H and $^{18}\text{O}/^{16}\text{O}$ ratios of water in the crater lake at Kusatsu-Shirane volcano, Japan. *Journal of Volcanology and Geothermal Research* 97, 329–346.
- Ohminato, T., 2006. Characteristics and source modeling of broadband seismic signals associated with the hydrothermal system at Satsuma-Iwojima volcano, Japan. *Journal of Volcanology and Geothermal Research* 158, 467–490.
- Ohminato, T., Chouet, B.A., 1997. A free-surface boundary condition for including 3D topography in the finite difference method. *Bulletin of the Seismological Society of America* 87, 494–515.
- Ohminato, T., Ereditato, D., 1997. Broadband seismic observations at Satsuma-Iwojima Volcano, Japan. *Geophysical Research Letters* 24, 2845–2848.
- Ohminato, T., Chouet, B.A., Dawson, P.B., Kedar, S., 1998. Waveform inversion of very-long-period impulsive signals associated with magmatic injection beneath Kilauea Volcano, Hawaii. *Journal of Geophysical Research* 103, 23,839–23,862.
- Ohminato, T., Takeo, M., Kumagai, H., Yamashina, T., Oikawa, J., Koyama, E., Tsuji, H., Urabe, T., 2006. Vulcanian eruptions with dominant single force components observed during the Asama 2004 volcanic activity in Japan. *Earth Planets Space* 58, 583–593.
- Okada, Y., Yamamoto, E., 1991. Dyke intrusion model for the 1989 seismovolcanic activity off Ito, central Japan. *Journal of Geophysical Research* 96 (B6), 10,361–10,376.
- Okubo, P.G., Wolfe, C.J., 2008. Swarms of similar long-period earthquakes in the mantle beneath Mauna Loa Volcano. *Journal of Volcanology and Geothermal Research* 178, 787–794.
- Osher, S., Fedkiw, R., 2003. *Level Set Methods and Dynamic Implicit Surfaces*. Springer, New York. (273 pp.).
- Oshima, H., Maekawa, T., 2001. Excitation process of infrasonic waves associated with Merapi-type pyroclastic flow as revealed by a new recording system. *Geophysical Research Letters* 28, 1099–1102.
- Ottomeller, L., 2008. Seismic hybrid swarm precursors to a major lava dome collapse: 9–12 July 2003, Soufrière Hills Volcano, Montserrat. *Journal of Volcanology and Geothermal Research* 177, 903–910.
- Pallister, J.S., Thornber, C.R., Cashman, K.V., Clyne, M.A., Lowers, H.A., Mandeville, C.W., Brownfield, I.K., Meeker, G.P., 2008. Petrology of the 2004–2006 Mount St. Helens lava dome—implications for magmatic plumbing and eruption triggering. In: Sherrod, D.R., Scott, W.E., Stauffer, P.H. (Eds.), *A Volcano Rekindled: The Renewed Eruption of Mount St. Helens, 2004–2006*. U.S. Geological Survey Professional Paper 1750, pp. 647–702 (Chap. 30).
- Pallister, J.S., McCausland, W.A., Jónsson, S., Lu, Z., Zahran, H.M., El Hadidy, S., Aburukbah, A., Stewart, I.C.F., Lundgren, P.R., White, R.A., Moufti, M.R.H., 2010. Broad accommodation of rift-related extension recorded by dike intrusion in Saudi Arabia. *Nature Geoscience* 3, 705–712.
- Palo, M., Ibanez, J.M., Cisneros, M., Bretón, M., Del Pezzo, E., Ocana, E., Orozco-Rojas, J., Posadas, A.M., 2009. Analysis of the seismic wavefield properties of volcanic explosions at Volcán de Colima, Mexico: insights into the source mechanism. *Geophysical Journal International* 177, 1383–1398.
- Papale, P., 1999. Strain-induced magma fragmentation in explosive eruptions. *Nature* 397, 425–428.
- Patanè, D., Privitera, E., 2001. Seismicity related to the 1989 and 1991–1993 Mt. Etna, Italy, eruptions: kinematic constraints by fault plane solution analysis. *Journal of Volcanology and Geothermal Research* 109, 77–98.
- Patanè, D., Di Grazia, G., Cannata, A., Montalto, P., Boschi, E., 2008. Shallow magma pathway geometry at Mt. Etna volcano. *Geochemistry, Geophysics, Geosystems* 9, Q12021. <http://dx.doi.org/10.1029/2008GC002131>.
- Patrick, M., Wilson, D., Fee, D., Orr, T., Swanson, D., 2011. Shallow degassing events as a trigger for very-long-period seismicity at Kilauea Volcano, Hawaii. *Bulletin of Volcanology* 73, 1179–1186. <http://dx.doi.org/10.1007/s00445-011-0475-y>.
- Petersen, T., 2007. Swarms of repeating long-period earthquakes at Shishaldin Volcano, Alaska, 2001–2004. *Journal of Volcanology and Geothermal Research* 166, 177–192.
- Pettford, N., 2003. Rheology of granitic magmas during ascent and emplacement. *Annual Review of Earth and Planetary Sciences* 31, 399–427.
- Picozzi, M., Parolai, S., Bindi, D., Strollo, A., 2009. Characterization of shallow geology by high-frequency seismic noise tomography. *Geophysical Journal International* 176, 164–174.
- Pitt, A.M., Hill, D.P., 1994. Long-period earthquakes in the Long Valley caldera region, eastern California. *Geophysical Research Letters* 21 (16), 1679–1682.
- Pitt, A.M., Hill, D.P., Walter, S.W., Johnston, M.J.S., 2002. Midcrustal, long-period earthquakes beneath Northern California volcanic areas. *Seismological Research Letters* 73 (2), 144–152.
- Podvin, P., Lecomte, I., 1991. Finite difference computation of traveltimes in very contrasted velocity models: a massively parallel approach and its associated tools. *Geophysical Journal International* 105, 271–284.
- Pollard, D.D., Delaney, P.T., Duffield, W.A., Endo, E.T., Okamura, A.T., 1983. Surface deformation in volcanic rift zones. *Tectonophysics* 94, 541–584.
- Poupinet, G., Ellsworth, W.L., Frechet, J., 1984. Monitoring velocity variations in the crust using earthquake doublets: an application to the Calaveras fault, California. *Journal of Geophysical Research* 89, 5719–5731.
- Powell, T.W., Neuberg, J., 2003. Time dependent features in tremor spectra. *Journal of Volcanology and Geothermal Research* 128, 177–185.
- Power, J.A., Lalla, D.J., 2010. Seismic observations of Augustine Volcano, 1970–2007. In: Power, J.A., Coombs, M.L., Freymueller, J.T. (Eds.), *The 2006 Eruption of Augustine Volcano, Alaska: U. S. Geological Survey Prof. Pap. 1769*, pp. 3–40 (Ch. 1).
- Power, J.A., Stihler, S.D., White, R.A., Moran, S.C., 2004. Observations of deep long-period (DLP) seismic events beneath Aleutian arc volcanoes; 1989–2002. *Journal of Volcanology and Geothermal Research* 138, 243–266.

- Prejean, S., Stork, A., Ellsworth, W., Hill, D., Julian, B., 2003. High precision earthquake locations reveal seismogenic structure beneath Mammoth Mountain, California. *Geophysical Research Letters* 30 (24), 2247. <http://dx.doi.org/10.1029/2003GL018334>.
- Prieto, G.A., Beroza, G.C., 2008. Earthquake ground motion prediction using the ambient seismic field. *Geophysical Research Letters* 35, L14304. <http://dx.doi.org/10.1029/2008GL034428>.
- Proussevitch, A.A., Sahagian, D.L., 1996. Dynamics of coupled diffusive and decompressive bubble growth in magmatic systems. *Journal of Geophysical Research* 101, 17,447–17,455.
- Proussevitch, A.A., Sahagian, D.L., 1998. Dynamics and energetics of bubble growth in magmas: analytical formulation and numerical modeling. *Journal of Geophysical Research* 103, 18,223–18,251.
- Proussevitch, A.A., Sahagian, D.L., Anderson, A.T., 1993. Dynamics of diffusive bubble growth in magmas: isothermal case. *Journal of Geophysical Research* 98, 22,283–22,307.
- Qamar, A., St. Lawrence, W., Moore, J.N., Kendrick, G., 1983. Seismic signals preceding the explosive eruption of Mount St. Helens, Washington, on 18 May 1980. *Bulletin of the Seismological Society of America* 73, 1797–1813.
- Rabiner, L., Juang, B.-H., 1993. Fundamentals of Speech Recognition. Prentice-Hall, Englewood Cliffs, N.J.
- Ratdomopuro, A., Poupinet, G., 1995. Monitoring a temporal change of seismic velocity in a volcano: application to the 1992 eruption of Mt. Merapi (Indonesia). *Geophysical Research Letters* 22 (7), 775–778.
- Reid, R.C., 1978a. Superheated liquids: a laboratory curiosity and, possibly, an industrial curse. Part 1: laboratory studies and theory. *Chemical Engineering Education* 12, 60.
- Reid, R.C., 1978b. Superheated liquids: a laboratory curiosity and, possibly, an industrial curse. Part 2: industrial and vapor explosions. *Chemical Engineering Education* 12, 108.
- Reid, R.C., 1978c. Superheated liquids: a laboratory curiosity and, possibly, an industrial curse. Part 3: discussion and conclusions. *Chemical Engineering Education* 12, 194.
- Reid, R.C., 1979. Possible mechanism for pressurized-liquid tank explosions or BLEVE's. *Science* 203, 1263–1265.
- Reyners, M., Ebehardt-Phillips, D., Stuart, G., 2007. The role of fluids in lower-crustal earthquakes near continental rifts. *Nature* 446, 1075–1078.
- Ripepe, M., Poggi, P., Braun, T., Gordeev, E., 1996. Infrasonic waves and volcanic tremor at Stromboli. *Geophysical Research Letters* 23, 181–184.
- Ripepe, M., Marchetti, E., Olivieri, G., 2007. Infrasonic monitoring at Stromboli volcano during the 2003 effusive eruption: insights on the explosive and degassing process of an open conduit system. *Journal of Geophysical Research* 112, B09207. <http://dx.doi.org/10.1029/2006JB004613>.
- Ripepe, M., De Angelis, S., Lacanna, G., Poggi, P., Williams, C., Marchetti, E., Delle Donne, D., Olivieri, G., 2009. Tracking pyroclastic flows at Soufrière Hills Volcano. *Eos, Transactions American Geophysical Union* 90 (27).
- Ripperger, J., Igel, H., Wasserman, J., 2003. Seismic wave simulation in the presence of real volcano topography. *Journal of Volcanology and Geothermal Research* 128, 31–44.
- Rivet, J.-P., Boon, J.P., 2001. Lattice Gas Hydrodynamics. Cambridge University Press, Cambridge. (289 pp.).
- Rodgers, P.W., 1968. The response of the horizontal pendulum seismometer to Rayleigh and Love waves, tilt, and free oscillations of the earth. *Bulletin of the Seismological Society of America* 58, 1385–1406.
- Roggensack, K., 2001. Unraveling the 1974 eruption of Fuego volcano (Guatemala) with small crystals and their young melt inclusions. *Geology* 29 (10), 911–914.
- Roman, D.C., 2005. Numerical models of volcanotectonic earthquake triggering on non-ideally oriented faults. *Geophysical Research Letters* 32, L02304. <http://dx.doi.org/10.1029/2004GL021549>.
- Roman, D.C., Cashman, K.V., 2006. The origin of volcano-tectonic earthquake swarms. *Geology* 34 (6), 457–460.
- Roman, D.C., Heron, P., 2007. Effect of regional tectonic setting on local fault response to episodes of volcanic activity. *Geophysical Research Letters* 34, L13310. <http://dx.doi.org/10.1029/2007GL030222>.
- Roman, D.C., Moran, S.C., Power, J.A., Cashman, K.V., 2004. Temporal and spatial variation of local stress fields during the 1992 eruptions of Crater Peak vent, Mount Spurr Volcano, Alaska. *Bulletin of the Seismological Society of America* 94, 2366–2379.
- Roman, D.C., Neuberg, J., Luckett, R.R., 2006. Assessing the likelihood of volcanic eruption through analysis of volcanotectonic earthquake fault-plane solutions. *Earth and Planetary Science Letters* 248, 244–252.
- Roman, D.C., De Angelis, S., Lachtman, J.L., White, R., 2008. Patterns of volcanotectonic seismicity and stress during the ongoing eruption of Soufrière Hills Volcano, Montserrat (1995–2007). *Journal of Volcanology and Geothermal Research* 173, 230–244.
- Roux, P., Sabra, K.G., Kuperman, W.A., Roux, A., 2005. Ambient noise cross correlation in free space: theoretical approach. *Journal of the Acoustical Society of America* 117 (1), 79–84.
- Rowe, C., Aster, R., Kyle, P., Schlué, J., Dibble, R., 1998. Broadband recording of Strombolian explosions and associated very-long-period seismic signals on Mount Erebus Volcano, Ross Island, Antarctica. *Geophysical Research Letters* 25 (13), 2297–2300.
- Rowe, C., Thurber, R.C.H., White, R.A., 2004. Dome growth behavior at Soufrière Hills Volcano, Montserrat, revealed by relocation of volcanic event swarms, 1995–1996. *Journal of Volcanology and Geothermal Research* 134, 199–221.
- Rowland, J.V., Baker, E., Ebinger, C.J., Keir, D., Kidane, T., Biggs, J., Hayward, N., Wright, T.J., 2007. Fault growth at a nascent slow-spreading ridge: 2005 Dabbahu rifting episode. *Geophysical Journal International* 171, 1226–1246.
- Rubin, A.M., 1995. Propagation of magma-filled cracks. *Annual Review of Earth and Planetary Sciences* 23, 287–336.
- Rubin, A.M., Gillard, D., 1998. Dike-induced earthquakes: theoretical considerations. *Journal of Geophysical Research* 103 (B5), 10,017–10,030.
- Rubin, A.M., Pollard, D.D., 1988. Dike-induced faulting in rift zones of Iceland and Afar. *Geology* 16, 413–417.
- Rust, A.C., Cashman, K.V., Wallace, P.J., 2004. Magma degassing buffered by vapor flow through brecciated conduit margins. *Geology* 32, 349–352.
- Rust, A.C., Balmforth, N.J., Mandre, S., 2008. The feasibility of generating low-frequency volcano seismicity by flow through a deformable channel. In: Lane, S.J., Gilbert, J.S. (Eds.), *Fluid Motions in Volcanic Conduits: A Source of Seismic and Acoustic Signals*. Geol. Soc., London, Special Publications, 307, pp. 45–56.
- Sabra, K.G., Gerstoft, P., Roux, P., Kuperman, W.A., Fehler, M.C., 2005a. Surface wave tomography from microseisms in Southern California. *Geophysical Research Letters* 32, L14311. <http://dx.doi.org/10.1029/2005GL023155>.
- Sabra, K.G., Gerstoft, P., Roux, P., Kuperman, W.A., Fehler, M.C., 2005b. Extracting time-domain Green's function estimates from ambient seismic noise. *Geophysical Research Letters* 32, L03310. <http://dx.doi.org/10.1029/2004GL021862>.
- Saccorotti, G., Chouet, B., Dawson, P., 2001. Wavefield properties of a shallow long-period event and tremor at Kilauea Volcano, Hawaii. *Journal of Volcanology and Geothermal Research* 109, 163–189.
- Saccorotti, G., Chouet, B., Dawson, P., 2003. Shallow-velocity models at the Kilauea Volcano, Hawaii, determined from array analyses of tremor wavefields. *Geophysical Journal International* 152, 633–648.
- Saccorotti, G., Lokmer, I., Bean, C.J., Di Grazia, G., Patane, D., 2007. Analysis of sustained long-period activity at Etna Volcano, Italy. *Journal of Volcanology and Geothermal Research* 109, 163–189.
- Sassa, K., 1935. Volcanic micro-tremors and eruption earthquakes (Part 1 of the geophysical studies on the volcano Aso). *Memoirs of the College of Science, Kyoto, Imperial University*, 18, pp. 255–293.
- Savage, M.K., Wessel, A., Teanby, N.A., Hurst, A.W., 2010. Automatic measurement of shear wave splitting and applications to time varying anisotropy at Mount Ruapehu volcano, New Zealand. *Journal of Geophysical Research* 115, B12321. <http://dx.doi.org/10.1029/2010JB007722>.
- Scandone, R., Malone, S.D., 1985. Magma supply, magma discharge and readjustment of the feeding system of Mount St. Helens during 1980. *Journal of Volcanology and Geothermal Research* 23, 239–262.
- Schlindwein, V., Wassermann, J., Scherbaum, F., 1995. Spectral analysis of harmonic tremor signals. *Geophysical Research Letters* 22 (13), 1685–1688.
- Schmidt, R.O., 1986. Multiple emitter location and signal parameter estimation. *IEEE Transactions on Antennas and Propagation* 34, 276–280.
- Scott, W.E., Sherrod, D.R., Gardner, C.A., 2008. Overview of the 2004–2006, and continuing, eruption of Mount St. Helens. Washington. In: Sherrod, D.R., Scott, W.E., Stauffer, P.H. (Eds.), *A Volcano Rekindled: The Renewed Eruption of Mount St. Helens, 2004–2006*: U.S. Geological Survey Professional Paper 1750, pp. 3–22 (Chap. 1).
- Sciven, L.E., 1959. On the dynamics of phase growth. *Chemical Engineering Science* 10, 1–13.
- Sens-Schönfelder, C., Wegler, U., 2006. Passive image interferometry and seasonal variations of seismic velocities at Merapi Volcano, Indonesia. *Geophysical Research Letters* 33, L21302. <http://dx.doi.org/10.1029/2006GL027797>.
- Shapiro, N.M., Campillo, M., 2004. Emergence of broadband Rayleigh waves from correlations of the ambient seismic noise. *Geophysical Research Letters* 31, L07614. <http://dx.doi.org/10.1029/2004GL101949>.
- Shapiro, N.M., Campillo, M., Stehly, L., Ritzwoller, M.H., 2005. High-resolution surface-wave tomography from ambient seismic noise. *Science* 307, 1615–1618.
- Shaw, H.R., 1972. Viscosities of magmatic silicate liquids: an empirical method of prediction. *American Journal of Science* 272, 870–893.
- Shaw, H.R., Chouet, B., 1989. Singularity spectrum of intermittent seismic tremor at Kilauea Volcano, Hawaii. *Geophysical Research Letters* 16 (2), 195–198.
- Shaw, H.R., Chouet, B., 1991. Fractal hierarchies of magma transport in Hawaii and critical self-organization of tremor. *Journal of Geophysical Research* 96 (B6), 10,191–10,207.
- Shelly, D.R., Hill, D.P., 2011. Migrating swarms of brittle-failure earthquakes in the lower crust beneath Mammoth Mountain, California. *Geophysical Research Letters* 38, L20307. <http://dx.doi.org/10.1029/2011GL049336>.
- Shevenell, L., Goff, F., 1993. Addition of magmatic volatiles into the hot spring waters of Loowit Canyon, Mount St. Helens, Washington, USA. *Bulletin of Volcanology* 55, 489–503.
- Shimomura, Y., Nishimura, T., Sato, H., 2006. Bubble growth processes in magma surrounded by an elastic medium. *Journal of Volcanology and Geothermal Research* 155, 307–322.
- Sisson, T.W., Lane, G.D., 1993. H_2O in basalt and basaltic andesite glass inclusions from four subduction-related volcanoes. *Earth and Planetary Science Letters* 117, 619–635.
- Smith, K.D., von Seggern, D., Blewitt, G., Preston, L., Anderson, J.G., Wernicke, B.P., Davis, J.L., 2004. Evidence for deep magma injection beneath Lake Tahoe, Nevada-California. *Science* 305, 1277–1280.
- Sniieder, R., Grêt, A., Douma, H., Scales, J., 2002. Coda wave interferometry for estimating nonlinear behavior in seismic velocity. *Science* 295, 2253–2255.
- Sniieder, R., Miyazawa, M., Slob, E., Vasconcelos, I., Wapenaar, K., 2009. A comparison of strategies for seismic interferometry. *Surveys in Geophysics* 30, 503–523.
- Soosalu, H., Key, J., White, R.S., Knox, C., Einarsson, P., Jakobsdóttir, S.S., 2010. Lower-crustal earthquakes caused by magma movement beneath Askja Volcano on the north Iceland rift. *Bulletin of Volcanology* 72, 55–62.
- Sparks, R., 1978. The dynamics of bubble formation and growth in magmas: a review and analysis. *Journal of Volcanology and Geothermal Research* 3, 1–38.
- Sparks, R.S.J., 1997. Causes and consequences of pressurization in lava dome eruptions. *Earth and Planetary Science Letters* 150, 177–189.
- Sparks, R.S.J., Pinkerton, H., 1978. Effect of degassing on rheology of basaltic lava. *Nature* 276 (5686), 385–386.
- St. Lawrence, W., Qamar, A., 1979. Hydraulic transients: a seismic source in volcanoes and glaciers. *Science* 203, 654–656.
- Stankiewicz, J., Ryberg, T., Haberland, C., Fauzi, Natawidjaja, D., 2010. Lake Toba Volcano magma chamber imaged from ambient seismic noise tomography. *Geophysical Research Letters* 37, L17306. <http://dx.doi.org/10.1029/2010GL044211>.

- Stasiuk, M.V., Barclay, J., Carroll, M.R., Jaupart, C., Ratté, J.C., Sparks, R.S.J., Tait, S.R., 1996. Degassing during magma ascent in the Mule Creek vent (USA). *Bulletin of Volcanology* 58, 117–130.
- Steely, L., Campillo, M., Froment, B., Weaver, R.L., 2008. Reconstructing Green's function by correlation of the coda of the correlation (C^3) of ambient seismic noise. *Journal of Geophysical Research* 113, B11306. <http://dx.doi.org/10.1029/2008JB005693>.
- Stein, R.S., 1999. The role of stress transfer in earthquake occurrence. *Nature* 402, 605–609.
- Stephens, C.D., Chouet, B.A., 2001. Evolution of the December 14, 1989 precursory long-period event swarm at Redoubt Volcano, Alaska. *Journal of Volcanology and Geothermal Research* 109, 133–148.
- Succi, S., 2001. The Lattice Boltzmann Equation for Fluid Dynamics and Beyond. Clarendon Press, Oxford. (288 pp.).
- Suckale, J., Nave, J.-C., Hager, B.H., Elkins-Tanton, L.T., Nave, J.-C., 2010a. It takes three to tango: 1. Simulating buoyancy-driven flow in the presence of large viscosity contrasts. *Journal of Geophysical Research* 115, B07409. <http://dx.doi.org/10.1029/2009JB006916>.
- Suckale, J., Hager, B.H., Elkins-Tanton, L.T., Nave, J.-C., 2010b. It takes three to tango: 2. Bubble dynamics in basaltic volcanoes and ramifications for modeling normal Strombolian activity. *Journal of Geophysical Research* 115, B07410. <http://dx.doi.org/10.1029/2009JB006917>.
- Suckale, J., Hager, B.H., Elkins-Tanton, L.T., Nave, J.-C., 2011. Reply to the comment by Mike R. James et al. on "It takes three to tango: 2. Bubble dynamics in basaltic volcanoes and ramifications for modeling normal Strombolian activity". *Journal of Geophysical Research* 116, B06208. <http://dx.doi.org/10.1029/2011JB008351>.
- Sukop, M.C., Thorne, D.T., 2006. Lattice Boltzmann Modeling – An Introduction for Geoscientists and Engineers. Springer, New York. (172 pp.).
- Takei, Y., Kumazawa, M., 1994. Why have the single force and torque been excluded from seismic source models? *Geophysical Journal International* 109, 163–189.
- Tanaka, H.K.M., Nakano, T., Takahashi, S., Yoshida, J., Oshima, H., Maekawa, T., Watanabe, H., Niwa, K., 2007a. Imaging the conduit size of the dome with cosmic-ray muons: the structure beneath Showa-Shinzan Lava Dome, Japan. *Geophysical Research Letters* 34, L22311. <http://dx.doi.org/10.1029/2007GL031389>.
- Tanaka, H.K.M., Nakano, T., Takahashi, S., Yoshida, J., Takeo, M., Oikawa, J., Ohminato, T., Aoki, Y., Koyama, E., Tsuji, H., Niwa, K., 2007b. High resolution imaging in the inhomogeneous crust with cosmic-ray muon radiography: the density structure below the volcanic crater floor of Mt. Asama, Japan. *Earth and Planetary Science Letters* 263, 104–113.
- Tanaka, H.K.M., Nakano, T., Takahashi, S., Yoshida, J., Takeo, M., Oikawa, J., Ohminato, T., Aoki, Y., Koyama, E., Tsuji, H., Oshima, H., Maekawa, T., Watanabe, H., Niwa, K., 2008. Radiographic imaging below a volcanic crater floor with cosmic-ray muons. *American Journal of Science* 308, 843–850.
- Tanaka, H.K.M., Uchida, T., Tanaka, M., Takeo, M., Oikawa, J., Ohminato, T., Aoki, Y., Koyama, E., Tsuji, H., 2009a. Detecting a mass change inside a volcano by cosmic-ray muon radiography (muography): first results from measurements at Asama Volcano, Japan. *Geophysical Research Letters* 36, L17302. <http://dx.doi.org/10.1029/2009GL039448>.
- Tanaka, H.K.M., Uchida, T., Tanaka, M., Shinohara, H., Taira, H., 2009b. Cosmic-ray muon imaging of magma in a conduit: degassing process at Satsuma-Iwojima Volcano, Japan. *Geophysical Research Letters* 36, L01304. <http://dx.doi.org/10.1029/2008GL036451>.
- Tanaka, H.K.M., Uchida, T., Tanaka, M., Takeo, M., Ohminato, T., Aoki, Y., Nishitama, R., Shoji, D., Tsuji, H., 2010. Three-dimensional computational axial tomography scan of a volcano with cosmic ray muon radiography. *Journal of Geophysical Research* 115, B12332. <http://dx.doi.org/10.1029/2010JB007677>.
- Tanimoto, T., 1999. Excitation of normal modes by atmospheric turbulence: source of long-period seismic noise. *Geophysical Journal International* 149, 755–767.
- Thelen, W.A., Crosson, R.S., Creager, K.C., 2008. Absolute and relative locations of earthquakes at Mount St. Helens, Washington using continuous data: implications for magmatic processes. In: Sherrod, D.R., Scott, W.E., Stauffer, P.H. (Eds.), *A Volcano Rekindled: The Renewed Eruption of Mount St. Helens, 2004–2006*. U.S. Geological Survey Professional Paper 1750, pp. 71–95 (Chap. 4).
- Thelen, W., West, M., Senyukov, S., 2010. Seismic characterization of the fall 2007 eruptive sequence at Bezymianny Volcano, Russia. *Journal of Volcanology and Geothermal Research* 194, 201–213.
- Thiéry, R., Mercury, L., 2009a. Explosive properties of water in volcanic and hydrothermal systems. *Journal of Geophysical Research* 114, B05205. <http://dx.doi.org/10.1029/2008JB005742>.
- Thiéry, R., Mercury, L., 2009b. Explosive conditions of aqueous solutions. *Journal of Solution Chemistry* 38, 893–905.
- Thomas, M.E., Neuberg, J., 2012. What makes a volcano tick – a first explanation of deep multiple seismic sources in ascending magma. *Geology* 40 (4), 351–354.
- Thurber, C.H., 1983. Earthquake locations and three-dimensional crustal structure in the Coyote Lake Area, Central California. *Journal of Geophysical Research* 88 (B10), 8226–8236.
- Thurber, C.H., 1993. Local earthquake tomography: velocities and V_p/V_s – theory. In: Iyer, H., Hirahara, K. (Eds.), *Seismic Tomography, Theory and Practice*. CRC Press, Boca Raton, Florida, pp. 563–583.
- Thurber, C.H., Atre, S.R., Eberhardt-Phillips, D., 1995. Three-dimensional V_p and V_p/V_s structure at Loma Prieta, California. *Geophysical Research Letters* 22, 3079–3082.
- Toda, S., Stein, R.S., Sagiya, T., 2002. Evidence from the AD 2000 Izu islands earthquake swarm that stressing rate governs seismicity. *Nature* 419, 58–61.
- Toramaru, A., 1989. Vesication process and bubble size distributions in ascending magmas with constant velocities. *Journal of Geophysical Research* 94, 17,523–17,542.
- Toramaru, A., 1995. Numerical study of nucleation and growth of bubbles in viscous magmas. *Journal of Geophysical Research* 100, 1913–1931.
- Traversa, P., Lengliné, O., Macedo, O., Metaxian, J.P., Grasso, J.R., Inza, A., Taipe, E., 2011. Short term forecasting of explosions at Ubinas Volcano, Perú. *Journal of Geophysical Research* 116, B11301. <http://dx.doi.org/10.1029/2010JB008180>.
- Tuffen, H., Dingwell, D., 2005. Fault textures in volcanic conduits: evidence for seismic trigger mechanisms during silicic eruptions. *Bulletin of Volcanology* 67, 370–387.
- Tuffen, H., Dingwell, D.B., Pinkerton, H., 2003. Repeated fracture and healing of silicic magma generates flow banding and earthquakes? *Geology* 31, 1089–1092.
- Tuffen, H., Smith, R., Sammonds, P.R., 2008. Evidence for seismogenic fracture of silicic magma. *Nature* 453, 511–514.
- Uhira, K., Takeo, M., 1994. The source of explosive eruptions of Sakurajima volcano, Japan. *Journal of Geophysical Research* 99 (B9), 17,775–17,789.
- Uhira, K., Yamashita, H., Takeo, M., 1994. Source mechanism of seismic waves excited by pyroclastic flows observed at Unzen Volcano, Japan. *Journal of Geophysical Research* 99, 17,757–17,773.
- Ukawa, M., 2005. Deep low-frequency earthquake swarm in the mid crust beneath Mount Fuji (Japan) in 2000 and 2001. *Bulletin of Volcanology* 68, 47–56.
- Ukawa, M., Tsukahara, H., 1996. Earthquake swarms and dike intrusions off the east coast of Izu Peninsula, central Japan. *Tectonophysics* 253, 285–303.
- Um, J., Thurber, C., 1987. A fast algorithm for two-point seismic ray tracing. *Bulletin of the Seismological Society of America* 77 (3), 972–986.
- Umakoshi, K., Shimizu, H., Matsuo, N., 2001. Volcano-tectonic seismicity at Unzen Volcano, Japan, 1985–1999. *Journal of Volcanology and Geothermal Research* 112, 117–131.
- Valade, S., Donnadieu, F., Lesage, P., Mora, M.M., Harris, A., Alvarado, G.E., 2012. Explosion mechanisms at Arenal volcano, Costa Rica: an interpretation from integration of seismic and Doppler radar data. *Journal of Geophysical Research* 117, B01309. <http://dx.doi.org/10.1029/2011JB008623>.
- Vallance, J.W., Schneider, D.J., Schilling, S.P., 2008. Growth of the 2004–2008 lava-dome complex at Mount St. Helens, Washington. In: Sherrod, D.R., Scott, W.E., Stauffer, P.H. (Eds.), *A Volcano Rekindled: The Renewed Eruption of Mount St. Helens, 2004–2006*. U.S. Geological Survey Professional Paper 1750, pp. 169–224 (Chap. 9).
- Vargas-Bracamontes, D.M., Neuberg, J.W., 2012. Interaction between regional and magma-induced stresses and their impact on volcano-tectonic seismicity. *Journal of Volcanology and Geothermal Research*. <http://dx.doi.org/10.1016/j.jvolgeores.2012.06.025>.
- Varley, N.R., Arambula-Mendoza, R., Reyes-Davila, G., Sanderson, R., Stevenson, J., 2010a. Generation of Vulcanian activity and long-period seismicity at Volcan de Colima, Mexico. *Journal of Volcanology and Geothermal Research* 198, 45–56.
- Varley, N.R., Arambula-Mendoza, R., Reyes-Davila, G., Stevenson, J., Harwood, R., 2010b. Long-period seismicity during magma movement at Volcan de Colima. *Bulletin of Volcanology* 72, 1093–1107.
- Vergniolle, S., Caplan-Auerbach, J., 2006. Basaltic thermals and sub-Plinian plumes: constraints from acoustic measurements at Shishaldin Volcano, Alaska. *Bulletin of Volcanology* 68, 611–630.
- Vergniolle, S., Brandeis, G., Mareschal, J.C., 1996. Strombolian explosions, 2. Eruption dynamics determined from acoustic measurements. *Journal of Geophysical Research* 101, 20,449–20,466.
- Vidale, J., 1988. Finite-difference calculations of traveltimes. *Bulletin of the Seismological Society of America* 78, 2062–2076.
- Vidale, J., 1991. Finite-difference calculation of traveltimes in three dimensions. *Geophysics* 55, 521–526.
- Voight, B., 1988. A method for prediction of volcanic eruptions. *Nature* 332, 125–130.
- Voight, B., Sparks, R.S.J., Miller, A.D., Stewart, R.C., Hoblitt, R.P., Clarke, A., Ewart, J., Aspinall, W.P., Baptie, B., Calder, E.S., Cole, P., Druitt, T.H., Hartford, C., Herd, R.A., Jackson, P., Lejeune, A.M., Lockhart, A.B., Loughlin, S.C., Luckett, R., Lynch, L., Norton, G.E., Robertson, R., Watson, I.M., Watts, R., Young, S.R., 1999. Magma flow instability and cyclic activity at Soufrière Hills Volcano, Montserrat, British West Indies. *Science* 283, 1138–1142. <http://dx.doi.org/10.1126/science.283.5405.1138>.
- von Seggern, D.H., Smith, K.D., Preston, L.A., 2008. Seismic spatial-temporal character and effects of a deep (25–30 km) magma intrusion below North Lake Tahoe, California-Nevada. *Bulletin of the Seismological Society of America* 98 (3), 1508–1526.
- Wagner, W., Pruss, A., 2002. The IAPWS formulation 1995 for the thermodynamic properties of ordinary water substance for general and scientific use. *Journal of Physical and Chemical Reference Data* 31 (2).
- Waite, G.P., Chouet, B.A., Dawson, P.B., 2008. Eruption dynamics at Mount St. Helens imaged from broadband seismic waveforms: interaction of the shallow magmatic and hydrothermal systems. *Journal of Geophysical Research* 113, B02305. <http://dx.doi.org/10.1029/2007JB005259>.
- Walder, J.S., Schilling, S.P., Vallance, J.W., LaHusen, R.G., 2008. Effects of lava-dome growth on the Crater Glacier of Mount St. Helens, Washington. In: Sherrod, D.R., Scott, W.E., Stauffer, P.H. (Eds.), *A Volcano Rekindled: The Renewed Eruption of Mount St. Helens, 2004–2006*. U.S. Geological Survey Professional Paper 1750, pp. 257–276 (Chap. 13).
- Waldhauser, F., 2001. HypoDD: a computer program to compute double-difference hypocenter locations: U.S. Geol. Surv. Open File Rep., 01–113 (25 pp.).
- Waldhauser, F., Ellsworth, W., 2000. A double-difference earthquake location algorithm: method and application to the northern Hayward fault, California. *Bulletin of the Seismological Society of America* 90, 1353–1368.
- Walker, K.T., Hedin, M.A.H., 2010. A review of wind-noise reduction methodologies. In: Le Pichon, A., Blanc, E., Hauchecorne, A. (Eds.), *Infrasound Monitoring for Atmospheric Studies*. Springer, Netherlands, pp. 141–182 (Chap. 5).
- Wapenaar, K., Fokkema, J., 2006. Green's function representations for seismic interferometry. *Geophysics* 71, SI33–SI46.
- Wapenaar, K., van der Neut, J., Ruigrok, E., Dragonov, D., Hunziker, J., Slob, E., Thorbecke, J., Snieder, R., 2011. Seismic interferometry by crosscorrelation and by multidimensional deconvolution: a systematic comparison. *Geophysical Journal International* 185, 1335–1364.
- Watada, S., Kanamori, H., 2010. Acoustic resonant oscillations between the atmosphere and the solid earth during the 1991 Mt. Pinatubo eruption. *Journal of Geophysical Research* 115, B12319. <http://dx.doi.org/10.1029/2010JB007747>.

- Webb, S.L., Dingwell, D.B., 1990. Non-Newtonian rheology of igneous melts at high stresses and strain rates: experimental results for rhyolite, andesite, basalt, and nepheline. *Journal of Geophysical Research* 95 (B10), 15,695–15,701.
- Wegler, U., Lühr, B.-G., Snieder, R., Ratdomopurbo, A., 2006. Increase in shear wave velocity before the 1998 eruption of Merapi Volcano (Indonesia). *Geophysical Research Letters* 33, L09303. <http://dx.doi.org/10.1029/2006GL025928>.
- White, R.A., 1996. Precursory deep long-period earthquakes at Mount Pinatubo: spatio-temporal links to a basaltic trigger. In: Newhall, C.G., Punongbayan, R.S. (Eds.), *Fire and Mud. Eruptions and Lahars of Mount Pinatubo, Philippines*. Univ. of Washington Press, Seattle, Washington, pp. 307–328.
- White, R.S., Drew, J., Martens, H.R., Key, J., Soosalu, H., Jakobsson, S.S., 2011. Dynamics of dyke intrusion in the mid-crust of Iceland. *Earth and Planetary Science Letters* 311, 300–312.
- Wilson, L., Head, J.W., 1981. Ascent and eruption of basaltic magma on the earth and moon. *Journal of Geophysical Research* 86, 2971–3001.
- Wohletz, K.H., 1986. Explosive magma–water interactions: thermodynamics, explosion mechanisms, and field studies. *Bulletin of Volcanology* 48, 245–264.
- Wohletz, K., Heiken, G., 1992. *Volcanology and Geothermal Energy*. University of California Press.
- Wright, T.L., Klein, F.W., 2006. Deep magma transport at Kilauea Volcano, Hawaii. *Lithos* 87, 50–79.
- Wright, T.J., Ebinger, C., Biggs, J., Ayele, A., Yirgu, G., Keir, D., Stork, A., 2006. Magma-maintained rift segmentation at continental rupture in the 2005 Afar dyking episode. *Nature* 442, 291–294.
- Yamamoto, M., Kawakatsu, H., 2009. An efficient method to compute the dynamic response of a fluid-filled crack. *Geophysical Journal International* 174, 1174–1186.
- Yamamoto, M., Kawakatsu, H., Kaneshima, S., Mori, T., Tsutsui, T., Sudo, Y., Morita, Y., 1999. Detection of a crack-like conduit beneath the active crater at Aso Volcano, Japan. *Geophysical Research Letters* 26, 3677–3680.
- Yamamoto, M., Kawakatsu, H., Yomogida, K., Koyama, J., 2002. Long-period (12 sec) volcanic tremor observed at Usu 2000 eruption: seismological detection of a deep magma plumbing system. *Geophysical Research Letters* 29 (9), 1329. <http://dx.doi.org/10.1029/2001GL013996>.
- Yamasato, H., 1997. Quantitative analysis of pyroclastic flows using infrasonic and seismic data at Unzen volcano, Japan. *Journal of Physics of the Earth* 45 (6), 397–416.
- Yamasato, H., 1998. Nature of infrasonic pulse accompanying low frequency earthquake at Unzen Volcano, Japan. *Bulletin of the Volcanological Society of Japan* 43, 1–13.
- Yao, H., van der Hilst, R.D., de Hoop, M.V., 2006. Surface-wave array tomography in SE Tibet from ambient seismic noise and two-station analysis – I. Phase velocity maps. *Geophysical Journal International* 166, 732–744.
- Yao, H., Beghein, C., van der Hilst, R.D., 2008. Surface-wave array tomography in SE Tibet from ambient seismic noise and two-station analysis – II. Crustal and upper-mantle structure. *Geophysical Journal International* 173, 205–219.
- Yoshimura, S., Nakamura, M., 2010. Fracture healing in a magma: an experimental approach and implications for volcanic seismicity and degassing. *Journal of Geophysical Research* 115, B09209. <http://dx.doi.org/10.1029/2009JB000834>.
- Yue, P., Feng, J.J., Liu, C., Shen, J., 2004. A diffuse-interface method for simulating two-phase flows of complex fluids. *Journal of Fluid Mechanics* 515, 293–317.
- Zhang, H., Thurber, C.H., 2003. Double-difference tomography: the method and its application to the Hayward Fault, California. *Bulletin of the Seismological Society of America* 93 (5), 1875–1889.
- Zhang, Y., Xu, Z., Liu, Y., 2003. Viscosity of hydrous rhyolitic melts inferred from kinetic experiments: a new viscosity model. *American Mineralogist* 88, 1741–1752.
- Zimanowski, B., Frohlich, G., Lorenz, V., 1991. Quantitative experiments on phreatomagmatic explosions. *Journal of Volcanology and Geothermal Research* 48, 341–358.
- Zobin, V., 2012. 2nd edition. *Introduction to Volcanic Seismology*. Elsevier.
- Zobin, V.M., Reyes, G.A., Guevara, E., Breton, M., 2008. Seismological constraints on the position of the fragmentation surfaces in the volcano conduit. *Earth and Planetary Science Letters* 275, 337–341.
- Zobin, V.M., Reyes, G.A., Guevara, E., Breton, M., 2009. Scaling relationship for Vulcanian explosions derived from broadband seismic signals. *Journal of Geophysical Research* 114, B03203. <http://dx.doi.org/10.1029/2008JB005983>.